



**HAL**  
open science

# Manipulation magnétoélectrique de parois de domaine transverses dans des nanostructures magnétoélastiques

Théo Mathurin

► **To cite this version:**

Théo Mathurin. Manipulation magnétoélectrique de parois de domaine transverses dans des nanostructures magnétoélastiques. Micro and nanotechnologies/Microelectronics. Ecole Centrale de Lille, 2017. English. NNT : 2017ECLI0014 . tel-01784606

**HAL Id: tel-01784606**

**<https://theses.hal.science/tel-01784606>**

Submitted on 3 May 2018

**HAL** is a multi-disciplinary open access archive for the deposit and dissemination of scientific research documents, whether they are published or not. The documents may come from teaching and research institutions in France or abroad, or from public or private research centers.

L'archive ouverte pluridisciplinaire **HAL**, est destinée au dépôt et à la diffusion de documents scientifiques de niveau recherche, publiés ou non, émanant des établissements d'enseignement et de recherche français ou étrangers, des laboratoires publics ou privés.

Numéro d'ordre : 328

CENTRALE LILLE

# THÈSE

pour obtenir le grade de :

DOCTEUR

dans la spécialité

« MICRO ET NANO TECHNOLOGIES, ACOUSTIQUE ET TÉLÉCOMMUNICATIONS »

par

Théo Mathurin

Doctorat délivré par Centrale Lille

Manipulation magnétoélectrique de parois de domaine  
transverses dans des nanostructures magnétoélastiques

---

Magnetoelectric manipulation of transverse domain walls  
in magnetoelastic nanostructures

Soutenance le 14 novembre 2017 devant le jury composé de :

Mme. URSULA EBELS	Ingénieure-chercheuse CEA, SPINTEC	(Rapporteure)
M. ANDRÉ THIAVILLE	Directeur de recherche CNRS, LPS	(Rapporteur)
Mme. ANNE BERNAND-MANTEL	Chargée de recherche CNRS, Institut Néel	(Examinatrice)
M. MICHEL HEHN	Professeur à l'Université de Lorraine, IJL	(Examinateur)
M. PHILIPPE LECOEUR	Professeur à l'Université Paris-Sud, C2N	(Examinateur, président)
M. PHILIPPE PERNOD	Professeur à Centrale Lille, IEMN	(Co-directeur de thèse)
M. NICOLAS TIERCELIN	Chargé de recherche CNRS, IEMN	(Co-directeur de thèse)
M. STEFANO GIORDANO	Chargé de recherche CNRS, IEMN	(Co-encadrant)
M. YANNICK DUSCH	Maître de conférence à Centrale Lille, IEMN	(Invité, co-encadrant)
M. VLADIMIR PREOBRAZHENSKY	Professeur émérite à Centrale Lille, IEMN	(Invité)

**Thèse préparée au Laboratoire International Associé (LIA) LEMAC/LICS**

IEMN - CITÉ SCIENTIFIQUE - AVENUE HENRI POINCARÉ

CS 60069 - 59 652 VILLENEUVE D'ASCQ CEDEX

ECOLE DOCTORALE SPI 072

(LILLE I, LILLE III, ARTOIS, ULCO, UVHC, CENTRALE LILLE)





I heard you're doing a PhD on magnetism.

Could your hands help ease that backpain?

Oh no, I'm sorry. I work on a different kind of magnetism

...  
the one that exists

This thesis is dedicated to my grandparents

## Acknowledgments

First, I would like to express my sincere gratitude to my supervisor Philippe Pernod, who made this PhD possible by finding the funding, and who created the research environment required for the development of the activity on which rests this work. The same goes for my co-supervisor Nicolas Tiercelin, who developed the expertise on rare-earth-based magnetoelastic thin films at the core of this work and managed the overall research project. I also want to thank my PhD advisor Yannick Dusch who was always available from the start to help me get a sense of the science and the software, and who set up the Kerr microscope. Finally, I am deeply indebted to Stefano Giordano—without whom this thesis would not have taken this course—for his unfailing support and the countless thoughtful discussions on various matters, scientific and otherwise.

Besides my supervisors and advisors, I am very much obliged to Anne Bernand-Mantel, Philippe Lecoer, Michel Hehn and Vladimir Preobrazhensky for their participation as members of my thesis committee, and to Ursula Ebels and André Thiaville for kindly accepting to review this manuscript.

I should, but reasonably cannot, mention every one of the permanent and temporary members of the AIMAN-FILMS group in which I have been fully integrated. For those whom I have worked with, I will specifically mention Isabela for having devised and built a convenient substrate mount, Claire without whom I would never have achieved the fabrication process and Olivier for allowing me to get teaching experience at Centrale Lille. Outside the group, I am grateful to Dominique for his time and patience on the AFM/MFM characterization. I also have to acknowledge the key contribution of many people in the clean room personnel and IEMN as a whole.

Among colleagues were also friends, beginning with the now legendary Barrois team with which I have had so many good moments at lunch time over those three years. Among these team mates, I have a special thought for Stefano, Fabio, Ilyesse and Carmelo, to whom I wish all the best for what lies ahead. Outside work, many thanks to the Science Pop gang and the Zoreilles squad. Now on to family members: thanks specifically to my siblings and siblings-in-law, my future stepfather, my mother-in-law and my two parents as well as my late and living grandparents. At last, these acknowledgments would be nothing if I failed to mention my long standing friend and life partner Céline. I am deeply grateful for the laughter, the support, the fulfillment and so much more that her presence brought over the years, and I expect the best is yet to come.

# Contents

<b>Résumé en français</b>	<b>9</b>
<b>Introduction</b>	<b>19</b>
<b>1 Fundamentals and context</b>	<b>21</b>
1.1 Brief introduction to (micro)magnetism . . . . .	21
1.1.1 Magnetization and energy contributions . . . . .	22
1.1.2 Macroscopic behavior of ferromagnetic bodies . . . . .	24
1.1.3 Magnetic configurations and domain walls . . . . .	26
1.1.4 Typology and physical features of domain walls . . . . .	28
1.2 Domain wall motion . . . . .	32
1.2.1 Overview of technological relevance . . . . .	33
1.2.2 The Landau-Lifshitz-Gilbert equation . . . . .	36
1.2.3 Field-based motion . . . . .	38
1.2.4 Current-based motion . . . . .	41
1.3 Magnetoelectric materials . . . . .	44
1.3.1 Intrinsic magnetoelectric materials . . . . .	44
1.3.2 Magnetostriction . . . . .	46
1.3.3 Piezoelectricity . . . . .	47
1.3.4 Artificial magnetoelectric materials . . . . .	48
1.4 Motion induced by uniform stress in magnetoelastic materials . . . . .	51
1.4.1 The need for symmetry breaking . . . . .	51
1.4.2 Symmetry breaking based on bias magnetic field . . . . .	55
1.4.3 Description of the proposed system . . . . .	57
1.4.4 Engineering of cross section . . . . .	60
1.4.5 Proof of concept through micromagnetic simulations . . . . .	61
1.5 Conclusion . . . . .	64

<b>2</b>	<b>Static behavior in magnetoelastic nanostructures</b>	<b>66</b>
2.1	Variational approach to micromagnetism . . . . .	66
2.1.1	Overview . . . . .	67
2.1.2	Definition of the energy functional . . . . .	68
2.1.3	Derivation of classical equations . . . . .	69
2.2	Equilibrium distribution in nanostructures . . . . .	71
2.2.1	Definition of the energy functional . . . . .	72
2.2.2	Effective anisotropy . . . . .	75
2.2.3	Derivation of the main equation . . . . .	76
2.2.4	Boundary conditions and stable states . . . . .	79
2.3	Numerical procedure . . . . .	83
2.3.1	Presentation . . . . .	83
2.3.2	Convergence and test against analytical solution . . . . .	86
2.4	Results . . . . .	89
2.4.1	Motion, confinement and ejection . . . . .	90
2.4.2	Stress-position relationship . . . . .	93
2.4.3	Energetic interpretation . . . . .	95
2.4.4	Piezoelectric generation of stress . . . . .	99
2.5	Conclusion . . . . .	102
<b>3</b>	<b>Dynamics of stress-induced domain wall motion</b>	<b>103</b>
3.1	Equations governing domain wall dynamics . . . . .	103
3.1.1	Overview . . . . .	103
3.1.2	Definition of the energy functional . . . . .	105
3.1.3	Determination of effective field . . . . .	106
3.1.4	Derivation of dynamical equations . . . . .	107
3.2	Numerical procedure . . . . .	109
3.2.1	Presentation . . . . .	110
3.2.2	Convergence and test against analytical solution . . . . .	113
3.3	Dynamics in hourglass geometry . . . . .	115
3.3.1	Shape of domain walls . . . . .	116
3.3.2	Trajectory of domain walls . . . . .	118
3.3.3	Velocity and applied electric field . . . . .	119
3.4	Dynamics in an infinite nanostripe . . . . .	121
3.4.1	Simulating infinite nanostripes . . . . .	121
3.4.2	Steady-states in infinite nanostripes . . . . .	124

3.4.3	Electric and magnetic field dependence of velocity . . . . .	126
3.4.4	Code failure and breakdown phenomenon . . . . .	129
3.5	Conclusion . . . . .	131
<b>4</b>	<b>Experimental investigations</b>	<b>132</b>
4.1	Materials . . . . .	132
4.1.1	Magnetoelastic multilayers . . . . .	132
4.1.2	PMN-PT piezoelectric substrate . . . . .	134
4.1.3	Mechanical coupling . . . . .	135
4.2	Fabrication . . . . .	137
4.2.1	Polishing of the PMN-PT substrate . . . . .	137
4.2.2	Lithography . . . . .	139
4.2.3	Deposition of multilayers . . . . .	141
4.2.4	Lift-off and dry-etching methods . . . . .	144
4.3	Characterization . . . . .	148
4.3.1	Strain gauge measurements . . . . .	148
4.3.2	Magnetic characterization of sputtered layers . . . . .	151
4.3.3	Atomic and Magnetic Force Microscopy . . . . .	154
4.3.4	Magneto-optic Kerr microscopy . . . . .	160
4.4	Prospects . . . . .	163
4.4.1	Optimization of fabrication process . . . . .	163
4.4.2	Control of domain walls in nanostructures . . . . .	164
4.4.3	PMN-PT studs . . . . .	165
4.5	Conclusion . . . . .	167
	<b>Conclusion</b>	<b>169</b>
	<b>Appendix A Domain wall with exchange and anisotropy energy</b>	<b>173</b>
	<b>Appendix B Variational procedure</b>	<b>177</b>
	<b>Appendix C Calculation of the demagnetization field</b>	<b>181</b>
	<b>Appendix D Analytical treatment of domain wall motion</b>	<b>185</b>
	<b>Bibliography</b>	<b>188</b>
	<b>Abstract</b>	<b>219</b>

# Résumé en français

Dans les matériaux possédant un ordre magnétique, la distribution spatiale d'aimantation n'est pas toujours uniforme. Typiquement, des régions d'aimantation uniformes de directions données sont séparées par des *parois de domaine*, au sein desquelles la variation spatiale d'aimantation est importante. Les outils issus de la théorie du micromagnétisme permettent d'interpréter et prédire ces configurations qui correspondent à des minimums d'énergie magnétique, en considérant l'ensemble des contributions énergétiques pertinentes (Zeeman, anisotropie, échange etc.)

La manipulation de structures magnétiques à l'échelle micrométrique ou nanométrique revêt un grand intérêt à la fois fondamental et technologique. En particulier, le déplacement de parois de domaine est le sujet de nombreuses recherches récentes. Le développement rapide de la spintronique et les avancées technologiques associées laissent envisager de nombreuses applications, notamment en microélectronique. L'application de champs magnétiques et de courants électriques offre des possibilités de contrôle aujourd'hui maîtrisées et de mieux en mieux comprises sur le plan théorique. Par exemple, des modèles simples permettent de prédire le comportement d'une paroi de domaine soumise par exemple à un champ magnétique. Jusqu'à un champ seuil, le mouvement est caractérisé par un régime stationnaire et une vitesse augmentant avec le champ appliqué. Au-delà d'une limite communément appelée *Walker breakdown*, la mobilité de la paroi chute de façon abrupte et la dynamique devient plus complexe.

D'autres méthodes moins classiques de manipulation locale de l'aimantation ont fait l'objet de recherches exploratoires. Celles-ci sont entre autres motivées par des considérations de consommation d'énergie, puisque l'utilisation de courants électriques (que ce soit directement ou pour générer des champs magnétiques) est relativement peu performante de ce point de vue. En particulier, l'approche magnétoélectrique, qui consiste à contrôler l'aimantation par des champs électriques plutôt que des courants, représente un candidat prometteur. En utilisant des hétérostructures magnétoélastique/piézoélectrique, il est possible d'obtenir de bons couplages magnétoélectriques. Ainsi, un substrat piézoélectrique

pourra générer une déformation sous l'effet d'un champ électrique et la transmettre à une couche magnétoélastique déposée dessus, qui réagira magnétiquement. Cette opportunité a notamment inspiré le concept derrière une mémoire magnétoélectrique développée à l'IEMN baptisée MELRAM. Un élément magnétoélastique à anisotropie uniaxiale est soumis à un champ de biais statique perpendiculaire à la direction d'anisotropie, qui brise la symétrie quadratique. Cette configuration crée deux états stables. Sous l'effet d'une contrainte appliquée selon une bissectrice de ces deux directions (par exemple par un substrat piézoélectrique), il est possible de favoriser l'un d'eux et ainsi de déterminer l'état dans lequel se trouvera l'élément (voir Fig. A pour une représentation schématique.) En considérant des paramètres réalistes, la dissipation d'énergie associée au basculement d'aimantation peut être réduite de plusieurs ordres de grandeur.

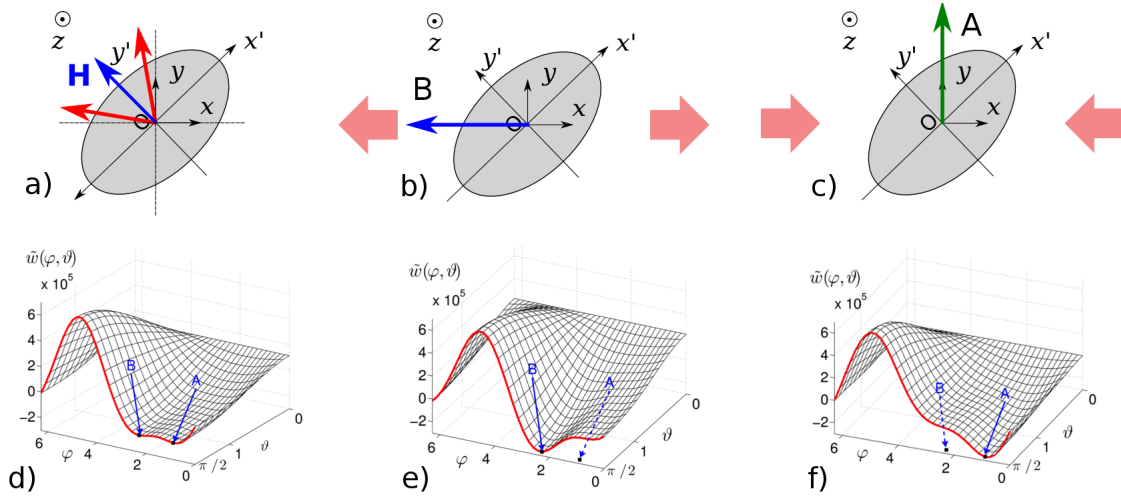


Figure A – Principe de fonctionnement de la mémoire magnétoélectrique (MELRAM), où une contrainte uniforme permet de passer d'un état stable à l'autre de manière non-équivoque. Les sous-figures a) b) et c) présentent schématiquement l'élément magnétoélastique au repos et soumis à des contraintes positives (resp. négatives). Les sous-figures d) e) and f) sont des représentations 3D de l'énergie en fonction des angles.

En se basant sur ce concept, ce travail de thèse propose une technique innovante de déplacement magnétoélectrique de paroi de domaine à basse énergie. Dans ce système, la combinaison d'un champ de biais statique  $H_0$  et d'une contrainte uniaxiale uniforme  $\sigma$  dans la même configuration que pour la MELRAM permet le déplacement unidirectionnel d'une paroi au sein d'une structure magnétoélastique à anisotropie uniaxiale de constante  $K_u$  (voir Fig. B). Le champ de biais est un élément crucial responsable d'une brisure de symétrie, car typiquement, une contrainte uniforme seule ne peut pas engendrer le

mouvement d'une paroi à 180°. L'application d'une contrainte entraîne un écart d'énergie volumique entre les deux domaines, ce qui pousse l'un d'entre eux à s'étendre aux dépens du second, résultant ainsi en un déplacement de paroi unidirectionnel prévisible. Des simulations numériques préliminaires effectuées à l'aide du package Nmag ont permis d'apporter une preuve de principe de ce phénomène.

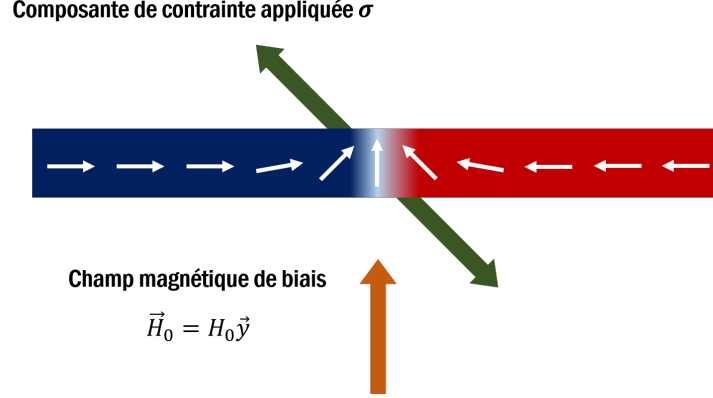


Figure B – Schéma du système considéré : une structure magnétoélastique à deux domaines comportant une paroi de domaine transverse.

Pour étudier le comportement statique du système, un modèle *ad-hoc* a été construit. La géométrie générale choisie, représentée sur la Fig. C, est celle d'une nanostructure ferromagnétique (saturation  $M_s$ ) et magnétoélastique (coefficient  $\lambda_s > 0$ ) de faible épaisseur  $h \leq 20$  nm, de largeur constante ou variable  $\ell \leq 100$  nm et de longueur  $L > 400$  nm. Le modèle est basé sur des hypothèses allégeant considérablement le traitement numérique : on considère que l'aimantation  $\vec{M} = M_s \vec{w}$  demeure dans le plan de la couche et qu'elle ne dépend que d'une variable d'espace  $x$ , de sorte que la seule inconnue est  $\Phi(x)$ .

La première étape consiste à écrire la forme de l'énergie en prenant en considération toutes les contributions sous forme volumique : énergie d'anisotropie quadratique, énergie Zeeman, énergie d'échange, énergie du champ de désaimantation et énergie magnétoélastique. Ainsi, l'expression de l'énergie totale  $U$  peut être exprimée comme suit :

$$U = \int_{-\frac{L}{2}}^{\frac{L}{2}} h\ell(x) \left[ -K_u \cos^2 \Phi + A \left( \frac{d\Phi}{dx} \right)^2 - \mu_0 M_s H_0 \sin \Phi + \frac{3}{2} \lambda_s \sigma \sin \Phi \cos \Phi \right] dx$$

$$- \iint_{V^2} \frac{1}{2} \mu_0 M_s^2 \vec{w}(\vec{r}) \cdot \overline{\vec{N}}(\vec{r}, \vec{r}_0) \vec{w}(\vec{r}_0) d\vec{r}_0 d\vec{r}.$$

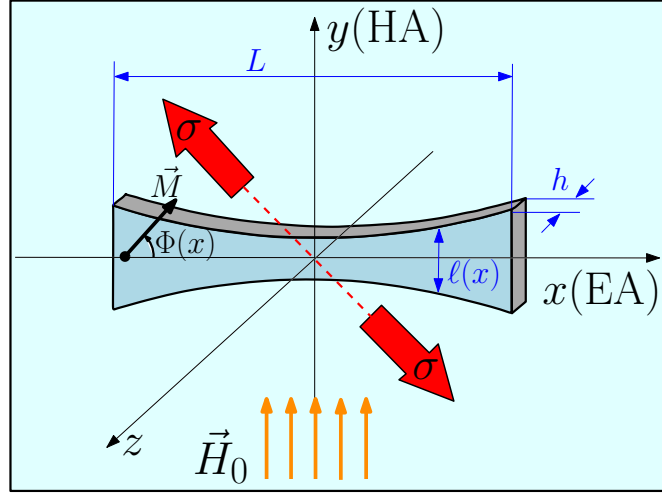


Figure C – Configuration et géométrie de la structure ferromagnétique considérée.

Le dernier terme de cette équation est relatif au champ de désaimantation. Pour trouver la configuration magnétique correspondant à l'état d'équilibre, une méthode variationnelle a été adoptée. Celle-ci consiste à calculer l'expression de la dérivée de Gâteaux de l'énergie, qui doit être nulle pour la configuration d'équilibre.

$$\Phi''(x) + \Phi'(x) \frac{\ell'(x)}{\ell(x)} - \frac{1}{2A} \left[ 2K_u \cos \Phi \sin \Phi - \mu_0 M_s H_0 \cos \Phi + \frac{3}{2} \lambda_s \sigma \cos 2\Phi \right. \\ \left. + \mu_0 M_s \sin \Phi \langle \vec{H}_{dx} \rangle_{y,z} - \mu_0 M_s \cos \Phi \langle \vec{H}_{dy} \rangle_{y,z} \right] = 0.$$

Il est clair qu'une telle équation intégrale-différentielle non-linéaire aux dérivées partielles ne peut être résolue analytiquement. Un traitement numérique est donc nécessaire. L'approche choisie est basée sur une procédure itérative, ou de relaxation, où l'on cherche le zéro d'une fonction par la méthode de la dichotomie, implémentée sous MATLAB. Une méthode originale et très efficace de calcul du champ de désaimantation a par ailleurs été développée. La procédure numérique ainsi construite a été validée par une comparaison avec des solutions analytiques connues.

Les résultats obtenus ont confirmé la possibilité de déplacer une paroi de cette manière. Dans un nanoruban (largeur  $\ell$  constante) la paroi se déplace jusqu'à être éjectée et laisser une configuration monodomaine. Dans une géométrie à largeur variable, il est possible de confiner la paroi qui trouve une position d'équilibre. Celle-ci dépend de la contrainte appliquée, comme illustré sur la Fig. D.

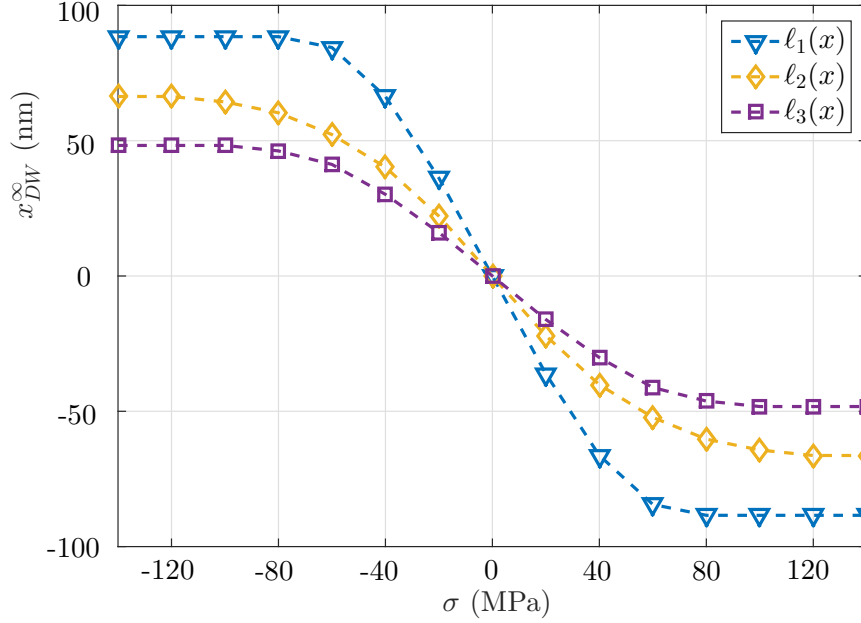


Figure D – Position d'équilibre  $x_{DW}^{\infty}$  de la paroi de domaine en fonction de la contrainte appliquée pour trois profils de section quadratiques différents.

Des analyses sur les différentes contributions énergétiques ainsi qu'un travail sur un second modèle encore plus simple ont permis de clarifier les mécanismes à l'origine du mouvement de la paroi et d'interpréter la relation entre position d'équilibre et contrainte. De plus, une adaptation de l'équation pour considérer les composantes de contraintes  $\sigma$  et  $\tau$  correspondant à l'actionnement par champ électrique d'un substrat piézoélectrique de PMN-PT de coupe (011) est fournie. Enfin, des calculs basés sur des paramètres réalistes ont pu démontrer le gain énergétique associé à cette technique de déplacement de paroi de domaine par rapports aux techniques usuelles.

Le premier modèle présenté ne traite que de l'état d'équilibre du système. Pour obtenir des informations sur la dynamique, et ainsi caractériser correctement le mouvement de la paroi, il est nécessaire d'adjoindre au modèle l'équation de Landau-Lifshitz-Gilbert (LLG) qui régit la dynamique des systèmes magnétiques. Ici, on doit considérer un vecteur d'aimantation décrit par deux angles  $\Phi$  et  $\Theta$  libre de s'orienter dans l'espace (voir Fig. E). Dans le cas général, l'équation LLG donnant le comportement de l'aimantation localement soumise à un champ magnétique  $\vec{H}$  peut s'écrire de la sorte :

$$\frac{\partial \vec{w}}{\partial t} = -\frac{\gamma_0}{1 + \alpha^2} \left( \vec{w} \times \vec{H}_{\text{eff}} + \alpha \vec{w} \times \left( \vec{w} \times \vec{H}_{\text{eff}} \right) \right), \quad (1)$$

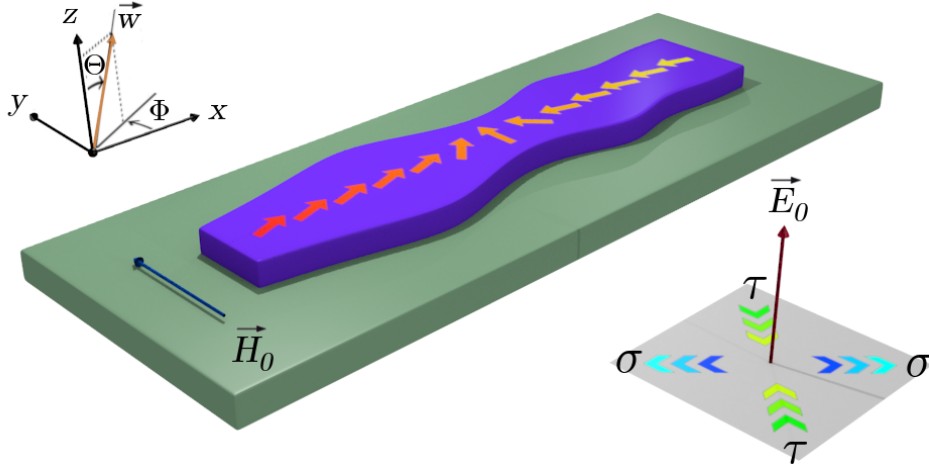


Figure E – Schéma du système étudié. Le champ électrique appliqué selon  $\vec{z}$  génère dans le substrat piézoélectrique (type PMN-PT) une distribution de contraintes avec deux composantes  $\sigma$  et  $\tau$  de signes opposés.

où  $\alpha$  est le coefficient d'amortissement de Gilbert et  $\gamma_0$  est le rapport gyromagnétique de l'électron. De manière similaire à précédemment, une méthode variationnelle est suivie afin de déterminer l'expression du champ magnétique effectif local  $\vec{H}_{\text{eff}}$  prenant en compte l'effet de toutes les contributions. L'intégration de ce champ effectif dans l'équation LLG donne le système d'équation ci-dessous.

$$\begin{cases} \dot{\Phi} = \frac{1}{\sin \Theta} \frac{\gamma_0}{1 + \alpha^2} (-s + \alpha r), \\ \dot{\Theta} = \frac{\gamma_0}{1 + \alpha^2} (r + \alpha s), \end{cases} \quad (2)$$

où l'on a introduit les quantités  $r$  et  $s$  :

$$\begin{aligned} r = & -\sin \Phi H_{dx} + \cos \Phi H_{dy} + \cos \Phi H_0 + \frac{2}{\mu_0 M_s} \left( -K_u \cos \Phi \sin \Phi \sin \Theta \right. \\ & \left. + \frac{3}{4} \lambda_s (\tau - \sigma) \cos 2\Phi \sin \Theta + A \left( \frac{\ell'}{\ell} \sin \Theta \Phi' + 2 \cos \Theta \Phi' \Theta' + \sin \Theta \Phi'' \right) \right), \end{aligned} \quad (3)$$

et

$$\begin{aligned}
s = & \cos \Phi \cos \Theta H_{dx} + \sin \Phi \cos \Theta H_{dy} - \sin \Theta H_{dz} + \sin \Phi \cos \Theta H_0 \\
& + \frac{2}{\mu_0 M_s} \left( K_u \cos^2 \Phi \sin \Theta \cos \Theta + \frac{3}{4} \lambda_s ((\tau + \sigma) \cos \Theta \sin \Theta \right. \\
& \left. + 2(\tau - \sigma) \cos \Phi \sin \Phi \cos \Theta \sin \Theta) + A \left( \frac{\ell'}{\ell} \Theta' + \Theta'' - \cos \Theta \sin \Theta \Phi'^2 \right) \right). \quad (4)
\end{aligned}$$

De même que pour l'équation statique, le recours au traitement numérique est ici obligatoire. De par les propriétés de l'équation LLG, le choix d'un algorithme implicite est de rigueur afin de garantir stabilité et précision du calcul. Ensuite, la méthode de Newton a été intégrée pour la résolution. Pour vérifier la validité des résultats de ce nouveau programme, également développé sous MATLAB, on s'est d'abord attaché à comparer les positions d'équilibre de la paroi à l'issue de la simulation dynamique à celles obtenues avec le programme de relaxation (*cf.* Fig. D). Ensuite, on a pu vérifier que la vitesse de la paroi obtenue dans le cas d'un déplacement induit par un champ magnétique correspond bien à la valeur prédite par un modèle analytique analogue à celui de Walker.

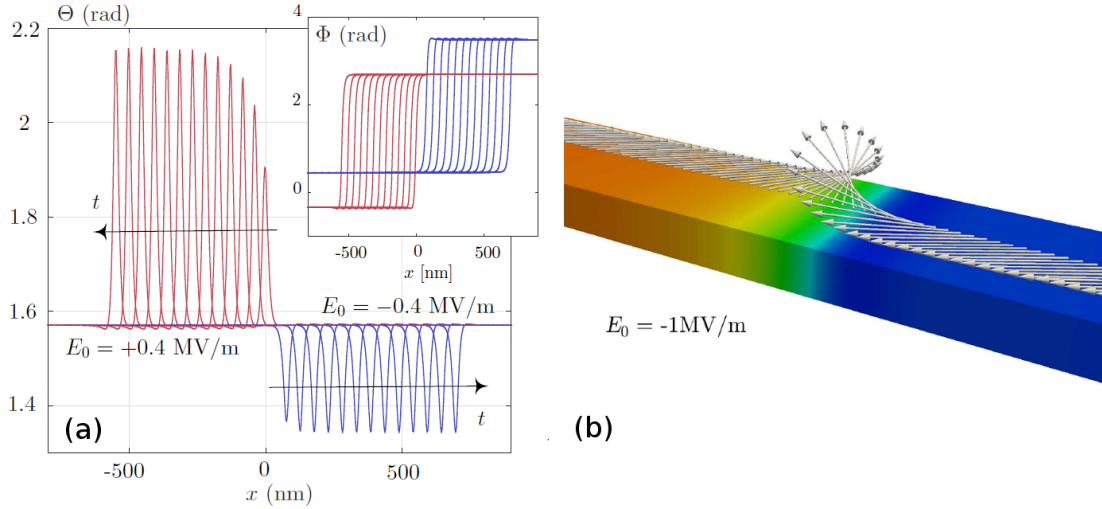


Figure F – (a) Angles  $\Phi$  et  $\Theta$  de l'aimantation au cours d'une simulation dynamique. (b) Représentation 3D de la distribution d'aimantation en régime stationnaire le long d'un nanoruban ( $\ell = 100$  nm et  $h = 10$  nm), avec un champ électrique de  $-1$  MV/m.

Les études dynamiques se sont concentrées sur l'analyse du comportement de l'aimantation au sein d'une nanostructure à largeur variable identique à celle étudiée en statique, ainsi qu'au sein d'un nanoruban à largeur constante. Elles ont pu mettre en évidence un mouvement unidirectionnel caractérisé par une forme particulière de paroi de domaine.

Un comportement hors plan spécifique est notamment remarqué, et celui-ci s'évanouit tandis que la paroi s'approche de sa position d'équilibre dans le cas d'une géométrie à largeur variable confinant la paroi. Au sein d'une structure à largeur constante, l'existence d'un régime stationnaire a été mise en évidence. Celui-ci confirme une forme de paroi présentant une composante hors plan significative (voir Fig. F), dont l'ampleur varie en fonction de l'amplitude du champ électrique appliqué et de son signe. Ce phénomène est imputable à l'importance relative des anisotropie uniaxiale et planaire associées aux contraintes positive et négative, respectivement.

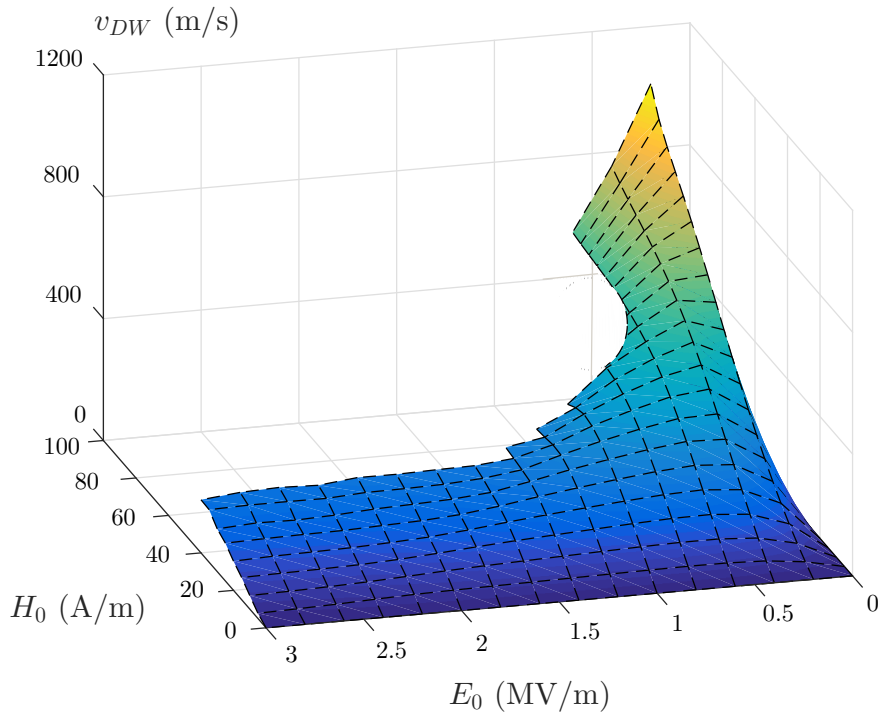


Figure G – Vitesse de la paroi de domaine en fonction du champ électrique appliqué et de la valeur du champ magnétique de biais pour un coefficient d'amortissement de 0,12.

Les différentes simulations ont montré que des vitesses très importantes ( $> 800$  m/s) peuvent être obtenues en choisissant bien les valeurs du champ électrique appliqué (et donc des contraintes) et du champ magnétique de biais, dont la combinaison est à l'origine du mouvement. Ces résultats sont présentés dans la Fig. G. Comme évoqué plus haut, ces performances peuvent en principe être obtenues pour de très faibles consommations d'énergie. Il faut également noter que le code ne fonctionne plus au-delà de certaines valeurs du couple champ électrique - champ magnétique. On peut supposer que cela est dû à un changement qualitatif de régime dynamique, à l'instar du Walker breakdown observé

dans le cadre du mouvement induit par un champ magnétique longitudinal. En effet, un comportement similaire du code a été constaté dans ce cas classique, où le code échouait à décrire la dynamique pour un champ magnétique supérieur au seuil du breakdown.

Ces travaux numériques ont permis de poser une base solide au concept de déplacement de paroi induit par des contraintes uniformes, en présence d'un champ magnétique de biais. Devant l'intérêt que présente cette technique, il serait intéressant de la mettre en œuvre expérimentalement. Pour cela, le choix des matériaux s'est porté vers le PMN-PT de coupe (011) et un multicouche magnétoélastique  $\text{TbCo}_2/\text{FeCo}$ . L'association des deux phases retenue pour ce travail de thèse est un dépôt d'une couche mince magnétoélastique sur un substrat piézoélectrique. Ces derniers sont des produits obtenus dans le commerce spécialisé, nécessitant au préalable un polissage pour rendre possible la nanofabrication sur leur surface. La procédure développée a permis d'obtenir une rugosité de l'ordre du nanomètre. Une lithographie (résine positive) a donc pu être mise au point sur ces surfaces, permettant de développer les motifs du masque préparé, pour ensuite poursuivre avec un dépôt par pulvérisation cathodique du matériau multicouche (20 nm). Après quelques ajustements, il a été possible d'effectuer avec succès une procédure de lift-off, de telle sorte que les motifs obtenus, visibles sur la Fig. H, reflètent fidèlement ceux du masque.

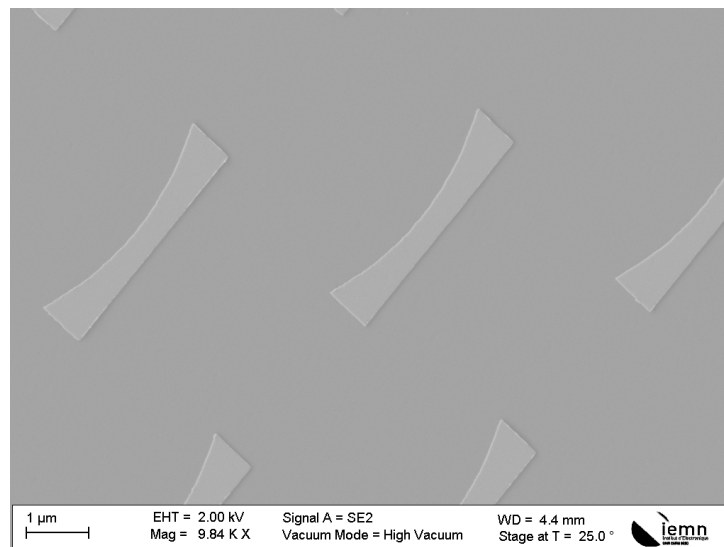


Figure H – Image au microscope électronique à balayage des nanostructures magnétoélastiques obtenues par lift-off.

La caractérisation des matériaux et structures obtenues a donné lieu à plusieurs résultats. Tout d'abord, les propriétés piézoélectriques du PMN-PT ont été obtenues à l'aide

d'une jauge de contrainte. Les mesures révèlent un comportement non-linéaire cohérent avec ce qui se trouve dans la littérature. Les propriétés magnétiques et magnétoélastiques des matériaux multicouches utilisés ont été respectivement obtenues par des mesures VSM (anisotropie, aimantation à saturation) et par la méthode de la poutre encastrée fléchissante. Globalement, les valeurs mesurées sont cohérentes avec les paramètres choisis lors des simulations numériques.

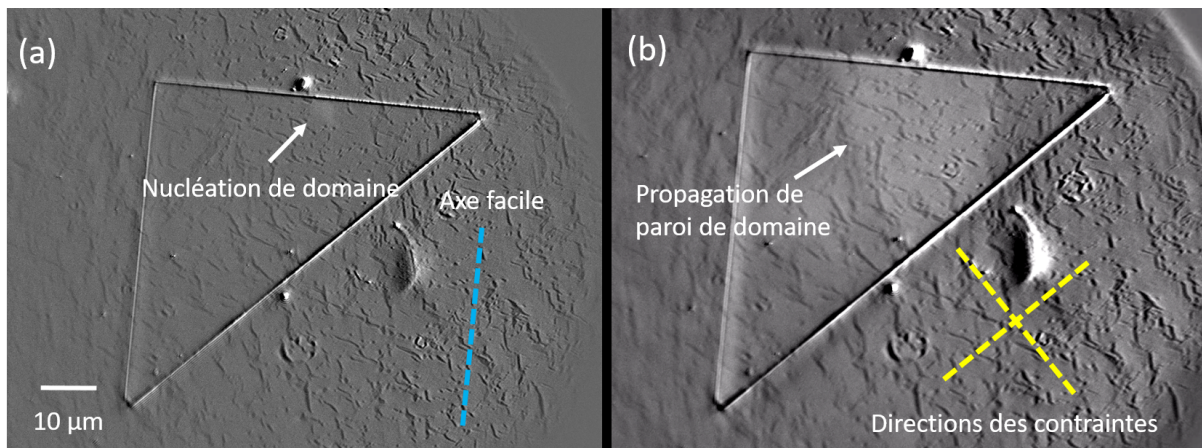


Figure I – Images Kerr d'un grand motif magnétoélastique soumis à un champ magnétique et des contraintes mécaniques induites par le substrat piézoélectrique. La configuration multidomaine est clairement visible.

La topologie des nanostructures a été déterminée par microscopie à force atomique (AFM), révélant des profils satisfaisants. Par la suite, la configuration magnétique au sein des nanostructures magnétiques a pu être étudiée par microscopie à force magnétique (MFM). Ces observations ont mis en évidence le fait que les éléments étaient quasiment systématiquement de configuration monodomaine, en dépit des efforts pour induire la création de parois de domaine. Sur des éléments plus grands, il a été possible de faire des observations Kerr tout en appliquant champ magnétique et contraintes mécaniques. Un effet magnétoélectrique par déplacement de paroi a pu être observé dans ces conditions (voir Fig. I). Par ailleurs, des travaux préliminaires pour une fabrication intégrée des nanostructures magnétoélastiques sur substrat PMN-PT gravé permettent d'envisager des perspectives encourageantes pour la poursuite de ces travaux.

# Introduction

Magnetism is known to everyone, if only through the widespread use of simple fridge magnets. However, relatively few people realize how heavily all the technology essential to our modern lifestyle relies on magnetism. From electric generators to hard-drive disks and functional magnetic resonance imaging, the use of magnetic materials, tools and devices is ubiquitous. Of course, all these fruitful applications of magnetism were made possible by the work of generations of researchers dedicating their careers to these matters, from Oersted, Ampère and Faraday onward. Only a fraction of them could foresee that their work would lead to such spectacular developments.

Today, a coherent and comprehensive body of knowledge helps us understand the origin of magnetism and successfully accounts for the behavior of magnetic materials. In particular, domain walls—which separate regions of uniform magnetization in ferromagnets—have long been a subject of interest because of their importance from the fundamental point of view as well as their relevance in magnetic devices. Their manipulation is linked to a dynamic and competitive area of research. Magnetic field-driven domain wall motion has been thoroughly investigated, and with the advent of spintronics, the various ways of inducing domain wall motion with an electrical current have been widely studied and reported in the literature in recent years. Motivated by potential advances on the fronts of energy consumption, facilitated implementation or operation, innovative methods as well as refinements of well-known techniques allowing control of magnetization and domain walls are constantly put forward by researchers. Among the proposed candidates, magnetoelectric materials have been recently gaining tremendous attention. The main reason for this is that the use of an electric field instead of an electric current is an elegant way to dramatically reduce the energy required to control magnetization. While magnetoelectric effects can exist in single-phase materials, the superior opportunities offered by heterostructures tend to direct research efforts in this direction.

In this thesis, we present an innovative approach to domain wall manipulation based on a stress-mediated magnetoelectric effect. We build on concepts developed at IEMN,

more specifically within the LEMAC/LICS International Associated Laboratory. These previous works culminated with the development of magnetoelectric memories implemented through the mechanical coupling of a piezoelectric substrate and a magnetoelastic layer. We contend that the combination of a uniform stress and a bias magnetic field breaking the symmetry can result in the controlled motion of a transverse domain wall. We show that such a motion is associated with unusual physical features, competitive performances and low energy consumption, while its experimental implementation appears realistic.

The first chapter provides the necessary background. The basics of magnetism required are briefly presented, followed by an account of the literature on domain wall motion. The proposed concept is then introduced in the context of current research trends, with a focus on magnetoelectric materials. This chapter also contains preliminary numerical validation of the concept. The second chapter brings new evidence through an *ad hoc* one dimensional model able to calculate the equilibrium magnetization distribution in systems with nanostripe geometry. Based on variational methods, it takes into account the relevant physical contributions. After a short presentation of the code, the results obtained on nanostructures of variable width are described in greater detail. The third chapter goes on to address the dynamics of the motion. The outcome of variational methods is combined with the Landau-Lifshitz-Gilbert equation and is solved using another *ad hoc* model developed over the course of the PhD. The approach chosen is briefly explained and results are discussed in more depth, as the dynamics happen to be characterized by interesting features. The fourth chapter deals with experimental investigations undertaken during the PhD. The materials chosen are described, namely the commercial piezoelectric substrates and the rare-earth-based multilayers routinely used at IEMN. Details are given on the fabrication process. The subsequent efforts to characterize the materials and devices are reported. Finally, a general conclusion closes this manuscript. It reviews the general approach adopted as well as its most prominent findings. A discussion on the possible lines of research for future investigations is also included.

# Chapter 1

## Fundamentals and context

The work that is to be presented in this thesis involves various concepts of micromagnetism, namely basic properties of ferromagnetic materials at the microscopic scale. They are part of a comprehensive and consistent theoretical framework which successfully describes a wide range of physical phenomena encountered experimentally. In this chapter, we will first aim at providing some physical background and description of the building blocks on which our developments depend, including magnetic domain walls which are of critical importance in ferromagnetism. Special attention will be paid to magnetoelasticity (or magnetostriction), since this property is essential to the phenomena studied in this thesis. From these fundamentals, an overview of the very dynamic research area of domain wall motion and its applications will be given. The different techniques used to manipulate domain walls will be discussed in terms of the physical mechanisms at play as well as their potential and weaknesses. Emphasis will be put on magnetoelectric coupling paradigms, including the emergent stress-based approaches. In this context, we will present the idea of combining uniform stress and a symmetry-breaking magnetic field to control magnetization. This combination has been proposed and successfully implemented in the context of the magnetization switching of monodomain magnetoelastic particles. Then, we will present the subject matter of this thesis, that is the extension of this paradigm to two-domain magnetoelastic elements in order to drive domain wall motion. The advantages of this method will be detailed and preliminary numerical proofs of the concept will be shown.

### 1.1 Brief introduction to (micro)magnetism

This first section consists in a short introduction to basic matters in magnetism. These developments are essential to the subsequent description of the context of the work presented

in this thesis. After presenting the main concepts and physical quantities of magnetism in materials, the link between macroscopic behavior in magnetism and microscopic phenomena is explored and magnetic domain walls are thereby introduced. Then, some physical details on domain walls are given.

### 1.1.1 Magnetization and energy contributions

The basis for the understanding of micromagnetism comes from pioneering work by Landau (most remarkably in his landmark 1935 paper with Lifshitz), Becker, Weiss, Bloch, Néel and Brown among others. The latter provided a comprehensive account of the subject in his 1963 book entitled *Micromagnetics* [1], as Chikazumi later did [2]. All the concepts and developments below can be traced to the mainstream theory of micromagnetism described in these reference books. In this work, we will exclusively deal with ferromagnetic materials. Other forms of magnetic behavior such as paramagnetism or diamagnetism will therefore not be addressed.

In a ferromagnetic material, individual atoms have a spontaneous magnetic moment  $\vec{m}$  (unit  $\text{Am}^2$ ). It is mostly due to electrons, through their intrinsic property called *spin* (arising from the combination of relativistic and quantum effects [3]) and to their net orbital angular momenta. This can confer a net magnetic moment to the atom depending of the particular arrangement of electrons. Also, the spin of neutrons and protons means there is also a small contribution of the nucleus to the overall magnetic moment. Ferromagnetic materials are characterized by the fact that these moments interact with their immediate neighbors. This interaction of quantum nature is positive in ferromagnetic materials (resp. negative in ferrimagnetic and antiferromagnetic materials), so that neighboring atoms will tend to have the same spin orientation (resp. opposite spin orientation). A macroscopic collection of magnetic moments oriented in the same direction can give rise to the macroscopic phenomena everyone has witnessed in magnetic materials.

Given the length scales involved and according to the classical approach of micromagnetics, we can define a vector field of a quantity commensurable with a volumic magnetic moment ( $\text{A/m}$ ), *i.e.* a density of magnetic moment. It is called magnetization—referred to as  $\vec{M}$ —and is thus defined within the magnetic body at all points of its volume  $V \subset \mathbb{R}^3$ . A basic assumption of micromagnetism is that the magnitude of  $\vec{M}$  in a ferromagnetic material depends only on temperature and is constant in time and uniform in space, *i.e.*  $\vec{M} = M_s \vec{w}(\vec{r}, t)$ , where  $M_s$  is the magnetization at saturation and  $\vec{w} = (w_x, w_y, w_z)$  is a space dependant and time varying unit vector.

Another main aspect of micromagnetism is that at rest, the magnetization distribution is such that the corresponding free energy of the system is minimum, at least locally in phase space. This quantity is the sum of a set of contributions, with sometimes conflicting influences. Below is a very short qualitative description of the origins and effects of the contributions relevant in this work.

**Zeeman energy** Magnetic moments are affected by surrounding magnetic fields. The effect of magnetic fields is accounted for through the Zeeman energy, which reflects the tendency of magnetic moments to align with applied fields. A magnetic field is generally noted  $\vec{H}$  and its dimension is the same as magnetization (measured in A/m). Induction, which is often noted  $\vec{B}$ , has the same dimension as  $\mu_0 H$  (measured in Tesla).

**Demagnetization energy** In addition to external fields, the magnetization distribution is subject to the field that it itself generates, that will thereafter be called *demagnetizing field*. Its effects are of longer range and are not always easily predicted. Thus, they add significant complexity to the behavior of magnetic systems.

**Anisotropy energy** The crystalline arrangement of atoms in a magnetic material can give rise to anisotropic behavior in ferromagnetic materials, for instance through spin-orbit interaction. Specific magnetization orientations are therefore energetically favored depending on the association of the chemical elements constituting the material, and its crystalline/amorphous structure. The anisotropy found in materials is at the origin of some of the hysteretic behaviors observed and of the distinction between soft (low anisotropy) and hard (high anisotropy) magnetic materials.

**Exchange energy** Collective behavior in ferromagnetic materials arises from the interaction between adjacent magnetic moments. This interaction is *positive* in ferromagnetic materials and therefore tends to align adjacent magnetic moments. Despite its quantum origin, it can be written in terms suitable for continuous modeling. By putting a cost to inhomogeneous distributions, this contribution tends to align all magnetic moments in the same direction.

**Magnetoelastic energy** Magnetoelastic materials are a subset of ferromagnetic materials with a significant coupling between mechanical and magnetic quantities. Changes in magnetizations in a magnetoelastic body are associated with changes in strain and

vice-versa. This physical phenomenon is of paramount importance in this work and thus will be discussed in further detail in subsection 1.3.2.

Additional contributions may appear and have in some cases critical influence on the energy landscape of magnetic structures. For instance, interface interactions between two materials as well as other forms of exchange energy are subjected to increasing research interest. However, the phenomenon studied in this work only involves the contributions listed above. Dynamic behaviors can be studied by solving the Landau-Lifshitz-Gilbert equation, introduced in subsection 1.2.2.

### 1.1.2 Macroscopic behavior of ferromagnetic bodies

Ferromagnetic behavior can be observed in some materials below a critical temperature  $T_c$ , called the Curie point. Beyond this temperature, the material becomes *paramagnetic*, which means that because of thermal motion the magnetic moment is linear with respect to any applied magnetic field and the magnetization drops to zero in the absence of field. In other words, moments will align with a strong magnetic field, and will have a random distribution at zero field. It is important to note that in general, the term "ferromagnetic materials" arbitrarily refers to materials which Curie temperature happens to be above room temperature. Leaving alloys aside, the most common chemical elements exhibiting ferromagnetic behavior are iron, cobalt and nickel. Other forms of ordered magnetism exist, such as in ferrimagnetic and antiferromagnetic materials, which are characterized by distributions with opposing magnetic moments. Unlike antiferromagnets, ferrimagnetic materials retain a spontaneous magnetization because the antiparallel magnetic moments are unequal. The Curie temperatures of several materials are given in Fig. 1.1.

From an empirical point of view, the behavior of a macroscopic bulk ferromagnetic material can be studied through the application of an external field along any given direction. A typical sample magnetization as a function of the applied magnetic field is represented in Fig1.2. From a demagnetized initial state, the progressive application of a (for instance) positive magnetic field yields the curve of first magnetization, until the sample reaches saturation. The amplitude of magnetization at this point is what has been referred to as magnetization at saturation in subsection 1.1.1 and is noted  $M_s$ . When the applied field is reduced to zero, one can measure the remanent magnetization of the sample. The application of a negative magnetic field will reduce the magnetization until it becomes zero, which defines the coercitivity of the sample. This quantity is important in that it is the basis for the distinction between hard and soft magnets. Hard

Element	Atomic No.	Name	Magnetic Type	Curie Point (°K)	Neel Point (°K)
Cr	24	Chromium	Antiferromagnetic		393
Mn	25	Manganese	Paramagnetic		100
Fe	26	Iron	Ferromagnetic	1043	
Co	27	Cobalt	Ferromagnetic	1394	
Ni	28	Nickel	Ferromagnetic	631	
Ce	58	Cerium	Paramagnetic		125
Nd	60	Neodymium	Paramagnetic		192
Sm	62	Samarium	Paramagnetic		106
Eu	63	Europium	Paramagnetic		90.5
Gd	64	Gadolinium	Ferromagnetic	292	
Tb	65	Terbium	Paramagnetic	222	230
Dy	66	Dysprosium	Paramagnetic	87	178
Ho	67	Holmium	Paramagnetic	20	132
Er	68	Erbium	Paramagnetic	32	82
Tm	69	Thulium	Paramagnetic	25	56

Figure 1.1 – Table showing the Curie point of several materials. The Néel point is the ferrimagnetic equivalent of the Curie point (note that some elements can be ferromagnetic, ferrimagnetic or paramagnetic, depending on temperature). Figure from [4].

(resp. soft) magnets have a strong (resp. weak) coercivity, meaning that a relatively strong (resp. weak) magnetic field is required to switch most of the magnetic moments in its direction. Of course, this all depends on the axis along which the magnetic field is applied, and therefore the concept of coercitivity is related to the notion of anisotropy. When subjected to the reverse operation (starting from a strong negative field) the sample will follow a symmetrical path toward saturation. From a saturated state, a sample can be subjected to a demagnetization loop, by performing hysteresis loops with diminishing field amplitudes until the vanishing of the overall magnetization.

Depending on the nature and size of the sample subjected to the hysteresis loop, the changes in magnetization are brought about by a combination of different phenomena at the microscopic scale. The most intuitive of them is the coherent rotation of all magnetic moments. Other phenomena involve the local variation of magnetization, with regions of nonuniform distribution. This leads to the notion of domain walls, introduced historically in order to account for the above-described macroscopic behavior of ferromagnets.

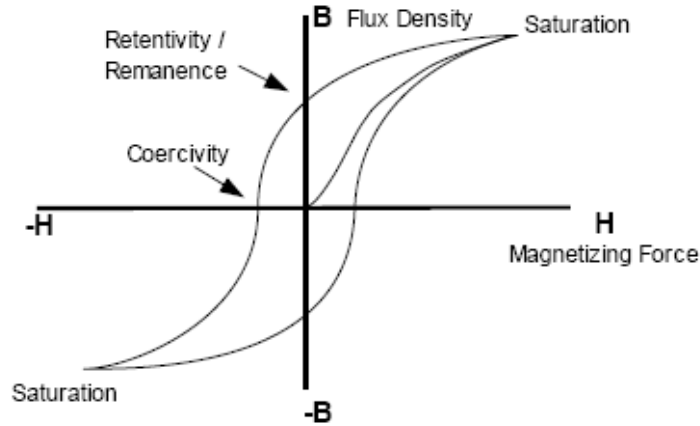


Figure 1.2 – Typical hysteresis loop plot featuring curve of first magnetization, saturation and corecitivity, as described in the main text. Here, the flux density is shown instead of the magnetization, but the discussion is unchanged. Figure from *TDK-Lambda*.

### 1.1.3 Magnetic configurations and domain walls

At rest, the contributions cited in subsection 1.1.1 (as well as others like temperature, distribution of defects *etc.*) influence the equilibrium distribution, which is associated with a minimum value of the free energy. Taken together, the joint contributions sum up and are then associated with an *effective field*, noted  $\vec{H}_{\text{eff}}$ . Then, the equilibrium distribution within the volume  $V$  of the ferromagnetic body satisfies the equation:

$$\vec{w} \times \vec{H}_{\text{eff}} = 0. \quad (1.1)$$

This equation states that the local torque at any point vanishes when the equilibrium is reached, so that the direction of magnetization within the material is that of the local effective field  $\vec{H}_{\text{eff}}$ . On the surface  $\partial V$  of the material (if we note  $\vec{n}$  the surface normal vector) the boundary condition is:

$$\frac{\partial \vec{w}(\vec{r})}{\partial \vec{n}} = 0, \quad (1.2)$$

under conditions on the materials which will apply in our case. Greater details on these equations will be given in chapter 2.2.

Finding the equilibrium distribution of magnetization involves the resolution of these equations, oftentimes using variational techniques. In a ferromagnetic body, a compromise has to be found between sometimes conflicting contributions, even in the absence of any external stimulus. As stated in subsection 1.1.1, the exchange energy will have the

tendency to align all magnetic moments. Depending on the geometry and lengthscales involved, however, the demagnetization energy associated with uniform magnetization can be very large. Spatial variation of magnetization is thus bound to arise in some conditions to avoid such magnetostatic issues. In soft ferromagnets, the reduction of demagnetization energy can be achieved by flux closures, *i.e.* forming loops to close magnetic field lines created by the distribution or more generally with smooth variations throughout the ferromagnetic body (see Fig. 1.3). This configuration can be particularly favored in ring geometry [5].

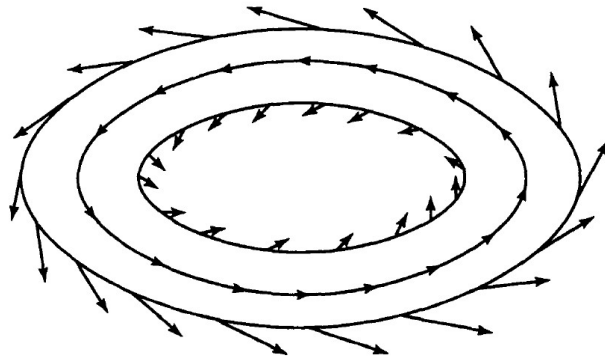


Figure 1.3 – When the anisotropy is low, the magnetization is free to assume any direction. It can therefore create vortex-like patterns like on this schematic. Figure from [6].

In the presence of some form of anisotropy, the magnetization can vary more abruptly within the ferromagnet. The overall energy of the system is thus dramatically cut by the creation of multiple distinct domains inside which the magnetization is uniform. They are usually called *magnetic domains* or *Weiss domains* and are separated by *domain walls*, where the magnetization rapidly changes from one direction to another one and forms peculiar patterns such as in Fig. 1.4. Their existence has been postulated by Weiss in order to account for the macroscopic behavior of ferromagnetic materials. Indeed, the distribution in a macroscopic ferromagnet can consist of a multitude of small domains with uncorrelated orientations, so that the overall magnetization can be zero even though  $M_s$  is not. As is also the case of soft magnets, the spatial variation of magnetization brings a satisfying explanation to the absence of net magnetization generally observed in macroscopic samples. More direct experimental validations began with visualizations using magnetic powders and later magneto-optical techniques (Kerr effect), magnetoresistance, magnetic force microscopy (MFM) and X-ray magnetic circular dichroism microscopy (XMCD).

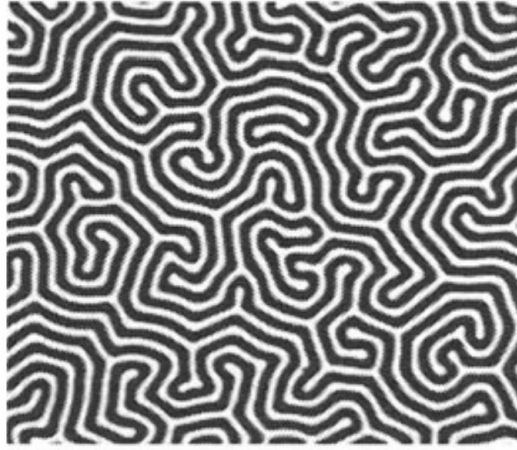


Figure 1.4 – Magneto-optical visualization of typical brain-like patterns of magnetic domains, here with magnetic garnet. Each color correspond to one magnetization direction. Figure from [6].

Magnetic domain walls have then been subjected to extensive theoretical and experimental investigations and the physical theory of magnetic domains is a long established [7] pillar on which modern micromagnetics is based [8].

#### 1.1.4 Typology and physical features of domain walls

Generally speaking, a domain wall can be defined as the magnetic structure between two adjacent domains of different magnetization directions  $\vec{w}_1$  and  $\vec{w}_2$ , which need not be opposite. The spatial delimitation of a domain wall is necessarily arbitrary due to the continuous nature of the magnetization distribution in the micromagnetic formalism, and a domain wall is not a well defined entity strictly speaking. This does not preclude the use of the concept of domain wall, referring to the region of greater magnetization gradients within the material as a magnetic object. In this thesis, we will only cover ferromagnetic domain walls, and it is worth mentioning that the behavior of domain walls in antiferromagnets is qualitatively different [9–11].

Although it is easier to describe and depict domain walls between two domains of opposite magnetization, this needs not be the case. The orientation of magnetization in domains depends heavily on local anisotropy and other parameters. Domains with antiparallel magnetizations are bound to arise in materials with strong uniaxial anisotropy, but other configurations such as orthogonal domains can exist in materials with cubic anisotropy.

Depending on parameters, temperature, external stimuli and the geometry of the considered ferromagnetic body, a whole variety of domain walls and magnetic objects can be observed. In particular, tremendous interest has recently been drawn on skyrmions, which are very small topological oddities [12]. In thin and narrow layers of ferromagnetic materials, there are two general types of domain walls—although others have been described [13]—which can be called *vortex* and *transverse* walls (see Fig. 1.5) (the latter can be symmetric or asymmetric [14]). In the absence of any external influence, exchange energy, magnetocrystalline anisotropy, and demagnetization energy are the sole players and will determine which one of the vortex or transverse wall will be the favored. As an aside, in many ways the influence of the latter is akin to a form of anisotropy. For instance, in a very elongated nanostructure—with one of its dimensions very large with respect to the other two—the demagnetizing field will create an apparent uniaxial anisotropy. Some authors refer to this as the *shape anisotropy*. It can thus be considered much in the same way as is the magnetocrystalline anisotropy, as long as we keep in mind that in doing so we focus on the form it assumes rather than on its physical origin. Many investigations on domain wall configurations have thus focused on permalloy ( $\text{Ni}_{81}\text{Fe}_{19}$ ) because of its negligible magnetocrystalline anisotropy. Therefore, the role of geometry can be studied independently of other factors for many purposes, leading to the construction of ever more refined phase diagrams to determine the most stable type of wall [14–16]. A good rule of thumb is that the wider and thicker the layer, the more energetically favored a vortex wall will be.

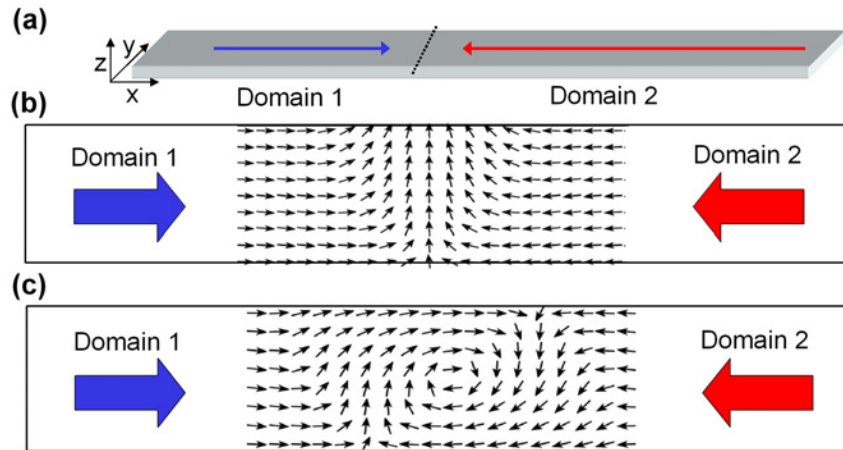


Figure 1.5 – (a) Schematic of two antiparallel domains in nanostripe geometry with in-plane anisotropy. Top view of magnetization distribution relating to (b) transverse and (c) vortex domain walls. Figure from [17].

There are two subtypes of transverse domain walls, which can also be hybridized [18]. The default domain wall type and first to be described, is the *Bloch wall*. Let us for instance consider two antiparallel domains separated by a domain wall in a macroscopic sample. The need to reduce demagnetization energy puts a constraint on the spatial variation of the magnetization from one domain to the other. It is best interpreted as the tendency to avoid the creation of magnetic charges  $\rho_m$  within the domain wall. Since  $\rho_m = -\text{div}(M)$ , this condition is equivalent to  $\frac{dw_x}{dx} = 0$  (if we consider the axes of Fig. 1.6). Therefore, there is no variation of the magnetization component corresponding to the axis perpendicular to the domain wall, as can be visualized in Fig. 1.6. In this configuration, the magnetization rotates around the  $x$ -axis.

In thin films, except in the case of perpendicular magnetic anisotropy (PMA), the magnetization tends to remain in the plane of the film to minimize demagnetization energy (*cf.* so-called *shape anisotropy*). This constraint affects the energetic trade-off of the domain wall. Indeed, there is a strong incentive for the magnetization in the domain wall to also stay in-plane, which means in-plane rotation across the domain wall (Fig. 1.6b) to prevent the appearance of large magnetostatic energy, as seen in Fig. 1.6a. From here, the fact that the condition  $\frac{dw_x}{dx} = 0$  cannot be respected in thin films is quite straightforward. Refined considerations as well as subcategories within Néel and Bloch walls can be found in [19].

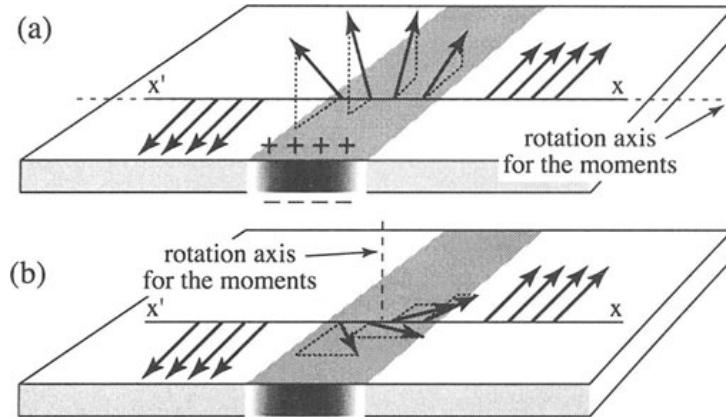


Figure 1.6 – Schematic of (a) Bloch and (b) Néel wall in a ferromagnetic layer. Figure from [6].

Given a transverse domain wall configuration (be it of Bloch or Néel type), the combined influence of competing physical constraints governs the distribution within the domain

wall, most notably the rate of spatial change from one magnetization direction to the other. On the one hand, the exchange energy tends to discourage any abrupt gradient of magnetization and thus favors wide domain walls. On the other hand, the magnetization has to deviate from the axis favored by the anisotropy, along which is the magnetization within the two domains. Depending on the relative weights of these two contributions to the domain wall energy, the width of a transverse domain wall can vary as shown in Fig. 1.7. The exchange energy is proportional to an exchange constant  $A$ , (units: J/m) while the uniaxial anisotropy is proportional to a constant noted  $K_u$  (units:  $\text{Jm}^{-3}$ ), or equivalently, an anisotropy field  $H_a$  (so that  $K_u = \frac{1}{2}\mu_0 M_s H_a$ , where  $\mu_0$  is the vacuum permeability). The  $A/K_u$  ratio therefore plays an important role in determining the spatial extension of a domain wall.

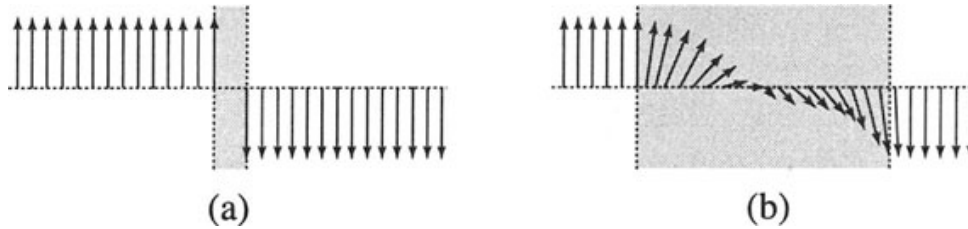


Figure 1.7 – Schematic of comparatively wide and thin domain walls. In a ferromagnetic body, this is dictated by the particular local set of physical constraints to which the domain wall is subjected. Figure from [6].

Although domain walls usually allow for a substantial reduction in overall energy, they are nonetheless associated with a local increase of energy. Indeed, in the domain wall vicinity, contributions of exchange, Zeeman, demagnetization and anisotropy may be increased. Whether or not the width of the domain wall is negligible with respect to its other dimensions, a surface energy can be defined and be expressed as a function of  $A$  and  $K_u$ .

First proposed in 1932 by Bloch, the Bloch wall is treated analytically by Landau and Lifshitz in their 1935 paper [20]. Their wall calculation has been carried out multiple times thereafter with small changes and adaptations. They considered an infinite ferromagnet which magnetization only varies with one dimension (let it be called  $x$ ), with only uniaxial anisotropy and exchange involved. The in-plane magnetization unit vector  $\vec{w}$  can be described using one angle  $\Phi \in [0, 2\pi]$ . At the boundaries ( $x = -\infty$  and  $x = +\infty$ ), values of  $\Phi$  are antiparallel along the  $x$ -axis:  $\Phi(-\infty) = 0$  and  $\Phi(+\infty) = \pi$ . In this case, the

calculation is relatively straightforward and can be carried out analytically. The solution  $\Phi$  function is as follows (see appendix A for derivation):

$$\Phi = \pi - \arccos \left( \sqrt{\frac{K_u}{A}} x \right), \quad (1.3)$$

which can also be written

$$\Phi = 2 \arctan \left( \exp \left( \sqrt{\frac{K_u}{A}} x \right) \right). \quad (1.4)$$

Again one can see the importance of the relative magnitude of anisotropy and exchange through the ratio of the corresponding constants. The larger the ratio, the thinner the domain wall, as is visible in Fig. 1.8. Domain wall thickness in this case is of the order of  $\pi \sqrt{\frac{A}{K_u}}$  [6]. In general, the value considered for the exchange constant  $A$  is around  $9 \times 10^{-12}$  J/m for all materials [21] while the strength of the anisotropy can vary from negligible to very large values in hard ferromagnets (anisotropy field in the order of magnitude of  $10^6$  A/m). Therefore, domain wall width typically ranges from less than a nanometer to tens of nanometers. We have seen that the magnetic distribution in a very soft material is often smoothly varying, so that the notion of domain wall becomes meaningless in practice. There is therefore a blurry line for some materials, where it can be difficult to distinguish between a clearly defined domain wall and a large areas of slowly varying magnetization. As already mentioned, a domain wall is not a rigorously defined object but is used to help the understanding.

If the system has a finite length, the boundary conditions at its extremities lead to another solution involving elliptic functions, as demonstrated in appendix A. Despite the utter simplicity of this model, the calculation above can actually be a decent approximation depending on the configuration studied. This analytical distribution has therefore been used extensively to this day in research dealing with domain walls in ferromagnets, including the dynamics of domain wall motion, a subject of tremendous interest which will be addressed below.

## 1.2 Domain wall motion

Domain walls are fundamental to the modern understanding of magnetism in materials. This section begins with an account of their importance in modern technological applications, and the resulting interest in their manipulation. Before moving on to the main

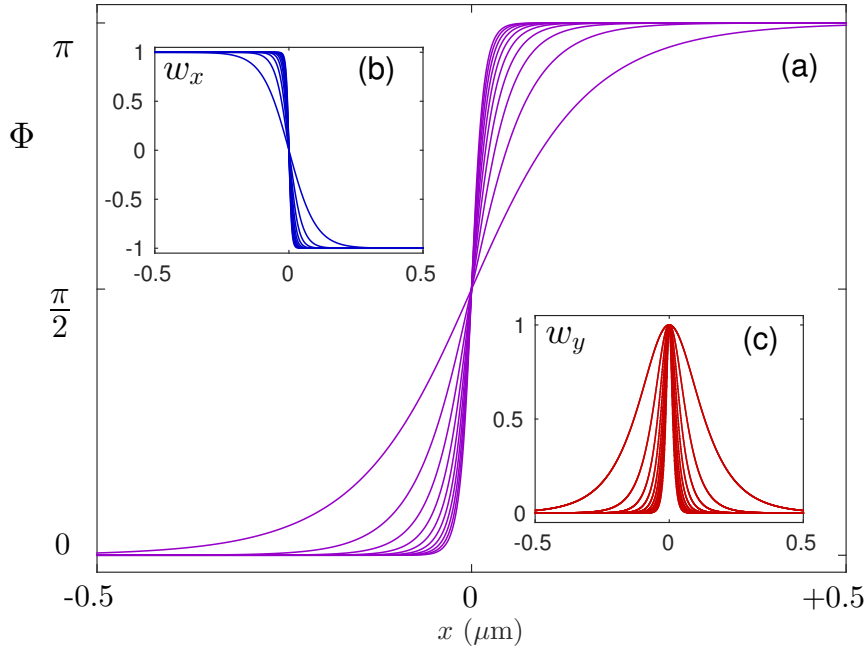


Figure 1.8 – Magnetization distributions along the  $x$ -axis as originally calculated by Landau, where each curve is associated with a given  $K_u/A$  ratio. Plot (a) shows the angle  $\Phi$ , while the magnetization vector component  $w_x = \cos \Phi$  and  $w_y = \sin \Phi$  can be seen respectively in plots (b) and (c).

techniques to induce domain wall motion, a brief presentation of the equations governing magnetization dynamics is provided.

### 1.2.1 Overview of technological relevance

Magnetic domain walls and their manipulation have drawn significant interest and have been widely studied both for fundamental and application-oriented purposes. Over the last decades, domain wall motion has been a very dynamic area of research, from theoretical explorations to experimental investigations. Compared to ferroelectric domain walls, magnetic domain walls are quite complex objects. They possess internal degrees of freedom and come in a variety of types as we have shown above [22]. This complexity is one of the reasons for the widespread interest in domain walls from a fundamental physics point of view as well as for applications.

The starting point to understand where a large part of the technological importance of domain walls and micromagnetism in general comes from is the fact that information can be stored in a magnetic medium. In other words, bits of data can be written (and

read) in the direction of local magnetization. The classical and most famous example is the magnetic hard drive technology widely used in computers over the last decades. While this technology has seen drastic changes in terms of performances since being first introduced by IBM in the 1950s, the basic working principle remains the same. The writing part is achieved by applying a magnetic field locally on a ferromagnetic material through a small coil mounted on a ferromagnetic head, see Fig. 1.9.

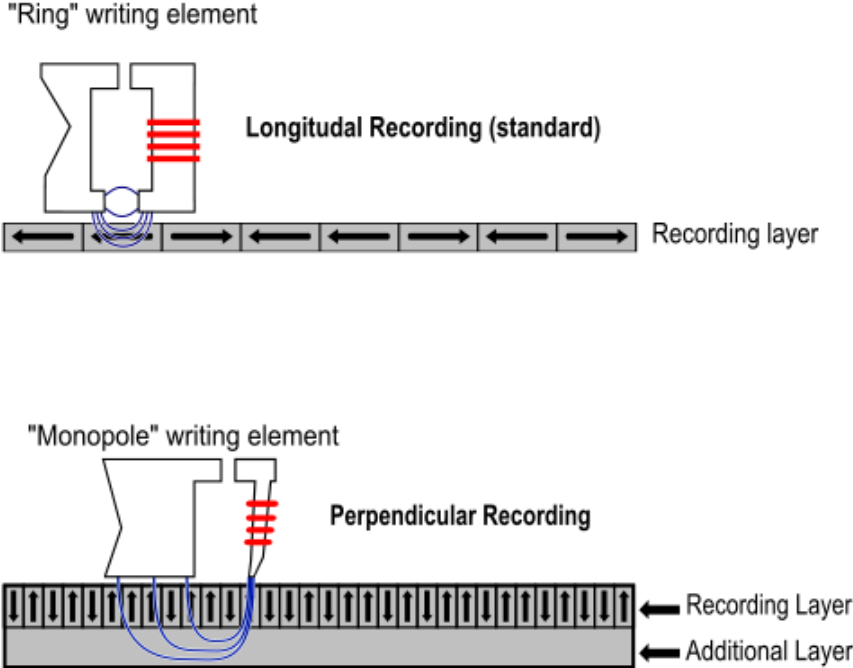


Figure 1.9 – Working principle of a hard disk drive. A moving head writes and reads using current-induced magnetic fields applied locally on a ferromagnetic strip. Figure from *Public domain*.

While this technology is now quite mature, there is still research focused on optimization, for instance illustrated by recent developments of heat-assisted recording [23–25] and earlier, bit-patterned media [26]. Also, it has recently encountered competition, most notably from Solid-State Drives (SSDs) which rely on non-volatile NAND-based flash memory (a technology that can also be found in USB drives). Although still significantly more expensive than HDDs per stored bit, SSDs are likely to continue gaining traction as prices drop because of several advantages that will not be discussed here.

In any case, the study of domain walls is nowadays a dynamic research area with relevance in various fields. Recent technological developments made the design, processing,

and characterization of magnetic thin films and nanoscale structures increasingly convenient. This turned out to be a great source of knowledge and insight into the physics of magnetic domains and domain walls. Indeed, before the advent of nanotechnology only the surface of bulk materials could be characterized, while precise magnetic structure patterns can now be studied with more control on geometry, phase and composition [27]. In recent years for instance, samples with perpendicular magnetic anisotropy (which enables greater density) have been seen as very promising [28].

Because of the many advantages such as reliability, fast operation, low power consumption and non-volatility, devices based on domain walls (and spin systems in general) are widely seen as promising tools for various applications, including memory, sensing and logic [25, 29–31]. A notorious example of such innovative proposals is the racetrack memory [32, 33]. The idea is to use magnetic domain walls in a nanowire to encode data, with an electric current flowing through the nanowire inducing a controlled motion of domain walls (see Fig. 1.10). Other memories based on domain walls [34, 35] have been proposed in recent years.

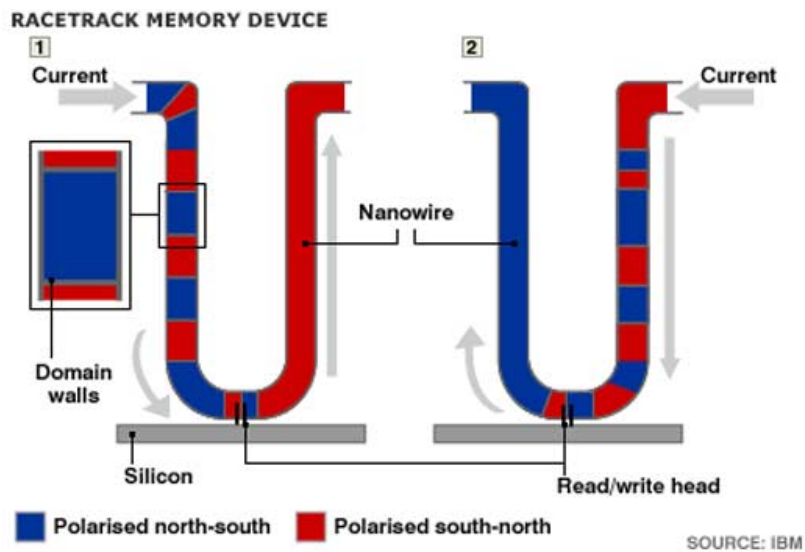


Figure 1.10 – Schematic of the racetrack memory. Figure from *IBM*.

Another field of interest concerns all-magnetic logic. Indeed, logic gates and whole architectures for logic operations and nanocomputing based on magnetic domains manipulated with magnetic fields have been proposed [36–42]. The manipulation of domain walls has also been put forward in the context of unconventional paradigms of information processing, including neuromorphic computing systems based on memristive devices. The

latter are seen as good candidates for artificial synapses, and can be based on domain walls [43–46]. A wide variety of other related applications are considered for spin-based devices [47, 48]. Finally, the magnetic gradient created by stray fields in the vicinity of a domain wall has the potential to attract magnetic beads down to the nanoscale, making their capture, manipulation [49–53] or detection [54] possible.

### 1.2.2 The Landau-Lifshitz-Gilbert equation

The dynamics of DW motion is ultimately governed by a single strongly nonlinear differential partial equation describing the time evolution of single magnetic moments in the presence of a given effective magnetic field. First described in 1935 by Landau and Lifshitz [20], this equation has been refined over time as more insight was gained into the underlying physics. Additional terms to be included to the effective field were proposed to account for specific phenomena (*e.g.* spin-orbit torques, Dzyaloshinskii-Moriya interaction...). In its simplest form, two terms influence the evolution of a magnetic moment in the presence of a magnetic field. The first one is the torque caused by that external magnetic field, and the other is a phenomenological term introducing a damping, on the basis of the observation that a magnetic moment obviously does not precess forever around the direction of a effective field but eventually ends up aligned with it. Fig. 1.11 is a schematic of a typical damped precession. Gilbert’s work on this subject led him to propose a form of the dissipative term [55–57]. Hence, one either talks about the Landau-Lifshitz (LL) equation or Landau-Lifshitz-Gilbert (LLG) equation. Other variants exist for the treatment of dissipation, including the so-called LLBar equation (Landau-Lifshitz Baryakhtar equation) [58, 59] and a generalization of the Gilbert model to describe more diverse dissipation phenomena, *e.g.* dry friction [60–62]. In any case, this equation exhibits interesting properties and its treatment remains challenging even in the simplest systems [63].

The original version of the equation by Landau and Lifshitz in the presence of a magnetic field  $\vec{H}$  can be written as follows:

$$\frac{\partial \vec{M}}{\partial t} = -\gamma_0 \left( \vec{M} \times \vec{H} + \frac{\alpha}{M_s} \vec{M} \times (\vec{M} \times \vec{H}) \right). \quad (1.5)$$

Here,  $\gamma_0 = \mu_0 \gamma$  and  $\gamma$  is the gyromagnetic ratio of the electron,  $\alpha$  is the damping coefficient and  $\vec{M}$  has already been defined as the magnetization vector. The form of the equation

brought by Gilbert is slightly different:

$$\frac{\partial \vec{M}}{\partial t} = -\gamma_0^G \vec{M} \times \vec{H} + \frac{\alpha}{M_s} \vec{M} \times \frac{\partial \vec{M}}{\partial t}. \quad (1.6)$$

It can be shown that the two equations are mathematically equivalent, by taking the cross product of Eq. (1.5) with  $\vec{M}$ . Then, one can determine the following relation between the coefficients by identification [64, 65]:

$$\gamma_0^G = (1 + \alpha^2)\gamma_0. \quad (1.7)$$

Hence, the Landau-Lifshitz-Gilbert equation can be written as follows:

$$\frac{\partial \vec{M}}{\partial t} = -\frac{\gamma_0^G}{1 + \alpha^2} \left( \vec{M} \times \vec{H} + \frac{\alpha}{M_s} \vec{M} \times (\vec{M} \times \vec{H}) \right). \quad (1.8)$$

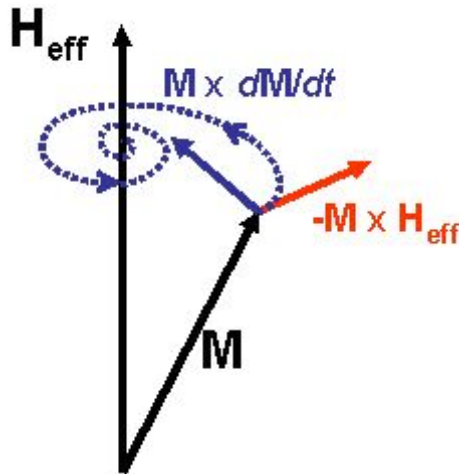


Figure 1.11 – Typical damped precession of a magnetic moment in the presence of a magnetic field  $H_{\text{eff}}$ . The trajectory of magnetization is the dashed blue line, with the terms of precession in red and the damping in blue. Figure from *Public domain*.

There has been substantial debate on the relative relevance of these two equations, in particular which damping term should be used [66–71]. They are equivalent when dealing with conservative torques, and while they may be equally valid in describing real phenomena, the "best" version would be that which correctly separates damping and precession terms. This could in principle be determined experimentally with RF magnetic fields [64]. It is not in the scope of this thesis to propose a definitive answer to this question. However, primarily because it is more widespread, we chose the LLG equation (*i.e.* with Gilbert damping) in this work (see chapter 3).

### 1.2.3 Field-based motion

The most studied and simplest way to induce domain wall motion is to use a (usually static) magnetic field that will energetically favor one of two domains of opposite magnetizations. The difference of Zeeman energy resulting from the presence of the field will make one domain expand at the expense of the other. The dynamics of this phenomenon have been extensively studied theoretically and experimentally over several decades in different materials and geometries. Initial work published in the 1960s and 1970s paved the way for future investigations of field-induced domain wall motion, most notably the landmark contribution of Schryer and Walker [72–76]. Indeed, under simple approximations, it was shown that an analytical treatment of the LLG equation in one dimension could be carried out. The behavior of a moving domain wall in the presence of an external magnetic field could then be described and is quite intriguing. Under a threshold field, the motion reaches a steady-state regime, with a velocity which can be determined analytically, as well as the magnetization distribution. Indeed, the Landau solution for the resting wall (shown in subsection 1.1.4) is also a solution of the dynamical system. An approximation of the transient regime has also been proposed [77]. Collective coordinates approaches introduced by Thiele in the 1970s [78] also describe the same steady-state dynamics and have been generalized and refined over time [79–81]. Here is the solution of the dynamical system as provided in [75] (see Fig. 1.12, for the geometry considered):

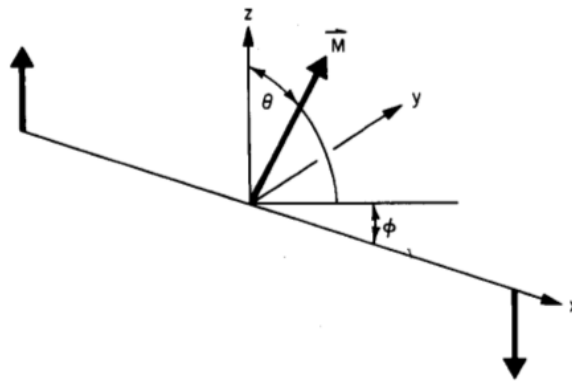


Figure 1.12 – Configuration considered in Walker’s original paper, with angles  $\phi$  and  $\theta$ . Figure from [75].

$$v(H) = -\frac{\gamma_0 H}{\alpha} \sqrt{\frac{A}{K_u + \mu_0 M_s^2 \cos^2 \phi_0}}, \quad (1.9)$$

$$\sin 2\phi_0 = \frac{H}{2\alpha M_s} = \frac{H}{H_c}. \quad (1.10)$$

We can see that the angle  $\phi$  is uniform and assumes the value  $\phi_0$  given by Eq. (1.10).  $H_c$  is a critical field beyond which this equation has no solution. Contrary to what is often stated, the relation between magnetic field and velocity is not linear and that is because of the influence of  $\phi_0$  which varies with  $H$ . The nonlinearity is barely visible if there is a strong anisotropy [82], but otherwise, it can be significant (see Fig. 1.13). Because of the resulting demagnetizing field, the geometry considered also has an effect akin to an anisotropy, which will influence the dynamics [83]. Another point that is not often stressed is that the Walker solution is not always stable [84], depending on anisotropy parameters. Other analytical solutions exist—including the Kolmogorov-Petrovskii-Piskunov (KPP) solution—which have shown to match the results of numerical simulations [85,86].

When the applied field is increased beyond the so-called *Walker breakdown* (*i.e.*  $H > H_c$ ), the system enters an oscillatory regime. This complex behavior requires further approximations or the use of numerical treatment. In any case, a strong reduction of velocity (negative mobility  $\frac{dv}{dH}$ ) is observed. Overall, both numerical and experimental investigations (see Fig. 1.14) have supported the existence of an abrupt transition around a critical magnetic field [87–89]. The motion beyond the breakdown field is characterized by an oscillating velocity—to the point of sometimes causing retrograde motion—as well as internal dynamics of the domain wall [76,88,90,91]. They are also reports that oscillations may even occur before breakdown [92] and in the case of spin wave emissions [93].

Apart from the two regimes described above (steady-state flow regime and oscillatory regime), experimental investigations have shown the existence of another regime at low fields. Labeled *creep regime*, it is characterized by very small velocities and a stochastic process of step by step domain wall motion [94], see Fig. 1.15. At the microscopic scale, this is interpreted by the pinning of the domain wall on local defects or inhomogeneities of various origins in materials. From here, models have been developed [95] describing this phenomenon, yielding a velocity proportional to  $\exp(-Cf^{-\mu}/T)$  where  $f$  is the external force and  $\mu$  is the critical exponent. The motion is thus a thermally activated process: velocity is decreased with lower temperature in thin films [96]. The mechanism behind depinning has also been studied [97] and there appears to be a linear relationship between

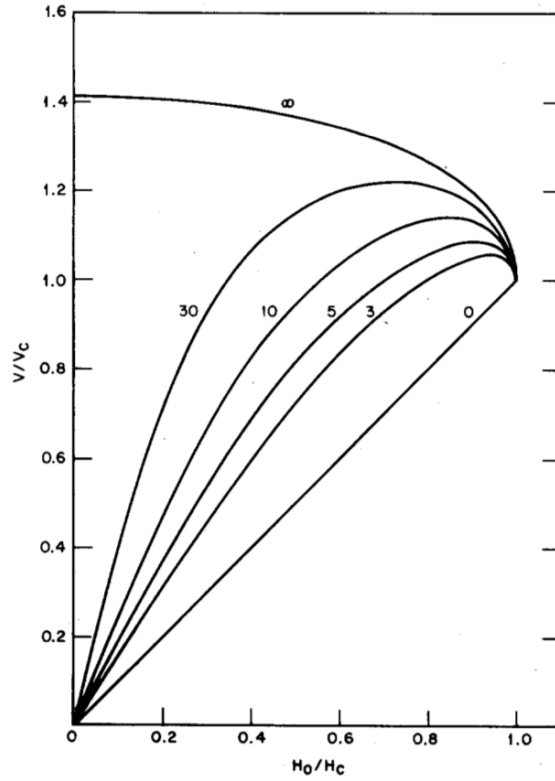


Figure 1.13 – Set of curves representing the velocity as a function of the applied magnetic field for several values of the ratio  $\frac{M_s^2}{K_u}$ . With relatively weak anisotropy, the nonlinearity yields a concave shape which can exhibit a maximum below  $H_c$ . Figure from [75].

depinning field and edge roughness [98]. While it is often modeled by elastic interfaces [99], this is valid only for domain walls in 2D configurations. In confined geometries such as narrow ferromagnetic stripes, the creep regime turns linear: considering the domain wall as a rigid or point-like entity propagating in a one dimensional disordered medium shows good agreement with experimental data while the regular scaling law breaks down [100].

Although most of the research focuses on domain wall motion in thin films or nanowire geometries with constant sections, deliberate engineering of patterns to influence domain walls is also present in the literature. First, it is interesting to note that a widespread technique used to generate domain walls in nanowires is to use special shapes in the design of the extremities [101]. Once created, domain walls can be pinned at local constrictions or notches along the nanowire, as has been shown experimentally [102–105], which is an example of shape-induced potential landscape engineering. In the case of real pinning (*i.e.* with a trapped domain wall), the depinning field increases with the size of the

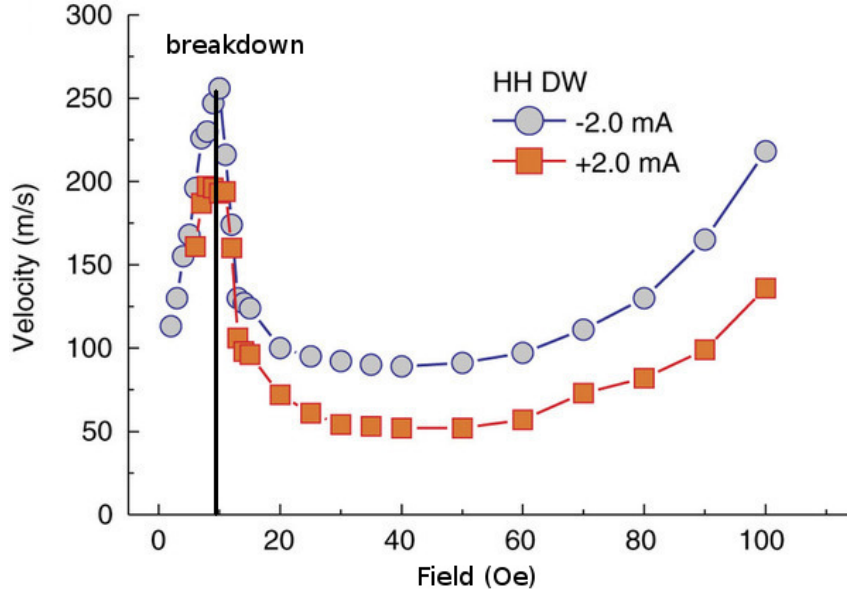


Figure 1.14 – Experimental results showing the complex dynamics of field-driven domain wall motion, as a function of a magnetic field. One can clearly identify the breakdown field around 10 Oe. Figure from [89].

notch, and depends on the chirality of the domain wall [106], although the particular shape of the notch does not seem to matter systematically [107, 108]. A collection of notches can be used to arrange stability at multiple locations [109]. As will be explained in subsection 1.4.1, engineering of the cross section can also be used in cat-eye-shaped elements in order to break the symmetry [110]. Edge roughness and pinning effects in general do affect the dynamics beyond the creep regime [111, 112], but does not seem to change the breakdown field [98] (although it has been reported that this can be achieved by the deliberate engineering of cross section [113, 114]). However, there is evidence that a transverse field has an influence on the value of the Walker breakdown field [115], allowing significant increases of the domain wall velocity [116]. The same can be said of domain wall motion in materials with strong Dzyaloshinskii-Moriya interaction [117].

## 1.2.4 Current-based motion

With discoveries such as giant magnetoresistance [118] and spin-polarized currents, coupled to new opportunities provided by nanotechnology, the field of spintronics has been growing very rapidly. A major research area of spintronics deals with current-induced domain wall motion, first proposed in 1978 [119]. In this subsection, we will give a very

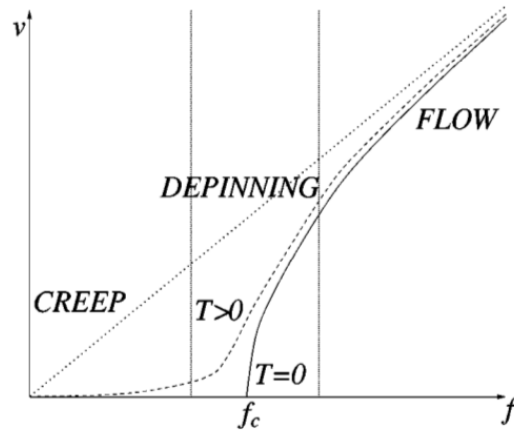


Figure 1.15 – Typical dependance of velocity on the applied field, showing the creep regime at low fields (breakdown field not shown). Figure from [97].

brief account on this subject. For more detailed information on theoretical matters, see Refs. [81,120], and for an experimental review Ref. [121].

The research for a full understanding of the physical mechanisms behind current-induced motion is still ongoing, but a lot has been explored nonetheless through micromagnetic studies [122, 123], theoretical [124–126] and experimental investigations [127, 128], in particular in thin films and nanostripes. The motion is induced by torques applied to the domain wall by the current flowing through it (be in-plane or out-of-plane). Indeed, a current flowing in a ferromagnet tends to be polarized along the local magnetization, and will exert a torque on local magnetization in case it is not parallel to its spin polarization. Two types of torques have been well identified: an adiabatic torque and a nonadiabatic torque, which relative importance depends on the values of parameters such as domain wall width and typical lengths describing spin transfer. The adiabatic torque dominates in the case of wide domain walls, while nonadiabatic torques are notably involved with thin domain walls and strong pinning [125].

Relatively high velocities (hundreds of m/s) have been achieved experimentally in current-driven motion [128, 129], especially in ultrathin nanostripes [130]. The velocity will also depend on domain wall configuration (*i.e.* the type of domain wall) and current injection scheme [131]. There are indeed different ways to inject a current to move a domain wall: in a nanostripe, the current can flow along the nanostripe but also perpendicularly to it, be it in-plane or out-of-plane (vertically) [46]. On this matter, it is also worth mentioning that while the motion can be induced by a local electric current flowing

through the domain wall, it can also be done remotely with spin-current injection [132] (also known as non-local spin injection). Indeed, a conversion between electric and spin current through the spin-Hall effect is possible, and the use of a pure spin current has the advantage of dramatically reducing local heating. As an aside, thermal gradients—for instance generated by Joule heating—have also been used to manipulate domain walls [133].

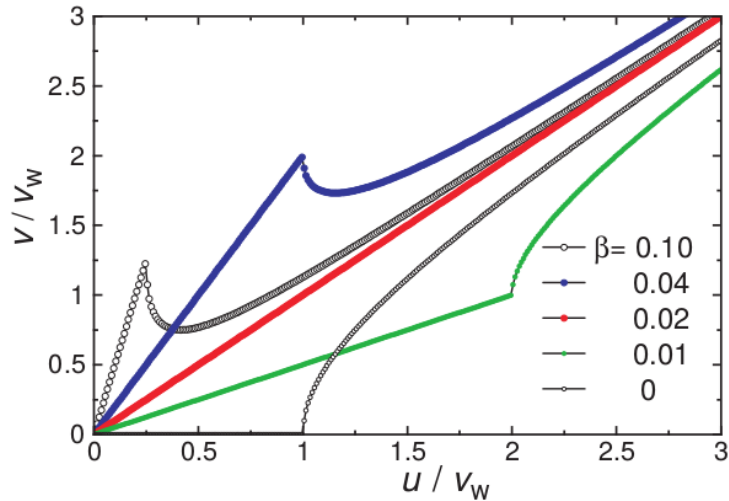


Figure 1.16 – Typical velocity-current relationship, from a one dimensional model by Thiaville et al. Figure from [123].

In any case, the dynamics of current-driven domain wall motion have many features in common with field-driven motion (see Fig. 1.16). The current dependence of velocity exhibits a Walker-like delineation (current density limit) beyond which the velocity is significantly reduced [123, 134, 135]. The steady-state regime is replaced by an oscillatory behavior [136]. Below a threshold current, one can also notice a creep regime similar to what can be observed with field-driven motion [137], where the nonadiabatic torque seems to play a major role [138]. There has been substantial debate over the universality of creep regime and thermal activation [139–143]. The question is about whether or not the stochastic process governing creep motion in current-driven motion is the same as with field-driven motion.

## 1.3 Magnetolectric materials

Domain wall motion and control of magnetization at small scales in general is thus a very active area of research. In this thesis, the main goal is to explore the possibilities regarding domain wall motion and a magnetolectric effect mediated by mechanical stress in artificial multiferroic structures. Indeed, this approach offers significant advantages over standard methods, such as enhanced functionality and lower power consumption. Because it relies on the magnetoelastic coupling, a subsection is dedicated to a short description of magnetostriction.

### 1.3.1 Intrinsic magnetolectric materials

The magnetolectric effect was first proposed by P. Curie in 1894 [144] and later observed experimentally by Astrov [145,146] in chromium oxide  $\text{Cr}_2\text{O}_3$ , also following the prediction of Landau and Lifshitz [147] that this material should exhibit a magnetolectric effect in its antiferromagnetic phase [148]. This phenomenon deals with the coupling between electric and magnetic quantities. The adjective direct or inverse is sometimes used to identify if the stimulus is magnetic or electric. The application of a magnetic field (resp. electric field) will result in an electric (resp. magnetic) effect. This coupling can be found in some materials where it arises spontaneously. While the term magnetolectric is often confused with multiferroic, they refer to distinct properties. Indeed, magnetolectric materials are thus sensitive to both magnetic and electric field, but need not show any magnetic or electric order (see Fig. 1.17).

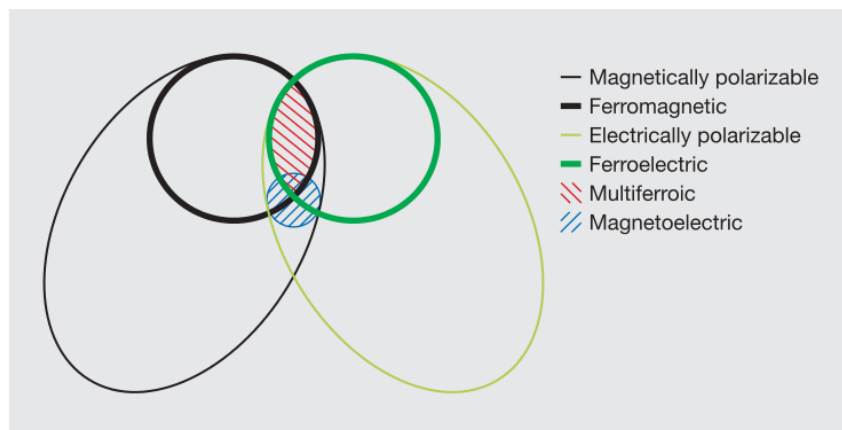


Figure 1.17 – Schematic showing the relationship between classes of materials. Figure from [149].

There are two reasons why, despite the interesting potential of intrinsic magnetoelectric materials, these have not yet encountered much success. One of them is the fact that in any case the intrinsic magnetoelectric effect is relatively weak, with a fundamental upper bound for the components of the magnetoelectric susceptibility tensor [150], as is predicted for specific materials [151]. Furthermore, most materials only exhibit interesting properties at low temperatures, which is for example the case of  $\text{Cr}_2\text{O}_3$  [152] or  $\text{BiFeO}_3$  [153]. One way of getting a strong magnetoelectric response is to work in the vicinity of phase transitions. The application of a magnetic or electric field can then induce a large magnetoelectric effect, including at room temperature [154, 155]. While it does not involve the magnetoelectric effect *per se*, another quite recent activity deals with ultrathin films [156] and materials with perpendicular magnetic anisotropy, where it is possible to influence anisotropy and magnetization [157–164] through subtle interface effects. Electric fields pave the way for a control of magnetic properties—including the phase—without resorting to annealing or other kinds of temperature-based procedures [165]. In the case of domain wall motion, nucleation and pinning have been obtained or influenced by electric fields [164, 166, 167], as well as modulations of domain wall dynamics in the creep [168] and flow [164, 169, 170] regimes. These effects are sometimes called *charge-mediated magnetoelectric* effects. Finally, interesting developments concern the voltage-control magnetic anisotropy in magnetic tunnel junctions. Tunnel junctions are a crucial element of spintronics and the fact that electric fields can to some extent affect their behavior has not gone unnoticed by the research community [171–173].

Interestingly, the possibility to induce domain wall motion in intrinsic magnetoelectric antiferromagnets (such as  $\text{Cr}_2\text{O}_3$ ) using an electric field has been theoretically investigated [174]. As in magnetic field-driven motion, there seems to be a Walker-like breakdown and a maximum velocity achieved at or before this point. The authors also describe how the situation can be improved by adding an in-plane stress or, for that matter, any kind of in-plane anisotropy in order to hinder precession.

Several reviews have covered the subject of magnetoelectric materials. They acknowledge the weaknesses of the intrinsic effect, but also present the opportunities and potential applications of more recent research, especially in thin films [149, 175]. Some even mention a *revival* of the magnetoelectric effect [176], in light of all the applications considered. In particular, various opportunities come from the use of antiferromagnets and the rapid development of artificial magnetoelectric materials.

### 1.3.2 Magnetostriction

Before discussing artificial magnetoelectric materials, it is important that we have a short description of magnetostriction and its modeling. Indeed, artificial magnetoelectric materials often involve magnetostriction because they rely on the mechanical coupling of ferroelectric and ferromagnetic phases. This is also the case in this thesis.

Magnetostriction has numerous applications, most notably in sensing and actuation, and is also a responsible for the typical "humming" noise heard near electrical power transformers. Basically, magnetostriction is the process by which a magnetic material will undergo a deformation following the modification of its magnetization (for example by the application of a magnetic field). The converse effect, sometimes called inverse magnetostriction or Villari effect, deals with the change of the magnetic susceptibility of a material on which a given mechanical stress is applied. It is important to point out that the transformation caused by magnetostriction is associated with anisotropic deformations but is isovolumic. While magnetostriction was first described by Joule in the 19th century [177], its physical origin is still a subject of theoretical investigations.

The phenomenon is better understood for rare-earth elements (from Ce to Lu), although most of them have Curie temperatures below room temperature. Their magnetostrictive properties stem from the angular distribution of orbitals in their unfilled 4f subshell, which is partly responsible for the overall atomic magnetic moment. These orbitals are significantly aspherical (see Fig. 1.18). Therefore when the magnetic moment is rotated, the strong spin-orbit coupling will tend to also reorient the orbitals. This results in a change of charge distributions and, because of the documented asphericity of the orbitals, this will have a direct influence on electrostatic forces and strong magnetostrictive strains [178]. Given the oblate (as in *e.g.* terbium) or prolate (as in *e.g.* samarium) aspect of the orbitals, a positive and negative magnetostriction will be respectively measured. Of all elements, terbium has the largest magnetostriction known today, which leads to an elongation of nearly 1% at 0 K [179].

While there are still some unknowns on the physical workings of magnetostriction, especially in alloys with transition metals, one could argue that efforts to formalize [147, 181, 182] this phenomenon have been quite successful. A first level of description deals with the interaction energy of neighboring magnetic moments, for instance as proposed by Néel [183] based on the cosines of the angle between magnetization and the direction between two atoms. A Taylor expansion of this expression will yield familiar forms of the magnetoelastic interaction, depending on the symmetry considered [6, 184]. Other, more

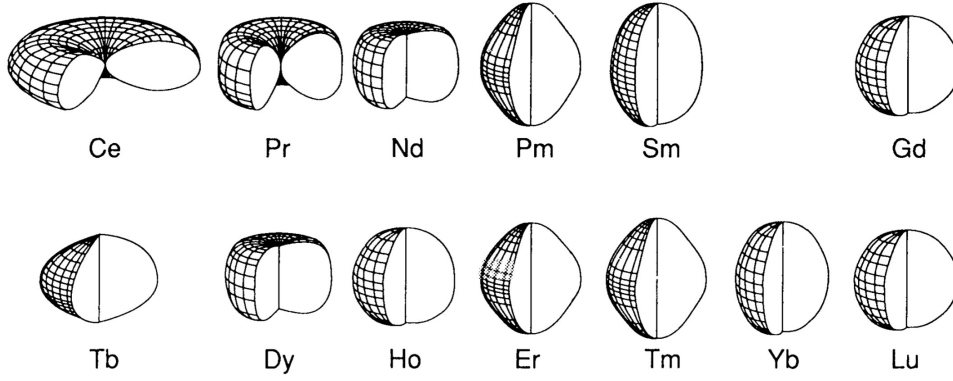


Figure 1.18 –  $4f$  electron charge density in rare-earth elements. Figure from [180].

phenomenological, approaches focus on the constitutive laws considered in the behavior of magnetoelastic materials. This leads to the following expression of the energy density:

$$u_{me} = -T_{ik}\hat{\epsilon}_{ik}^{\mu}, \quad (1.11)$$

where  $\hat{T}$  refers to the local Cauchy stress tensor, and  $\hat{\epsilon}^{\mu}$  is the free strain of the material (*i.e.* the strain measured if the body is perfectly free to deform itself). From there, it follows that in an isotropic material and in the presence of a uniaxial stress, the energy density associated with the magnetoelastic interaction is often written (see chapter 2 for a detailed derivation of this expression from Eq. (1.11)):

$$u_{me} = -\frac{3}{2}\lambda_s\sigma\cos^2\Phi, \quad (1.12)$$

where  $\Phi$  is the angle between the magnetization and the direction of the stress  $\sigma$ . This expression will be used throughout the work presented in this thesis. Here, one can see that mathematically, it is tantamount to the creation of an induced quadratic anisotropy. The end physical result will depend on the sign of  $\lambda_s$ : if positive (resp. negative), the magnetization will tend to align along (resp. perpendicular to) the direction of the stress.

### 1.3.3 Piezoelectricity

In a stress-based magnetoelectric coupling, the most straightforward counterpart of magnetostriction is piezoelectricity. Contrary to magnetic materials, where piezomagnetism is in principle possible [147] but in practice confined to antiferromagnets [185], it is quite common to find materials with a linear relation between electric field and polarization. The origin of this effect is due to crystallography and the existence of polar axes in the

material (amorphous materials cannot be piezoelectric). The total number of symmetry types has been somewhat debated, but recent works concluded that there was 15 irreducible symmetry types [186]. As a way of turning mechanical signals into electrical signals or the reverse, the piezoelectric effect is found to have multiple applications today, such as sensing, transducing, generation of voltage and so forth.

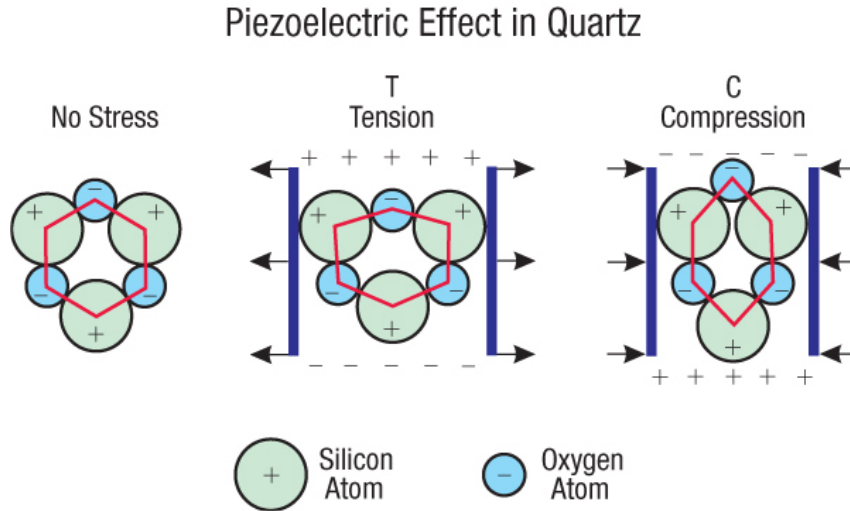


Figure 1.19 – Schematic of the piezoelectric effect in quartz. A compression or a tension creates charges due to the crystalline arrangement. Figure from *dev.nsta.org*.

The coefficients  $d_{ij}$  which we will have use of in the following work are defined in this way:

$$D_i = d_{ijk}T_{jk} + \epsilon_{ij}E_j, \quad (1.13)$$

where  $D$  is the electric induction,  $\overline{\overline{T}}$  is the local Cauchy stress tensor and  $\overline{\overline{\epsilon}}$  is the local strain. In principle, the piezoelectric tensor  $d_{ijk}$  can have a maximum of 18 components, although this number is often dramatically reduced depending on the particular symmetries exhibited by the material considered.

### 1.3.4 Artificial magnetoelectric materials

One way to lift the two constraints mentioned above in intrinsic magnetoelectric materials—namely, weakness of coupling and low temperature requirements—is to arrange an indirect coupling in heterostructures (usually with two phases, but three-phase systems also exist [187, 188]). Possible ways of achieving the coupling are shown in Fig. 1.20. The intermediate between electric fields and magnetism is most often mechanical, although exchange-bias and charge-mediated effects are also studied [189]. The association

of a piezoelectric material—which will convert an electric field in mechanical stress—and a magnetoelastic material—which will be magnetically sensitive to the transmitted stress—gives rise to well-known heterostructures. Basically, a piezoelectric phase and a magnetoelastic phase are elastically coupled, so that the strain generated by an applied electric field in the former will be transmitted to the latter, prompting a magnetic effect. Essentially, this effect is tantamount to an induced anisotropy. In practice, this elastic coupling can for instance be implemented in laminates, in which theoretical investigations of the magneto-electro-elastic coupling in such systems covered the linear [190, 191] and nonlinear [192] regimes. For more information on the different artificial magnetoelectric materials proposed in the literature, see reviews [188, 189, 193].

Experimental research on stress-mediated magnetoelectric effects go back to the proposition of two-phase materials [194] and subsequent work in the 1970s with composite materials made of melted [195] and sintered [196] ferroelectric and ferromagnetic phases. Later, progress in thin film technologies made possible the stacking of piezoelectric and magnetoelastic layers to form laminates. The development of new materials, including the search for better piezoelectric properties, contributed to the optimization of the magnetoelectric coupling [197]. As a result, the magnetoelectric coupling, often measured in  $\text{Vcm}^{-1}\text{Oe}^{-1}$ , has dramatically increased over the years [198–200]. Several examples are shown in Fig. 1.21.

The basic effect of an induced stress is a modification of anisotropy and has been observed repeatedly, including in Pt/Co [201] and in (Ga,Mn)As [202]. Similar effects (inversion of anisotropy) have been noticed in nickel [203]. These changes can then result in reversible modifications of domain wall configurations [204] as well as magnetization switching [205–213] at room temperature, including at the nanoscale [214]. Also, significant change to domain wall mobility and other kinds of influence on domain wall dynamics [201, 215–218] have been mentioned in the literature and will be further described in subsection 1.4.1. Dynamic strains associated with the propagation of acoustic waves have also been shown to influence magnetic structures [219]. Manipulation of domain walls in more specific systems exhibiting misfit strains between different layers has also been reported [220, 221]. Another quite remarkable phenomenon involves changes in the value of magnetization (saturation), with the possibility that the Curie temperature would depend on strain [222].

Artificial magnetoelectric materials are thus linked to a very dynamic area of research of current interest [153]. For a more comprehensive account of the technological outlook of magnetoelectric materials, one can consider several reviews [153, 188, 189, 193, 197].

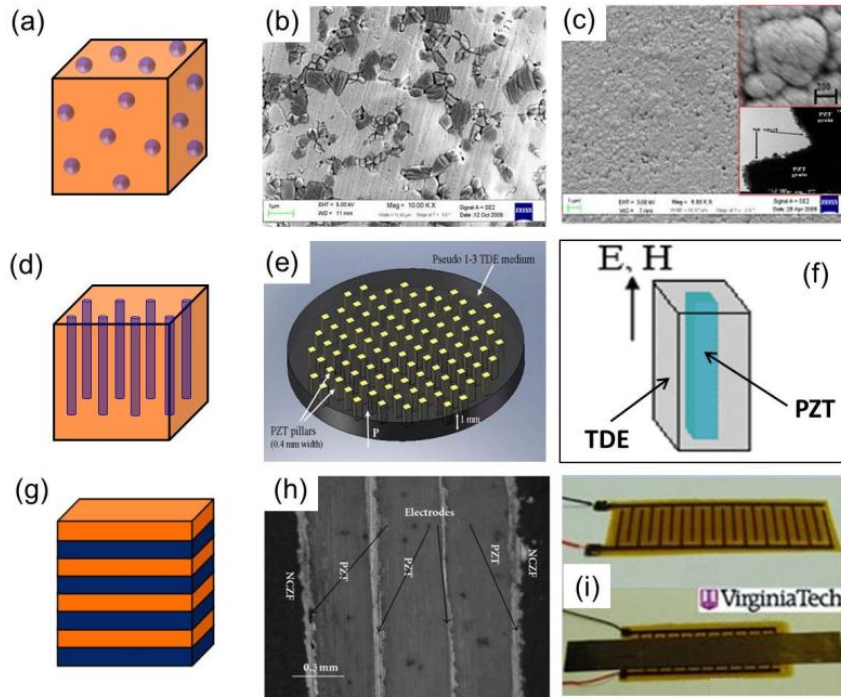


Figure 1.20 – Schematic showing the possible arrangements of magnetolectric heterostructures and examples of their practical implements. Figure from [197].

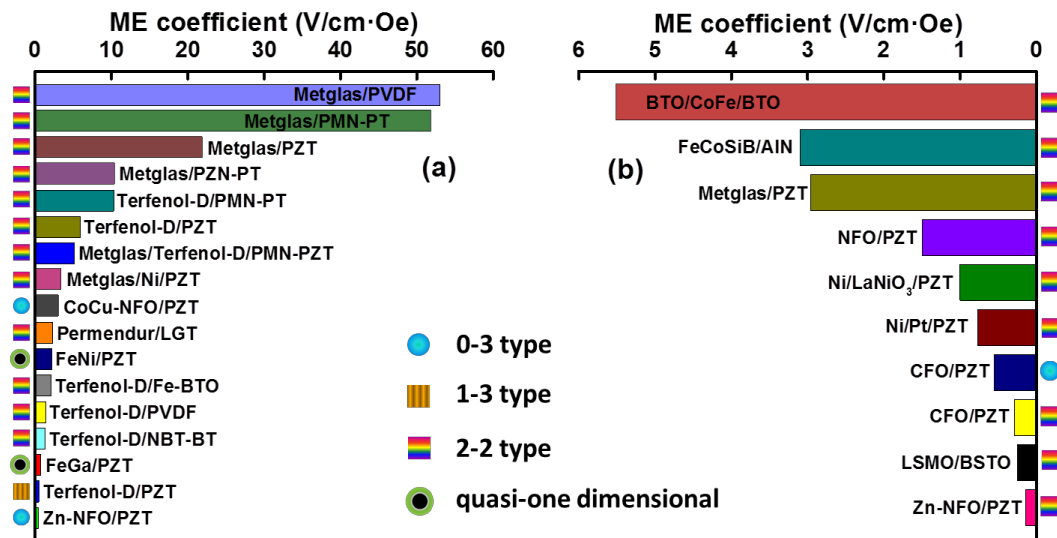


Figure 1.21 – Overview of the values of magnetolectric coupling obtained and reported in the literature with the associated materials in (a) bulk and (b) film structures. Figure from [197].

Much like domain wall-based devices, the integration of stress-mediated devices in microelectronics has been proposed in the context of several practical applications in the literature. Some have coined and used the term *straintronics* to refer to strain-based systems [214, 223]. A first application often considered is memory. Mentioned as early as 2000 [224], the potential of magnetoelectric materials in memory applications have been repeatedly put forward [225–228]. Beside information storage, there are also possibilities in information processing, with Bennett-clocking and magnetic logic devices in general [229–232] paving the way for all spin logic [233]. Proponents of magnetoelectric materials have even mentioned their use as recovery devices for nonclassical information processing systems [234]. Other, more specific uses have also been proposed, such as electrically assisted magnetic recording [235].

## 1.4 Motion induced by uniform stress in magnetoelastic materials

This section contains a presentation of the system proposed and studied in this thesis, which deals with domain wall motion driven by a uniform stress in a magnetoelastic ferromagnet. Before it is addressed, the necessity of breaking the magnetic symmetry will be illustrated. The solution adopted here comes from earlier work, which will be detailed. Finally, preliminary studies showing the validity of the concept will be discussed.

### 1.4.1 The need for symmetry breaking

Regarding domain wall motion induced by an electric field, several methods have been presented in the literature. Again, the interest generally mentioned here lies in the prospects of improved convenience of operation as well as reduced energy consumption [236]. However, due to symmetry reasons linked to the fact that the magnetoelastic energy has a quadratic form, a uniform stress typically cannot discriminate between two antiparallel magnetization states. It follows that it cannot induce unidirectional motion of  $180^\circ$  walls (while to be fair, it could do so for  $90^\circ$  domain walls in principle, for instance in materials with cubic anisotropy [221]).

However, an applied stress can certainly have an influence on the dynamics of motion induced by other means. This should not come as a surprise: as mentioned above, the effect of the magnetoelastic interaction is essentially the creation of a new anisotropy. It is quite obvious from Eq. (1.9) giving the steady-state velocity, that a change in the anisotropy will result in a change of velocity. This phenomenon has been verified experimentally

with magnetic field-driven domain wall motion in amorphous microwires [216–218]. One can conclude from the experimental evidence available that the influence of a mechanical stress through the magnetoelastic interaction has the general effect of decreasing domain wall velocity in the configurations studied. This result is corroborated by other reports that the application of a stress can increase the coercivity (or propagation threshold fields) and therefore block domain wall motion [237]. Similar effects have been observed in the case of electric current pulses in materials with perpendicular anisotropy, with mobility variations up to 500% reported by researchers [215]. Analytical treatments have also been proposed in recent works to describe the influence of a mechanical stress on the dynamics of spin current-driven motion [238]. Another related and intriguing proposition deals with domain wall motion induced by the propagation of polarized elastic waves, which exert a torque and a force on domain walls [239].

The fundamental hurdle of symmetry has led researchers to propose alternatives for stress-induced domain wall motion. The most obvious idea is to use non-uniform stress distributions, *i.e.* stress gradients. Indeed, the spatial variation of stress distribution offers the possibility to create potential wells in which a domain wall can be trapped (see Fig. 1.22). Again, this amounts to the creation of local variations of anisotropy that will affect the energy landscape seen by the domain wall. In the first account on this idea published in the literature, micromagnetic simulations have shown that stress gradients can indeed induce domain wall motion in the absence of any magnetic field or electric current [240]. A later analysis based on a simplified model gives support to original micromagnetic simulations [241].

As mentioned in the beginning of this subsection, a uniform stress cannot induce unidirectional domain wall motion. However, in a ring geometry, it can force a domain wall to move toward a given position determined by the particular stress directions, in combination with particular shapes [53] (see Fig. 1.23). Further modifications can be brought to the geometry to actually break the symmetry [110]. Here, a particular shape of the magnetoelastic element will allow the displacement of the domain wall, achieving 180 ° "switching" after each application of the stress. For continuous domain wall motion in ring geometry, one can also resort to the use of an arrangement with multiple electrodes along with the necessary time actuation signals, a possibility already explored numerically [242].

A completely different approach is to take advantage of the strong pinning that magnetic domain walls can have on ferroelectric domain walls [243]. This pinning is again linked to local stress-induced anisotropy caused by the presence of a ferroelectric domain wall between orthogonal domains. The result is a patterning of the magnetic material

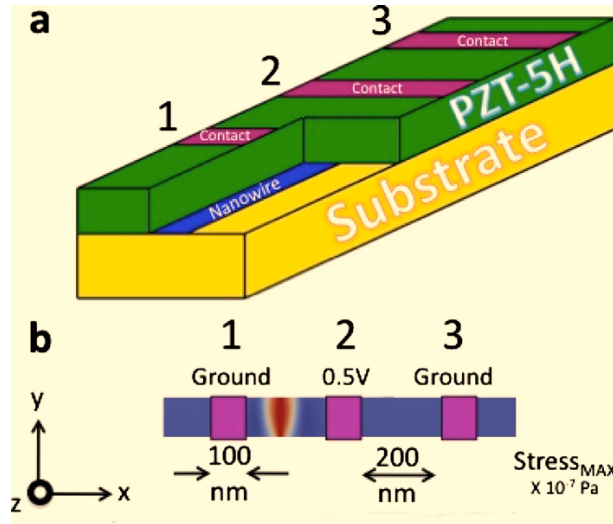


Figure 1.22 – Schematic of the systems based on stress-gradients considered by Dean et al. Localized stress generated by separate electrodes create potential wells. Figure from [240].

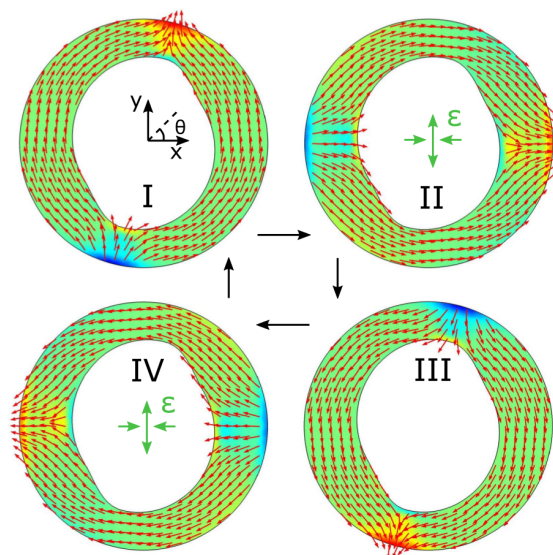


Figure 1.23 – Results of micromagnetic simulations showing the behavior of domain walls in so-called cat eye-shaped magnetoelastic magnets subjected to in-plane stress. The width is variable but is typically around 100 nm. The outer diameter is 500 nm. Figure from [110].

domain configuration on that of the ferroelectric on which it is deposited as illustrated in Fig. 1.24. The application of an electric field will have the effect of changing the domain configuration and therefore induce domain wall motion, as shown experi-

mentally [236, 244]. Micromagnetic simulations showed that distinct dynamical regimes existed, and mentioned the absence of breakdown [245] although researchers later claimed that depinning was possible and somehow linked to the Walker breakdown [246].

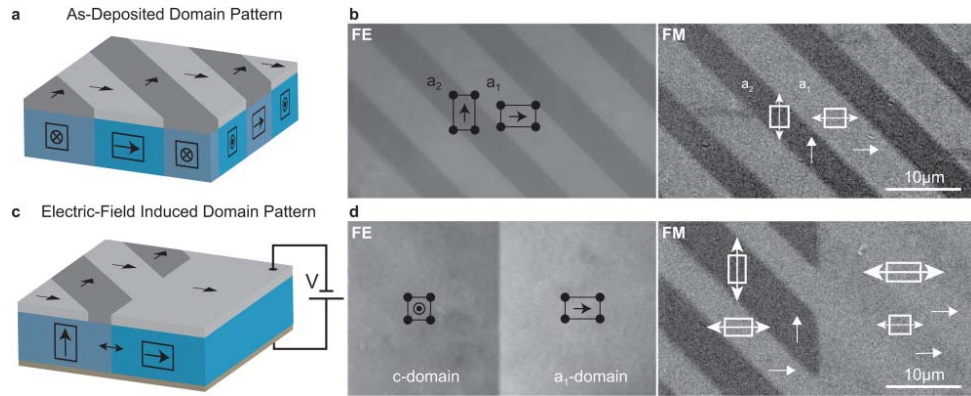


Figure 1.24 – Ferroelectric domain pattern can be imprinted on magnetic materials. Figure from [236].

The same symmetry problem can be found in the context of magnetization switching of monodomain magnetic particles using a uniaxial stress. Indeed, if a stress is applied on a monodomain magnet so that the magnetization goes from one state along the easy axis to a state along the hard axis, the subsequent disappearing of the stress will force the magnetization to choose between two stable states along two equally favorable paths. As a consequence, various solutions have been put forward in the literature. One of them is to fine-tune the electric field pulse to ensure that the magnetization does end up in the desired state [209, 223, 247] (also described for intrinsic magnetoelectric materials [248]). Here, pulse duration, magnitude and orientation have to be tightly controlled, otherwise there are high risks that such systems would be unreliable. In addition, any imperfection in shape or within the material will tend to induce a bias toward one position or the other, which would make this scheme even more difficult to implement successfully. More importantly, this system can only function as a toggle, which can be a serious limitation in the context of memory applications. Indeed, any stimulation will change the state regardless of its previous state, so that writing always has to be preceded by a non-destructive readout in order to know if the system is already in the desired state. Another idea is to use multiple electrodes, again with a more complex operation but with reduced energy requirements [227, 249]. Like with domain wall motion, geometry can also be used to break the symmetry and trigger  $180^\circ$  switching of magnetization with an applied stress [110].

## 1.4.2 Symmetry breaking based on bias magnetic field

To break the symmetry in stress-mediated systems, an interesting alternative to what has been heretofore mentioned is the use of a static magnetic field bias. This idea was implemented in a concept baptized MELRAM because of its potential use as a magnetoelectric memory. Here, a uniaxial magnetoelastic element is subjected to an in-plane static magnetic field  $\vec{H}_0$  perpendicular to its easy axis, tilting toward its direction the two stable states of equal energy. The subsequent application of a uniaxial stress  $45^\circ$  from its easy axis can energetically favor one of these states, and therefore determine unequivocally the final state of magnetization regardless of its initial state (see Fig. 1.25). A basic understanding can be obtained by an energetic analysis, taking into account anisotropy energy, Zeeman energy and magnetoelastic energy.

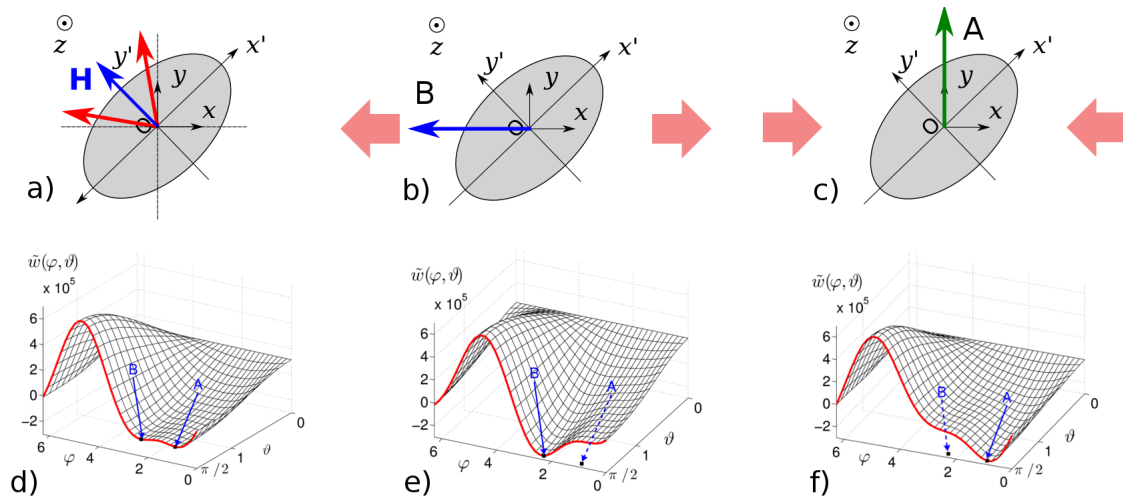


Figure 1.25 – Principle of operation of MELRAM, where a uniform stress can unequivocally discriminate between two states A and B. Subfigures a) b) and c) show a schematic of the magnetoelastic element at rest and subject to tensile resp. compressive stress, while subfigures d) e) and f) is a 3D plot of the corresponding free energy showing the energy landscape as a function of the azimuthal  $\phi$  and polar angle  $\theta$ .

MELRAM has been the object of a patent [250], a PhD thesis [251], a book chapter [252] as well as several publications [226, 253–257]. Experimental validation of stress-mediated switching was carried out at IEMN and showed its non-volatility. This concept was also implemented at the nanoscale by independent authors [214]. This shows the feasibility of a stress-mediated control of magnetization with non-volatile operation. For memory applications, this system has several advantages detailed below:

- Non-toggle: the symmetry breaking allows for unequivocal operation, which ensures that knowledge of the prior magnetization state of the memory is not required for writing.
- Fast operation: studies of its dynamical behavior showed subnanosecond switching [251, 257].
- Non-volatility: once the stress has disappeared, the information written in the direction of magnetization is not lost. Besides, if appropriate structural design is carried out, a significant energy barrier can be arranged between the two stable states so that the system can retain information for a chosen (to some extent) period of time.
- Non-destructive readout: in MELRAM, reading by electrical means can be achieved if coupled to a giant magnetoresistance or tunnel magnetoresistance structure [258]. These techniques can work with low voltages so as not to disrupt the system. Therefore, it is possible to read the state of a cell without altering it. Also, an all magnetoelectric non-destructive readout can be adopted to avoid the use of additional structures allowing magnetoresistance measurements [259].
- Energy consumption: the main advantage of MELRAM and indeed stress-mediated memories in general lies in the low-power operation that they require. Most of the energy dissipated corresponds to the charge and discharge of the piezoelectric phase, which is a dielectric. The gap is substantial: proponents of magnetoelectric memories claim that the power requirements can be reduced by several orders of magnitude. Various estimates have put the total energy consumption for writing one bit at less than  $10^3 k_B T$  while a flash memory based on NAND logic gates needs 10 nJ, or  $10^{13} k_B T$  [260].

For the system to work, there are important constraints on the value of the applied magnetic field which must stay within a certain range. If it is too large, the Zeeman effect become strong enough to sideline anisotropy (*i.e.*  $H_0 > H_a$ ), and only one stable state remain for the magnetization. If it is too small, the operation does not work properly as the magnetization will not switch to the desired states [251]. The threshold value for the field here is  $\frac{H_a}{\sqrt{2}}$ , which corresponds to stable states which are  $90^\circ$  apart from each other, symmetrically with respect to the magnetic field. Therefore we have the following constraint:  $\frac{H_a}{\sqrt{2}} < H_0 < H_a$ .

### 1.4.3 Description of the proposed system

The functionality of MELRAM rests on the possibility to favor energetically one magnetization direction over another, which is possible because of the bias magnetic field. In a one-domain nanomagnet, this can lead to the control of magnetization and magnetization reversal as previously shown. The question we raise in this work is about the opportunities offered by this mechanism in the context of a two-domain magnetoelastic element, *i.e.* the effect of the combination of a bias magnetic field and a uniform stress on a domain wall.

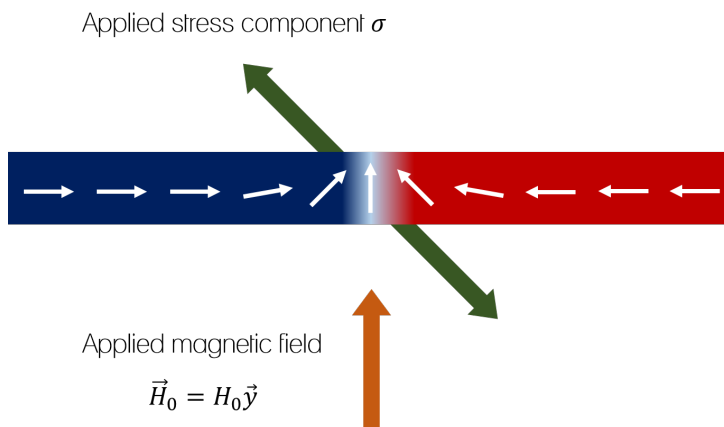


Figure 1.26 – Schematic of the general system considered: a two-domain magnetoelastic ferromagnet with a transverse domain wall.

We therefore consider a uniaxial ferromagnet with magnetoelastic properties elongated in the direction of its easy axis (let us call it  $x$ ), within which the magnetization is distributed in two distinct domains separated by a transverse domain wall, as shown in Fig. 1.26. A bias magnetic field is applied perpendicular to the easy axis, *i.e.* along the  $y$ -axis. A uniform stress  $\sigma$  corresponding to the tension or compression of the direction defined by the vector  $\frac{1}{\sqrt{2}}(\vec{y} - \vec{x})$  is then transmitted to the magnetoelastic layer by a piezoelectric substrate subjected to an appropriate electric field. The rationale behind the proposition of such a system to achieve domain wall motion—although less amenable to qualitative description—is close to the mechanism implemented in MELRAM and involves making one state more energetically favorable than the other. The result of the interplay of competing energetic contribution on the stable states of magnetization are illustrated in Fig. 1.27. The overall difference in volumic energy is at the origin of motion: the domain with lower volumic energy will expand at the expense of the other.

Presumably, the amplitude of the energy gap should have an influence on the motion, this will be explored in later developments.

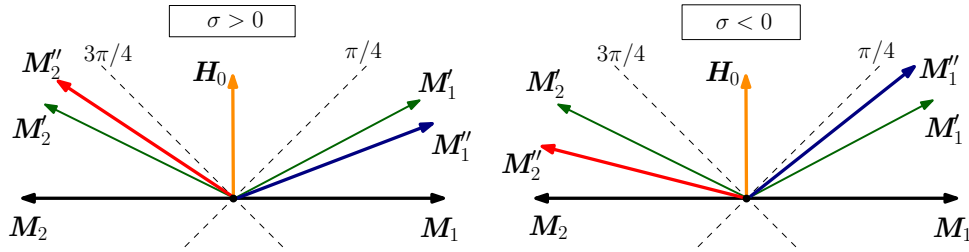


Figure 1.27 – Stable magnetization states within the nanostripe. The uniaxial anisotropy without  $\vec{H}_0$  and the stress  $\sigma$  induces two opposite states  $\vec{M}_1$  and  $\vec{M}_2$ . When  $\vec{H}_0$  is applied, we have  $\vec{M}'_1$  and  $\vec{M}'_2$ , still symmetric. Further, the mechanical stress leads to the tilted states  $\vec{M}''_1$  and  $\vec{M}''_2$ , which are asymmetric for both positive and negative stress.

One way to expose the mechanism behind motion in a more intuitive fashion is to detail sequentially the effect of the stress and only then that of the bias magnetic field, instead of the reverse. Fig. 1.28 shows how the two-domain magnet reacts, and helps grasp the crucial role of the bias magnet field as a symmetry-breaker. The combined effect of uniaxial anisotropy and magnetoelastic interaction is an equivalent anisotropy tilted with respect to the  $x$ -axis. This tilt—better explored in chapter 2—allows for the discrimination between the two states based on their Zeeman energy, see subsection 2.2.2. As such, the phenomenon is *stress-triggered*, because the tilt is induced by the stress, but *field-driven* because the Zeeman energy gap is responsible for the motion. Again, these matters are detailed in the following chapter.

The reason for considering a uniform stress stems from the fact that a setup with multiple electrodes somewhat limits the downscaling of the whole device. Furthermore, if a large piezoelectric substrate is used (commercial or grown), the hypothesis of a uniform stress is reasonable. Stress gradients can indeed exist in patterned nanostructures depending on the properties of the materials used and the dimensions of the layers. True enough, moderate stress gradients would certainly affect the behavior of the domain wall and its dynamics, but would not necessarily preclude operation and therefore do not diminish the relevance of the mechanism proposed. Admittedly, considering the effect of stress gradients would be useful in terms of representing a real device in the context of an engineering endeavor. However, it would add unnecessary complexity in the pursuit of physical insight because there would be a risk of distinct phenomena being confounded. As for the bias magnetic field, it can be generated by neighboring burrowed permanent

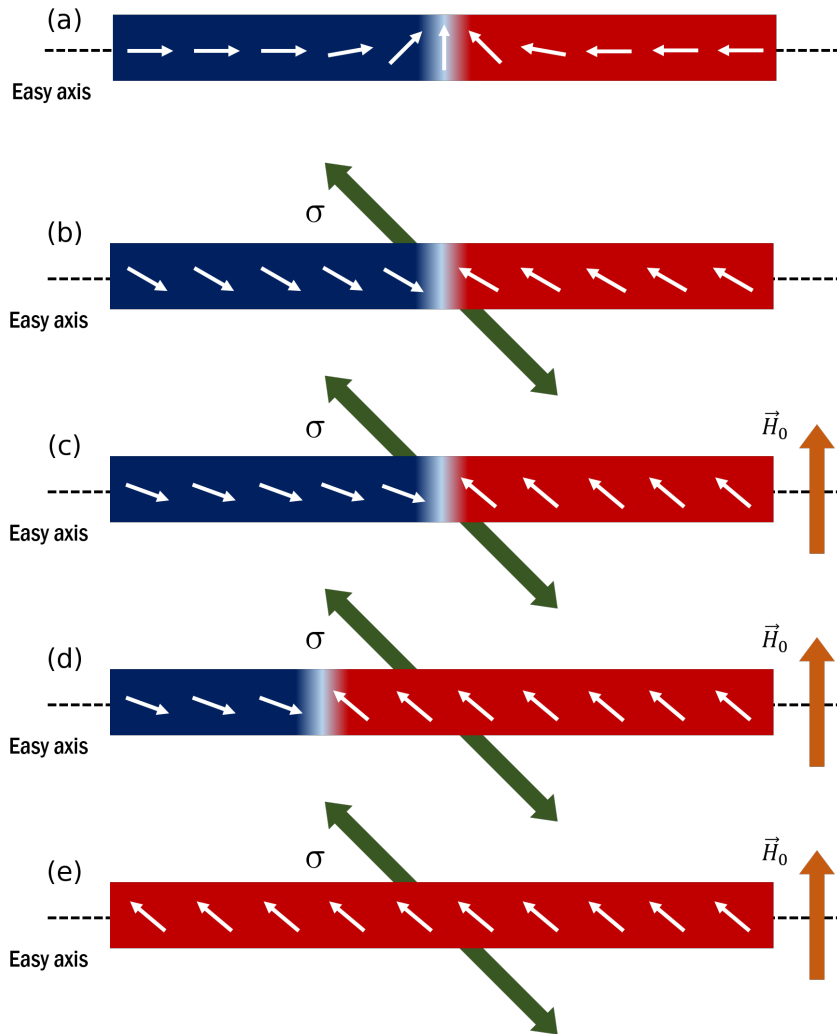


Figure 1.28 – Schematic of a two-domain ferromagnet (a) at rest, (b) with the application of a stress, (c) with the application of a stress and a magnetic field (c) where the symmetry is broken, inducing domain wall motion as a result (d-e).

magnets [261] (and thus does not contribute to the overall energy consumption). However, it is important to keep in mind that resorting to *in situ* structures is not essential to the practical implementation, and macroscopic structures can be used, as the magnetic field is simply a static bias breaking the symmetry. The substrate can indeed be placed in the air gap of a surrounding magnetic circuit which includes an arrangement of permanent magnets. Given the lengthscales involved (micrometers at most) one can expect that the homogeneity of the magnetic field generated by such a device would be secured over the spatial extent of the system.

Because this system is essentially based on the same concept, there are several features in common with MELRAM, including the advantage in terms of energy consumption compared to other domain wall motion techniques (see chapters 2 and 3 for details), as well as the unequivocal operation (the direction of motion can be fully predicted from the stress applied on the magnetoelastic stripe). However, there are some important details on which the two systems differ. In particular, the constraints on the value of the magnetic field mentioned for the case of MELRAM are somewhat lifted. Indeed, a consequence of the shape anisotropy arising from the stripe geometry is to strengthen the uniaxial anisotropy, so that the existence of two stable states is ensured well beyond what would be predicted if only anisotropy and Zeeman energy are taken into account (see subsection 2.2.4 of chapter 2). Besides, the lower magnetic field limit for the MELRAM system to work does not exist here, as the movement of the domain wall does not rely on the *trajectory* of magnetization but ultimately depends only on the *difference in volumic energy* of the two domains.

#### 1.4.4 Engineering of cross section

As mentioned in subsection 1.2.3, the patterning or engineering of the edges in a nanostructure has an influence on domain wall motion. This work includes the study of systems with variable cross section (through a variable width) on the behavior of a domain wall moved by uniform stress, as depicted in Fig. 1.29. To the best of our knowledge, discrete pinning sites have been investigated theoretically and experimentally, but no systematic study of the generic effect of altering the potential landscape of the domain wall through engineering of the cross section actually exists (including in the case of field- and current- driven motion, for that matter).

Simply put, a magnetic domain wall will have the tendency to shift toward regions of lower width (constrictions) because of the energy pay-off related to reduced exchange and anisotropy energy. Indeed, as explained in subsection 1.1.4, a domain wall is associated with a local increase of volumic energy. Therefore, the larger the domain wall, the larger the increase of energy. It follows that any local minimum of width will represent a potential well—and hence a stable location—for a domain wall. Conversely, any local maximum will represent a potential barrier. As a result, complex potential landscape can in principle be designed. This leads to many interesting lines of investigation in relation to domain wall motion in nanostripes of variable width. With regard to applications, one can think of devices with multiple local minima in which domain walls will be trapped, a concept of possible interest for logic tasks. Besides, on more theoretical considerations, many

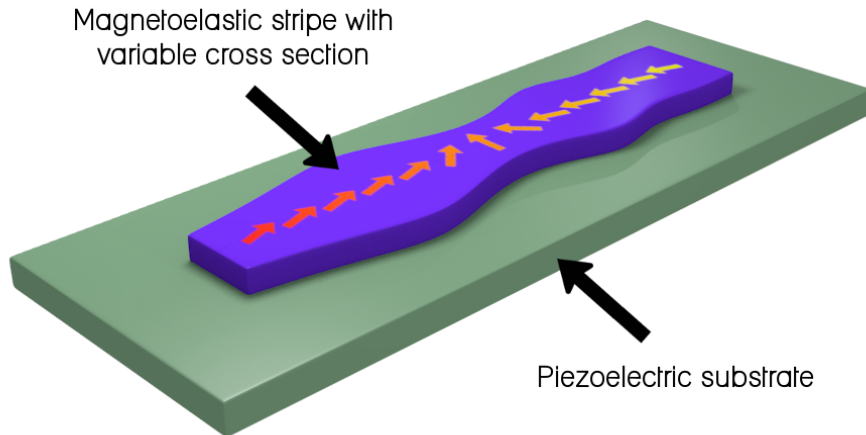


Figure 1.29 – In this work, we consider a nanostripe with a width free to vary with  $x$ .

unanswered questions lie in the influence of a variable width in the dynamics of domain wall motion. Indeed, it is established that the dimensions of the medium in which the domain wall travels do affect the dynamics (steady-state velocity, Walker breakdown field...). What happens in the different dynamic regimes with a variable width, for instance considering low and high spatial periodicity, remains an open question.

In this work, we focus on two cases: constant section and parabolic section (symmetrical with respect to the middle of the stripe). Under some conditions, the latter can ensure confinement, with a stable position in the middle and potential barriers to the ejection of the domain wall, *i.e.* its disappearance from the stripe. As an aside, we considered profiles which were perfectly smooth, and we did not investigate the influence of rough edges. Presumably, the findings of such an analysis would be similar to what is observed for field- and current-driven motion (see subsections 1.2.3 and 1.2.4).

### 1.4.5 Proof of concept through micromagnetic simulations

The Nmag free and open-source package [262] based on finite elements was used to provide a proof of the concept proposed above. The software allows the user to perform micromagnetic simulations with a wide range of material parameters and information describing the problem, all specified in a Python script located in a dedicated file. Information about the geometry and the mesh is provided by a meshfile generated for instance using the gmsh software [263].

The minimum length of the mesh elements in all our simulations was 5 nm. Since the goal was not to perform detailed analyses but to gain insight in the validity of the concept, no computations with better resolution than this were carried out. Anyway, the result of simulations showed that the typical width of domain walls in this context was several times the size of elements, so that domain walls could be described correctly. Several geometries have been considered (mainly the two cases mentioned in subsection 1.4.4), all with their largest dimension along  $x$ , and their smallest along  $z$  (vectors contained in the  $xy$ -plane are called *in-plane*). In the Python script, one can specify an arbitrary anisotropy. In the present case, we study the behavior of materials with uniaxial anisotropy along  $x$  (quadratic anisotropy energy proportional to  $w_x^2$ ). An external magnetic field of a given amplitude and along a given direction can be easily implemented in Nmag, in our case it was introduced along the  $y$ -axis. As for the magnetoelastic energy, there is no dedicated tool in Nmag to take it into account. However, it can easily be integrated into the arbitrary anisotropy defined by the user: as we have shown in subsection 1.3.2, the magnetoelastic energy can be written as a simple quadratic anisotropy. Below is an excerpt of the Python input file to Nmag, showing the definition of the arbitrary anisotropy.

```
# define anisotropy
xx = [1, 0, 0]      # The (normalized) x axis
yy = [0, 1, 0]      # The (normalized) y axis
zz = [0, 0, 1]      # The (normalized) z axis
def my_anisotropy(m):
    ax = scalar_product(xx, m)
    ay = scalar_product(yy, m)
    az = scalar_product(zz, m)
    return -K_u*ax**2 - 3.0/2.0*lambda_S*sigma*(ax**2+ay**2-ax*ay)
```

The various parameters chosen (anisotropy constant, magnetization at saturation etc) correspond to the well-known magnetoelastic material Terfenol-D. These will be detailed in the following chapter. A Gilbert damping of 0.1 was used. Here, one needs to work with an initial situation where a domain wall is present. This is fairly straightforward with Nmag since the user can decide what the initial distribution of magnetization will be. Typically, specifying two regions of opposite magnetization (along  $+\vec{x}$  and  $-\vec{x}$ ) separated by a small area of intermediate magnetization (along  $\pm\vec{y}$ ) and allowing the system to relax will secure the desired outcome. Another option backed by experimental data [264] is to apply a strong magnetic field along  $\pm\vec{y}$  and then reducing it to a small value. Once the initial magnetization is obtained, the dynamical study can begin with the application of a stress. Dedicated routines help save relevant data at fixed time intervals.

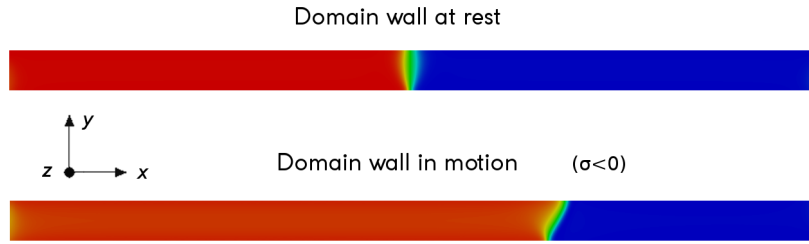


Figure 1.30 – The combination of a static magnetic field in the  $y$  direction and in plane uniform stress is able to induce the motion of a domain wall in a predictable direction. The first image shows the distribution of  $w_x$  at rest with a static magnetic field, the second image shows the distribution of  $w_x$  1 ns after applying a constant negative stress. Here, the nanostripe is 2  $\mu\text{m}$ -long, 10 nm-thick and 100 nm-wide.

Visualization of the data was done using ParaView which is an open source software supporting interactive visualization of vtk files. The fields that are of primary interest here are the three components of magnetization. The simulations showed that the application of a stress in the presence of a transverse magnetic field does indeed result in domain wall motion. In the case of a constant section, the domain wall moves toward the end of the nanostripe until there is only one domain left (see Fig. 1.30). In the case of a parabolic profile of cross section, the domain wall moves until it reaches an equilibrium position (see Fig. 1.31). If relaxed, the domain will go back to its initial position in the middle of the simulated magnetic element. However, another behavior is observed if the magnetic field and/or the applied stress is too large: the domain wall shift leftward or rightward until it reaches the extremity of the simulated magnet, much like in the case of constant section. The intuitive interpretative of these two different situations is that if the "driving force" behind the motion of the domain wall is too strong, it will go past the exchange-related energy barrier formed by the geometry.

This is all that can be said here on this subject, as these time consuming preliminary studies were not performed to address any other matter than the validity of the concept. Indeed, since Nmag simulations work like a black box to a large extent, it is often difficult to get an understanding of the physical phenomena involved. In order to better grasp the underlying physics and to ensure that all parameters are within control, simplified models were built and will be presented in the following chapters.

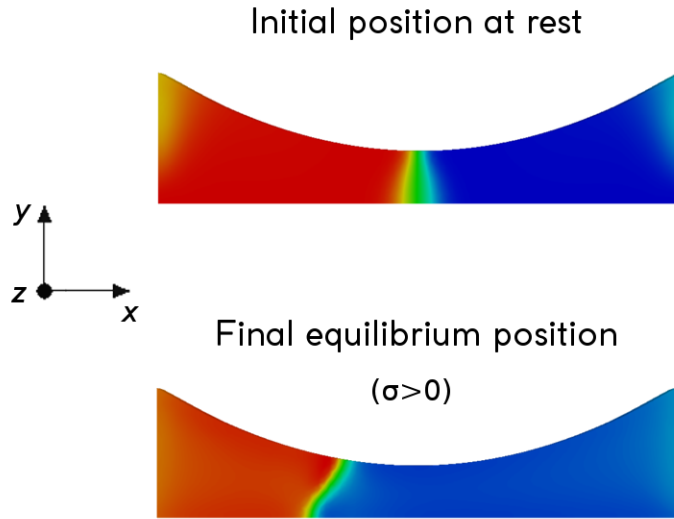


Figure 1.31 – With a parabolic profile, the domain wall can be confined in a region. With the application of a stress, the domain wall will reach an equilibrium position.

## 1.5 Conclusion

In this chapter, we saw that domain walls are prominent elements of modern research in areas such as micromagnetism, microelectronics and nanotechnology. Their manipulation is a subject of great interest, most notably in relation to their potential in various applications. While domain wall motion and control of magnetization is most often mediated by magnetic fields or electric currents, there is a wide interest in the search for alternatives. Among what has been put forward, stress-mediated artificial magnetoelectric materials appear promising. Indeed, the convenience of an electrical control—that is, using voltage—over magnetization is often highlighted. More importantly, the ultra-low-power requirements of such systems make them good candidates for future technological and commercial developments.

In this context, the present thesis proposes a new paradigmatic system involving the application of a uniform stress on a two-domain magnetoelastic nanostructure. However, a uniform stress alone cannot induce motion of  $180^\circ$  domain walls, hence the need to break the symmetry. A way of doing that was introduced by the AIMAN-FILMS group at IEMN several years ago in the context of magnetization switching of uniaxial magnetoelastic magnets. It involves the application of a static magnetic field perpendicular to the easy axis, which enables a subsequent uniform stress to create an energy gap between the two

stable states. In a two-domain ferromagnet, this would amount to domain wall motion, since one domain will expand at the expense of the other. This is the idea proposed here, and it has been shown how preliminary 3D simulations showed that this idea seemed valid. The following chapter will detail how we studied this phenomena with *ad hoc* theoretical and numerical procedures.

# Chapter 2

## Static behavior in magnetoelastic nanostructures

In chapter 1, we made an innovative proposal for domain wall motion. Preliminary results based on standard numerical simulations suggest that the idea presented in the previous chapter might lead to new ways of moving domain walls. However, while micromagnetic simulations are interesting in that they are an easy way to study complex systems in 3D geometry, there are two significant downsides to their systematic use. First, the computational effort necessary to carry out those simulations is enormous, especially for time-resolved computations [265]. Second, although these softwares are easy to handle, there are necessarily used as black boxes to some extent. The user usually specifies inputs and collects outputs with only limited control on the computation itself. For these reasons, another approach based on a new numerical tool has been devised and will hereby be presented. Tailored to match the requirements of nanostripe geometry, this 1D model yields satisfying results with moderate computational effort. Moreover, the total control over the calculation helps understand the underlying physical mechanisms at play.

The work presented in this chapter was the subject of two publications [266, 267].

### 2.1 Variational approach to micromagnetism

In this section we present a brief introduction of the classical equations derived from a variational approach [1, 147, 182]. While the following development does not introduce anything that has not been previously reported, it is an attempt to present a proper synthetic derivation of Brown's equation from a mathematical point of view. In particular, an emphasis is put on the requirements of the variational procedure regarding the magnetic field in appendix C.

### 2.1.1 Overview

In a standard micromagnetic software such as nmag, a 3D object is divided into a finite number of small elements with a chosen geometry (oftentimes tetrahedra). Then when prompted to find an equilibrium distribution, an algorithm usually based on variational methods is used to determine an approximated solution to a boundary value problem. The equations solved involve a quantity that can be called the energy of the system, which will be minimum—at least locally—when the system has reached its equilibrium state.

The calculus of variations provides a set of techniques aimed at finding the extrema of a functional [268]. In our case we want to find the minimum of a quantity which can be equated with the total energy of the ferromagnetic region (which includes the relevant contributions such as anisotropy, Zeeman etc). The first step is therefore to define rigorously what is the energy, which corresponds to our functional. This is not as straightforward as it seems, and sometimes the logic of the subtle choices made in the expression of the contributions is not fully explained. Here in particular we give a detailed description of how the problem concerning the demagnetization vector field is addressed. Once the energy of the system is determined, appropriate constraints have to be taken into account. The outcome of the variational procedure (minimization process) yields an equation of which the equilibrium magnetization distribution is a solution.

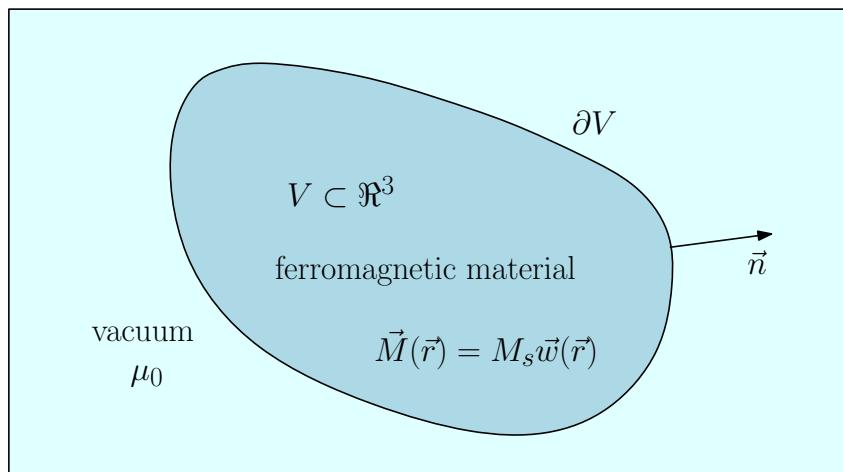


Figure 2.1 – Geometry of the ferromagnetic material occupying a region  $V$  with external surface  $\partial V$  and normal unit vector  $\vec{n}$ .

The system taken into consideration is a region  $V \subset \mathbb{R}^3$  with external surface  $\partial V$  and normal unit vector  $\vec{n}$  (see Fig. 2.1). We suppose that the region  $V$  is filled with a

ferromagnetic material with magnetoelastic (or magnetostrictive) properties, while the external region  $\mathbb{R}^3 \setminus V$  is composed of a linear magnetic material characterized by the vacuum permeability  $\mu_0$ . As described in the previous chapter, the ferromagnetic material is described by a magnetization vector  $\vec{M}$ , defined within the region  $V$  by its space varying direction  $\vec{w}(\vec{r})$ . It means that  $\vec{M}(\vec{r}) = M_s \vec{w}(\vec{r})$ , where  $M_s$  represents the magnetization at saturation.

## 2.1.2 Definition of the energy functional

The functional to be minimized here is the total energy of the system. In the following, the different energetic contributions relevant to our problem are defined. The energy density is the sum of these terms written in their most general form, as follows:

$$u = u_{an} + u_{ex} + u_{me} + u_{Ze}. \quad (2.1)$$

Let us now define these contributions and give general expressions.

- $u_{an}$  represents the anisotropy energy density and takes into consideration specific directions where the magnetization is preferably oriented. This term is due to the crystalline structure of the ferromagnetic material [20]. We consider here an arbitrary form

$$u_{an} = f_{an}(\vec{w}). \quad (2.2)$$

- $u_{ex}$  takes into consideration the exchange interaction among magnetic dipoles of the magnetization distribution. Using the Einstein notation, its general form follows [147]

$$u_{ex} = \frac{1}{2} \beta_{ij} \frac{\partial w_l}{\partial x_i} \frac{\partial w_l}{\partial x_j}, \quad (2.3)$$

where  $\vec{w}$  is the magnetization direction and  $\beta_{ij}$  is a symmetric tensor.

- $u_{me}$  is the energy associated to the magnetoelastic effect. Its general form can be written as [1, 147, 182]

$$u_{me} = -a_{iklm} T_{ik} w_l w_m = -T_{ik} \epsilon_{ik}^\mu. \quad (2.4)$$

Here,  $T_{ik}$  is the Cauchy stress tensor, which is considered known and imposed to the structure. The problem of determining the actual stress distribution in  $V$ , taking into account the coupling between magnetostriction and elastic quantities when the body is embedded in a different elastic environment is treated elsewhere

and not considered in the present development (see *e.g.*, Ref. [255]).  $a_{iklm}$  is a tensor with the symmetry properties  $a_{iklm} = a_{kilm}$  and  $a_{iklm} = a_{ikml}$ . The quantity  $\epsilon_{ik}^\mu(\vec{w}) = a_{iklm}w_lw_m$  is the so-called eigenstrain characterizing the magnetoelastic effect. It means that the constitutive equation from the elastic point of view is given by  $\bar{\bar{T}} = \bar{\bar{L}}(\bar{\bar{\epsilon}} - \bar{\bar{\epsilon}}^\mu)$ , where  $\bar{\bar{T}}$  and  $\bar{\bar{\epsilon}}$  are the actual stress and strain tensors, and  $\bar{\bar{L}}$  is the elastic stiffness tensor (satisfying the same symmetries as  $\bar{\bar{a}}$  plus the additional property  $L_{iklm} = L_{lmik}$ ). This constitutive equation must be interpreted as follows. If the stress is zero (elastically free body), then we find  $\bar{\bar{\epsilon}} = \bar{\bar{\epsilon}}^\mu$ , *i.e.* the real strain corresponds to the eigenstrain, which assumes the character of strain imposed by the magnetization. It means that, when  $\vec{w}$  is fixed in a given region, then  $\bar{\bar{\epsilon}}$  will tend to be equal to  $\bar{\bar{\epsilon}}^\mu(\vec{w})$ . In the situation where  $\bar{\bar{T}}$  is not zero (region  $V$  constrained or embedded in a given elastic matrix), the actual strain  $\bar{\bar{\epsilon}}$  cannot assume the value  $\bar{\bar{\epsilon}}^\mu$ , and the system finds a compromise between the effects of magnetization and elastic interactions with the matrix.

- $u_{Ze}$  is the energy corresponding to the local interaction between magnetization and magnetic field. It is called the Zeeman term and its general expression is [269]

$$u_{Ze} = -\mu_0 M_S \vec{H}_l \cdot \vec{w}. \quad (2.5)$$

It is important to underline that  $\vec{H}_l$  is the *local* magnetic field that one can measure at any given point  $\vec{r}$ . Typically, it is composed of two contributions: an externally applied field  $\vec{H}_0$  and a magnetic field  $\vec{H}_d$  generated by the magnetization distribution  $\vec{M}(\vec{r})$  itself. The latter is referred to as the demagnetizing field. Therefore, we have  $\vec{H}_l = \vec{H}_0 + \vec{H}_d$ , where  $\vec{H}_d$  directly depends on  $\vec{w}(\vec{r})$ . As a first step, the choice is made of joining demagnetization and external field in the same Zeeman energy term to better introduce a necessary discussion proposed in the next subsection.

We can finally introduce the total energy stored within the region  $V$ :

$$\begin{aligned} U &= \int_V u \, d\vec{r} \\ U &= \int_V \left[ f_{an}(\vec{w}) + \frac{1}{2} \beta_{ij} \frac{\partial w_l}{\partial x_i} \frac{\partial w_l}{\partial x_j} - T_{ik} \epsilon_{ik}^\mu - \mu_0 M_s H_{li} w_i \right] d\vec{r}. \end{aligned} \quad (2.6)$$

### 2.1.3 Derivation of classical equations

Written as such,  $U$  depends on the function  $\vec{w} = \vec{w}(\vec{r})$ , while  $\bar{\bar{T}}$  and  $\vec{H}_l$  are imposed quantities. The behavior of the ferromagnetic material in the region  $V$  can be summarized

through the following statement: at equilibrium, the magnetization distribution within  $V$  is found by minimizing  $U$  with respect to  $\vec{w}(\vec{r})$ , with  $\overline{\overline{T}}(\vec{r})$  and  $\vec{H}_l(\vec{r})$  fixed beforehand. From the mathematical point of view, this is a problem of the calculus of variations. However, the minimization as formulated above is hardly applicable to real situations, and therefore it is not the problem we have to solve. While it is possible to fix the external field  $\vec{H}_0$ , it is typically not the case for the total field  $\vec{H}_l$ . The reason for this is that the demagnetizing field  $\vec{H}_d$  itself depends on  $\vec{w} = \vec{w}(\vec{r})$ , being the sum of all contributions generated by the elementary dipoles of the overall distribution [269]:

$$\vec{H}_d(\vec{r}) = M_s \int_V \overline{\overline{N}}(\vec{r}, \vec{r}_0) \vec{w}(\vec{r}_0) d\vec{r}_0, \quad (2.7)$$

with

$$\overline{\overline{N}}(\vec{r}, \vec{r}_0) = \frac{1}{4\pi} \left[ \frac{3(\vec{r} - \vec{r}_0) \otimes (\vec{r} - \vec{r}_0)}{\|\vec{r} - \vec{r}_0\|^5} - \frac{\overline{\overline{I}}}{\|\vec{r} - \vec{r}_0\|^3} \right]. \quad (2.8)$$

In Eq. (2.8),  $\vec{a} \otimes \vec{b}$  represents the tensor product between two vectors  $\vec{a}$  and  $\vec{b}$ , *i.e.* we have  $(\vec{a} \otimes \vec{b})_{ij} = a_i b_j$ , and  $\overline{\overline{I}}$  is the identity operator. The notation  $\|\cdot\|$  is used for the euclidian norm. From this expression, one can prove that  $\overline{\overline{N}}$  exhibits the following symmetry properties:

$$\overline{\overline{N}}(\vec{r}, \vec{r}_0) = \overline{\overline{N}}^T(\vec{r}_0, \vec{r}), \quad (2.9a)$$

$$\overline{\overline{N}}(\vec{r}, \vec{r}_0) = \overline{\overline{N}}(\vec{r}_0, \vec{r}). \quad (2.9b)$$

The principle described above suggests to minimize  $U$  with  $\overline{\overline{T}}$  and  $\vec{H}_l$  fixed. Since this is not suitable for our physical problem, we have to find an equivalent result based on a different functional  $\tilde{U}$  minimized with a stress tensor  $\overline{\overline{T}}$  and an external field  $\vec{H}_0$  (instead of local field  $\vec{H}_d$ ) fixed. Besides, there is a constraint on the norm of the unit vector  $\vec{w}$ . In other words, we have to find another functional  $\tilde{U}$  satisfying the following equivalence

$$\min_{\vec{w}: \|\vec{w}\|=1} U \Big|_{\vec{H}_l \text{ fixed}} \Leftrightarrow \min_{\vec{w}: \|\vec{w}\|=1} \tilde{U} \Big|_{\vec{H}_0 \text{ fixed}}. \quad (2.10)$$

We prove in appendix B that the exact mathematical form of  $\tilde{U}$  is the following

$$\begin{aligned} \tilde{U} = & \int_V \left[ f_{an}(\vec{w}) + \frac{1}{2} \beta_{ij} \frac{\partial w_l}{\partial x_i} \frac{\partial w_l}{\partial x_j} - T_{ik} \epsilon_{ik}^\mu - \mu_0 M_s H_{0i} w_i \right] d\vec{r} \\ & - \iint_{V^2} \frac{1}{2} \mu_0 M_s^2 \vec{w}(\vec{r}) \cdot \overline{\overline{N}}(\vec{r}, \vec{r}_0) \vec{w}(\vec{r}_0) d\vec{r}_0 d\vec{r}, \end{aligned} \quad (2.11)$$

where the last term represents the demagnetization energy, with the noteworthy presence of a factor  $\frac{1}{2}$ . The minimization of  $\tilde{U}$  with respect to the direction  $\vec{w}$ , with  $\vec{T}$  and  $\vec{H}_0$  imposed, leads to an equation giving actual equilibrium magnetization distribution within the ferromagnetic body. Incidentally, it is interesting to point out that this mathematical problem completely describes the emergence of the domains structure typical of the ferromagnetic materials. The result of this minimization, proved in appendix B, follows

$$\vec{w} \times \vec{H}_{\text{eff}} = 0, \quad (2.12)$$

where

$$\begin{aligned} \vec{H}_{\text{eff}} = & \vec{H}_0 + \vec{H}_d - \frac{1}{\mu_0 M_s} \frac{\partial f_{an}}{\partial \vec{w}} \\ & + \frac{\beta_{ij}}{\mu_0 M_s} \frac{\partial^2 \vec{w}}{\partial x_i \partial x_j} + \frac{2}{\mu_0 M_s} \vec{a} : \vec{T} \vec{w}. \end{aligned} \quad (2.13)$$

What this equation means is that at equilibrium, the torque generated by all local effective fields is zero. These results are in perfect agreement with classical developments [1, 147, 182, 270, 271]. One can also consider the last three terms as effective fields—which all depend on  $\vec{w}$ —and label them with the energy from which they derive ( $\vec{H}_{an}$ ,  $\vec{H}_{ex}$  and  $\vec{H}_{me}$ ).

To complete the discussion, boundary conditions must be imposed on the external surface of the region  $V$  (see again appendix B for details):

$$\beta_{ij} \epsilon_{lst} w_t \frac{\partial w_l}{\partial x_j} n_i = 0 \quad \forall s \text{ on } \partial V. \quad (2.14)$$

In particular, with isotropic exchange ( $\beta_{ij} \propto \delta_{ij}$ , the Kronecker delta) this can be further simplified. As  $\vec{w}$  is always perpendicular to  $\frac{\partial \vec{w}}{\partial \vec{n}}$  (conservation of magnetization amplitude), the boundary conditions simplify to

$$\frac{\partial \vec{w}}{\partial \vec{n}} = 0 \quad \text{on } \partial V. \quad (2.15)$$

To conclude, the behavior of the ferromagnetic region  $V$  can be summarized by observing that Eq. (2.12) must be satisfied within  $V$  with boundary conditions stated in Eq. (2.14) for the general case, or in Eq. (2.15) for isotropic exchange.

## 2.2 Equilibrium distribution in nanostructures

We now use an adapted version of the above general procedure to demonstrate the possibility to induce the motion of a domain wall through a uniform mechanical stress in

uniaxial ferromagnets. The same variational method is used, but with the specifics of the geometry and hypotheses integrated from the start. The equation obtained is that on which the numerical work presented in the rest of this chapter is based.

### 2.2.1 Definition of the energy functional

The geometry of the ferromagnetic region  $V$  considered is as shown on Fig. 2.2. It is constituted by a nanostructure of thickness  $h$ , length  $L$  and variable width  $\ell(x)$ . To simplify, the geometry is considered symmetrical with respect to the  $yz$ -plane so that the region  $V$  filled by the magnetoelastic material is defined by

$$V = \left\{ -\frac{L}{2} \leq x \leq +\frac{L}{2}, -\frac{\ell(x)}{2} \leq y \leq +\frac{\ell(x)}{2}, -\frac{h}{2} \leq z \leq +\frac{h}{2} \right\}. \quad (2.16)$$

Two major hypotheses will be assumed for our analysis: (i) the magnetization  $\vec{M} = M_s \vec{w}$  lies in the  $xy$ -plane, and (ii) the magnetization depends only on  $x$ . Hence, we have

$$\vec{w} = \vec{w}(x) = (\cos \Phi(x), \sin \Phi(x), 0), \quad (2.17)$$

where  $\Phi(x)$  is the angle between  $\vec{w}$  and the  $x$ -axis. Therefore, our hypothesis implies that  $\vec{M}$  is considered constant within  $yz$  cross sections at  $x$  constant. This is reasonable as long as the thickness and width of the nanomagnet are relatively small compared to its length (nanostripe geometry). However, it is worth keeping this strong assumption in mind: this model cannot describe vortex walls, or for that matter the tilt of transverse walls, as can be seen for instance in the micromagnetic results obtained with nmag in chapter 1. As for hypothesis (i), it is justified by the fact that the geometry that we plan to study is such that the dimensions along the  $z$ -axis is much smaller than the others. Therefore, at equilibrium it is unlikely that the magnetization will exhibit a finite component  $w_z$ .

From the point of view of the physical response of the ferromagnetic material, we assume a uniaxial behavior with an easy axis along  $\vec{x}$  described by the energy density:

$$u_{an} = -K_u w_x^2 = -K_u \cos^2 \Phi. \quad (2.18)$$

Because of the uniaxial symmetry of the ferromagnet, the exchange energy described in Eq. (2.3) simplifies by considering two different constants:  $\beta_{11} = A$ ;  $\beta_{22} = \beta_{33} = B$  and  $\beta_{ij} = 0, \forall i \neq j$ . More explicitly, we have

$$u_{ex} = A \left( \frac{\partial \vec{w}}{\partial x} \right)^2 + B \left[ \left( \frac{\partial \vec{w}}{\partial y} \right)^2 + \left( \frac{\partial \vec{w}}{\partial z} \right)^2 \right]. \quad (2.19)$$

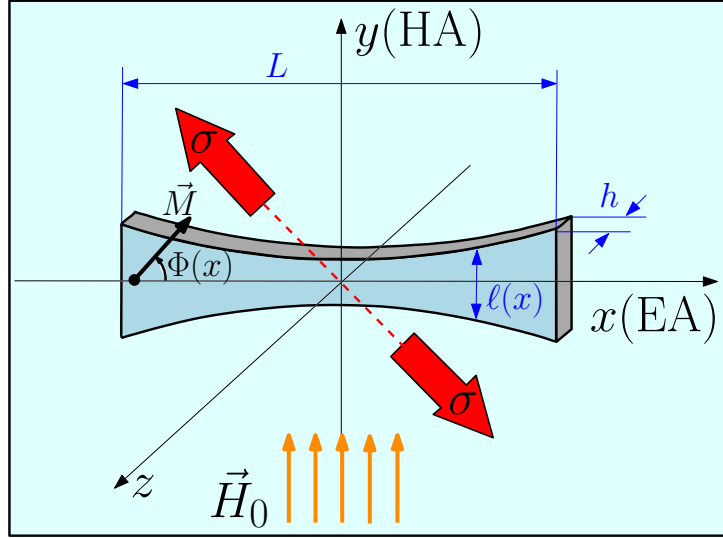


Figure 2.2 – Ferromagnetic nanostructure characterized by a variable width  $\ell(x)$  (here, a parabola is shown as an example). The ferromagnetic easy-axis (EA) is aligned with the  $x$ -axis, while the hard-axis (HA) corresponds to the  $y$ -axis. The magnetization  $\vec{M}$  is described by the angle  $\Phi(x)$  (measured anticlockwise) and the magnetic field  $\vec{H}_0$  and mechanical action  $\sigma$  are applied to the system.

With the assumption in Eq. (2.17), we easily get

$$\begin{aligned}
 u_{ex} &= A \left[ \left( \frac{\partial \cos \Phi}{\partial x} \right)^2 + \left( \frac{\partial \sin \Phi}{\partial x} \right)^2 \right] \\
 &= A \left[ \left( -\sin \Phi \frac{\partial \Phi}{\partial x} \right)^2 + \left( \cos \Phi \frac{\partial \Phi}{\partial x} \right)^2 \right] \\
 u_{ex} &= A \left( \frac{\partial \Phi}{\partial x} \right)^2.
 \end{aligned} \tag{2.20}$$

The applied magnetic field considered is along the  $y$ -axis, leading to the contribution:

$$u_{ze} = -\mu_0 M_s \vec{H}_0 \cdot \vec{w} = -\mu_0 M_s H_0 \sin \Phi. \tag{2.21}$$

Attention must be paid to the fact that this energy only covers the interaction with the applied field. As described in chapter 1, this field is able to break the symmetry and to modify the two stable positions of the magnetization induced by the anisotropy. Indeed, with the sole influence of the anisotropy, we have the couple of positions  $(0, \pi)$ . Adding the magnetic field, we obtain the tilt of the stable states toward the magnetic field (here, along  $+\vec{y}$ ).

We now introduce the magnetoelastic interaction. First of all we define the mathematical form of the magnetostriction.  $\bar{\epsilon}^\mu(\vec{w})$  corresponds to the strain tensor associated with the magnetization direction  $\vec{w}$  for a free body (no stress). We point out that the displacement field describing a uniform deformation along  $\vec{w}$  can be written as  $\vec{u}_l(\vec{x}) = \epsilon_l(\vec{x} \cdot \vec{w})\vec{w}$ , where  $\epsilon_l$  is the so-called longitudinal deformation. On the other hand, a displacement field corresponding to a uniform transversal deformation  $\epsilon_t$  is given by  $\vec{u}_t(\vec{x}) = \epsilon_t[\vec{x} - \vec{w}(\vec{x} \cdot \vec{w})]$ . The sum of the two contributions leads to a strain tensor  $\epsilon_{ij} = \epsilon_l w_i w_j + \epsilon_t(\delta_{ij} - w_i w_j)$ .

It is a well established fact that magnetostriction is isovolumic, and thus we have  $\text{Tr}\bar{\epsilon}^\mu = 0$ , *i.e.*  $\epsilon_{ii}^\mu = \epsilon_l + 2\epsilon_t = 0$ , from which we can derive that  $\epsilon_t = -\frac{\epsilon_l}{2}$ . By defining  $\lambda_s = \epsilon_l$ , typically referred to as the magnetostriction coefficient, we have

$$\epsilon_{ij}^\mu = \frac{\lambda_s}{2}(3w_i w_j - \delta_{ij}), \quad (2.22)$$

and, introducing a positive magnetostriction coefficient  $\lambda_s$  the general form of the magnetoelastic energy is

$$\begin{aligned} u_{me} &= -\bar{T} : \bar{\epsilon}^\mu = -T_{ij}\epsilon_{ij}^\mu \\ &= -\frac{\lambda_s}{2}(3w_i w_j - \delta_{ij})T_{ij} \\ u_{me} &= -\frac{\lambda_s}{2}(3w_i w_j T_{ij} - T_{ii}). \end{aligned} \quad (2.23)$$

In our case, we apply a unidirectional stress along the direction identified by  $\Phi_\sigma = \frac{3\pi}{4}$ . It is thus convenient to work with axes  $(x', y')$  tilted with respect to the  $(x, y)$  frame by an angle of  $\frac{\pi}{4}$  (see figure) in which we write  $\vec{w} = (w_{x'}, w_{y'})$ . Then, if  $T_{y'y'} = \sigma$  and all of its other components are zero, we obtain

$$u_{me} = -\frac{\lambda_s}{2}(3\sigma w_{y'}^2 - \sigma) = -\frac{3}{2}\lambda_s \sigma w_{y'}^2 + \text{const}. \quad (2.24)$$

In order to obtain the corresponding energy density, we have to come back to the original  $(x, y)$  system of axes. We have

$$\vec{w} = \cos \Phi \vec{e}_x + \sin \Phi \vec{e}_y = \cos(\Phi - \frac{\pi}{4}) \vec{e}_{x'} + \sin(\Phi - \frac{\pi}{4}) \vec{e}_{y'}. \quad (2.25)$$

Now, in the  $(x', y')$  frame we have a unidirectional stress along the second axis ( $y'$ ) and, therefore, the energy density is given by Eq. (2.24), with

$$\begin{aligned} w_{y'}^2 &= \sin^2(\Phi - \frac{\pi}{4}) \\ &= (\sin \Phi \cos \frac{\pi}{4} - \sin \frac{\pi}{4} \cos \Phi)^2 \\ &= \frac{1}{2} \sin^2 \Phi + \frac{1}{2} \cos^2 \Phi - \sin \Phi \cos \Phi \\ w_{y'}^2 &= -\sin \Phi \cos \Phi + \text{const}. \end{aligned} \quad (2.26)$$

Finally, we have proved that

$$u_{me} = \frac{3}{2}\lambda_s\sigma \sin \Phi \cos \Phi. \quad (2.27)$$

It is straightforward to check that a positive stress will tend to favor a magnetization along a direction defined by an angle  $\frac{3\pi}{4} + k\pi$ , and a negative stress will favor any magnetization perpendicular to this axis.

In summary, the energy density of the system is:

$$u = -K_u \cos^2 \Phi + A \left( \frac{d\Phi}{dx} \right)^2 - \mu_0 M_s H_0 \sin \Phi + \frac{3}{2}\lambda_s\sigma \sin \Phi \cos \Phi - \frac{1}{2}\mu_0 M_s \vec{H}_d \cdot \vec{w}, \quad (2.28)$$

where the last term represents the demagnetization energy density, as shown in Eq. (2.11). We determine the total energy  $U = \int_V u d\vec{r}$  by integrating Eq. (2.28) in the region  $V$ . For the first four terms, one can note that they depend only on  $x$ .

$$U = \int_{-\frac{L}{2}}^{\frac{L}{2}} h\ell(x) \left[ -K_u \cos^2 \Phi + A \left( \frac{d\Phi}{dx} \right)^2 - \mu_0 M_s H_0 \sin \Phi + \frac{3}{2}\lambda_s\sigma \sin \Phi \cos \Phi \right] dx - \iint_{V^2} \frac{1}{2}\mu_0 M_s^2 \vec{w}(\vec{r}) \cdot \overline{\vec{N}}(\vec{r}, \vec{r}_0) \vec{w}(\vec{r}_0) d\vec{r}_0 d\vec{r}. \quad (2.29)$$

## 2.2.2 Effective anisotropy

Before getting to the derivation of the equation, it is appropriate to reflect on the physics behind some of the energy terms. It is key to understand the reason for domain wall shift in a simple way. If we consider only the magnetic anisotropy and the magnetoelastic energy terms above, it is clear that it is equivalent to an effective anisotropy, since both are quadratic quantities (see Fig. 1.28). Therefore we can go further by actually writing this effective anisotropy  $u_{\text{eff}}$  comprising the combined effect of magnetic anisotropy and magnetoelastic energy:  $u_{\text{eff}} \equiv u_{an} + u_{me}$ . Let us define an angle  $\Phi_{\text{eff}}$  characterizing the direction of this new anisotropy, and  $K_{\text{eff}}$  its constant (unit:  $\text{Jm}^{-3}$ ). Their form can be found by writing the following:

$$-K_{\text{eff}} \cos^2 (\Phi - \Phi_{\text{eff}}) = -K_u \cos^2 \Phi + \frac{3}{2}\lambda_s\sigma \cos \Phi \sin \Phi. \quad (2.30)$$

A few lines of basic trigonometry calculation yields to the expression of  $K_{\text{eff}}$  and  $\Phi_{\text{eff}}$  by identification:

$$K_{\text{eff}} = \sqrt{K_u^2 + \left(\frac{3}{2}\lambda_s\sigma\right)^2}, \quad (2.31)$$

$$\Phi_{\text{eff}} = -\frac{1}{2} \arctan\left(\frac{3}{2}\frac{\lambda_s\sigma}{K_u}\right). \quad (2.32)$$

The direction of the effective anisotropy thus depends on  $\sigma$ . While it is along the  $x$ -axis when  $\sigma = 0$ , it can vary and is part of the interval  $]-\frac{\pi}{4}, +\frac{\pi}{4}[$ . The two bounds correspond to values of  $\sigma$  for which the magnetoelastic energy dominates the uniaxial anisotropy ( $\frac{3}{2}\lambda_s|\sigma| \gg K_u$ ).

Now it is obvious that applying a uniform stress has the effect of generating a tilted anisotropy. The two stable states with respect to this anisotropy are not equivalent in terms of Zeeman energy, hence the symmetry-breaking role of the external magnetic field along  $\vec{y}$ . As an aside, it is interesting to notice that in principle, if we apply a stress with an angle closer to  $\frac{\pi}{2}$  instead of the value  $\frac{3\pi}{4}$  chosen here, the Zeeman energy gap would be even greater and the system more efficient.

### 2.2.3 Derivation of the main equation

We follow the same approach as in subsection 2.1.3 to derive the equation that the magnetization distribution should satisfy at equilibrium. Here, we will explicitly give the developments that lead to the desired equation. Let us consider  $U$  as a functional of  $\Phi(x)$ . We can apply the Gâteaux derivative, by introducing a perturbation function  $k$  and a constant  $\beta$  as follows

$$\begin{aligned} \frac{d}{d\beta} U(\Phi(x) + \beta k(x)) \Big|_{\beta=0} &= \int_{-\frac{L}{2}}^{\frac{L}{2}} h\ell(x) \left[ +2K_u \cos \Phi \sin \Phi k(x) \right. \\ &\quad \left. - \mu_0 M_s H_0 \cos \Phi k(x) + \frac{3}{2}\lambda_s \sigma \cos(2\Phi) k(x) + 2A \frac{d\Phi}{dx} \frac{dk}{dx} \right] dx \\ &\quad - \frac{1}{2} \mu_0 M_s^2 \left( \iint_{V^2} \frac{\partial \vec{w}}{\partial \Phi}(x) \cdot \overline{\overline{N}}(\vec{r}, \vec{r}_0) \vec{w}(x_0) k(x) d\vec{r}_0 d\vec{r} \right. \\ &\quad \left. + \iint_{V^2} \vec{w}(x) \overline{\overline{N}}(\vec{r}, \vec{r}_0) \frac{\partial \vec{w}}{\partial \Phi}(x_0) k(x_0) d\vec{r}_0 d\vec{r} \right). \quad (2.33) \end{aligned}$$

To continue, the exchange term is integrated by part, giving

$$\int_{-\frac{L}{2}}^{\frac{L}{2}} h\ell(x)2A\frac{d\Phi}{dx}\frac{dk}{dx}dx = \left[2h\ell(x)A\frac{d\Phi}{dx}k(x)\right]_{-\frac{L}{2}}^{\frac{L}{2}} - \int_{-\frac{L}{2}}^{\frac{L}{2}} 2hA\frac{d}{dx}\left(\ell(x)\frac{d\Phi}{dx}\right)k(x)dx. \quad (2.34)$$

The demagnetization term is non-local in that its value for each point depends on the magnetization distribution in the whole region. Symmetries of the tensor  $\overline{\overline{N}}$ , as shown previously in Eq. (2.9a) and Eq. (2.9b), allow to equate the last two integrals of Eq. (2.33) involving  $\overline{\overline{N}}$ .

$$\begin{aligned} & \left( \iint_{V^2} \frac{\partial \vec{w}}{\partial \Phi}(x) \cdot \overline{\overline{N}}(\vec{r}, \vec{r}_0) \vec{w}(x_0) k(x) d\vec{r}_0 d\vec{r} + \iint_{V^2} \vec{w}(x) \overline{\overline{N}}(\vec{r}, \vec{r}_0) \frac{\partial \vec{w}}{\partial \Phi}(x_0) k(x_0) d\vec{r}_0 d\vec{r} \right) \\ & = 2 \iint_{V^2} \frac{\partial \vec{w}}{\partial \Phi}(x) \cdot \overline{\overline{N}}(\vec{r}, \vec{r}_0) \vec{w}(x_0) k(x) d\vec{r}_0 d\vec{r}. \end{aligned} \quad (2.35)$$

This can be rewritten with explicit integration domains, for the magnetic field integrals. Since  $\vec{H}_d = M_s \int_V \overline{\overline{N}}(\vec{r}, \vec{r}_0) \vec{w}(\vec{r}_0) d\vec{r}$ , we eventually obtain

$$\begin{aligned} \iint_{V^2} M_s \frac{\partial \vec{w}}{\partial \Phi}(x) \cdot \overline{\overline{N}}(\vec{r}, \vec{r}_0) \vec{w}(x_0) k(x) d\vec{r}_0 d\vec{r} &= \int_{-\frac{L}{2}}^{+\frac{L}{2}} \int_{-\frac{\ell(x)}{2}}^{+\frac{\ell(x)}{2}} \int_{-\frac{h}{2}}^{+\frac{h}{2}} \frac{\partial \vec{w}}{\partial \Phi}(x) \cdot \vec{H}_d k(x) dx dy dz \\ &= \int_{-\frac{L}{2}}^{+\frac{L}{2}} h\ell(x) \frac{\partial \vec{w}}{\partial \Phi}(x) \cdot \langle \vec{H}_d \rangle_{y,z} k(x) dx, \end{aligned} \quad (2.36)$$

where  $\langle \vec{H}_d \rangle_{yz} = \frac{1}{h\ell} \int_{-\frac{\ell(x)}{2}}^{+\frac{\ell(x)}{2}} \int_{-\frac{h}{2}}^{+\frac{h}{2}} \vec{H}_d(\vec{r}) dz dy$  (a function of  $x$ ), is the average value of the field  $\vec{H}_d$  over sections at  $x$  constant. By substituting Eqs. (2.34) and (2.36) in Eq. (2.33) we

eventually get

$$\begin{aligned}
\frac{d}{d\beta} U(\Phi(x) + \beta k(x)) \Big|_{\beta=0} = & \\
& \int_{-\frac{L}{2}}^{+\frac{L}{2}} h\ell(x)k(x) \left[ 2K_u \cos \Phi \sin \Phi - \mu_0 M_s H_0 \cos \Phi + \frac{3}{2} \lambda_s \sigma \cos 2\Phi \right] dx \\
& - \int_{-\frac{L}{2}}^{+\frac{L}{2}} 2hA \left( \frac{d\ell}{dx} \frac{d\Phi}{dx} + \ell(x) \frac{d^2\Phi}{dx^2} \right) k(x) dx + \left[ 2hA\ell(x) \frac{d\Phi}{dx} k(x) \right]_{-\frac{L}{2}}^{+\frac{L}{2}} \\
& - \mu_0 M_s \int_{-\frac{L}{2}}^{+\frac{L}{2}} h\ell(x) \frac{\partial \vec{w}}{\partial \Phi}(x) \cdot \langle \vec{H}_d \rangle_{y,z} k(x) dx. \quad (2.37)
\end{aligned}$$

Since we wish to study the motion of a domain wall in the interval  $[-\frac{L}{2}, +\frac{L}{2}]$ , we fix the value of  $\Phi(-\frac{L}{2})$  and  $\Phi(+\frac{L}{2})$  in order to have a domain wall at  $x = 0$  when  $\sigma = 0$ . How these conditions are chosen will be explained in subsection 2.2.4. The perturbation function  $k$  must vanish at the interval end-points  $x = \pm\frac{L}{2}$ . Hence, Eq. (2.37) appears with a single integral and it is zero for any real function  $k$  when

$$\begin{aligned}
h\ell(x) \left[ 2K_u \cos \Phi \sin \Phi - \mu_0 M_s H_0 \cos \Phi + \frac{3}{2} \lambda_s \sigma \cos 2\Phi \right] \\
- 2hA \left( \frac{d\ell}{dx} \frac{d\Phi}{dx} + \ell(x) \frac{d^2\Phi}{dx^2} \right) - \mu_0 M_s h\ell(x) \frac{\partial \vec{w}}{\partial \Phi}(x) \cdot \langle \vec{H}_d \rangle_{y,z} = 0, \quad (2.38)
\end{aligned}$$

or, dividing by  $-2Ah\ell(x)$

$$\begin{aligned}
\Phi''(x) + \Phi'(x) \frac{\ell'(x)}{\ell(x)} - \frac{1}{2A} \left[ 2K_u \cos \Phi \sin \Phi - \mu_0 M_s H_0 \cos \Phi + \frac{3}{2} \lambda_s \sigma \cos 2\Phi \right] \\
+ \frac{1}{2A} \mu_0 M_s \frac{\partial \vec{w}}{\partial \Phi}(x) \cdot \langle \vec{H}_d \rangle_{y,z} = 0. \quad (2.39)
\end{aligned}$$

Now,  $\vec{w}$  being equal to  $(\cos \Phi, \sin \Phi, 0)$ , we can finally write

$$\begin{aligned}
\Phi''(x) + \Phi'(x) \frac{\ell'(x)}{\ell(x)} - \frac{1}{2A} \left[ 2K_u \cos \Phi \sin \Phi - \mu_0 M_s H_0 \cos \Phi + \frac{3}{2} \lambda_s \sigma \cos 2\Phi \right. \\
\left. + \mu_0 M_s \sin \Phi \langle \vec{H}_{dx} \rangle_{y,z} - \mu_0 M_s \cos \Phi \langle \vec{H}_{dy} \rangle_{y,z} \right] = 0. \quad (2.40)
\end{aligned}$$

This is the main equation governing the equilibrium behavior of the magnetization orientation within the considered structure. From a mathematical point of view it is a second

order integro-differential equation with fixed boundary conditions ( $\langle \vec{H}_d \rangle_{y,z}$  depends on  $\Phi$  through an integral operation). The original character of this equation can be underlined by observing that it describes a one-dimensional model but, at the same time, its second term in Eq. (2.40) takes into account the actual shape of the ferromagnetic region (through the variable width  $\ell$  and its derivative  $\ell'$ ). This point also represents a crucial modification introduced with respect to the classical development summarized in section 2.1. Therefore, this approach, specifically elaborated for the study of a two-domain nanostructure, allows for the analysis of domain wall configurations with a strong reduction of the necessary computational effort with respect to, *e.g.*, a standard finite element micromagnetic approach. The latter, while allowing to tackle a wide variety of magnetic problems, is less computationally efficient for such a simple system.

Having introduced a variable width, it is interesting to notice that it acts through the ratio  $\frac{\ell'}{\ell}$  on one of the exchange terms. In order to clearly highlight its influence, let us write the equation in the absence of any other contributions apart from the exchange energy, the equation can be written:

$$\begin{aligned} \ell(x)\Phi''(x) + \ell'(x)\Phi'(x) &= 0 \\ \Leftrightarrow \frac{d}{dx}(\ell(x)\Phi') &= 0 \\ \exists C_0 \Phi'(x) &= \frac{C_0}{\ell(x)} \end{aligned} \tag{2.41}$$

With this relationship between  $\Phi'$  and  $\ell$ , one can see that if the function  $\ell$  is not constant, the regions of greater spatial change of magnetization (for instance a domain wall) will tend to be concentrated in constrictions. A region of lower width is thus tantamount to a local stable position for a domain wall.

To complete the description of the model, we need to specify the boundary conditions, and to describe the numerical approach used to solve the problem.

## 2.2.4 Boundary conditions and stable states

Consistently with the variational procedure followed, the boundary conditions, *i.e.* the values of the magnetization assigned to both ends of the region, are fixed quantities. Therefore, they will not change throughout the simulations, and as a result, the choice of their values will be arbitrary to some degree. In order to put relevant values with regard to the expected behavior of the system, we chose to have the boundary values equal to

the angles  $\Phi_s$  ( $s \in 1, 2$ ) of the two stable states. Indeed, in the situation simulated, we can expect a distribution with a domain wall between two "plateau" regions with angles close to those of the stable states. This is corroborated by the result of our preliminary numerical investigations presented in chapter 1.

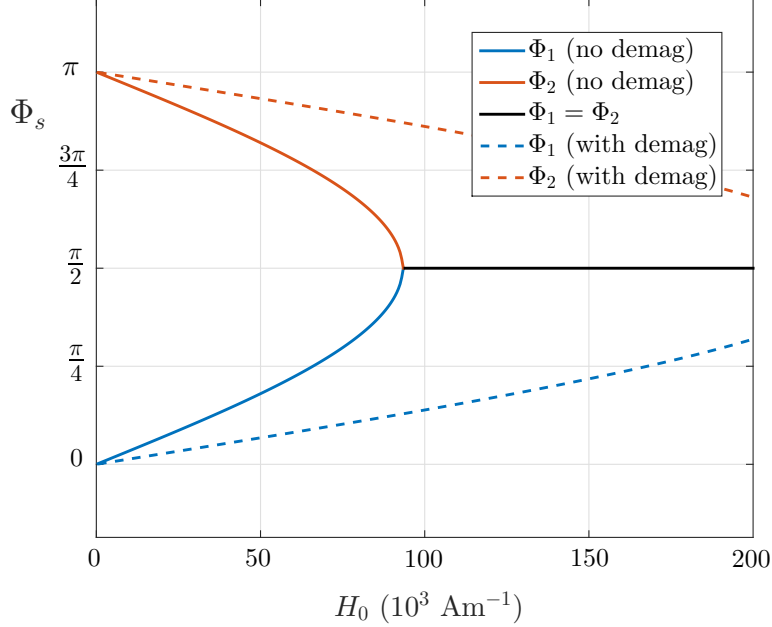


Figure 2.3 – Effect of the magnetic field on the stable states of the system (with  $\sigma = 0$ ). The two angles get closer as  $H_0$  increases until only one stable position remains ( $\Phi = \frac{\pi}{2}$ ) for  $H_0 \geq H_a$ . In dashed lines are represented the stable states when a simplified demagnetizing field is taken into account ( $N_y = 0.225$ ).

Let us now calculate those two values: we have to find the solutions to the minimization of the energy density in the simple case of a uniformly magnetized system, that is with  $\Phi'(x) = 0$  and  $\Phi''(x) = 0$ . Moreover, we first neglect the demagnetizing field in order to simplify the calculation. The equation for  $\Phi$  becomes

$$2K_u \cos \Phi \sin \Phi - \mu_0 M_s H_0 \cos \Phi + \frac{3}{2} \lambda_s \sigma \cos 2\Phi = 0. \quad (2.42)$$

The solutions of this equation are the angles of two magnetization directions generated by the combination of anisotropy, externally applied field and mechanical stress. To solve for  $\Phi$  we use the representations  $\cos \Phi = \frac{1-t^2}{1+t^2}$  and  $\sin \Phi = \frac{2t}{1+t^2}$ , where  $t = \tan \frac{\Phi}{2}$ . The final result is the following fourth-degree algebraic equation:

$$\left( -\mu_0 M_s H_0 + \frac{3}{2} \lambda_s \sigma \right) + 4K_u t - 9\lambda_s \sigma t^2 - 4K_u t^3 + \left( \mu_0 M_s H_0 + \frac{3}{2} \lambda_s \sigma \right) t^4 = 0. \quad (2.43)$$

Because it is a fourth-degree equation, and given the choice of parameters, there are potentially four distinct solutions, only two of which are relevant to our physical problem. However, it is not difficult to identify the correct solution from the numerical point of view.

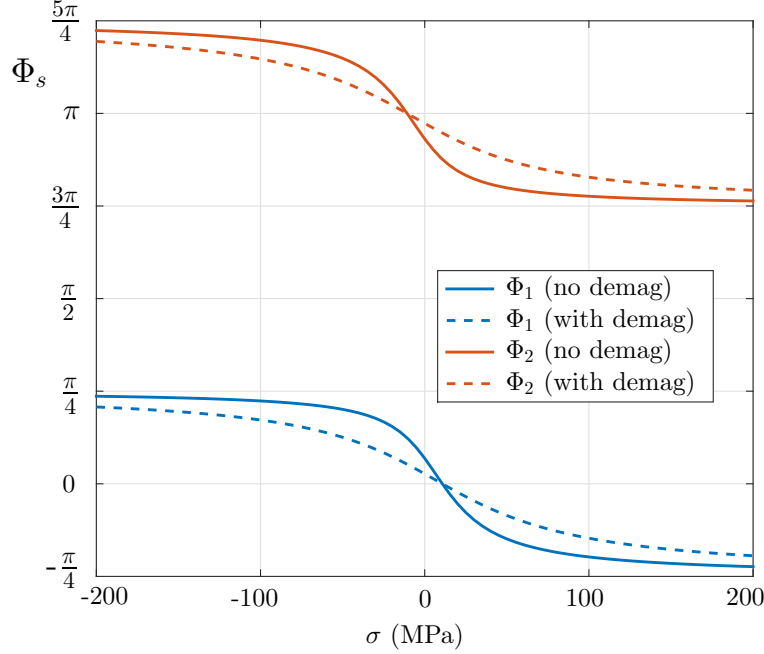


Figure 2.4 – Angles  $\Phi_1$  and  $\Phi_2$  of stable magnetization orientations as a function of the mechanical stress  $\sigma$ , with and without demagnetization.

To begin, let us look at the particular case where  $\sigma = 0$ :

$$4K_{ut} - \mu_0 M_s H_0 (1 + t^2) = 0. \quad (2.44)$$

This equation gives two symmetric solutions with respect to  $\Phi = \frac{\pi}{2}$  that are distinct provided that the magnetic field is not too strong (see chapter 1). Indeed, beyond  $H_0 = H_a$ , the only stable equilibrium state is defined by  $\Phi = \frac{\pi}{2}$ . Solutions  $\Phi_s$  are plotted in Fig. 2.3, with the transition at  $H_0 = 93 \times 10^3$  A/m. Also mentioned in the previous chapter is the fact that the demagnetizing field in a nanostripe geometry will add a shape anisotropy that will increase the uniaxial anisotropy. This effect is highly significant, as it appears from our calculations that it can increase the apparent anisotropy field more than twofold from the calculated value  $H_a$ . This can be seen in Fig. 2.3 where a simplified demagnetizing field has been introduced in the calculation of the stable states (hypothesis

of a uniformly magnetized ellipsoid of infinite length:  $\vec{H}_d = \overline{\overline{N}}\vec{w}$  with the diagonal tensor  $\overline{\overline{N}}$ ).

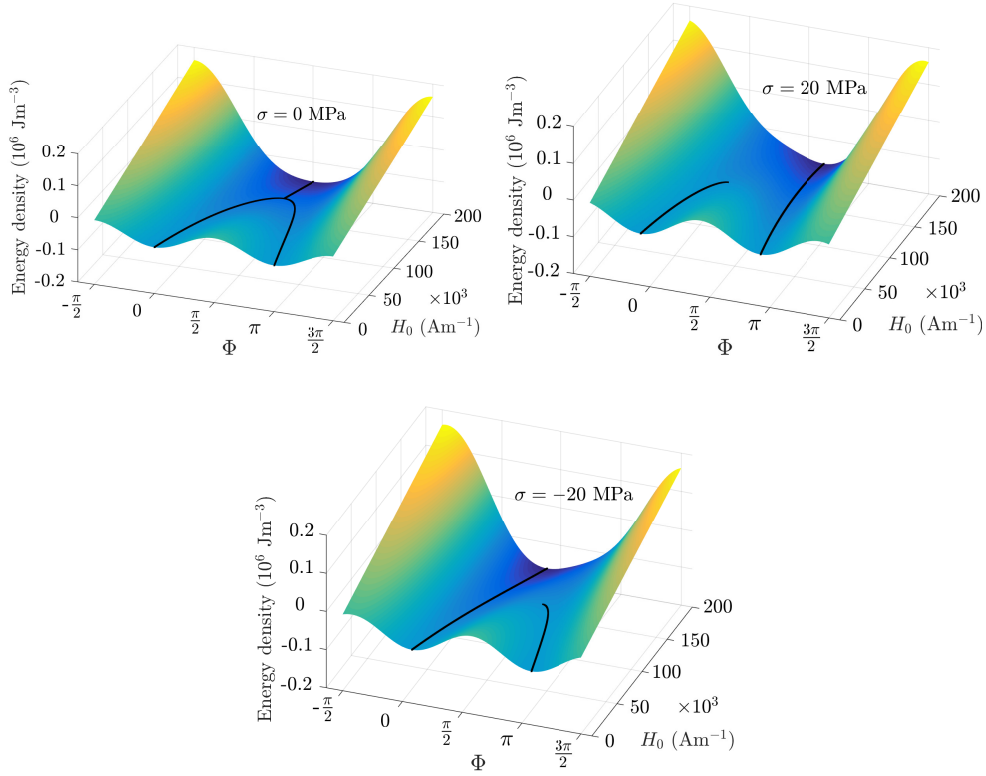


Figure 2.5 – Energy landscape as a function of the magnetization angle  $\Phi$  and applied magnetic field  $H_0$ . The application of a stress modifies the stable magnetization states and their energy densities, favoring a given state over the other one. In the first panel we considered  $\sigma = 0$ , in the second one  $\sigma > 0$  and in the third one  $\sigma < 0$ .

As for the case where  $\sigma \neq 0$  with  $H_0$  below  $H_a$ , there are also two stable states. Fig. 2.4 shows these angles for  $|\sigma| < 200$  MPa and  $H_0 = 20 \times 10^3$  A/m, with and without demagnetization (same approximation as in Fig. 2.3). As the stress increases, there is a shift of the stable state angles and a saturation that is quicker in the absence of demagnetization. In this chapter, in order to simplify the simulations we chose to ignore demagnetization in the calculation of the boundary conditions, as it is geometry-dependent. In any case, a small mismatch between the plateau angle and the boundary conditions do not seem to alter significantly the behavior of the system (see subsection 2.4.1).

To understand the interplay between field and stress, we can look at the energy landscape represented in Fig. 2.5. The three subfigures correspond to different values of stress

(one is zero, the other two are  $\pm 20$  MPa). We can observe the intrinsic bistability of the system under the threshold  $H_a$  of magnetic field and the effect of the mechanical stress, which generates an energy gap between the stable states (only when  $H_0 \neq 0$ ).

## 2.3 Numerical procedure

This section describes the numerical approach for solving the equation Eq. (2.40) since it cannot be treated analytically. It includes a quick description of the technique as well as the way it was checked for convergence and accuracy.

### 2.3.1 Presentation

The aim of this section is to describe the *ad hoc* numerical method proposed to solve Eq. (2.40). This is a second order nonlinear integro-differential equation with boundary conditions. Therefore, the standard Euler method or the more advanced Runge-Kutta techniques, which are relevant for problems with initial conditions, are not suited to this problem. Rather, the knowledge of the boundary conditions—see Eq. (2.43)—suggests that a nonlinear relaxation, or iterative, method would be appropriate [272]. The implementation was done with the MATLAB software (2014b version).

To introduce this technique, we consider a discretization of the interval  $[-\frac{L}{2}, +\frac{L}{2}]$  in  $N$  points and  $N - 1$  intervals. All quantities will therefore be discretized and defined over uniform regions  $[x_i, x_{i+1}] \times [-\frac{l(x_i)}{2}, +\frac{l(x_i)}{2}] \times [-\frac{h}{2}, +\frac{h}{2}]$  for  $i \in \{1, \dots, N - 1\}$ . The quantity  $\Delta x$  will be taken equal to  $\frac{L}{N-1}$ . Eq. (2.40) can be written in a discretized way:

$$\begin{aligned} & \frac{\Phi_m(x_{i+1}) - 2\Phi_{m+1}(x_i) + \Phi_m(x_{i-1}))}{(\Delta x)^2} + \frac{\Phi_m(x_{i+1}) - \Phi_m(x_{i-1}))}{2\Delta x} \times \frac{\ell'(x_i)}{\ell(x_i)} \\ & - \frac{1}{2A} \left[ K_u \sin 2\Phi_{m+1}(x_i) - \mu_0 M_s H_0 \cos \Phi_{m+1}(x_i) + \frac{3}{2} \lambda_s \sigma \cos 2\Phi_{m+1}(x_i) \right. \\ & \quad \left. + \mu_0 M_s \sin \Phi_{m+1}(x_i) \langle H_{dx} \rangle_{y,z} - \mu_0 M_s \cos \Phi_{m+1}(x_i) \langle H_{dy} \rangle_{y,z} \right] = 0. \end{aligned} \quad (2.45)$$

The unknown is  $\Phi_{m+1}$ , whereas quantities with the  $m$  index are given by the previous iteration. One can see that in order to compute the value of  $\Phi_{m+1}$  at location  $i$ , knowledge of the previous values at neighboring points is required. To solve this equation we can use an iterative procedure based on the bisection method, which allows for both fast convergence and arbitrarily high precision [273].

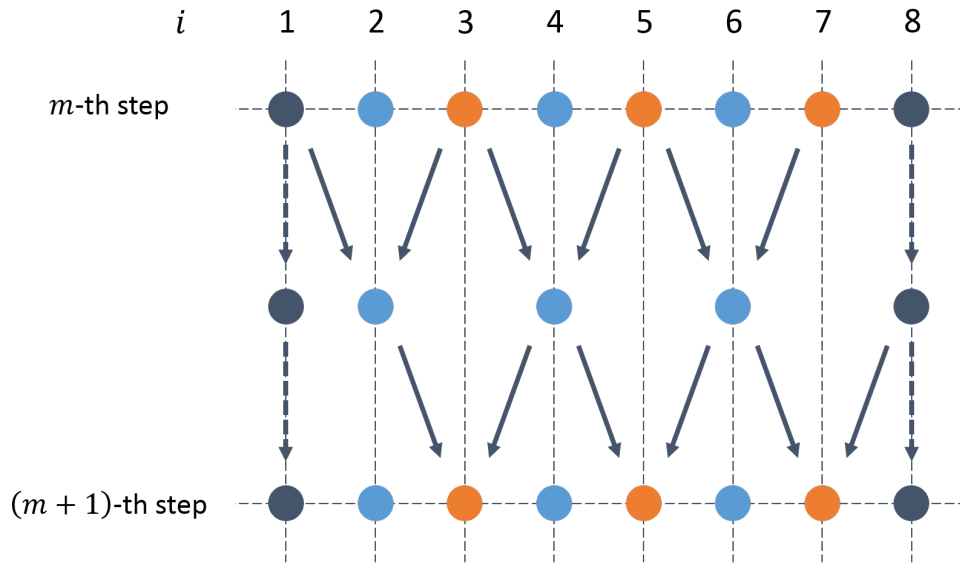


Figure 2.6 – Two-pass scheme used in the procedure with  $N = 8$ . A first pass performs the bisection for even indices (in blue) using values at odd indices (in orange) from the previous step, and the second pass performs the bisection for odd indices using values at even indices that have just been computed. Values at the extremities do not change since they are fixed boundary conditions (see dashed arrows). Solid line arrows indicate the inputs for the calculation. Both passes use demagnetization data from the previous step.

We can start the procedure with a given guess function  $\Phi_0(x_i)$  (*e.g.*, the linear function imposed by  $\Phi(x_1)$  and  $\Phi(x_N)$ ), and then proceed by iterations. A possible scheme to go from  $m$  to  $m + 1$  is represented in Fig. 2.6 and was used in the procedure. As  $\Phi(x_1) = \Phi(-\frac{L}{2})$  and  $\Phi(x_N) = \Phi(+\frac{L}{2})$  are fixed, vertical dashed arrows corresponding to  $\Phi_1$  and  $\Phi_N$  represent the fixed boundary conditions which are the same for any step of the procedure. As for other values, odd and even indices are computed separately in two successive substeps. For each even (resp. odd) point,  $\Phi_{m+1}(x_i)$  is computed using the values of its odd (resp. even) neighbors. Below is an excerpt of the MATLAB routine showing the classical bisection method, where  $r$  is the unknown and  $err$  is the threshold value for convergence (based on the absolute-value norm).

```

% definition of the function
function f = f1(r)
    f=(Phi(i+1)-2*r+Phi(i-1))/dx^2-1/(2*A)*(-mu0*H0*Ms*cos(r)
        +2*K_u*cos(r)*sin(r)+3/2*lambda_s*sigma*cos(2*r))
        +ld(i)/lx(i)*(Phi(i+1)-Phi(i-1))/(2*dx)
        +1/(2*A)*mu0*Ms*(-sin(r)*Hdx+cos(r)*Hdy);
end

% bisection procedure
if f1(a)*f1(b)>0
    disp('Problem: f(a)*f(b)>0')
else
    c = (a + b)/2;
    err = 1;
    while err > 1e-15
        if f1(a)*f1(c)<0
            b = c;
        else
            a = c;
        end
        err = abs(a-b);
        c = (a + b)/2;
    end
end
end

```

The only non-trivial term to compute is the demagnetization contribution. Indeed, although tools have been proposed [274, 275] for the purpose of simplifying the computation of the demagnetization, it often remains the least straightforward part. The numerical determination of the exact demagnetizing field is achieved through a scheme explained in appendix C. As a matter of fact, the demagnetizing field at each point depends on the magnetization of the whole ferromagnetic body, which, in addition, changes at each iteration. Therefore, a naive implementation is likely to be computationally intensive. Here, we consider the contributions of the  $N - 1$  parallelepipedal regions, which can be calculated through closed form expressions, as demonstrated in appendix C. Then, the total demagnetizing field, measured at any given point, is simply the sum of all contributions generated by all parallelepipedal regions. Of course, we introduce a small systematic error due to the fact that the system with variable width can be only approximately represented by the juxtaposition of all the parallelepipeds. However, the approximation is very good for a low derivative  $\ell'(x)$  relatively to the discretization. The terms  $\langle H_{dx} \rangle_{y,z}$  and  $\langle H_{dy} \rangle_{y,z}$  can then be computed with the magnetization distribution at the  $m$ -th step, which by and large represent the most computation-intensive elements from a numerical point of view. From a computational point of view, the key thing to notice is that in

Eqs. (C.19) and (C.20) geometry (derivatives of  $\mathcal{F}$  function) and physics (magnetization) can be decoupled. The former can be computed once and for all offline before the iteration procedure actually begins, and then components of the demagnetizing field can be computed from the current magnetization distribution. The result is a simple product between a matrix with (fixed) geometry-dependent factors and the magnetization, which represent an enormous benefit in terms of computation time. To compute the mean value of the demagnetizing field on the cross section plane of each point, in this chapter we considered the demagnetizing field calculated on the  $x$ -axis. This approximation requires to calculate the field at only one point per location  $i$ , which can be interesting depending on the time constraints of the offline calculation. Alternatively, one could also try to map more precisely the parallelepipedal region, for instance using adequate Gaussian quadratures.

### 2.3.2 Convergence and test against analytical solution

Numerical calculations have been carried out with a given set of physical properties corresponding to the magnetoelastic material Terfenol. Accordingly, we used a magnetization saturation  $M_s = 64 \times 10^4$  A/m [255], an exchange interaction coefficient  $A = 9 \times 10^{-12}$  J/m [21]. We also adopt an anisotropy constant  $K_u = 37.5 \times 10^3$  J/m<sup>3</sup> corresponding to an anisotropy field  $H_a = 92 \times 10^3$  A/m (defined through the expression  $K_u = \frac{1}{2}\mu_0 M_s H_a$ ), which can be easily obtained in real ferromagnetic layers [253]. We emphasize that  $H_a$  represents the bifurcation threshold shown in Fig. 2.3. The strong magnetostriction in Terfenol is characterized by a coefficient  $\lambda_s = 1 \times 10^{-3}$  [276]. Moreover, an applied field  $H_0 = 20 \times 10^3$  A/m is used throughout all simulations.

Within the code, convergence can be controlled using two stopping criterias. One will control the residual error in the bisection method, that is an upper bound for the distance between the solution found and the actual solution. The other is for the iterative procedure itself, it is the euclidian norm between values at steps  $m$  and  $m + 1$ , written  $\delta$ .

First, it seemed clear that for reasonable input parameters, the code did not crash or give absurd results for the angle  $\Phi$ . In particular, the application of a stress results in the motion of a region of high spatial variation (domain wall) in a predictable direction, while in the absence of stress, the distribution remains symmetric. In order to check that the result obtained is correct, we can compare it to a solution that can be handled analytically in a simple case. For that purpose, we consider a region with anisotropy and exchange

only, other terms being neglected and the width supposed constant. The total energy can be derived from Eq. (2.29)

$$U = \int_{-\frac{L}{2}}^{+\frac{L}{2}} h\ell(x) \left[ -K_u \cos^2 \Phi + A \left( \frac{\partial \Phi}{\partial x} \right)^2 \right] dx. \quad (2.46)$$

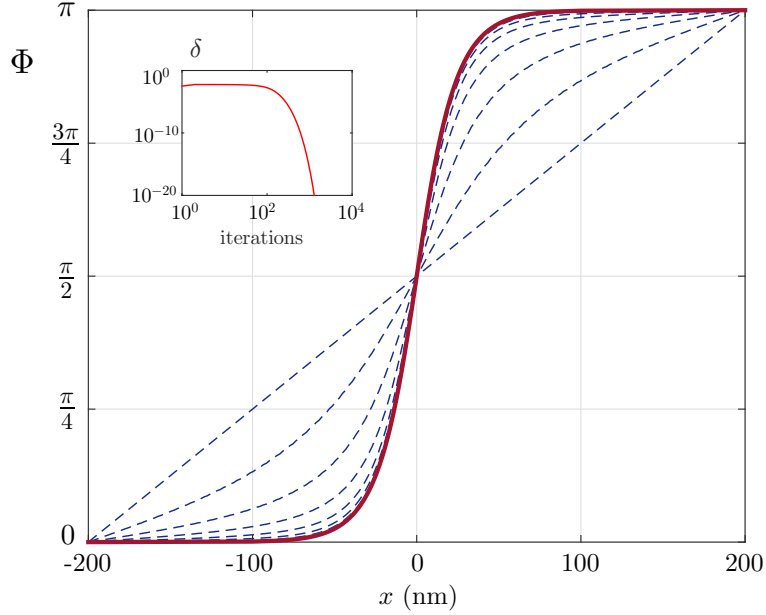


Figure 2.7 – Magnetization angle distribution  $\Phi(x)$  converging toward the analytical solution (red curve) for the simple system with only exchange and anisotropy contributions. The iteration process starts from a linear guess. The inset shows the relative error versus the number of iterations.

In this case the solution is given by the following closed form expressions

$$\sqrt{\frac{K_u}{A}} \left( x + \frac{L}{2} \right) = \frac{1}{\xi} F \left( \arcsin \frac{\xi \sin \Phi}{\sqrt{\xi^2 - \cos^2 \Phi}}, \frac{1}{\xi} \right), \quad (2.47)$$

$$\frac{1}{\xi} K \left( \frac{1}{\xi} \right) = \frac{L}{2} \sqrt{\frac{K_u}{A}}, \quad (2.48)$$

which are proved in appendix A (where we also define the elliptic functions  $F$  and  $K$ ). The second equation must be solved with respect to the parameter  $\xi$  and then the first one gives the relation between  $x$  and  $\Phi$  characterizing the specific domain wall under investigation (for details see appendix A). We underline that this result is consistent with

classical expressions obtained considering  $L \rightarrow +\infty$  [20] already discussed in chapter 1. This solution is now used to check the numerical technique by direct comparison. We consider a uniform nanostripe with a constant thickness  $h = 20$  nm, a constant width  $\ell = 40$  nm and a length  $L = 400$  nm. As one can see in Fig. 2.7, the numerical procedure correctly converges toward the expected solution, from an initial linear guess between two boundary conditions (here, 0 and  $\pi$ ). In the inset of Fig. 2.7 we have also shown the relative error  $\delta$  (the difference in norm between steps  $m$  and  $m + 1$ ) which approaches zero, proving the convergence of the sequence [277]. The stopping criterion of the iterative process is based on a threshold value of  $\delta$ , referred to as  $\delta_{min}$  (here we used  $\delta_{min} = 10^{-20}$ ).

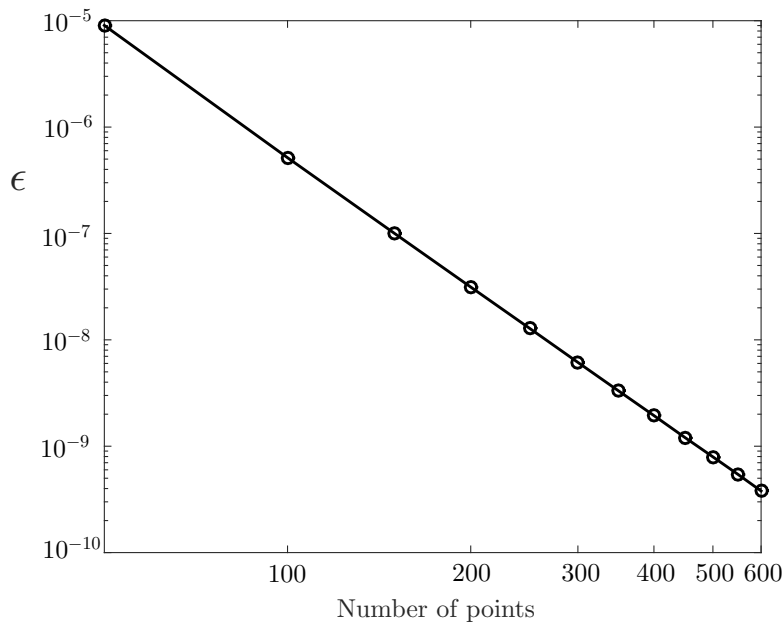


Figure 2.8 – Absolute error  $\epsilon$  between numerical and theoretical solutions versus the number  $N$  of points used in the discretization (all simulations have been performed with the same stopping criterion based on  $\delta_{min} = 10^{-20}$ )

The convergence of the procedure can be more closely monitored by quantifying the absolute error  $\epsilon$  defined as the difference between the numerical and the theoretical solution. We ran simulations with different levels of discretization but with the same stopping criterion  $\delta_{min} = 10^{-20}$ . In Fig. 2.8 we show  $\epsilon$  as a function of the number of points  $N$  used in the discretization. The relationship between the two is clearly represented by a power law, the exponent being about  $-4$ . It appears that this value of the exponent remains constant by varying the parameters  $A$  and  $K_u$  of the problem, thereby proving a universal

and fast convergence. In Fig. 2.9, we show the compromise between accuracy and computational load, which should come as no surprise. To do so, we look at the relative error  $\delta$  versus the number of iterations for different levels of discretization. By increasing the number of points we improve the accuracy but we slow down the convergence, as is visible from the slopes in the figure. The cost of accuracy here is twofold: first, with more points each iteration does take more time to compute and second, the convergence is obtained after a larger number of iterations.

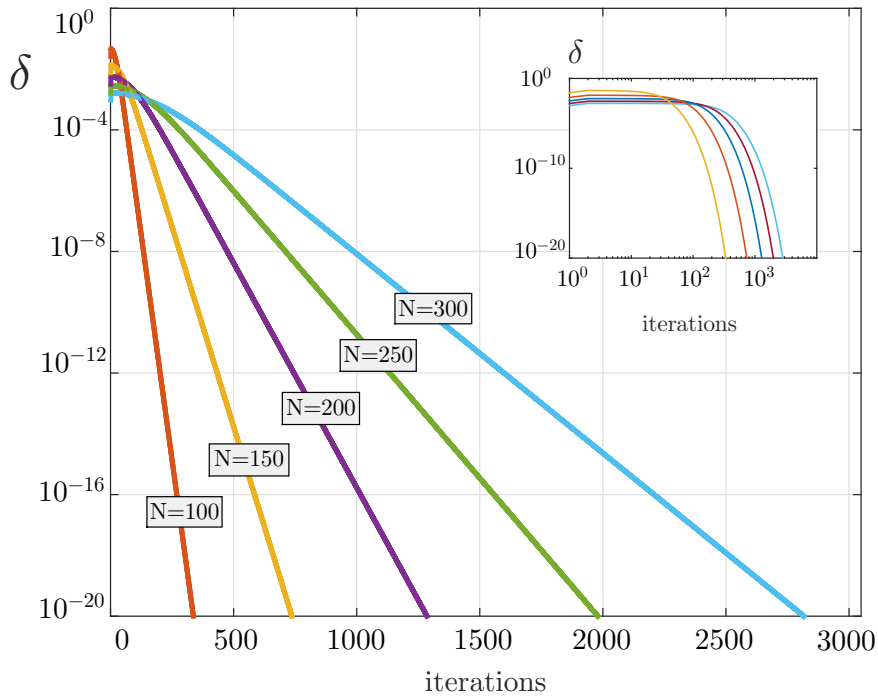


Figure 2.9 – Relative error  $\delta$  as a function of the number of iterations for different values of  $N$ . In all cases, the convergence is definitively exponential. Moreover, for a larger number of points the convergence is slower.

From these results, the proposed method appears to be reliable, efficient, and suitable for our purposes. In the simulations presented below, the number of points  $N$  was systematically taken equal to 400, which means that  $\Delta x \approx 1$  nm.

## 2.4 Results

Once some confidence could be placed in the output of this numerical procedure, a campaign of tests was carried out. The main results from the operation of the code will hereby

be presented. First, the possibility to induce motion is demonstrated. Depending on the geometry studied, the continued application of a stress can lead to the ejection of domain wall from the simulated ferromagnet (leaving a single domain), or to an equilibrium position. In the latter case, an exploration of the relationship between equilibrium position and applied stress will be presented. The section ends with an energy-based interpretation of this relationship, and a discussion on the piezoelectric option for the implementation of stress-mediated domain wall control.

### 2.4.1 Motion, confinement and ejection

In the previous section, it was shown how the procedure converged toward the correct domain wall shape in the absence of field or stress. When a bias magnetic field is applied along  $\vec{y}$ , the configuration is slightly changed (the gap between the plateau regions is more narrow) and the domain wall remains stable at  $x = 0$ . This solution can be used as an initial guess. As the simulation is carried out in material of positive magnetostriction and with a positive (resp. negative) applied stress, the domain wall shifts to the left (resp. right). Another important aspect is the quick adaptation of the plateau values when the system is subjected to a stress. We can verify here that the choice of boundary conditions is appropriate.

In a parallelepipedic geometry (constant width nanostripe), the sustained application of a constant stress leads to a single-domain configuration. Indeed, as long as the stress is applied, there is an incentive for domain wall shift, only eventually stopped by the fixed boundary condition. An example of such an "ejection" is shown in Fig. 2.10 where we considered a uniform nanostripe with  $h = 20$  nm,  $\ell = 40$  nm and  $L = 400$  nm. We adopted the boundary conditions described by Eq. (2.42). The symmetrical curve between  $-L/2$  and  $+L/2$  represents the solution with  $\sigma = 0$ , used as initial guess for the iterative procedure when  $\sigma = -100$  MPa. All the dashed lines represent iterations of the relaxation method. We plotted a curve every 1000 iterations to better show the evolution of the process and we used  $\delta_{min} = 10^{-10}$  for the stopping criterion. The domain wall arrives at the right extremity, eliminating the second magnetic domain. In the inset we also show the relative error  $\delta$  versus the iteration number. We can identify two relaxation regimes: in the first one the relative error decreases and the magnetization distribution assumes the correct shape (*e.g.*, in terms of the values in the plateau regions as well as the slope of the domain wall); in the second one the relative error is quite constant and the wall moves until ejection, corresponding to the final error drop. Additionally, we can

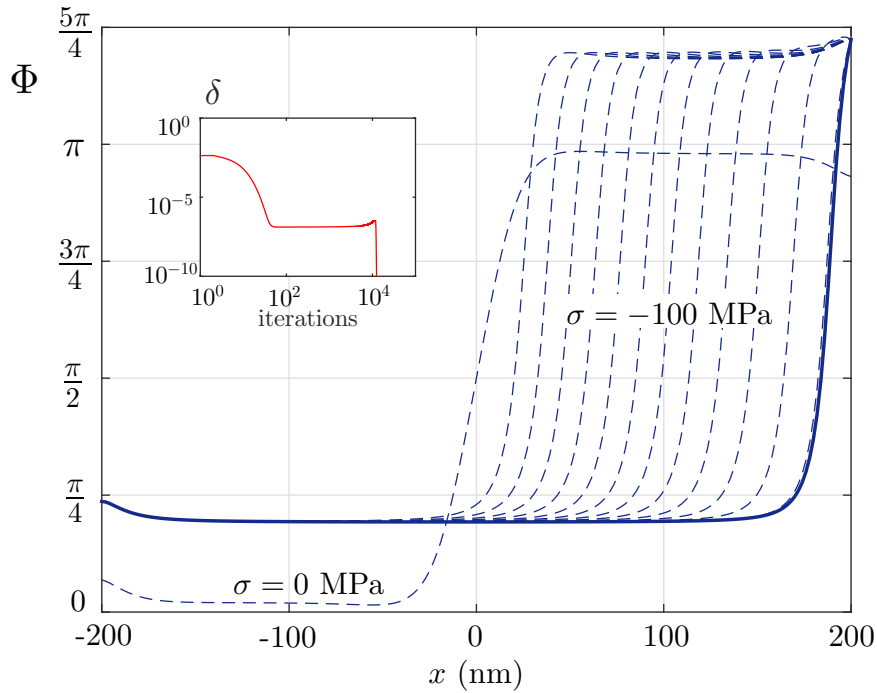


Figure 2.10 – Iterative process showing the ejection of the domain wall in a ferromagnet with constant rectangular section ( $h = 20$  nm and  $\ell = 40$  nm). In the inset the relative error  $\delta$  is plotted versus the iterations number. We used  $\delta_{min} = 10^{-10}$  and  $\sigma = -100$  MPa.

notice that the gap between the plateau values and boundary conditions (due to the effect of demagnetization) is consistent with what was found in Fig. 2.4 in that regard.

Although there may be a coincidental relationship between the speed at which the equilibrium distribution is reached and the intensity of the stress applied, the code is not able to provide any information about motion dynamics, which will be covered in chapter 3. Because this relaxation procedure is only made to find the magnetization distribution of the equilibrium state, the intermediate magnetization distributions as the simulations proceeds have no physical reality. As a result, simulations such as those with a constant section—which inevitably lead to the ejection of a domain wall—are of limited interest apart from showing that the numerical procedure devised to solve the equation appear to work and that its results support the conclusions of preliminary investigations of chapter 1. The end result will always be a single-domain configuration in this case. However, the possibility to introduce a variable width in the model paves the way for interesting analyses. As described in chapter 1, an increased width at the extremities creates a barrier for the domain wall. With an appropriate shape, it is therefore possible

to manipulate a confined domain wall. In the rest of this chapter, we focus on the study of confined domain walls.

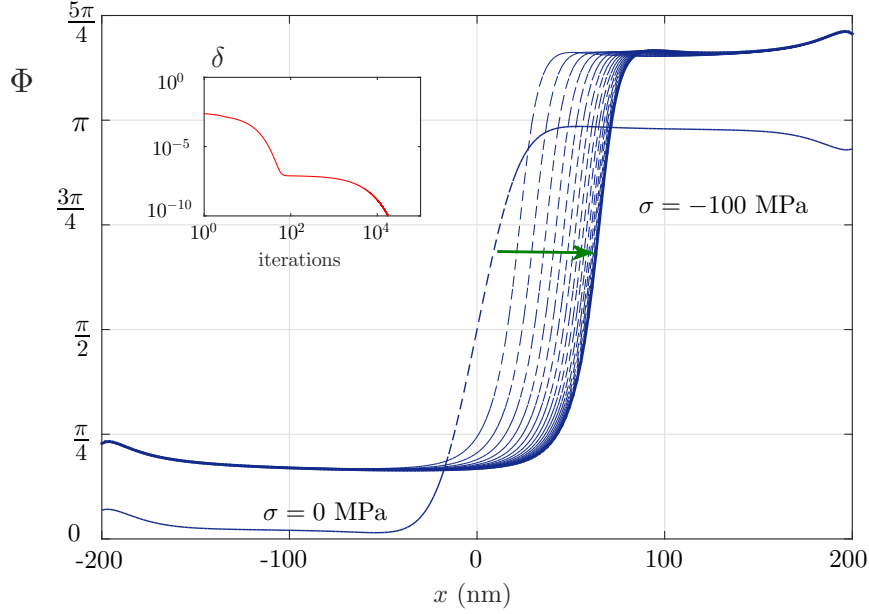


Figure 2.11 – Iterative process showing the path toward the equilibrium position of the domain wall for a hourglass-shaped nanostructure with central width  $\ell(0) = 40$  nm and width at extremities  $\ell(\pm L/2) = 70$  nm ( $h = 20$  nm). In the inset the relative error  $\delta$  is plotted versus the iterations number (log scale). We used  $\delta_{min} = 10^{-10}$  and  $\sigma = -100$  MPa.

In Fig. 2.11 we observe an equilibrium position obtained in a nanostructure with variable width (parabola-shaped). We considered a nanostructure with a thickness  $h = 20$  nm and a width  $\ell(x) = \ell(0) + 4\frac{\ell(\pm L/2) - \ell(0)}{L^2}x^2$  where  $\ell(0) = 40$  nm (central width),  $\ell(\pm L/2) = 70$  nm (width at extremities) and  $L = 400$  nm. Starting with the same initial guess used in Fig. 2.10, we apply  $\sigma = -100$  MPa and we obtain a final position at about 60 nm. As before, we note two scaling regimes for the relative error, namely (i) modification of the shape and (ii) displacement of the wall. The following section explores the influence of the stress value on the equilibrium position. It is important to point out that the distribution obtained at equilibrium is different from classical domain wall shapes, due to the influence of both the magnetoelastic energy and the variable width of the nanostructure.

As an aside, our simulations showed that this behavior (confinement) can also be observed with a magnetic field  $\vec{H}_1$  along the  $\vec{x}$  direction in the absence of a transverse

magnetic field and mechanical stress: below a threshold field the domain wall can move while remaining confined. The results allow to talk about an equivalent magnetic field, defined as the magnetic field along  $\vec{x}$  necessary to result in the same domain wall displacement. This shows the universality of the potential barrier-generating phenomenon of a variable width.

## 2.4.2 Stress-position relationship

The knowledge of the magnetization distribution for several values of  $\sigma$  allows us to determine the relationship between position of the domain wall  $x_{DW}^\infty$  and applied stress. Admittedly, the determination of the exact location of the domain is somewhat arbitrary, especially here where the width of the wall is significant with respect to the extent of the nanostructure. Here, we chose to consider the location where the slope is maximum to be the position of the wall. In other words, its position  $x_{DW}^\infty$  is determined with  $\max\left(\frac{d\Phi}{dx}\right)$ .

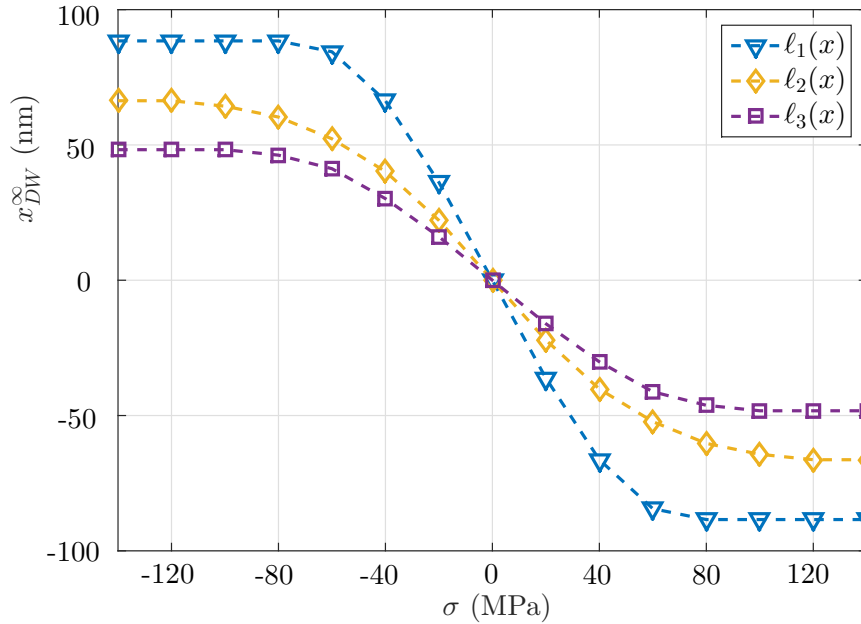


Figure 2.12 – Domain wall displacement at equilibrium  $x_{DW}^\infty$  as a function of the applied stress for three different parabolic profiles  $\ell_1$ ,  $\ell_2$  and  $\ell_3$  ( $\ell_1(0) = \ell_2(0) = \ell_3(0) = 40$  nm,  $\ell_1(\pm L/2) = \ell_2(\pm L/2) = 70$  nm,  $\ell_3(\pm L/2) = 80$  nm,  $h_1 = 10$  nm,  $h_2 = h_3 = 20$  nm). After a quite linear region for low values of  $\sigma$ , the response saturates, exhibiting a displacement range depending on the geometry. Also visible is the (anti)symmetry of the equilibrium position, such that  $x_{DW}^\infty(-E_0) = -x_{DW}^\infty(E_0)$ .

We performed this analysis for three slightly different geometries as shown in Fig. 2.12.

As a reminder, the important quantity which will influence the behavior of the domain wall is the ratio  $\frac{\ell'}{\ell}$ . In all cases we used a parabolic profile  $\ell(x)$  defined in the caption. Between  $\ell_1$  and  $\ell_2$ , the thickness is changed, while between  $\ell_2$  and  $\ell_3$ , the slope of the variable width is changed. The response exhibits a quite linear behavior for small values of  $\sigma$  and a saturation of the displacement for high values of  $\sigma$ . We underline that a larger section at the extremities of the nanostructure reduces the slope of the  $x_{DW}^\infty - \sigma$  curve and maximum displacement of the domain wall (it can be deduced by comparing the results for  $\ell_2$  and  $\ell_3$ ). This is due to the total exchange energy associated with the domain wall. Similarly, a larger thickness of the nanostructure reduces the slope of the curve and maximum displacement of the domain wall (it can be deduced by comparing the results for  $\ell_1$  and  $\ell_2$ ). This is due to the demagnetization energy, which is lower with thinner nanostructures (for additional information see subsection 2.4.3).

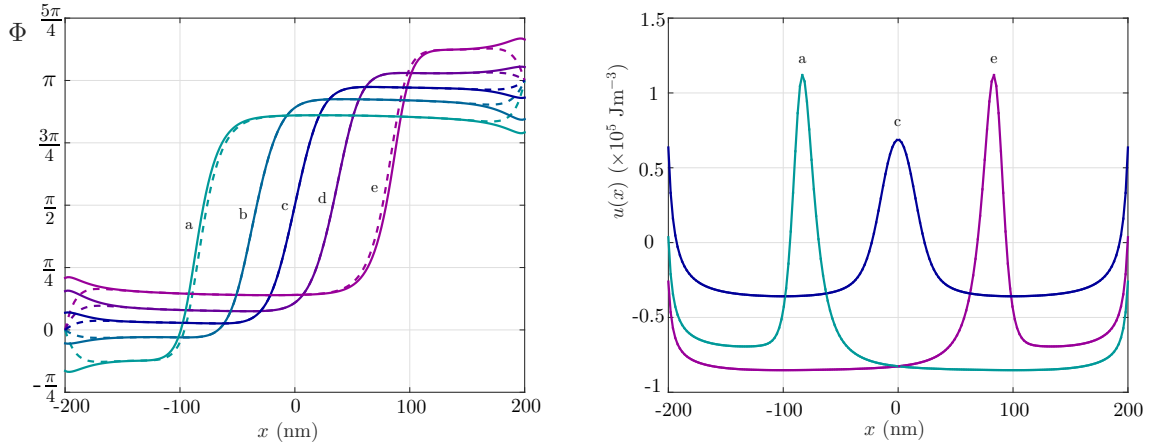


Figure 2.13 – (a) Magnetization distributions  $\Phi(x)$  for several values of the applied stress  $\sigma$  (a:  $\sigma = 60$  MPa; b:  $\sigma = 20$  MPa; c:  $\sigma = 0$  MPa; d:  $\sigma = -20$  MPa; and e:  $\sigma = -60$  MPa). Solid lines correspond to solutions with boundary conditions calculated as in Eq. (2.42), whereas dashed lines represent the solutions with  $\Phi(-L/2) = 0$  and  $\Phi(+L/2) = \pi$  as boundary conditions. One can notice that the influence of the difference between the two sets of boundary conditions is barely visible here. (b) Corresponding energy density profiles  $u(x)$ : the energy gap between the two plateau regions is clearly visible. Also, the region of increased energy marks the presence of the domain wall, which is thinner when a stress is applied.

The magnetization distributions corresponding to different values of the applied stress are shown in Fig. 2.13 together with the related energy density distributions within the nanostructure. These results have been obtained with the profile  $\ell_1(x)$ . The first plot deals with the magnetization distributions, with solid lines corresponding to solutions obtained

with the boundary conditions in Eq. (2.42) and dashed lines to the boundary conditions  $\Phi(-L/2) = 0$  and  $\Phi(+L/2) = \pi$ . We can observe that the boundary conditions do not influence the overall behavior of the domain wall in a dramatic fashion, although the effect is noticeable, especially for large stress values. The absence of significant effect will be especially true for long stripes with two large and clearly defined domains. The differences can indeed be only observed in the regions close to the extremities, and those far from them are hardly affected. The second plot shows the corresponding energy density profiles  $u(x)$  defined in subsection 2.2.1, such that  $U = \int_{-L/2}^{+L/2} u(x)h\ell(x)dx$ . It is not difficult to identify the regions corresponding to the two domains (with different energy densities) and the region related to the wall between them (peaks). It is interesting to note that an applied stress  $\sigma$  has the effect of making the domain wall thinner.

### 2.4.3 Energetic interpretation

It is clear that the motion is driven by the gap in energy density between the two domains. However, it is not straightforward to identify the role of each energy contribution. In order to better understand the interplay between all contributions, it is useful to look at their dependance on  $\sigma$ . Here, we used once again the boundary conditions as a proxy for the stable states of the system. As shown in subsection 2.2.4, the difference between the two sets of angles stems from the introduction of the geometry-dependant effect of the demagnetizing field and, while significant, does not change the overall behavior of the system. The quantities  $u'$  are defined as  $u_{Ze} + u_{an} + u_{me}$ .

In the first four subfigures in Fig. 2.14, individual contributions are plotted against  $\sigma$ , as well as the energy density. Whereas both anisotropy and magnetoelastic energy densities exhibit similar trends for  $\Phi_1$  and  $\Phi_2$ , this is absolutely not the case for the Zeeman energy. Indeed, it is increased for  $\Phi_1$  and decreased for  $\Phi_2$ . This is highlighted in the fifth subfigure, where the difference in energy density for those same contributions is plotted against  $\sigma$ . A striking observation is that the anisotropy and magnetoelastic gaps almost balance each other for any value of  $\sigma$  (they both reach their extremum when  $\frac{3}{2}\lambda_s\sigma = K_u$ , which corresponds to  $\sigma = 25$  MPa). As a result, the sum of these four terms is almost equal to the Zeeman energy gap. Therefore, as this gap is the cause of the motion, one could here talk about *stress-triggered field-driven* domain wall motion. Also, as the stable states get close to  $\{-\frac{\pi}{4}, \frac{3\pi}{4}\}$ , the saturation is associated with vanishing anisotropy and magnetoelastic energy gaps as those two states have the same energy density values for those two contributions.

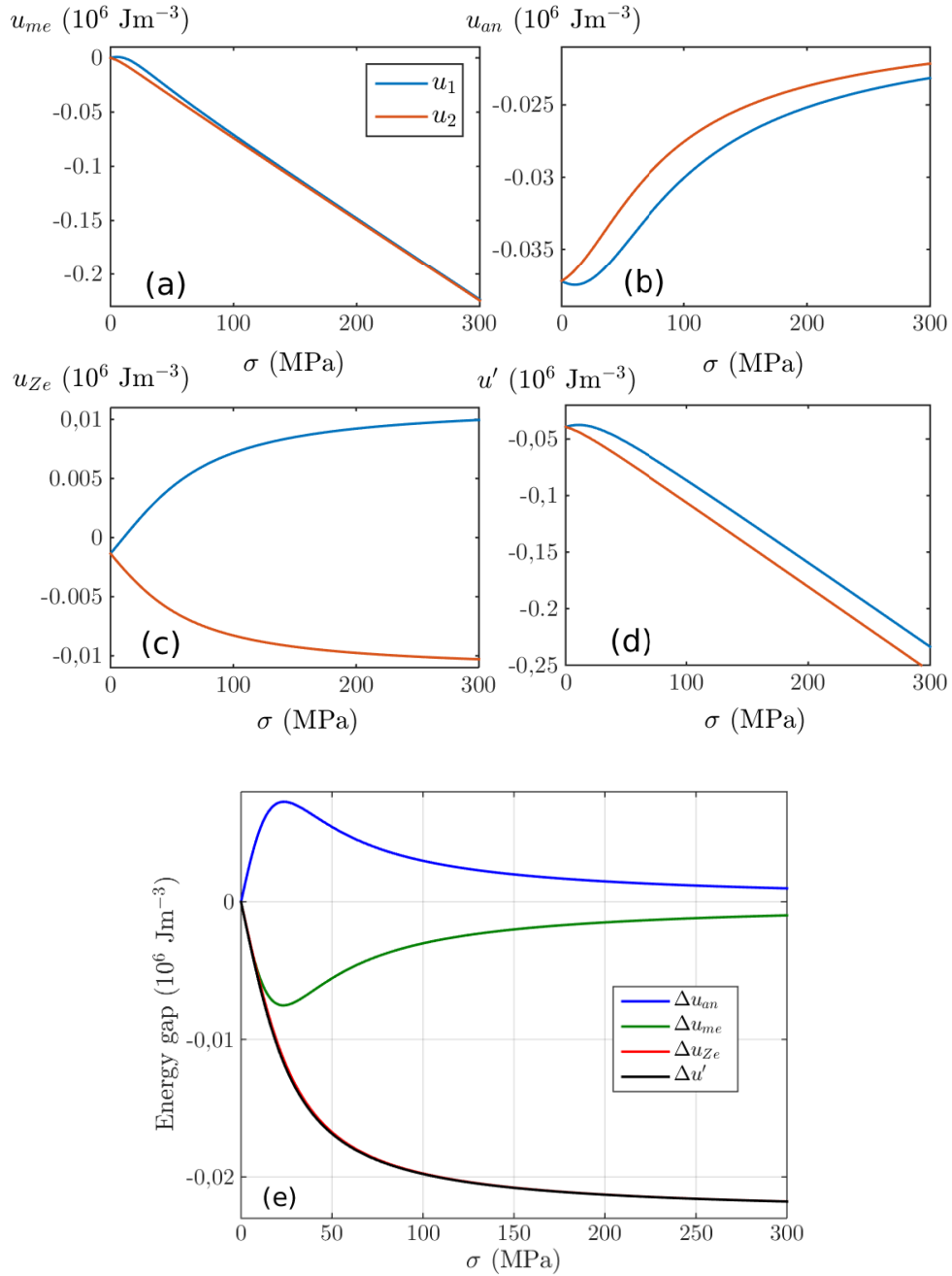


Figure 2.14 – (a) Magnetoelastic energy, (b) anisotropy energy, (c) Zeeman energy and (d) the sum of those three contributions associated with angles  $\Phi_1$  and  $\Phi_2$ , plotted against  $\sigma$  for  $H_0 = 20 \times 10^3$  A/m. (e) Difference in energy density  $u'_2 - u'_1 = u'(\Phi_2) - u'(\Phi_1)$ , and individual contributions, as functions of  $\sigma$ . In order to better appreciate the overall behavior,  $\sigma$  is taken between 0 and 300 MPa (there is complete antisymmetry for negative values).

In order to try to understand the link between the energy gap to the equilibrium position  $x_{DW}^\infty$ , we can develop an even simpler model. Let us consider a ferromagnet with variable width and two-domains characterized by the angles  $\Phi_1$  and  $\Phi_2$ , neglecting the demagnetization and with a magnetization distribution such that

$$\theta(x) = \begin{cases} \Phi_1 & \forall x \in [-\frac{L}{2}, x_0[ \\ \Phi_2 & \forall x \in [x_0, +\frac{L}{2}] \end{cases}$$

This means that there is an infinitely thin domain wall at the location  $x = x_0$ . Therefore the total energy of the system can be written as the sum of three terms:

$$U = \int_{-\frac{L}{2}}^{\frac{L}{2}} u(x)S(x) dx \quad (2.49)$$

$$U = \int_{-\frac{L}{2}}^{x_0} u'_1 S(x) dx + \int_{x_0}^{\frac{L}{2}} u'_2 S(x) dx + \int_{-\frac{L}{2}}^{+\frac{L}{2}} u_d dx + U_{DW}(x_0). \quad (2.50)$$

Obviously, the naive hypothesis of a wall with no width would yield an infinite exchange energy, which is not physical. The quantity  $U_{DW}$  introduced here is finite and represents the energy cost of the wall region (exchange, anisotropy and so forth). Moreover, we introduced the demagnetization energy density  $u_d = -\frac{1}{2}\mu_0 M_s \vec{H}_d \cdot \vec{w}$ . To continue, let us recall that  $u'_1$  and  $u'_2$  do not depend on  $x$  because the magnetization is considered uniform. The equilibrium position for the domain wall is found when  $U$  is minimum. This can be written as follows:

$$\begin{aligned} \frac{d}{dx_0} \left[ u'_1 \int_{-\frac{L}{2}}^{x_0} S(x) dx + u'_2 \int_{x_0}^{\frac{L}{2}} S(x) dx + \int_{-\frac{L}{2}}^{+\frac{L}{2}} u_d dx + U_{DW} \right] \Big|_{x_0=x_{DW}^\infty} &= 0 \\ \Leftrightarrow (u'_1 - u'_2)S(x_{DW}^\infty) + \frac{dU_d}{dx_0}(x_{DW}^\infty) + \frac{dU_{DW}}{dx_0}(x_{DW}^\infty) &= 0. \end{aligned}$$

Introducing the surface energy of the domain wall  $e_{DW}$ , then  $U_{DW} = S(x_0)e_{DW}$ , we can write the equation giving the value of  $x_{DW}^\infty$ :

$$\frac{S'(x_{DW}^\infty)}{S(x_{DW}^\infty)} + \frac{\Delta u'}{e_{DW}} + \frac{1}{S(x_{DW}^\infty)e_{DW}} \frac{dU_d}{dx_0} \Big|_{x_0=x_{DW}^\infty} = 0. \quad (2.51)$$

Again, one can see that the relevant quantity regarding the variable cross section is the ratio  $\frac{S'}{S} = \frac{\ell'}{\ell}$ . The only free parameter here is  $e_{DW}$  which can be estimated experimentally, theoretically, or even numerically for instance by using the relaxation-based numerical

procedure presented in this chapter (by finding the value of  $e_{DW}$  for which the solution of Eq. (2.51) matches the  $x_{DW}^\infty - \sigma$  relationship obtained using the relaxation method). In principle, this tremendously simple model could help design the cross section for a desired static response at minimal computational cost. For that purpose, it is necessary to have a good estimate of the demagnetizing term  $\frac{dU_d}{dx_0}$ . Indeed, without taking into account the demagnetizing field, it appears that a parabolic profile (hourglass-shaped) such as those we chose in subsection 2.4.2 is not able to confine the domain wall for reasonable values of  $e_{DW}$ . In a classical domain wall with only exchange and anisotropy, the surface energy can be written  $4\sqrt{AK_u}$  [6], which in our case gives is  $2 \times 10^{-3} \text{ Jm}^{-2}$ . With this order of magnitude, the profile required to prevent a single-domain outcome exchange alone is so stiff that overall the geometry cannot reasonably be considered akin to a nanostripe. This fact is important from the physical point of view here, as it means that the demagnetization is critical for the confinement. Without demagnetization, there can be no confinement for the geometries presented in this chapter, which means that there is no solution to Eq. (2.51) for  $|x_0| < \frac{L}{2}$  (a fact confirmed by independent testing with the relaxation procedure stripped of the influence of demagnetization).

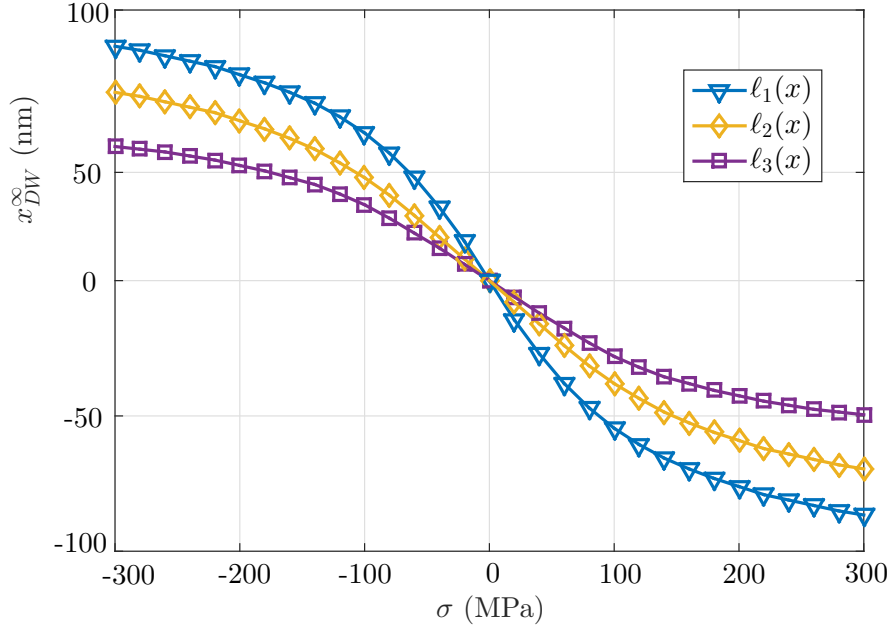


Figure 2.15 – Domain wall displacement as a function of the applied stress obtained by solving Eq. (2.51). Physical parameters are the same of those used previously, the geometry corresponds to the  $\ell_1$  width profile and  $e_{DW} = 5 \times 10^{-3} \text{ Jm}^{-2}$ .

Solving Eq. (2.51) for  $x_0$  yields the equilibrium position of the domain wall for a given value of  $\sigma$ . The result correctly predicts rightward motion for  $\sigma < 0$  and leftward motion for  $\sigma > 0$ , as well as the saturation as  $\sigma$  increases if  $e_{DW}$  is larger than a threshold value. The order of magnitude required happens to be very much consistent with basic theoretical predictions ( $\approx 10^{-3} \text{ Jm}^{-2}$ ). However, the crude assumption regarding the magnetization distribution (two uniform regions) yields a rather poor quantitative agreement between these results (see Fig. 2.15) and those previously obtained (see for instance Fig. 2.12). In particular, the saturation is not established as quickly. Nevertheless, this small model shows the relevance of considering the energy density gap between the two domains as the main drive for domain wall displacement.

#### 2.4.4 Piezoelectric generation of stress

In these simulations, we supposed that a uniform stress is applied to the system. For technological considerations, it is interesting to actually consider the possible ways to apply a uniform stress on a nanostructure. Depositing the magnetoelastic layers on piezoelectric substrates is an obvious option (see Fig. 2.16). For that purpose, ceramic materials such as lead magnesium niobate-lead titanate solid solution  $[\text{Pb}(\text{Mg}_{\text{frac}13}\text{Nb}_{\frac{2}{3}})\text{O}_3]_{(1-x)}[\text{PbTiO}_3]_x$  ( $0 < x < 1$ )—often abbreviated PMN-PT—has been drawing much attention. The reason for this is that its dielectric and piezoelectric properties are very interesting.

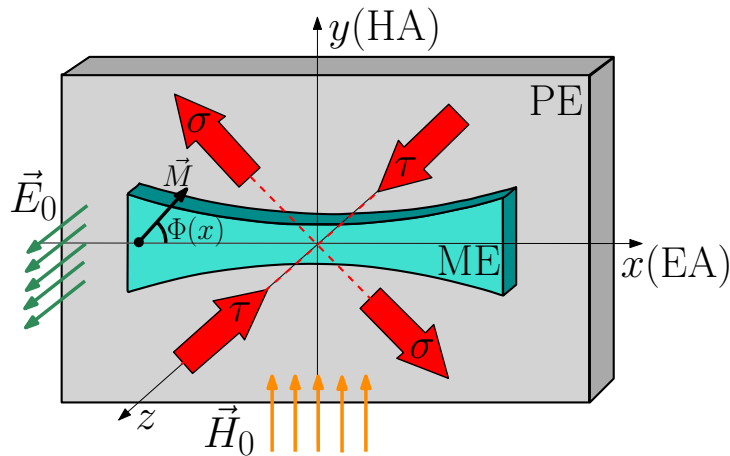


Figure 2.16 – Schematic of a magnetoelastic nanostructure (ME) mechanically coupled to a piezoelectric substrate (PE).

Because of these piezoelectric properties, the stress tensor applied to the magnetoelastic nanostructure will not be as simple as what was considered before. Let us re-

write the magnetoelastic term so that this is correctly taken into account. As in subsection 2.2.3, the general form of the energy density describing the magnetoelastic interaction is  $u_{me} = -T_{ij}\epsilon_{ij}^\mu$ . Its mathematical form is  $\epsilon_{ij}^\mu = \frac{\lambda_s}{2}(3w_i w_j - \delta_{ij})$ . If we consider a (011)-cut PMN-PT substrate, we have  $T_{x'x'} = \tau$  and  $T_{y'y'} = \sigma$ . Therefore, we obtain  $u_{me} = -\frac{3}{2}\lambda_s(\sigma - \tau)w_{y'}^2 + const$ . Now, within the piezoelectric material we suppose that the relationship between the strains and the electric field is linear. Admittedly, while most piezoelectric materials do exhibit a region where this assumption is valid, nonlinear behavior should be expected in experimental works and is reported in chapter 4. In any case, as a result of this hypothesis, one can write  $\epsilon_{11} = d_{31}E_0$  and  $\epsilon_{22} = d_{32}E_0$ . In a PMN-PT ceramic substrate,  $d_{32} = 600$  pC/N and  $d_{31} = -1900$  pC/N [278]. On the other hand, in the magnetoelastic material we have  $T_{ij} = 2\mu\epsilon_{ij} + \lambda\epsilon_{kk}$ , where  $\lambda$  and  $\mu$  are the Lamé coefficients (the strain within the substrate is supposed to be completely transmitted to the magnetoelastic layer which is very thin). By considering  $T_{33} = 0$  and  $\epsilon_{11}$  and  $\epsilon_{22}$  imposed by the piezoelectric substrate, we easily obtain  $T_{11} = \tau = 2\mu\frac{2(\lambda+\mu)d_{31}+\lambda d_{32}}{2\mu+\lambda}E_0$  and  $T_{22} = \sigma = 2\mu\frac{2(\lambda+\mu)d_{32}+\lambda d_{31}}{2\mu+\lambda}E_0$ . The corresponding energy density is therefore given by  $u_{me} = -3\lambda_s\mu E_0(d_{32} - d_{31})w_{y'}^2 + const$ . The rotated frame defined by the directions noted 1 and 2 is identical to what was used in subsection 2.2.1. Therefore, we must substitute  $w_{y'}^2 = \sin^2(\Phi - \frac{\pi}{4}) = -\sin\Phi\cos\Phi + const.$ , to eventually obtain

$$u_{me} = 3\lambda_s\mu E_0(d_{32} - d_{31})\sin\Phi\cos\Phi. \quad (2.52)$$

Instead of dealing directly with the applied stress, we have the electric field which generates two orthogonal stress components of opposite signs,  $\sigma$  and  $\tau$ . This is linked to the fact that  $d_{31}$  and  $d_{32}$  are negative and positive, respectively. We can now see the potential of such a substrate for technological applications. Here, while a tensile stress favors one dimension, an orthogonal compressive stress favors a plane containing this dimension. With this modification, Eq. (2.40) becomes:

$$\begin{aligned} \Phi''(x) + \Phi'(x)\frac{\ell'(x)}{\ell(x)} \\ - \frac{1}{2A} [2K_u \cos\Phi \sin\Phi - \mu_0 M_s H_0 \cos\Phi + 3\lambda_s\mu(d_{32} - d_{31})E_0 \cos 2\Phi \\ + \mu_0 M_s \sin\Phi \langle \vec{H}_{dx} \rangle_{y,z} - \mu_0 M_s \cos\Phi \langle \vec{H}_{dy} \rangle_{y,z}] = 0. \end{aligned} \quad (2.53)$$

It is clear from this equation that a stress  $\sigma' = \sigma - \tau$  would then have the exact same effect on the static behavior of the system. For this reason and because of the linear hypothesis, it should come as no surprise that the relationship between electric field and

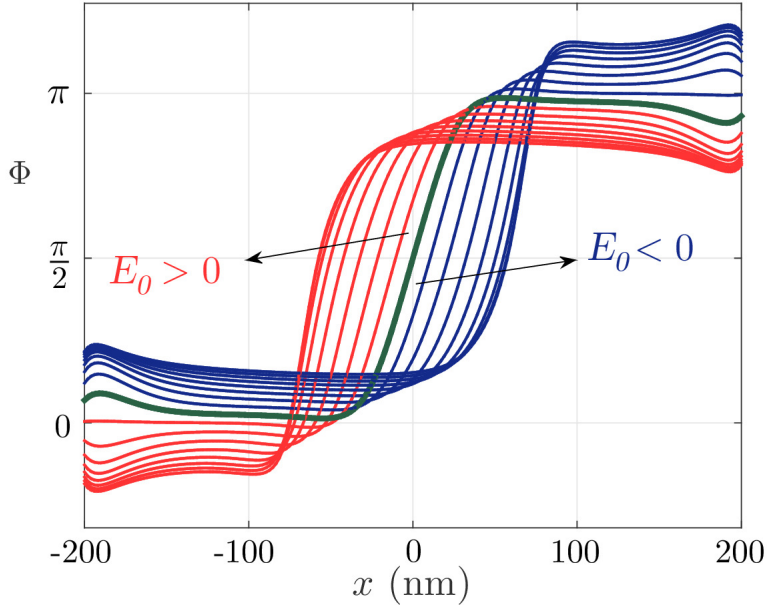


Figure 2.17 – Magnetization angle distributions  $\theta(x)$  within the nanostructure for a fixed magnetic field ( $H_0 = 20 \times 10^3$  A/m) and several values of electric field (17 values uniformly distributed in  $-3.5$  MV/m  $\leq E_0 \leq +1.1$  MV/m). We observe that the domain wall moves to the left for  $E_0 > 0$  and to the right for  $E_0 < 0$ .

displacement is the same as that between applied stress and displacement already obtained and shown in Fig. 2.12. For instance, Fig. 2.17 shows the angle  $\Phi$  of the magnetization distribution at equilibrium for several values of applied the electric field applied to the system. This approach, based on the electric field and a PMN-PT substrate is adopted in the work presented in chapter 3.

Introducing piezoelectric quantities allows the estimate of the energy consumption associated with the proposed technique. We can then draw a comparison with other methods based on the application of an external electric current and show that stress-based systems are promising from an energetic perspective, as stated in chapter 1. The total energy for moving the domain wall between two positions is the sum of the electrostatic energy stored within the piezoelectric substrate ( $CV^2$ ) and the magnetic energy dissipated within the magnetoelastic nanostructure. Nevertheless, the latter is typically negligible and the total energy is approximately equal to the electrostatic contribution [252, 257]. If we consider a piezoelectric PMN-PT substrate (length  $L = 400$  nm, width  $b = 80$  nm, and thickness  $d = 1$   $\mu$ m) with relative dielectric constant  $\epsilon_r = 5500$  for the structure described by  $\ell_1(x)$ , we obtain an energy  $\Delta E = \epsilon_r \epsilon_0 L b d E_0^2 = 1.5$  fJ  $= 3.6 \times 10^5 k_B T$  for moving the

wall between the maximum values of  $\pm x_{DW}^\infty$  (we used  $E_0 = \pm 10^6$  V/m generated by an electric potential difference of  $\pm 1$  V). For comparison, we can cite the energy dissipation  $\Delta E = 10^4$  fJ for one logic operation in a current-driven gate based on the domain wall motion [40]. In this case we numerically proved that the magnetic dissipation ( $\sim 10^{-17}$  J) is two order of magnitude smaller than the electrostatic contribution ( $\sim 10^{-15}$  J).

## 2.5 Conclusion

In this chapter, we presented a complete model describing the static behavior of magnetization in magnetoelastic nanostructures with variable width subjected to an external magnetic field and a mechanical stress, using an *ad hoc* numerical procedure.

In particular, we wrote the equation governing the magnetization distribution by taking into account anisotropy, exchange, demagnetization, magnetostriction and Zeeman effects. The approach chosen consisted in writing the total energy of the system in terms of the direction of the magnetization and then in applying the techniques of the calculus of variations in order to minimize the total energy itself. The end result is a nonlinear integro-differential partial equation which solution corresponds to the equilibrium state of the magnetic system. To solve this equation, we proposed an efficient numerical technique in order to solve the main nonlinear integro-differential equation with a relaxation, or iterative, method. We studied the convergence properties of this algorithm by applying it to a particular case, which can be handled analytically. With this convenient tool, we demonstrated the possibility to induce domain wall motion: in a constant section nanostripe, applying a uniform stress in time leads to the ejection of the domain wall so that the magnetization distribution becomes uniform. With an appropriate design of the cross section profile, we also demonstrated that it is possible to control a magnetic domain wall position in a ferromagnetic nanostructure with external mechanical actions. We showed that the origin of motion lies in the gap in Zeeman energy of the two domains induced by an effective anisotropy field modulated by the stress. This stress can be generated in multiferroic heterostructures (composed of piezoelectric and magnetoelastic subsystems). One of the key advantages of such a technique of domain wall motion is its relevance from the energetic point of view.

# Chapter 3

## Dynamics of stress-induced domain wall motion

In the previous chapter we presented a model which gives the equilibrium magnetic configuration of a 1D nanomagnet subjected to a magnetic field and mechanical action. However, all intermediate magnetization distributions taken from these simulations do not possess any physical reality nor do they represent actual magnetization states of the nanomagnet. This is because the path followed by the system as the simulation is carried out cannot be equated with a temporal evolution. For this reason, it is interesting to consider the possibility to devise a model which includes the Landau-Lifshitz-Gilbert equation that governs magnetization dynamics. This is the subject matter of this chapter, which includes the method followed to find the adequate equation, the numerical approach chosen to solve it, as well as the main results. Important physical insights pertaining to stress-induced magnetization dynamics are also presented.

The work of this chapter is the subject of one publication [279].

### 3.1 Equations governing domain wall dynamics

This section contains the path toward finding the right dynamical equation for the problem we chose to study. After the choice of notation are explained and energy contributions defined, the expression of the effective field is sought. From there, the corresponding Landau-Lifshitz-Gilbert equation is written.

#### 3.1.1 Overview

The logic behind the approach is similar to what was described in chapter 2, in that a variational procedure is followed to obtain the effective field. However, this is not the

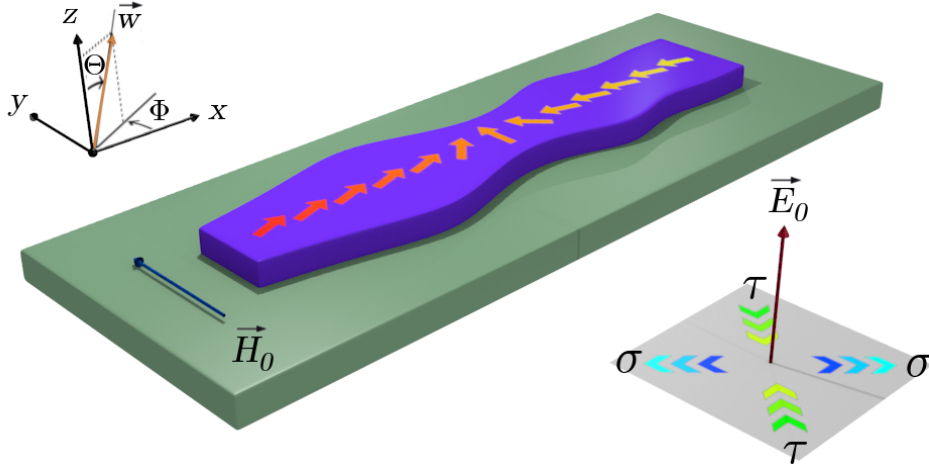


Figure 3.1 – Schematic of the system studied. The electric field applied along  $\vec{z}$  generates in the piezoelectric substrate a stress distribution with two components  $\sigma$  and  $\tau$  of opposite sign.

end result as the equation  $\vec{w} \times \vec{H}_{\text{eff}} = \vec{0}$  only describes the equilibrium state. Here, the expression of the effective field has to be taken as an input to the Landau-Lifshitz-Gilbert (LLG) equation that governs magnetization dynamics. The version of the equation used is as follows

$$\frac{\partial \vec{w}}{\partial t} = + \frac{\gamma_0}{1 + \alpha^2} \left( \vec{w} \times \vec{H}_{\text{eff}} - \alpha \vec{w} \times \left( \vec{w} \times \vec{H}_{\text{eff}} \right) \right), \quad (3.1)$$

where  $\alpha$  is the Gilbert damping coefficient, and  $\gamma_0 = \mu_0 \gamma$ ,  $\gamma$  being the gyromagnetic ratio of the test particle (both quantities should be negative to describe the electron precession). The effective field  $\vec{H}_{\text{eff}}$  already appeared in the previous developments and gathers within a single vector all the physical contributions involved. The same hypothesis of a one-dimensional system is assumed here, *i.e.* quantities depend only on  $x$ . One important change with respect to the previous study is that it is now compulsory to consider a magnetization field which direction is not bound to the  $xy$ -plane, defining a new angle  $\Theta \in [0, \pi]$  allowing the representation of out-of-plane magnetization components (see Fig. 3.1). However the approximation stating that  $\vec{M}$  depends only on  $x$  is preserved. As a result, one can write  $\vec{w} = (\cos \Phi \sin \Theta, \sin \Phi \sin \Theta, \cos \Theta)$ . Obviously, these two angular variables  $\Phi$  and  $\Theta$  now depend on  $x$  and  $t$ .

A minimization procedure similar to the previous example has to be carried out. However, the variable of interest in the function will be  $\vec{w} = (w_x, w_y, w_z)$  instead of  $\Phi$ . In

this context it is thus useful to rewrite all contributions in terms of this variable, with more specific forms for each term in relation to the configuration studied. Also, we considered the mechanical coupling of a magnetoelastic layer with PMN-PT, already mentioned in chapter 2.

### 3.1.2 Definition of the energy functional

Several of the energy terms are quite straightforward to write from prior expressions. The uniaxial anisotropy is simply  $u_{an} = -K_u w_x^2$ , while the Zeeman contribution becomes  $u_{Ze} = -\mu_0 M_s H_0 w_y$ . The exchange energy can be written  $u_{ex} = A \left( \frac{\partial \vec{w}}{\partial x} \right)^2 = A \left( \left( \frac{\partial w_x}{\partial x} \right)^2 + \left( \frac{\partial w_y}{\partial x} \right)^2 + \left( \frac{\partial w_z}{\partial x} \right)^2 \right)$ . A minor adaptation has to be made for the development of the magnetoelastic energy. Indeed, as  $\vec{w}$  is not restricted to the  $xy$ -plane, the expression is slightly different:

$$\begin{aligned} u_{me} &= -\frac{3}{2} \lambda_S (\tau w_{x'}^2 + \sigma w_{y'}^2), \\ u_{me} &= -\frac{3}{4} \lambda_S ((\tau + \sigma) (w_x^2 + w_y^2) + 2(\tau - \sigma) w_x w_y). \end{aligned} \quad (3.2)$$

with the same notations as used previously ( $w_{x'} = \vec{w} \cdot \vec{e}_{x'} = (\vec{e}_x + \vec{e}_y)/\sqrt{2}$  and  $w_{y'} = \vec{w} \cdot \vec{e}_{y'} = (\vec{e}_y - \vec{e}_x)/\sqrt{2}$ ). While  $(w_x^2 + w_y^2)$  was a constant in chapter 2, since we had  $\Theta = \frac{\pi}{2}$ , here this term will contribute to the Gâteaux derivative and thus to the dynamics.

The demagnetization contribution being unchanged,  $U$  is the functional of  $\vec{w}$  and reads

$$\begin{aligned} U &= \int_{-\frac{L}{2}}^{+\frac{L}{2}} h\ell(x) \left( -K_u w_x^2 + A \left( \frac{\partial \vec{w}}{\partial x} \right)^2 - \mu_0 M_s H_0 w_y \right. \\ &\quad \left. - \frac{3}{4} \lambda_S ((\tau + \sigma) (w_x^2 + w_y^2) + 2(\tau - \sigma) w_x w_y) \right) dx \\ &\quad - \frac{1}{2} \mu_0 M_s^2 \iint_{V^2} \vec{w}(\vec{r}_0) \cdot \overline{\vec{N}}(\vec{r}, \vec{r}_0) \vec{w}(\vec{r}_0) d\vec{r} d\vec{r}_0, \end{aligned} \quad (3.3)$$

where the factor  $\frac{1}{2}$  in the demagnetization term is still present for the reasons described in subsection 2.1.2.

### 3.1.3 Determination of effective field

As previously, this quantity has to be minimized with the constraint  $\|\vec{w}\| = 1$  (see appendix B):

$$\min_{\vec{w}: \|\vec{w}\|=1} U \Big|_{\vec{H}_0 \text{ fixed}} \Leftrightarrow \min_{\vec{w}} U + \int_V \lambda(\vec{w} \cdot \vec{w} - 1) d\vec{r} \Big|_{\vec{H}_0 \text{ fixed}}, \quad (3.4)$$

where we introduced the Lagrange multiplier  $\lambda(x)$  already mentioned in appendix B. Let us consider an arbitrary real vector  $\vec{k} = (k_x, k_y, k_z)$  and continue with the Gâteaux derivative, using the same properties and simplifications as previously:

$$\begin{aligned} \frac{d}{d\beta} U \left( \vec{w}(x) + \beta \vec{k}(x) \right) \Big|_{\beta=0} &= \int_{-\frac{L}{2}}^{+\frac{L}{2}} h\ell(x) \left( -2K_u k_x w_x + 2A \frac{\partial \vec{w}}{\partial x} \cdot \frac{d\vec{k}}{dx} - \mu_0 M_s H_0 k_y \right. \\ &\quad - \frac{3}{2} \lambda_s ((\tau + \sigma)(k_x w_x + k_y w_y) + (\tau - \sigma)(k_x w_y + k_y w_x)) \\ &\quad \left. + 2\lambda(x) \vec{w} \cdot \vec{k} dx \right) - \mu_0 M_s^2 \iint_{V^2} \vec{k} \cdot \vec{N}(\vec{r}, \vec{r}_0) \vec{w}(r_0) d\vec{r} d\vec{r}_0. \end{aligned} \quad (3.5)$$

Using integration by part again on the exchange term, and introducing the quantity  $\langle \vec{H}_d \rangle_{yz}$  as in subsection 2.2.3, one is left with a single integral

$$\begin{aligned} \frac{d}{d\beta} U \left( \vec{w}(x) + \beta \vec{k}(x) \right) \Big|_{\beta=0} &= \int_{-\frac{L}{2}}^{+\frac{L}{2}} h\ell(x) \vec{k} \cdot \left( -2K_u w_x \vec{x} - 2A \left( \frac{\partial^2 \vec{w}}{\partial x^2} + \frac{\ell'(x)}{\ell(x)} \frac{\partial \vec{w}}{\partial x} \right) \right. \\ &\quad - \frac{3}{2} \lambda_s ((\tau + \sigma)(w_x \vec{x} + w_y \vec{y}) + (\tau - \sigma)(w_y \vec{x} + w_x \vec{y})) \\ &\quad \left. - \mu_0 M_s \vec{H}_0 - \mu_0 M_s \langle \vec{H}_d \rangle_{yz} + 2\lambda \vec{w} \right) dx. \end{aligned} \quad (3.6)$$

This has to be true for any vector  $\vec{k}$ . Therefore we can write the following equation:

$$\begin{aligned} -2K_u w_x \vec{x} - 2A \left( \frac{\partial^2 \vec{w}}{\partial x^2} + \frac{\ell'(x)}{\ell(x)} \frac{\partial \vec{w}}{\partial x} \right) - \mu_0 M_s \left( \vec{H}_0 + \langle \vec{H}_d \rangle_{yz} \right) \\ - \frac{3}{2} \lambda_s ((\tau + \sigma)(w_x \vec{x} + w_y \vec{y}) + (\tau - \sigma)(w_y \vec{x} + w_x \vec{y})) + 2\lambda(\vec{r}) \vec{w} = 0. \end{aligned} \quad (3.7)$$

By taking the cross-product of Eq. (3.7) with  $\vec{w}$ , the Lagrange multiplier term can be deleted and one obtains

$$\vec{w} \times \vec{H}_{\text{eff}} = 0, \quad (3.8)$$

with

$$\begin{aligned} \vec{H}_{\text{eff}} = & \vec{H}_0 + \langle \vec{H}_d \rangle_{yz} + \frac{2}{\mu_0 M_s} \left( K_u w_x \vec{x} + \frac{A}{\ell(x)} \frac{\partial}{\partial x} \left( \ell(x) \frac{\partial \vec{w}}{\partial x} \right) \right. \\ & \left. + \frac{3}{4} \lambda_s ((\tau + \sigma)(w_x \vec{x} + w_y \vec{y}) + (\tau - \sigma)(w_y \vec{x} + w_x \vec{y})) \right). \end{aligned} \quad (3.9)$$

This is the effective field which has to be used in the Landau-Lifshitz-Gilbert equation.

### 3.1.4 Derivation of dynamical equations

The expression of the effective field in Eq. (3.9) has to be substituted in Eq. (3.1). The latter can be decomposed into the following three equations:

$$\frac{\partial w_x}{\partial t} = -\frac{\gamma_0}{1 + \alpha^2} ((w_y H_z - w_z H_y) + \alpha(w_y(w_x H_y - w_y H_x) - w_z(w_z H_x - w_x H_z))), \quad (3.10.1)$$

$$\frac{\partial w_y}{\partial t} = -\frac{\gamma_0}{1 + \alpha^2} ((w_z H_x - w_x H_z) + \alpha(w_z(w_y H_z - w_z H_y) - w_x(w_x H_y - w_y H_x))), \quad (3.10.2)$$

$$\frac{\partial w_z}{\partial t} = -\frac{\gamma_0}{1 + \alpha^2} ((w_x H_y - w_y H_x) + \alpha(w_x(w_z H_x - w_x H_z) - w_y(w_y H_z - w_z H_y))), \quad (3.10.3)$$

where we used  $\vec{H}$  instead of  $\vec{H}_{\text{eff}}$  to simplify expressions. To proceed from here, it is useful to develop the derivatives of the left side into explicit forms, using the expressions of  $\vec{w}$  components given in subsection 3.1.1. We adopt the common notation  $\dot{\square} \equiv \frac{\partial \square}{\partial t}$ .

$$\frac{\partial w_x}{\partial t} = \frac{\partial (\cos \Phi \sin \Theta)}{\partial t} = -\sin \Theta \sin \Phi \dot{\Phi} + \cos \Phi \cos \Theta \dot{\Theta}, \quad (3.11.1)$$

$$\frac{\partial w_y}{\partial t} = \frac{\partial (\sin \Phi \sin \Theta)}{\partial t} = \sin \Theta \cos \Phi \dot{\Phi} + \sin \Phi \cos \Theta \dot{\Theta}, \quad (3.11.2)$$

$$\frac{\partial w_z}{\partial t} = \frac{\partial (\cos \Theta)}{\partial t} = -\sin \Theta \dot{\Theta}. \quad (3.11.3)$$

Substituting Eq. (3.11.3) in Eq. (3.10.3), as well as Eq. (3.11.1) and Eq. (3.11.2) in Eq. (3.10.1) and Eq. (3.10.2), respectively, we can write

$$\begin{aligned} \sin \Theta \dot{\Phi} = \frac{\gamma_0}{1 + \alpha^2} & (-\cos \Phi \cos \Theta H_x - \sin \Phi \cos \Theta H_y + \sin \Theta H_z \\ & + \alpha(-\sin \Phi H_x + \cos \Phi H_y)), \end{aligned} \quad (3.12)$$

$$\begin{aligned} \dot{\Theta} = \frac{\gamma_0}{1 + \alpha^2} & (-\sin \Phi H_x + \cos \Phi H_y \\ & + \alpha(\cos \Phi \cos \Theta H_x + \sin \Phi \cos \Theta H_y - \sin \Theta H_z)), \end{aligned} \quad (3.13)$$

where Eq. (3.12) is obtained by calculating  $\cos \Phi \frac{\partial w_y}{\partial t} - \sin \Phi \frac{\partial w_x}{\partial t}$ . As an aside, considering that  $\frac{1}{\sin \Theta} \frac{\partial \vec{w}}{\partial \Phi} = (-\sin \Phi, \cos \Phi, 0)$  and  $\frac{\partial \vec{w}}{\partial \Theta} = (\cos \Phi \cos \Theta, \sin \Phi \cos \Theta, -\sin \Theta)$ , the equations can be rewritten as

$$\begin{cases} \sin \Theta \dot{\Phi} = \frac{\gamma_0}{1 + \alpha^2} \left( -\frac{\partial \vec{w}}{\partial \Theta} \cdot \vec{H} + \alpha \frac{1}{\sin \Theta} \frac{\partial \vec{w}}{\partial \Phi} \cdot \vec{H} \right) \\ \dot{\Theta} = \frac{\gamma_0}{1 + \alpha^2} \left( \frac{1}{\sin \Theta} \frac{\partial \vec{w}}{\partial \Phi} \cdot \vec{H} + \alpha \frac{\partial \vec{w}}{\partial \Theta} \cdot \vec{H} \right) \end{cases}. \quad (3.14)$$

A more explicit form of this equation requires the expressions of the three components of  $\vec{H}$ . Basic calculations not worth showing here give the following:

$$\begin{aligned} H_x = H_{dx} + \frac{2}{\mu_0 M_s} & \left( K_u \cos \Phi \sin \Theta + \frac{3}{4} \lambda_s ((\tau + \sigma) \cos \Phi \sin \Theta + (\tau - \sigma) \sin \Phi \sin \Theta) \right. \\ & + A \left( \frac{\ell'}{\ell} \left( -\sin \Phi \sin \Theta \frac{\partial \Phi}{\partial x} + \cos \Phi \cos \Theta \frac{\partial \Theta}{\partial x} \right) - \cos \Phi \sin \Theta \left( \left( \frac{\partial \Phi}{\partial x} \right)^2 + \left( \frac{\partial \Theta}{\partial x} \right)^2 \right) \right. \\ & \left. \left. - 2 \sin \Phi \cos \Theta \frac{\partial \Phi}{\partial x} \frac{\partial \Theta}{\partial x} - \sin \Phi \sin \Theta \frac{\partial^2 \Phi}{\partial x^2} + \cos \Phi \cos \Theta \frac{\partial^2 \Theta}{\partial x^2} \right) \right), \end{aligned} \quad (3.15.1)$$

$$\begin{aligned} H_y = H_0 + H_{dy} + \frac{2}{\mu_0 M_s} & \left( \frac{3}{4} \lambda_s ((\tau + \sigma) \sin \Phi \sin \Theta + (\tau - \sigma) \cos \Phi \sin \Theta) \right. \\ & + A \left( \frac{\ell'}{\ell} \left( \cos \Phi \sin \Theta \frac{\partial \Phi}{\partial x} + \sin \Phi \cos \Theta \frac{\partial \Theta}{\partial x} \right) - \sin \Phi \sin \Theta \left( \left( \frac{\partial \Phi}{\partial x} \right)^2 + \left( \frac{\partial \Theta}{\partial x} \right)^2 \right) \right. \\ & \left. \left. + 2 \cos \Phi \cos \Theta \frac{\partial \Phi}{\partial x} \frac{\partial \Theta}{\partial x} + \cos \Phi \sin \Theta \frac{\partial^2 \Phi}{\partial x^2} + \sin \Phi \cos \Theta \frac{\partial^2 \Theta}{\partial x^2} \right) \right), \end{aligned} \quad (3.15.2)$$

$$H_z = H_{dz} + \frac{2A}{\mu_0 M_s} \left( \frac{\ell'}{\ell} \sin \Theta \frac{\partial \Theta}{\partial x} - \cos \Theta \left( \frac{\partial \Theta}{\partial x} \right)^2 - \sin \Theta \frac{\partial^2 \Theta}{\partial x^2} \right). \quad (3.15.3)$$

After simplifications, Eq. (3.14) can be rewritten

$$\begin{cases} \dot{\Phi} &= \frac{1}{\sin \Theta} \frac{\gamma_0}{1 + \alpha^2} (-s + \alpha r), \\ \dot{\Theta} &= \frac{\gamma_0}{1 + \alpha^2} (r + \alpha s), \end{cases} \quad (3.16)$$

where we introduced the two quantities  $r$  and  $s$  such that

$$\begin{aligned} r &= -\sin \Phi H_{dx} + \cos \Phi H_{dy} + \cos \Phi H_0 + \frac{2}{\mu_0 M_s} (-K_u \cos \Phi \sin \Phi \sin \Theta \\ &\quad + \frac{3}{4} \lambda_s (\tau - \sigma) \cos 2\Phi \sin \Theta + A \left( \frac{\ell'}{\ell} \sin \Theta \Phi' + 2 \cos \Theta \Phi' \Theta' + \sin \Theta \Phi'' \right)), \end{aligned} \quad (3.17)$$

and

$$\begin{aligned} s &= \cos \Phi \cos \Theta H_{dx} + \sin \Phi \cos \Theta H_{dy} - \sin \Theta H_{dz} + \sin \Phi \cos \Theta H_0 \\ &\quad + \frac{2}{\mu_0 M_s} \left( K_u \cos^2 \Phi \sin \Theta \cos \Theta + \frac{3}{4} \lambda_s ((\tau + \sigma) \cos \Theta \sin \Theta \right. \\ &\quad \left. + 2(\tau - \sigma) \cos \Phi \sin \Phi \cos \Theta \sin \Theta) + A \left( \frac{\ell'}{\ell} \Theta' + \Theta'' - \cos \Theta \sin \Theta \Phi'^2 \right) \right). \end{aligned} \quad (3.18)$$

In Eq. (3.17) and (3.18), we used the notation  $\square' \equiv \frac{\partial \square}{\partial x}$  for  $\Phi$  and  $\Theta$  as was hitherto the case for  $\ell$ .

Incidentally, it is interesting to point out that the equations that dictate the equilibrium state are given by  $r = 0$  and  $s = 0$  (taking  $\dot{\Phi} = \dot{\Theta} = 0$ ). In the particular case where  $\Theta = \frac{\pi}{2}$ , we are left with  $r = 0$  which is equivalent to Eq. (2.40). Indeed, those assumptions are implicit in the hypotheses chosen in the beginning of section 2.2. Similarly to Eq. (2.40), Eq. (3.16) is such that theoretical insights on steady-state solutions akin to Walker-like calculations appear out of reach. Therefore, the numerical approach remains the only way to investigate the physics of stress-induced domain wall motion. In fact, we can identify the reason why the problem does not lend itself to analytical treatment, contrary to field-driven motion in the case explored by Schryer and Walker [75]. The problem lies with the tilted anisotropy introduced by the stress which prevents from obtaining the same kind of simple result of field-driven motion as in appendix D. Meanwhile, this feature has far-reaching consequences on the physical differences in the dynamics that will be explained in sections 3.3 and 3.4.

## 3.2 Numerical procedure

This section describes the numerical approach for solving equation Eq. (3.16) since it cannot be treated analytically. It includes a quick description of the technique as well as

the way it was checked for convergence and accuracy.

### 3.2.1 Presentation

The most obvious scheme that comes to mind in the context of the numerical treatment of differential equations is the explicit Euler method. However, implicit schemes are far superior to explicit schemes, which often appear insufficient in solving nonlinear problems. The reason for this is that the propagation of errors leads to strong constraints in terms of temporal discretization in order to prevent physically and numerically aberrant evolutions. Typically, in the case of the heat equation for instance—which shares some features with the Landau-Lifshitz-Gilbert equation, namely the order of the derivatives with respect to space and time—the time step  $dt$  should not be greater than a threshold value proportional to  $dx^2$  (spatial discretization) [273]. The computational cost of these constraints make convergence hard to achieve in practice. The choice was to use an implicit finite difference scheme, or backward Euler method. As for the solver chosen, despite our early attempts it appears that this system of two non-linear integro-differential equations cannot be solved using the built-in tools in Matlab. This led us to develop a dedicated algorithm, and we chose to implement Newton’s method which proved to work quite well. A general introduction to Newton’s method is followed by some details about our *ad hoc* implementation.

Newton’s method is routinely used in numerical analysis to find the root of a differentiable real-valued function. Let us define  $F : \mathbb{R}^k \rightarrow \mathbb{R}^k$  a vector function of real variables  $x = [x_1, \dots, x_k]^\top$  for which we have to find the root:

$$F(x) = 0. \tag{3.19}$$

A first estimate of the solution is found from a guess  $x^0$ , by calculating the value  $x^1$  where the first-order approximation to  $F$  at point  $x^0$  is zero. This involves the calculation of the Jacobian  $J$  of the  $F$  function:

$$J(x^0)(x^1 - x^0) = -F(x^0), \tag{3.20}$$

where  $J_{ij} = \frac{\partial F_i}{\partial x_j}$  is a  $k$ -by- $k$  square matrix of which all elements are calculated at the guess values  $x^0$ . The process is iterative: the solution  $x^1$  obtained is a better approximation of the root, and is used to find a new solution  $x^2$ , etc. For an arbitrary step  $m$  in this loop:

$$J(x^m)(x^{m+1} - x^m) = -F(x^m). \tag{3.21}$$

The procedure is stopped after a number of steps when sufficient precision is obtained, *i.e.* when the norm of  $F(x^m)$  is less than a predetermined value, and the solution  $x^{new}$  is thus assigned the value  $x^m$ .

In our case  $k = 2N$ , since we have two variables  $\Phi$  and  $\Theta$  of size  $N$ . Let us concatenate them and define the following variable:

$$X = \begin{bmatrix} \Phi_1 \\ \Theta_1 \\ \vdots \\ \Phi_N \\ \Theta_N \end{bmatrix}. \quad (3.22)$$

At any time step, the previous state is used as an input guess for finding the next, and there are  $2N$  equations to be solved,

$$F(X^{new}) = 0, \quad (3.23)$$

with

$$F(X^{new}) = X^{new} - X^{old} - \Delta t G(X^{new}). \quad (3.24)$$

Here,  $X^{new}$  is the unknown, and this equation shows that the procedure chosen is implicit. The vector function  $G$  corresponds to the right-hand side of Eq. (3.16). For each index  $i$  in  $\{1, \dots, 2N\}$ ,  $G_i$  depends on the variable  $X_i$ , but also on neighboring variables (such as  $X_{i-1}$  and  $X_{i+1}$ ) because of the presence of spatial derivatives  $X'$  and  $X''$  in Eq. (3.16) (expressions of discretized derivatives are identical to what is shown in Eq. (2.45)).

The procedure followed is iterative and includes a convergence check based on the comparison of the euclidian norm of  $F$  with a convergence parameter arbitrarily taken equal to  $2 \times 10^{-30}$ . We introduced here an exponent  $m$  as in Eq. (3.21) to refer to the steps in the Newton iterative loop. For any step  $m$ :

$$J(X^m)X^{m+1} = J(X^m)X^m - F(X^m), \quad (3.25)$$

where  $J$  is the Jacobian matrix. The right hand side can be expanded:

$$J(X^m)X^m - F(X^m) = X^{old} + \Delta t \left( G(X^m) - \frac{dG}{dX} X^m \right) \quad (3.26)$$

The derivative is defined as the sum  $\sum_i \frac{\partial G}{\partial X_i}$ . In practice, it is typically composed of six terms (since it depends on  $\Theta_i$ ,  $\Theta_{i-1}$ ,  $\Theta_{i+1}$ ,  $\Phi_i$ ,  $\Phi_{i-1}$  and  $\Phi_{i+1}$ ). Attention should also be brought on the fact that the first term of the right-hand side in Eq. (3.26) ( $X_i^{old}$ ) is a mere

parameter in the equation. In any case, the solution can then be found by calculating  $X^{m+1} = J(X^m)^{-1}B(X^m)$ , with the vector  $B$  is as follows:

$$B(X^m) = X^{old} + \Delta t \left( G(X^m) - \frac{dG}{dX}(X^m)X^m \right). \quad (3.27)$$

Below is an excerpt of the MATLAB code, which is the content of one step (from  $m$  to  $m + 1$ ) in the Newton procedure for a given time step. The first loop is the definition of the Jacobian matrix. It should be noted that the first two and last two elements of the diagonal are treated separately as  $\Phi_1$ ,  $\Theta_1$ ,  $\Phi_N$  and  $\Theta_N$  are unchanged through the simulation (boundary conditions). Names of variables are the same as above, except for  $dsrphi$ ,  $drsttheta$  and the like which refer to specific partial derivatives of  $G$ .

```
% the Jacobian matrix
J(1,1)=1; J(2,2)=1;
for i = 3:2:2*Npoints-3
    % odd indices: dot phi equations
    J(i,i)=1-dt*gamma0/(1+alpha^2)*dsrphi(floor(i/2));
    J(i,i+1)=-dt*gamma0/(1+alpha^2)*(dsrtheta(floor(i/2))...
        -((-s(floor(i/2))+alpha*r(floor(i/2)))...
        .*cos(ph(floor(i/2)))) ./ sin(ph(floor(i/2))).^2);
    J(i,i+2)=-dt*gamma0/(1+alpha^2)*dsrphip(floor(i/2));
    J(i,i+3)=-dt*gamma0/(1+alpha^2)*dsrthetap(floor(i/2));
    J(i,i-1)=-dt*gamma0/(1+alpha^2)*dsrthetam(floor(i/2));
    J(i,i-2)=-dt*gamma0/(1+alpha^2)*dsrphim(floor(i/2));
    % even indices: dot theta equations
    J(i+1,i+1)=1-dt*gamma0/(1+alpha^2)*drsttheta(floor(i/2));
    J(i+1,i+2)=-dt*gamma0/(1+alpha^2)*drsphip(floor(i/2));
    J(i+1,i+3)=-dt*gamma0/(1+alpha^2)*drsthetap(floor(i/2));
    J(i+1,i)=-dt*gamma0/(1+alpha^2)*drsphi(floor(i/2));
    J(i+1,i-1)=-dt*gamma0/(1+alpha^2)*drsthetam(floor(i/2));
    J(i+1,i-2)=-dt*gamma0/(1+alpha^2)*drsphim(floor(i/2));
end
J(2*Npoints-1,2*Npoints-1)=1;
J(2*Npoints,2*Npoints)=1;

% right side
B(1)=phi(1); B(2)=theta(1);
B(2*Npoints-1)=phi(Npoints);
B(2*Npoints)=theta(Npoints);
B(3:2:2*Npoints-3)=phi_old(2:Npoints-1)+dt*gamma0/(1+alpha^2)...
    *((-s+alpha*r) ./ sin(ph) - ((dsrtheta - (-s+alpha*r) .* cos(ph) ...
    ./ sin(ph).^2) .* ph + dsrthetam .* theta(1:Npoints-2) + dsrthetap ...
    .* theta(3:Npoints) + dsrphi .* th + dsrphim .* phi(1:Npoints-2) ...
    + dsrphip .* phi(3:Npoints)));
```

```

B(4:2:2*Npoints-2)=theta_old(2:Npoints-1)+dt*gamma0/(1+alpha^2)...
*(r+alpha*s-(drsthe_t.*ph+drsthe_t.*theta(1:Npoints-2)...
+drsthe_t.*theta(3:Npoints))+drsphi.*th+drsphi...
.*phi(1:Npoints-2)+drsphi.*phi(3:Npoints));

```

```

% solving equation
X=J\B';

```

The end result is then used to compute the value of  $F$  and check it against the convergence parameter. We should also mention that the demagnetizing field is held constant within the Newton's method procedure of a time step. It is recalculated before entering the procedure, hence it is not fully implicit. The code can be stopped either after a given amount of time, when the domain wall has reached a given position, or when the system has reached equilibrium (from a criteria similar to that used in the relaxation code).

### 3.2.2 Convergence and test against analytical solution

Using this computational scheme, convergence is achieved at each time step for reasonable inputs of parameters. It is intriguing to note that any attempt to remove demagnetization or introduce a simplified demagnetization in the presence of a stress entails the eventual failure of the code. However when convergence is achieved, it is very quick, demonstrating the efficiency of Newton's method. This allowed us to use a very small internal convergence parameter ( $2 \times 10^{-30}$ ).

The physical parameters considered here are the same than in chapter 2, except for  $\lambda_s$  which is taken equal to  $2 \times 10^{-4}$  here. As a matter of fact, it is this way closer to the value of magnetic multilayers such as those used in our laboratory and described in chapter 4. In any case, this change amounts to a simple rescaling of stress values. Furthermore, we chose to use the electric field as the variable dictating the mechanical stress applied to the system. Thus, the values of  $\sigma$  and  $\tau$  in Eq. (3.16) are given by expressions in subsection 2.4.4. One additional parameter that was not present in the previous study is the Gilbert damping constant. Its value is known to be typically higher in thin films than in bulk materials [280]. In all our simulations, it assumes four different values, from 0.12 to 0.06. A higher damping constant means less pronounced precession and smaller domain wall velocities for a given stimulus (see Eq. (1.9)). It should also be noted that throughout these simulations, the gyromagnetic ratio  $\gamma$  was taken equal to the opposite of its real value ( $\approx -1.76 \times 10^{11} \text{ s}^{-1}\text{T}^{-1}$ ), and is thus positive instead of negative. It results from this that the precession is carried out in the other direction, and that we are

looking at magnetism for a positive charge. While this mistake affects all the results, the dynamics will be unaffected. The consequences of a reversed precession will be mentioned as we go along in the discussion, every aspect of which will remain valid.

In chapter 2 we compared the result of the code to a known analytical solution for the magnetization distribution. We can check that this numerical tool dealing with magnetization dynamics also passes this test, and that it converges to the correct distribution with the application of a stress (as compared to the result of the previous code). While this turns out to be the case, it is not sufficient in itself. As a matter of fact, even if the code is able to find an equilibrium distribution, it only shows that the procedure is able to relax to a distribution given by  $r = 0$  and  $s = 0$  but it does not guarantee that the path followed is correct from the dynamical point of view. Therefore, there is a crucial need to check the procedure against a case where an analytical solution is known. As shown in subsection 1.2.3, the case of a field-driven motion can be handled analytically. Therefore, we chose to compare the output of the code with the velocity of the field-driven motion of a head-to-head domain wall. This case is different from what had been treated by Schryer and Walker who considered an easy axis perpendicular to the direction of motion. Here, the anisotropy is along the  $x$ -axis, as is the direction of motion. Contrary to the account given in Eqs. (1.9) and (1.10), this situation requires the contribution of demagnetization, introduced here in the simplified form  $\vec{H}_d = -\overline{\overline{N}}\vec{M}$ , as if it were generated by an infinitely long ellipsoid.  $\overline{\overline{N}}$  is diagonal (with  $\text{tr}(\overline{\overline{N}}) = 1$ ) and the elements of the diagonal are noted  $N_x$ ,  $N_y$  and  $N_z$ . This point is addressed further in appendix D. The result is the following:

$$v(H_1) = -\frac{\gamma_0 H_1}{\alpha} \sqrt{\frac{A}{K_u - \mu_0 M_s^2 / 2(N_z - \cos^2 \phi_0 N_x - \sin^2 \phi_0 N_y)}}, \quad (3.28)$$

$$\sin 2\phi_0 = \frac{2H_1}{\alpha M_s (N_y - N_x)} = \frac{H_1}{H_c}. \quad (3.29)$$

In Fig. 3.2 we show two sets of comparisons that have been made. The code is also suited to the computation of field-driven dynamics, when  $E_0 = 0$ ,  $H_0 = 0$ , and a magnetic field  $\vec{H}_1 = H_1 \vec{y}$  is introduced. For different values of  $H_1$  we compared the output of the code with the analytical expressions in Eqs. (3.28) and (3.29). A damping coefficient  $\alpha$  of 0.1 is assumed and  $M_s$  is taken equal to  $5 \times 10^5$  A/m. The two values of anisotropy considered are  $K_u = 10^3$  Jm<sup>-3</sup> and  $K_u = 10^5$  Jm<sup>-3</sup>. As for the demagnetization, we chose  $N_y = 0.995$  and  $N_z = 1 - N_y = 0.005$  (the hypothesis being that of an infinitely long ellipsoid we have  $N_x = 0$ ). The resulting breakdown field is  $24.75 \times 10^3$  A/m.

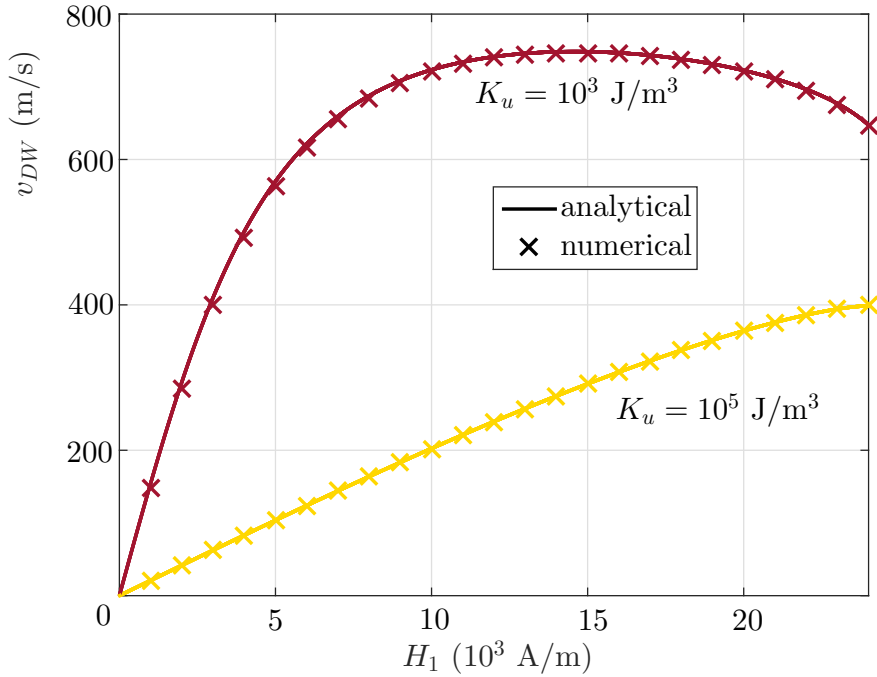


Figure 3.2 – Direct comparison of the output of the code with Walker’s analytical solution in the case of field-driven motion. The agreement is very good for both values of anisotropy.  $M_s$  is changed here compared to other simulations and is equal to  $5 \times 10^5$  A/m.

As visible in Fig. 3.2, there is an excellent agreement for both values of  $K_u$  between the numerical and analytical velocities. This gives confidence in the capacity of this numerical procedure to correctly represent the dynamical trajectories of domain walls. However, it should be noted that the code systematically crashes for  $H_1$  becomes superior to  $H_c = 24.75$  A/m, even only slightly superior. This indicates that there is a fundamental change in the dynamics beyond the Walker breakdown which cannot be accounted for by our numerical implementation.

### 3.3 Dynamics in hourglass geometry

This section deals with the results obtained concerning the dynamics of the system with variable width studied in chapter 2. The trajectory and shape of domain walls in such structures are explored. Then, the dependence on the electric field of domain wall velocity is studied and discussed. Also, the asymmetry that appears in the dynamics with respect to the electric field is explained in terms of the balance between compressive and tensile components of the corresponding applied stress.

### 3.3.1 Shape of domain walls

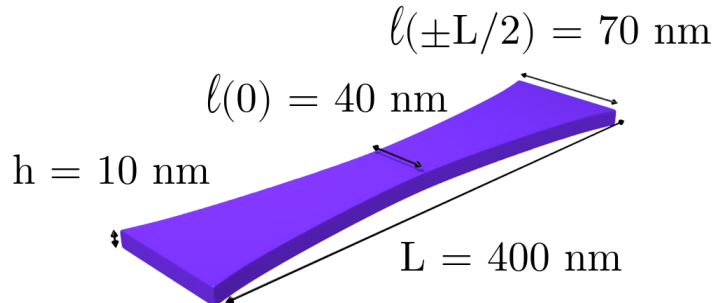


Figure 3.3 – Schematic of the parabolic geometry considered in the dynamical study.

Before getting to the analysis of the dynamics, it is reassuring to note that the equilibrium magnetization distribution given by this dynamical code is the same as the relaxation code for a given value of electric field. This fact also strongly substantiates hypothesis (i) in the model presented in subsection 2.2.1: as expected, there is no out-of-plane component in the equilibrium distribution (*i.e.*  $\Theta = \frac{\pi}{2}$ ). This is not true of the magnetization during the whole dynamics, however. There is indeed a noticeable out-of-plane behavior, and this phenomenon is transient: from a completely in-plane initial distribution at the beginning of the simulation,  $w_z$  increases steadily in the vicinity of the domain wall (*i.e.*  $\Theta$  deviates from  $\frac{\pi}{2}$ ) and vanishes as the domain wall reaches its final position  $x_{DW}^\infty$ . This out-of-plane excursion is upward or downward depending on the sign of  $E_0$ . Specifically, when the motion is rightward, the out-of-plane behavior is downward, and vice-versa. At this stage, it is important to note that the opposite outcome is obtained when the sign of  $\gamma$  is changed to describe electron-based magnetism instead of a positive charge-based magnetism: rightward motion is associated with upward out-of-plane behavior, and vice-versa. Apart from this change, there is no difference to mention.

These out-of-plane excursions look like a manifestation of a distinctive aspect of the differential equations solved, which differs from standard domain wall motion equations in a fundamental way. Indeed, in the case of field-driven motion, all the magnetization distribution is contained in a single plane (see appendix D or Ref. [75]). This means that, while the magnetization can be out of the plane of the simulated ferromagnet, there is always a tilted plane that contains all the magnetization vectors along the  $x$ -axis

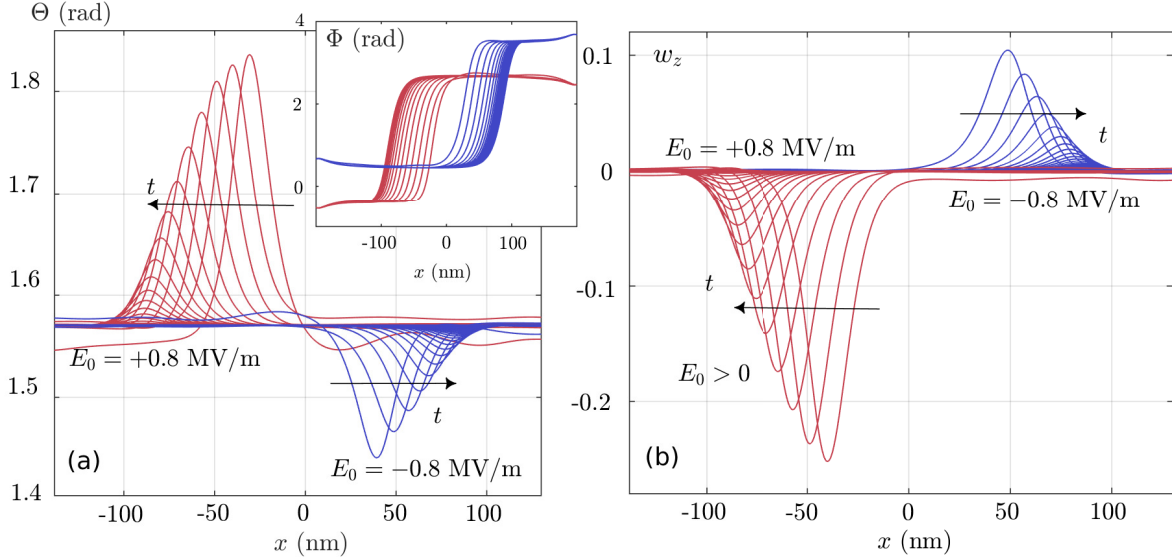


Figure 3.4 – The two angles describing the magnetization vector (a) and the out-of-plane magnetization component (b) are plotted every tenth of nanosecond while an electric field  $E_0$  of  $\pm 0.8$  MV/m and a magnetic field  $H_0$  of  $20 \times 10^3$  A/m are applied. There is a noticeable deviation of  $\Theta$  from  $\frac{\pi}{2}$ , which translates into a non-zero out-of-plane component. This behavior has no equivalent in the steady-state regime described by Schryer and Walker.

(defined by  $\phi_0$  in Eq. (1.10) or Eq. (3.29)). However, at this point it is not possible, strictly speaking, to assign this peculiar behavior to an intrinsic effect of the particular combination of field and stress studied here. It may be caused by the variable width, which is another difference with classical developments such as those of Schryer and Walker. Further analyses on constant-section nanostripes will help settle this question in section 3.4.

There is nonetheless another key finding that constitutes strong evidence that these out-of-plane excursions are somehow linked to the application of a mechanical stress. In Fig. 3.4, the asymmetry with respect to the electric field is quite conspicuous. One can observe that the out-of-plane excursion is more pronounced with positive electric fields than negative electric fields, although it is present in both cases. The difference between those two cases is the balance between compressive and tensile components of the stress tensor. This intriguing behavior explored in subsection 3.3.3 stems from the disparity  $d_{32} \neq -d_{31}$  and hence the relation  $|\tau| > |\sigma|$  (and they are always of opposite sign). It means that if  $E_0 > 0$ , the domain wall moves to the left ( $x < 0$ ) with a compression  $|\tau|$  larger than the tension  $\sigma$ ; conversely, if  $E_0 < 0$ , the domain wall moves to the right

( $x > 0$ ) with a tension  $\tau$  larger than the compression  $|\sigma|$ . Since a compression induces a *planar anisotropy* from the magnetic point of view (perpendicularly to its direction) and a traction induces an *axial anisotropy* for the magnetization (along its direction), the motions to the left and to the right are not dynamically equivalent. A stronger planar anisotropy facilitates the excursion of magnetization out of the  $xy$ -plane.

### 3.3.2 Trajectory of domain walls

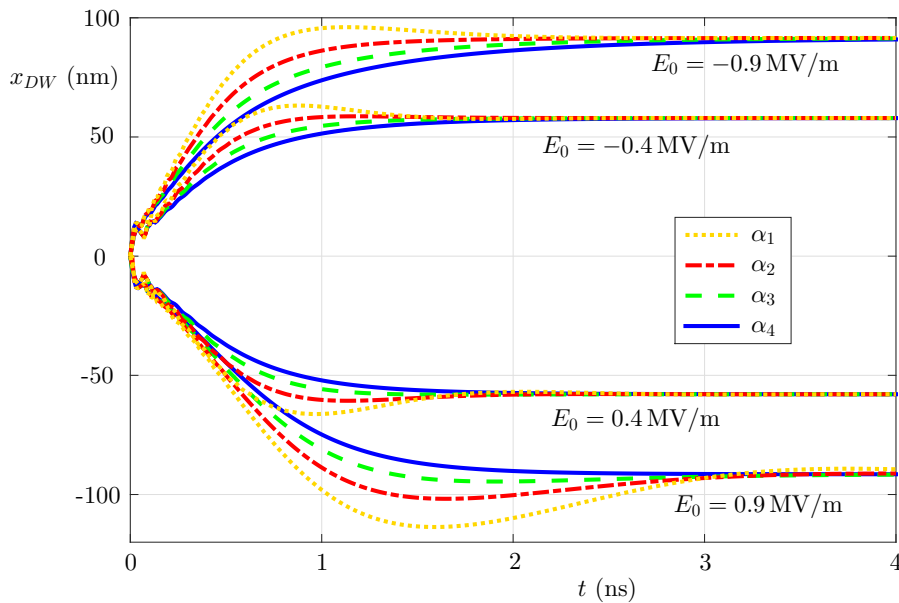


Figure 3.5 – The trajectory of the domain wall for several values of applied electric fields and Gilbert damping is plotted. The equilibrium position depends on  $E_0$  but not on  $\alpha$ . However, the dynamics is influenced by both. In these simulations and throughout this work, the values of damping coefficient are as follows:  $\alpha_1 = 0.06$ ,  $\alpha_2 = 0.08$ ,  $\alpha_3 = 0.10$  and  $\alpha_4 = 0.12$ .

As stated in subsection 3.3.1, the equilibrium distribution coincides with that of the relaxation code for the same set of inputs. What is new here though is the description of the real time-resolved evolution of the magnetization distribution toward this equilibrium.

The general procedure chosen to study the dynamics was as follows. First, the initial distribution for  $\Phi$  is taken from the relaxation code with  $E_0 = 0$ .  $\Theta$  is taken uniform and equal to  $\frac{\pi}{2}$ . Then, the dynamics are computed from this state following the instantaneous application of an electric field of finite value, and the position of the domain wall is considered to coincide with the location where  $\Phi'$  is maximum.

As shown in Fig. 3.5, what is observed after a short period of time due to precession is the motion of the domain wall toward its equilibrium position. The equilibrium position of the domain wall depends on the amplitude of the applied electric field and the relationship is antisymmetrical as already shown in chapter 2 (meaning  $x_{DW}^{\infty}(-E_0) = -x_{DW}^{\infty}(E_0)$ ). As an aside, it does not depend on  $\alpha$ , and this was expected since this coefficient is only involved in the dynamics (for instance, it does not appear in Eq. (2.40)). However, the dynamics are affected by both the electric field and the strength of the damping. The influence of  $\alpha$  is indeed quite clear. For instance at low damping coefficients, there is a tendency to "overshoot" before the domain wall reaches its final position with increasing electric fields. A large coefficient is associated with larger damping, and therefore less precession. Roughly speaking, it means that the magnetic system is more "rigid" and will exhibit only moderate oscillations. On the contrary, a weak damping will result in more dramatic variations of magnetization in time and, potentially, a longer time to reach equilibrium when the electric field is suddenly applied. This is clearly the case here with larger overshoots observed when the damping is weak. Also, the difference between the dynamics induced by a positive and negative electric field is clearly visible. The question of the origin of this difference has already been addressed in subsection 3.3.1 and will be explored further in subsection 3.3.3.

### 3.3.3 Velocity and applied electric field

When dealing with the dynamics of domain wall motion, it is only fair to mention domain wall velocity. Since the velocity is not constant in this system (see trajectory in Fig. 3.5), we chose to define the quantity  $\langle v_{DW} \rangle$  as the average velocity over the path from the origin to the position  $\frac{2}{3}x_{DW}^{\infty}$ . It is plotted against  $E_0$  in Fig. 3.6 for several damping coefficients. Here, a lower damping is associated with larger velocities. In the four curves, when the electric field is increased from 0, the value of  $|\langle v_{DW} \rangle|$  is increased. This increase is quite linear at the beginning, until the velocity reaches a maximum. Then, while for  $E_0 < 0$  a slight rate of decrease is observed, for  $E_0 > 0$  the minimum of  $\langle v_{DW} \rangle$  is immediately followed by a strong velocity reduction. Also, the maximum velocity is reached at lower electric fields for  $E_0 > 0$  compared to  $E_0 < 0$ . These remarks are additional signs of the asymmetry of the system regarding the electric field.

An explanation of the observed asymmetry based on the relative influence of compression and tension was put forward in subsection 3.3.1. When the compression is larger than the tension ( $E_0 > 0$ ), the prevailing planar anisotropy induces out-of-plane excursions with considerable deviation of  $\Theta$  from  $\pi/2$ , and domain wall propagation is sensibly

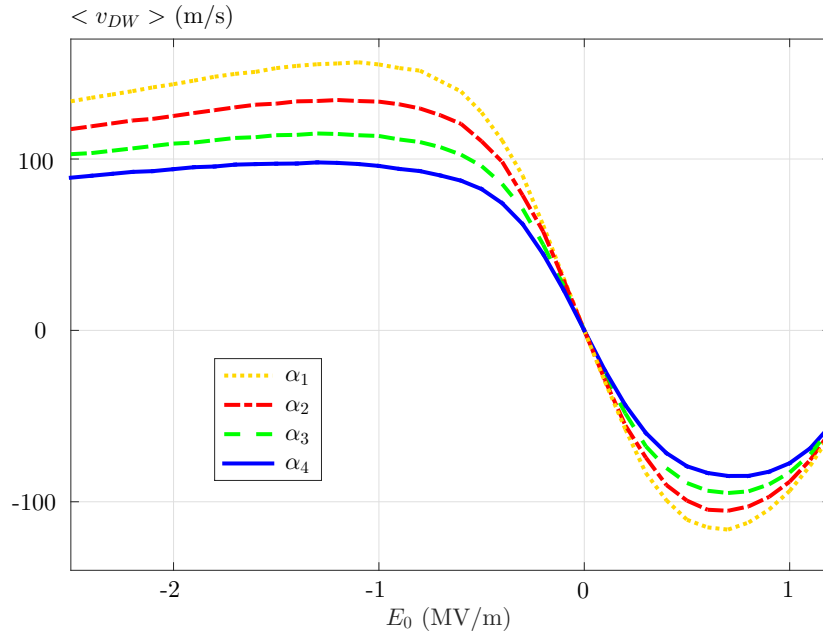


Figure 3.6 – Velocity is plotted against  $E_0$  for the same four values of  $\alpha$  as in Fig. 3.5.

hindered. On the other hand, when the tension is larger than the compression ( $E_0 < 0$ ), the out-of-plane excursions are comparatively reduced, and domain wall motion is facilitated. In order to test this hypothesis further, an investigation was carried out with different piezoelectric parameters. The original coefficients were  $d_{31} = -1900$  pC/N and  $d_{32} = 600$  pC/N, corresponding to (011)-cut PMN-PT ceramic substrate [278]. Four additional sets of inputs were chosen, keeping the sum  $|d_{31}| + |d_{32}|$  constant: one completely asymmetrical case with  $d_{31} = -2000$  pC/N and  $d_{32} = 500$  (such that  $\sigma = 0$ ), one completely symmetrical case with  $d_{31} = -d_{32} = -1250$  pC/N (such that  $\sigma = -\tau$ ), as well as two intermediate configurations. Results are shown in Fig. 3.7. One important fact is that all curves coincide in the linear portion (for low values of  $E_0$ ). Then, it is clear that the larger the gap between the amplitude of the stress components, the larger the asymmetry in the dynamics for large values of  $E_0$ . In particular, total symmetry is obtained when  $|d_{32}| = |d_{31}|$ . It is also apparent that the PMN-PT substrate is close to the fully asymmetrical piezoelectric material, so that in fact  $|\tau|$  is always much larger than  $|\sigma|$ .

In the end, these results lend more support to the interpretation based on the relative importance of mechanical compression and tension in the dynamics.

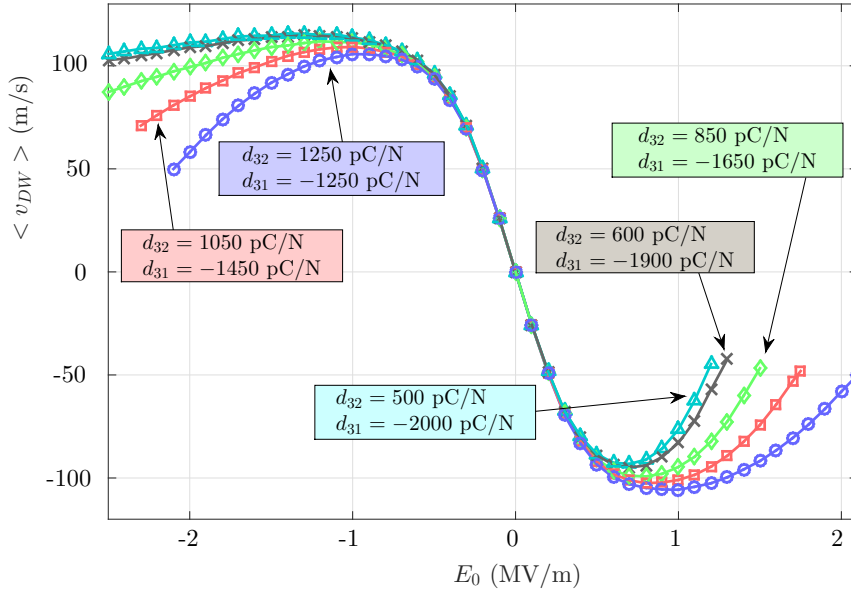


Figure 3.7 – Velocity as a function of the electric field for different values of the piezoelectric coefficients  $d_{31}$  and  $d_{32}$ . This enables to explore the various degrees of symmetry in the dynamics induced by the relative influence of compressive and tensile stress components.

### 3.4 Dynamics in an infinite nanostripe

In the previous section we explored the dynamics in a geometry with variable width. Another interesting case from a fundamental point of view is the film with uniform width. Indeed, if the effects of variable section are removed, one can focus on the specific features of stress-induced domain wall motion. This is especially the case in a nanostripe geometry, which is characterized by high aspect-ratios and thus vanishing edge effects. This section presents the way we simulated the evolution of a domain wall in infinite nanostripes. In these conditions, the study of steady-states is conceivable and is of great interest. In particular, the relationship between domain wall velocity and applied electric and magnetic field is a matter that demands investigation. A discussion on the instances where the code crashes closes the section.

#### 3.4.1 Simulating infinite nanostripes

The study of an infinitely long nanostripe with a constant width—as in Fig. 3.8—is interesting from the physical point of view. Considering such a geometry in Eq. (3.16) can be done by simplifying demagnetization (to model an infinitely long ellipsoid of compa-

rable dimensions) and removing terms related to the variable width. This was already done in subsection 3.2.2. Unfortunately, even then the equation obtained is still such that no analytical investigation seems possible. Again, one must rely only on numerical treatment.

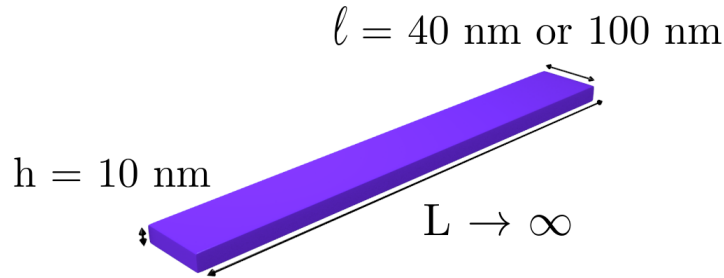


Figure 3.8 – Schematic of the constant section geometry considered in the dynamical study.

Obviously, the numerical approach entails the use of finite geometries. However, we can devise a way to simulate an infinite nanostripe with the existing code. If we consider a real system with infinite length, it is safe to assume that, far from the domain wall, magnetization will be fixed and equal to the stable magnetization states (including the influence of demagnetization). Therefore we can focus on computing the evolution of magnetization in a region around the domain wall, and consider the contribution to the demagnetizing field of two large parallelepipeds beyond  $\pm \frac{L}{2}$ . In practice, this was done by simulating the demagnetizing field generated by two regions of 1 mm length on each side in the calculation of the demagnetization factors.

Having done this, it is suitable to adapt the boundary conditions  $\Phi_1$  and  $\Phi_2$  which, until now, were calculated only by taking into account anisotropy, external magnetic field and applied stress. The goal is to find boundary conditions that closely match the value of the clearly identified plateau regions. To compute the stable states, we deal with a uniform magnetization and thus the simplified demagnetization  $\vec{H}_d = -\overline{\overline{N}}\vec{M}$  (as in subsection 3.2.2) is suitable. The appropriate terms are introduced in the calculation of the boundary conditions, giving a modified version of Eq. (2.42):

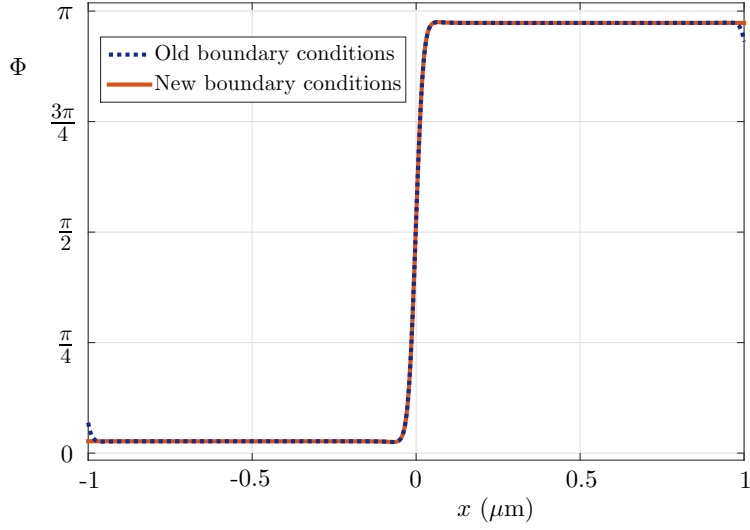


Figure 3.9 – Magnetization distribution exhibiting the difference between the boundary conditions with and without the simplified contribution of demagnetization. The width of the nanostripe is  $\ell(\pm L/2) = 40$  nm and the corresponding demagnetization tensor component is  $N_y = 0.225$ .

$$\begin{aligned} & \left( -\mu_0 M_s H_0 + \frac{3}{2} \lambda_s \sigma \right) + (4K_u + 2\mu_0 M_s^2 N_y) t - 9\lambda_s \sigma t^2 \\ & - (4K_u + 2\mu_0 M_s^2 N_y) t^3 + \left( \mu_0 M_s H_0 + \frac{3}{2} \lambda_s \sigma \right) t^4 = 0. \end{aligned} \quad (3.30)$$

For an infinite ellipsoid of semi-major axis length  $\ell_2$  and semi-minor axis  $h/2$ , the demagnetization factor  $N_y$  is equal to  $e/(e+1)$  where  $e = \ell/h$ . In practice, the value of  $N_y$  was determined by trial and error from the guess  $e/(e+1)$ , so that there is no visible difference between the boundary conditions and the value of the plateau regions. The difference between this adjusted boundary condition and the regular boundary condition excluding demagnetization is shown in Fig. 3.9, with the distribution of magnetization at rest ( $E_0 = 0$ ) as an example. More information on the influence of demagnetization on the boundary conditions can be found in subsection 2.2.4, in particular through Fig. 2.3. Importantly, since the  $N_y$  factor is purely geometrical, its value will be the same whatever the electric field or magnetic field applied to the system.

We should mention here that the number of points on the  $yz$ -plane used to compute the mean value of demagnetization at each point was the same for all geometries. As the width is changed between the three geometries, the precision is affected because the

resulting discretization is different. In principle, it may be a cause for concern as it is now clear that the demagnetization has a significant influence on the system. However we verified that the change in outcome was very limited: an overestimation of only a few percents on the value of the velocity is to be expected.

### 3.4.2 Steady-states in infinite nanostripes

The study of infinite nanostripes with constant width was carried out by first taking the domain wall shape associated with a moving domain wall from the relaxation code as the initial distribution. To do this, the relaxation code is run for a very short period of time so that the domain wall assumes its shape without travelling far from the center of the simulated ferromagnet. This distribution is used as the input of the dynamical code which will compute the dynamics from that initial state. Of course, the relaxation code only covers the distribution of  $\Phi$ , therefore the angle  $\Theta$  is initially set to the value  $\frac{\pi}{2}$  over the whole nanostripe.

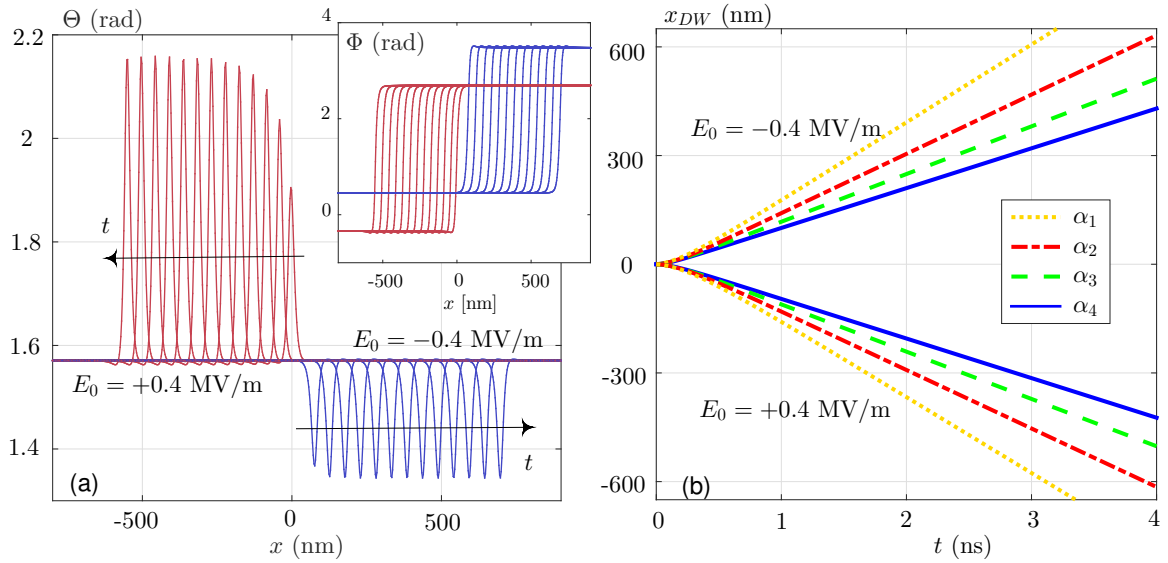


Figure 3.10 – Panel (a) features the distribution of angle  $\Phi$  as a function of time. One can clearly observe the onset of a steady-state. Panel (b) shows the trajectories of the domain wall for several electric fields  $E_0$  and Gilbert damping  $\alpha$ . The position of the domain wall tend to be linear as the steady-state is established. The applied field is still  $H_0 = 20 \times 10^3$  A/m.

Fig. 3.10 shows examples of the time evolution of magnetization from the initial state described above. One can see that  $\Theta$  has to assume a particular distribution with a

deviation from  $\frac{\pi}{2}$ , which is consistent with previous findings. Then, once magnetization has reached a given distribution, it appears that a steady-state is established. The motion is akin to the shift of a rigid domain wall structure. The presence of out-of-plane excursions is confirmed with these simulations, proving that they are a fundamental feature of the equations solved.

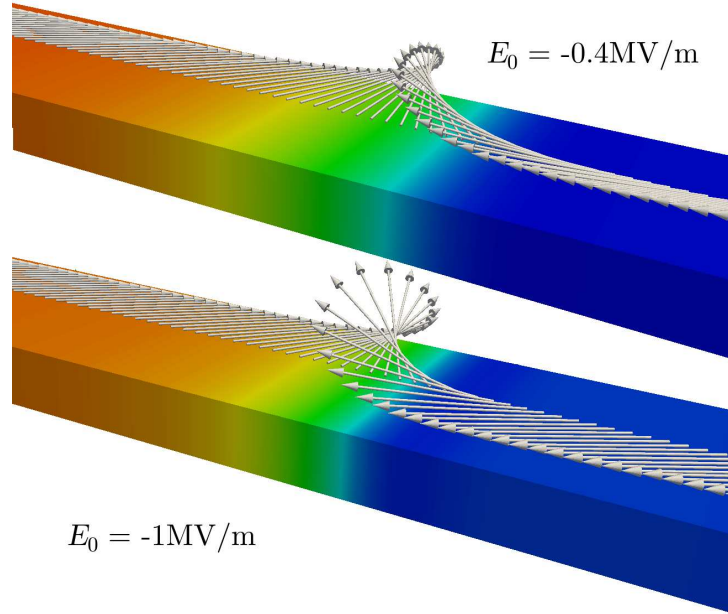


Figure 3.11 – Visualization of the steady-state shape of the travelling domain wall using the Paraview visualization software for two values of electric field  $E_0$ . The color corresponds to the value of  $w_x$ . The simulated ferromagnet has a 10 nm thickness and a 100 nm width.

Regarding the electric field, we can also confirm here that its influence on the shape of the domain wall is twofold: strength and sign of  $E_0$  play a major role in determining the steady-state shape adopted by the domain wall. When the amplitude of  $E_0$  is increased, the width of the domain wall decreases and the values of  $w_z$  is increased. This is illustrated on Fig. 3.11, which shows the magnetization distribution in the domain wall region using 3D vectors. One can see the peculiar shape of the domain wall with more clarity, as well as the effect of an increased amplitude of electric field on the out-of-plane excursion. The second important aspect of the electric field dependence of the domain wall is that a positive electric field is associated with more pronounced out-of-plane excursions. This is shown on Fig. 3.12 for an electric field of  $\pm 0.8 \text{ MV/m}$ . Here again we can confirm the observation made in subsection 3.3.1.

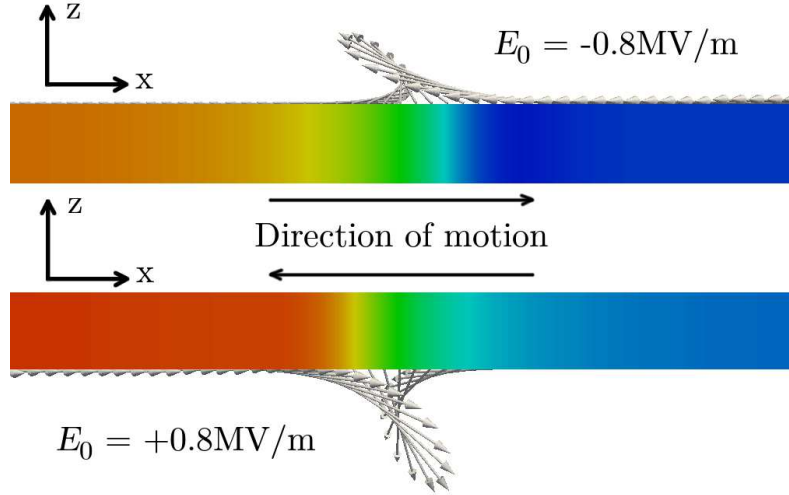


Figure 3.12 – Transverse view of the magnetization distribution for a positive and negative electric field. The difference in out-of-plane behavior is clearly visible.

Other parameters influencing domain wall shape include the Gilbert damping coefficient  $\alpha$  (the larger the damping, the smaller the deviation of  $\Theta$  from  $\frac{\pi}{2}$ ) and the external magnetic field (the larger the magnetic field, the larger the deviation). Of course, material parameters such as anisotropy must play a role too, but this was not investigated because the influence was either predictable or deemed of lesser interest.

### 3.4.3 Electric and magnetic field dependence of velocity

The existence of a steady-state in the dynamics means that for each couple  $(E_0, H_0)$ , there will be a corresponding domain wall shape but also a velocity associated with the motion. To numerically "measure" the velocity, we take advantage of the fact that the shape assumed by the domain wall is fixed when the steady-state is reached. Indeed, if we make the simple hypothesis that during the motion we have  $\Phi(x, t) = \tilde{\Phi}(\xi)$ , with  $\xi = x - v_{DW}t$  (introducing  $v_{DW}$  the velocity of the domain wall), we can then write:

$$\begin{aligned}
\frac{\partial}{\partial t} \langle \Phi(x, t) \rangle_x &= \frac{1}{L} \frac{\partial}{\partial t} \int_{-\frac{L}{2}}^{+\frac{L}{2}} \Phi(x, t) dx = \frac{1}{L} \int_{-\frac{L}{2}}^{+\frac{L}{2}} \frac{\partial \tilde{\Phi}}{\partial t}(\xi) dx \\
&= \frac{1}{L} \int_{-\frac{L}{2}}^{+\frac{L}{2}} \frac{\partial \xi}{\partial t} \frac{d\tilde{\Phi}}{d\xi}(\xi) dx \\
&= -\frac{v_{DW}}{L} \int_{-\frac{L}{2}-vt}^{+\frac{L}{2}-vt} \frac{d\tilde{\Phi}}{d\xi}(\xi) d\xi \\
\frac{\partial}{\partial t} \langle \Phi(x, t) \rangle_x &= \frac{v_{DW}}{L} \underbrace{\left( \tilde{\Phi} \left( -\frac{L}{2} - v_{DW}t \right) - \tilde{\Phi} \left( +\frac{L}{2} - v_{DW}t \right) \right)}_{\approx \Phi_1 - \Phi_2}
\end{aligned} \tag{3.31}$$

As a result, a precise estimate of the velocity can be determined numerically by simply calculating the average value of  $\Phi$  as the simulation is running and taking its variation in time:

$$v_{DW} = \frac{L}{(\Phi_1 - \Phi_2)} \frac{\partial}{\partial t} \langle \Phi(x, t) \rangle_x. \tag{3.32}$$

In order to let the steady-state develop, the simulation is stopped only when the domain wall has reached a point close to the edge of the simulated nanostripe. Then the velocity at the end of the trajectory is computed using Eq. (3.32).

The dependence of the velocity with the electric field happens to be very similar to what is obtained with the variable width in Fig. 3.6, although all values are higher since the steady-state regime has time to fully develop. What can be explored further here is the influence of the magnetic field. It has been shown in Fig. 2.14 that the energy gap between the two stable states of magnetization is dominated by the Zeeman energy, hence it is reasonable to think that modifying the magnetic bias will necessarily influence the dynamics. Fig. 3.13 shows the velocity as a function of the magnetic field, for several values of electric fields. The relationship is not simple, as we can see. While there is a general upward trend, the concavity is highly dependant on the damping coefficient and the electric field. Also, depending on the magnetic field, it appears that a lower damping is not systematically associated with higher velocities, especially at high magnetic fields.

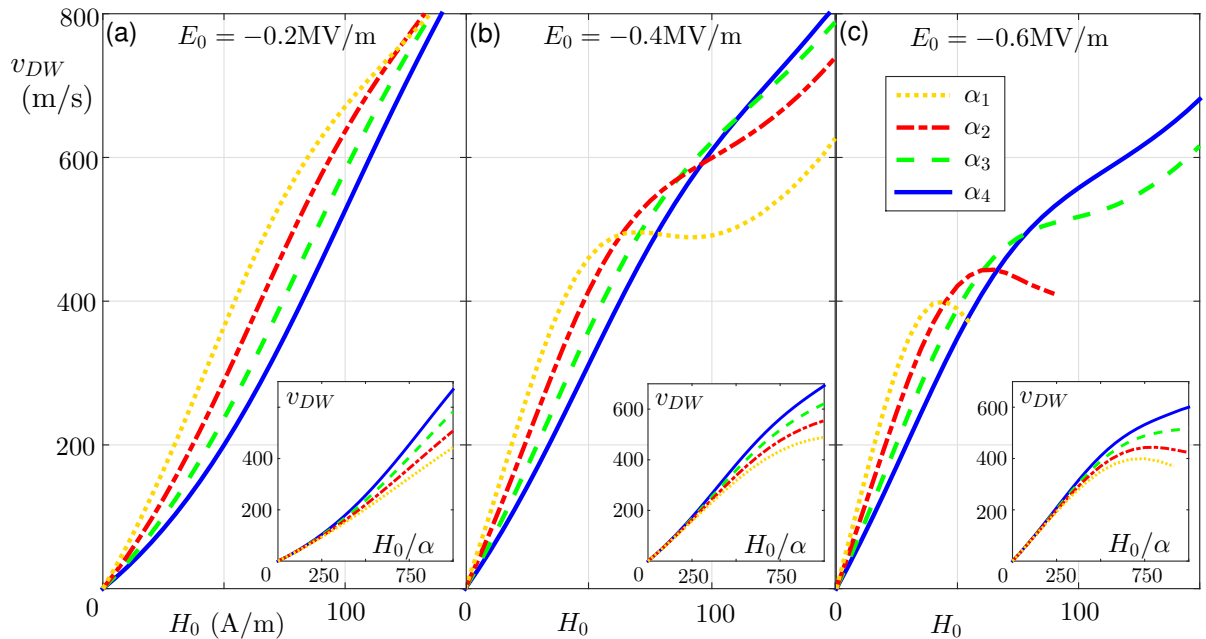


Figure 3.13 – Dependence of the velocity of the domain wall on the magnetic field, for several electric fields and damping coefficients. Insets represent the rescaling of the  $x$ -axis, showing a universal response at low fields. The width of the nanostripe is 40 nm.

We can conclude that the mechanically induced steady-state regime yields propagation velocities larger than 500 m/s, which are comparable to those obtained by current-driven domain wall motion [128, 129]. In the classical field-induced Walker propagation the dependence of the domain wall velocity on  $H_0$  and  $\alpha$  is mediated by the single variable  $H_0/\alpha$  (see Eq. (1.9)). Hence, we plot  $v_{DW}$  versus the ratio  $H_0/\alpha$  in the insets of Fig. 3.13. We observe that the curves corresponding to different  $\alpha$  collapse to a single universal response in the linear region. We also note that  $\partial v_{DW}/\partial \rho$  (for low values of  $\rho = H_0/\alpha$ ) is an increasing function of  $E_0$ , which is not surprising. However, for higher values of the magnetic field,  $v_{DW}$  depends on both  $H_0/\alpha$  and  $\alpha$  and the curves do not coincide, proving once again the essential difference between the mechanically-induced and the field-induced domain wall dynamics.

To get a more systematic view of the combined influence of the magnetic and electric fields on the velocity of the domain wall, a 2D scan was performed on a  $(H_0, E_0)$  grid, for all four damping coefficients  $\alpha_i$ . In order to remove the necessity to compute the dynamics for positive and negative values of  $E_0$ , a symmetric piezoelectric substrate was simulated ( $d_{31} = -d_{32}$  so that  $\sigma = -\tau$ ). Results for a large damping are shown in Fig. 3.14, where the velocity is plotted as a surface over the  $(H_0, E_0)$  grid. Results for a width of 40 nm

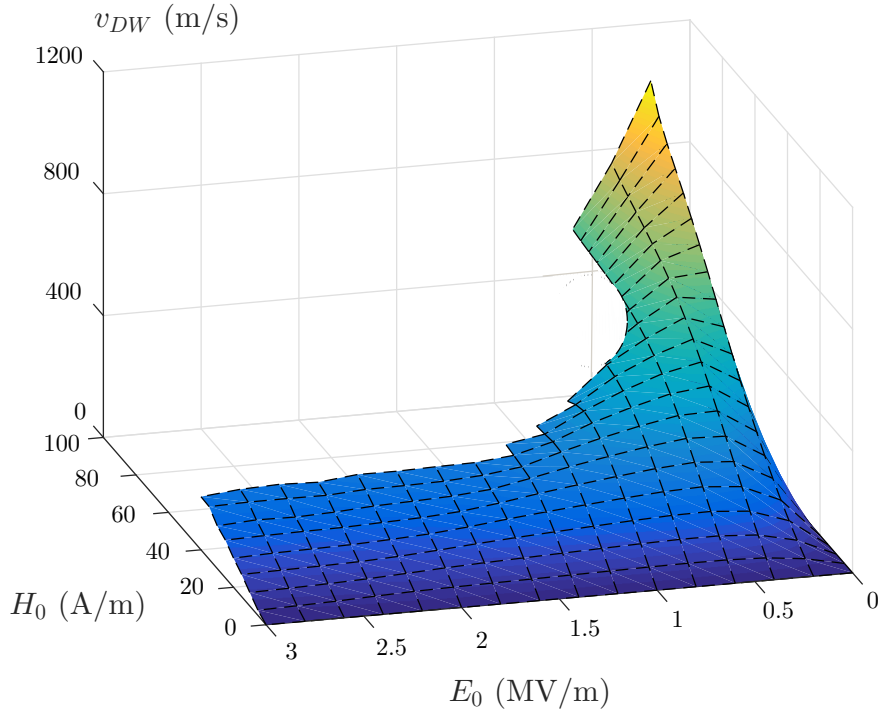


Figure 3.14 – 3D representation of the velocity of the domain walls as a function of the magnetic and electric fields for  $\alpha = \alpha_4 = 0.12$ . The width of the nanostripe is 100 nm.

are very similar qualitatively, although the values of velocity obtained are significantly smaller. At low magnetic fields, the variation of the electric field has a minimal influence on the velocity. At higher fields, the gradients are much higher. We can confirm here that the value of the magnetic field has a huge impact on the velocity reached by the domain wall. This observation—combined with the remark that the energy density gap between the two domains is equal to the Zeeman gap—really vindicates the view that the motion of the domain wall is *stress-triggered* and *field-driven*.

The fact that the surface does not cover the whole grid is due to the failure of the code in some instances (depending on the values of the fields used as inputs). It is also the reason why some of the curves in previous figures stopped at some point. This phenomenon is discussed in the following subsection.

### 3.4.4 Code failure and breakdown phenomenon

In some instances, the dynamical code fails to describe the steady-state corresponding to the inputs given. These crashes also happen with the variable width, as the code fails

to describe the motion of the domain wall toward its equilibrium position. No solution could be found to prevent this from happening (fourfold increase of spatial discretization, as well as the reduction of time step  $\Delta t$  have been tried). Fig. 3.15 shows the area where the code runs normally (colored regions) and the limits after which there is a crash. The different colors refer to the different damping coefficients.

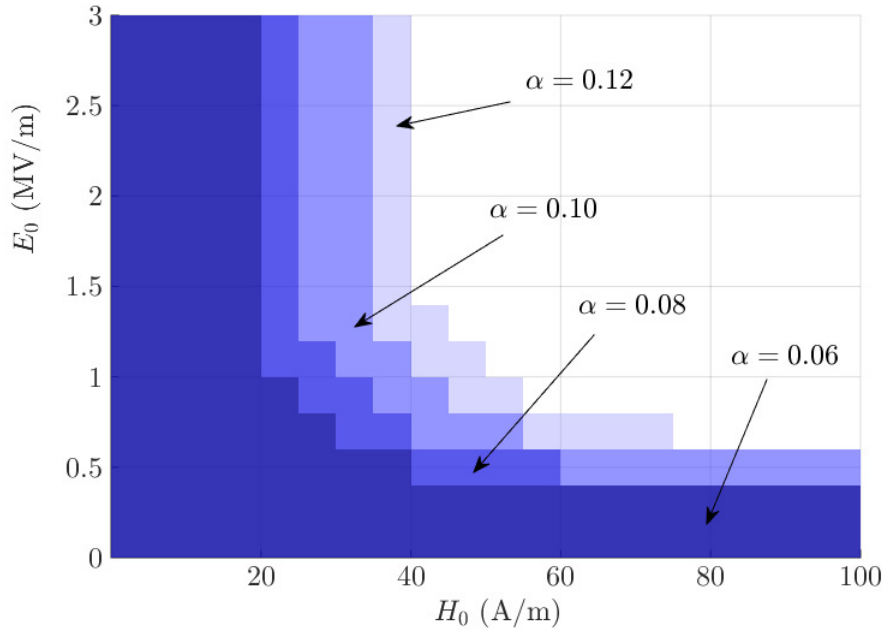


Figure 3.15 – Colored areas correspond to instances where the code successfully describes the steady-state associated with the corresponding inputs. The surfaces for the four values of  $\alpha$  are superimposed.

We already encountered limitations of the numerical procedure in classical field-driven motion (see subsection 3.2.2), where the code was unable to carry out the simulation for a longitudinal magnetic field  $H_1$  larger than the Walker breakdown field. The similarity in the symptoms are intriguing. Although it would still be speculation to say that this numerical phenomenon is an actual sign of a real physical breakdown in the system studied, we have to acknowledge the hypothesis is quite probable. For a start, it bears many of its apparent features. The errors that accumulate and eventually lead to the failure are reminiscent of what is observed beyond the Walker field in the context of regular field-driven motion. Also, there are small signs of oscillatory behavior which could be associated with the onset of a new regime of motion. The fact that the failure happens at lower fields when the damping is weak is also quite telling. As an aside, the numerical

failure happens irrespectively of the actual value of the velocity, and so it is not due to large rate of magnetization variation. Besides, we can argue on physical grounds that the existence of a phenomenon similar to the classical Walker breakdown should be expected here. In chapter 1, we saw that the breakdown was quite universal, since it is present in both field- and current-driven motion. Here, we deal with a motion that is essentially field-driven, this implies that the existence of a sudden transition in the dynamical behavior is plausible.

In any case, in the absence of analytical results, more in-depth analysis of the observed phenomenon is needed in order to rule out the hypothesis of a numerical artefact.

### 3.5 Conclusion

In this chapter, we numerically studied the motion of domain walls subjected to the combination of a bias magnetic field and an applied stress in magnetoelastic nanostructures. We devised a 1D model combining the effective field derived from variational methods with the Landau-Lifshitz-Gilbert equation. The outcome was implemented numerically using an implicit scheme based on Newton's method. Through the example of the parabolic geometry, we explored how the tailoring of the variable width allows one to precisely design static and dynamic features. The study of steady-state regimes in nanostripes of constant width confirmed that even though it is ultimately driven by a magnetic field, the resulting moving magnetic structure is fundamentally different from usual domain walls in nanostripes. In particular, the motion is characterized by specific out-of-plane phenomena which do not exist in field-driven domain wall motion. The influence of several parameters on the extent of these out-of-plane excursions has been reviewed. Besides, this new type of domain wall motion is associated with competitive velocities (hundreds of m/s). The numerical study, as well as physical considerations also brought several hints that a phenomenon akin to a Walker breakdown may be involved in the dynamics, although more research is needed to settle this question.

Many lines of investigation remain open in the study of such a system. For instance, it is possible to look at dynamical input fields (variable  $E_0(t)$  or  $H_0(t)$  signals). Also, new types of geometries can be considered, such as elements with two minima or more, exhibiting hysteretic behavior. Domain wall pinning as well as edge roughness or patterning may also influence the dynamics of this system as it is the case for standard field- or current-driven domain wall motion.

# Chapter 4

## Experimental investigations

After having established a strong theoretical and numerical basis to stress-triggered domain wall motion, it is worth investigating this phenomenon experimentally. This chapter includes a description of the different materials considered for the magnetoelastic and piezoelectric phases. It also gives an account of the preparation in the clean room of thin films made of magnetoelastic materials with appropriate size and geometry, as well as the preparation of suitable piezoelectric substrates. Finally, the techniques used to characterize both phases, the corresponding results and some of the prospects are discussed.

### 4.1 Materials

This section covers the characteristics of the materials chosen in the implementation of the magnetoelectric coupling involved in the physical phenomenon investigated. On one hand, terbium-based alloys are arranged in multilayers to constitute the magnetoelastic phase. On the other hand, commercial PMN-PT substrates with a specific growth orientation constitutes the piezoelectric phase.

#### 4.1.1 Magnetoelastic multilayers

The AIMAN-FILMS group at IEMN has extensive experience with the use of rare-earth-based magnetoelastic materials. In particular,  $\text{TbFe}_x$  (Terfenol) and  $\text{TbCo}_x$  alloys ( $x \approx 2$ ) are routinely used and exhibit strong magnetoelastic properties (positive magnetostriction). They are usually made by sputtering. However, because of the presence of terbium, the anisotropy in the resulting layer is often very large [281], hindering the manipulation of magnetization. Besides, in the case of  $\text{TbCo}_2$ , the value of the saturation is quite weak because of the ferrimagnetic order. To reduce the anisotropy and guarantee a substantial magnetization at saturation, these alloys are accompanied by

layers of ferromagnetic alloys based on metals such as Fe and Co in multilayered structures (see Fig. 4.1). Individual deposited layers are very thin (typically less than 10 nm). The magnetic coupling of such structures can be studied, with key insights that, for instance, led to the design of exchange-spring magnets [282]. The magnetic behavior can be complicated (with different layers switching at different applied fields). In previous chapters, we assumed that they behaved like a single equivalent homogeneous material, which is likely to be the case with very thin and thus strongly coupled layers. Such a mixing allows a satisfying compromise between anisotropy, magnetization at saturation and magnetostriction, to ensure facilitated manipulation and interesting performances.

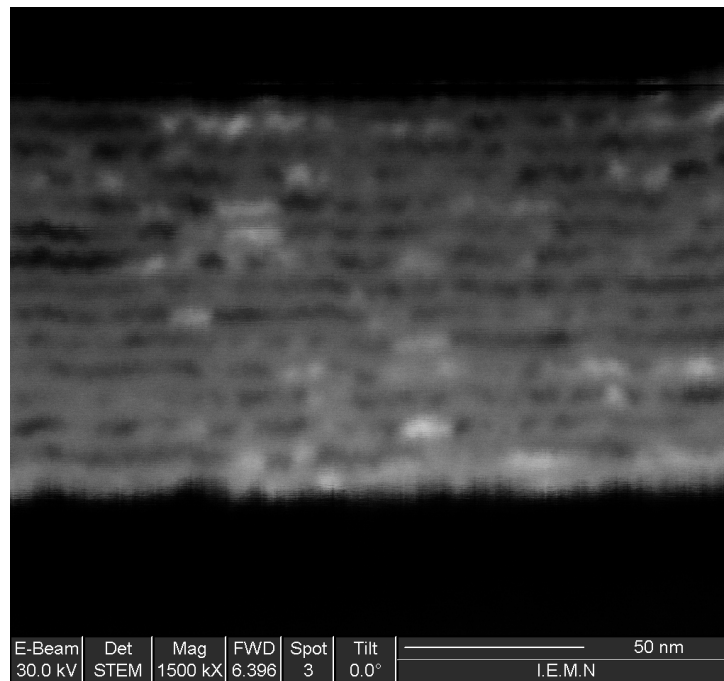


Figure 4.1 – Transmission Electron Microscope image showing a 110 nm-thick deposition of multilayers obtained at IEMN.

One of the interesting features of this multilayered material is the possibility to control the direction and—to some extent—the strength of the anisotropy [283]. In any case, the layers obtained by sputtering are typically amorphous. This is associated with a reduced anisotropy, already smaller in thin films than in bulk materials, which is helpful in our case. Despite the amorphous structure and the thin film geometry, significant magnetostriction is achieved.

### 4.1.2 PMN-PT piezoelectric substrate

Piezoelectric materials have found multiple applications, for instance in sensing and actuation. This led to significant advances in the preparation of highly efficient piezoelectric materials. In particular, perovskite ceramics such as lead zirconate titanate (PZT) have drawn tremendous interest. In our case, we need to find a piezoelectric substrate generating strong in-plane strains. For them to induce a magnetoelastic anisotropy in the ferromagnetic material, the two in-plane directions should not be characterized by equal strains (see Eq. (2.52)). In other words, the in-plane piezoelectric response should be anisotropic.

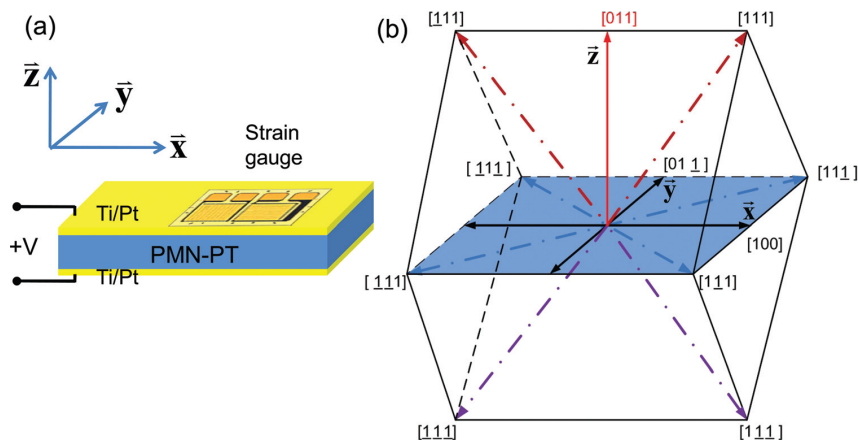


Figure 4.2 – (a) Axes and sample configuration showing the direction of the electric field (between Ti/Pt electrodes) and the plane in which the relevant strains appear. (b) Representation of a rhombohedral unit cell which appears to be present in PMN-PT, along with the different directions (the  $z$ -axis corresponds to the (011) direction of growth that is of interest here). Possible polarization directions are along the red and blue dot-dashed arrows. Figure from [284].

Very good candidates from this perspective are relaxor single crystals of (011)-cut  $[\text{Pb}(\text{Mg}_{\text{frac}13}\text{Nb}_{\frac{2}{3}})\text{O}_3]_{(1-x)}\text{-}[\text{PbTiO}_3]_x$  (orientation shown in Fig. 4.2). Their properties are especially impressive near the Morphotropic Phase Boundary (MPB), that is with the value of  $x$  in a given range ( $0.3 < x < 0.4$ ). PMN-PT single crystals of varying compositions, growing methods (flux-grown or melt-grown) and orientations have been investigated for a wide range of excitation frequencies [285–289]. Also, the properties of single [290] and multidomain [291] PMN-PT have been studied and compared. The very strong piezoelectric properties exhibited by PMN-PT are best understood as a consequence of the morphotropic phase boundary (MPB) which happens for given compositions of the solid

solution. The origin of this phenomenon is the subject of more general investigations [292]. In particular, it seems that around the MPB, different phases can simultaneously be present, namely rhombohedral, monoclinic, orthorhombic, tetragonal phases [284]. A fairly comprehensive set of measurements was carried out [278] and shows the promising potential of (011)-cut PMN-PT in the context of the magnetoelectric coupling sought here. Indeed, the piezoelectric coefficients  $d_{32}$  and  $d_{31}$  are of opposite signs and therefore a substrate can generate simultaneous compressive and tensile stress components along orthogonal directions. In addition, its hysteretic behavior is such that it is possible to benefit from two distinct permanent strain states. This point is addressed in greater detail in subsection 4.3.1.

One should mention that while commercial bulk PMN-PT is readily available in the form of single-crystal substrates, research has also shown the possibility to manufacture PMN-PT thin films [293–296].

### 4.1.3 Mechanical coupling

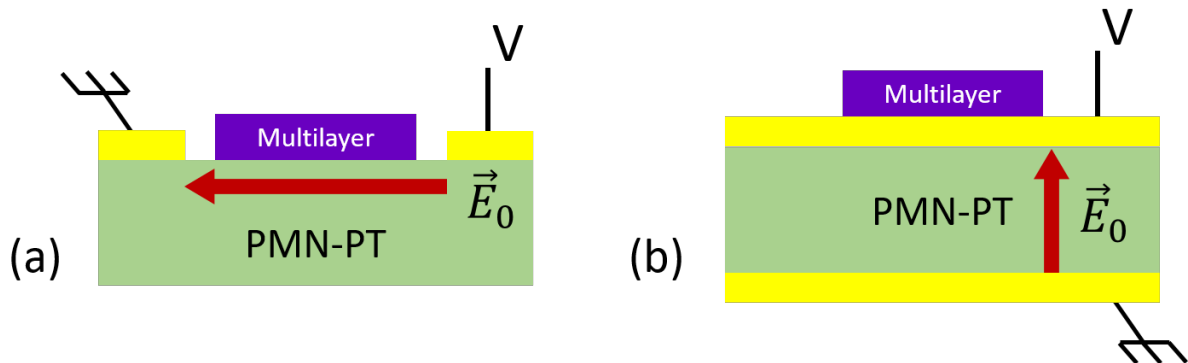


Figure 4.3 – Two different strategies—(a) longitudinal and (b) transversal—for the location of electrodes creating the electric field within the piezoelectric substrate.

As shown in previous chapters, the magnetoelastic and piezoelectric phases have to be coupled mechanically. While a magnetoelastic particle embedded in a piezoelectric matrix likely represents the most efficient mechanical coupling, its technological implementation is not straightforward. A more feasible alternative is to deposit the magnetoelastic layer on the piezoelectric material. As for the positions of the electrodes actuating the piezoelectric substrate, there are two obvious possibilities. The first solution is to place the electrodes next to the magnetoelastic element, so that the electric field is in-plane (see image (a) of

Fig. 4.3). In the context of bulk substrates, the main advantage of such an arrangement is the proximity of the two electrodes, meaning weaker voltages are needed to induce the desired electric field within the piezoelectric material. Although this option is sometimes considered, there is a major issue with regard to the path of the electric field. Since the multilayer in our case is metallic while the piezoelectric substrate is a dielectric, there is an incentive for the electric field to go through the ferromagnetic metal instead of the substrate beneath it. There is as a result a significant risk of having a weak strain. The other option is therefore to have electrodes on both sides of the piezoelectric substrate, creating an electric field along the vertical direction (see image (b) of Fig. 4.3) along the whole thickness of the substrate.

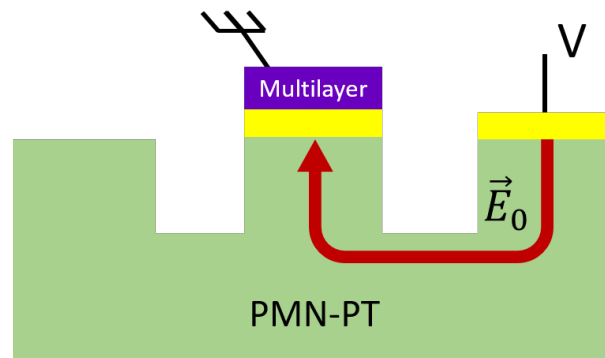


Figure 4.4 – Third option for the arrangement of the electrodes involving some structuring (etching) of the piezoelectric substrate.

Another issue relates to the possibility of the piezoelectric substrate to be free of actually generating the strain, especially in the context of strong piezoelectric response. If electric field lines are confined to a small portion of a piezoelectric material surrounded by the gist of the substrate where the electric field is zero, then there is a risk that it will prevent the creation of the expected strain. Worse, where strains are negative it can lead to fractures and mechanical damage of the material. A solution to this problem is to ease the portion of PMN-PT by engineering the surface of the substrate to create parallelepipedic studs (for instance with square cross section), as illustrated on Fig. 4.4. Note that this solution is also a good idea in the prospect of integration and low-power operation, as it considerably reduces the electrostatic energy  $CV^2$  that is proportional to the volume of dielectric involved.

This will be explored in subsection 4.4.3. In the following, we adopted solution (b) of Fig. 4.3, as concerns of integration and energy were secondary.

## 4.2 Fabrication

This section covers the process of fabrication, from the preparation of commercially-obtained piezoelectric substrates to the design and lithography, deposition and lift-off of magnetoelastic elements, including the relevant experimental parameters involved. All steps of the fabrication were performed within IEMN, and in particular using the clean room facilities.

### 4.2.1 Polishing of the PMN-PT substrate

Over the course of the PhD, we worked with two different sets of PMN-PT substrates.



Figure 4.5 – Individual PMN-PT substrates obtained from CTG Advanced materials, delivered with Au/Cr electrodes.

The first set of 20 PMN-PT substrates was obtained from CTG Advanced Materials, formerly known as H.C. Materials. Fig. 4.5 shows the substrates in their individual packaging. Each sample had a small red point intended as an indication of the direction of initial poling (through the thickness). The small dimensions (10x10x0.3 in millimeters) made their manipulation quite difficult and made them very fragile. Both faces of the samples were already covered with Au/Cr electrodes. However, the substrates were not polished and the surface roughness was very poor ( $R_a \approx 50$  nm). The image in Fig. 4.6 gives an idea of the initial surface quality. Given the layer thicknesses involved in future steps, it was obvious that some polishing process was necessary before proceeding any further.

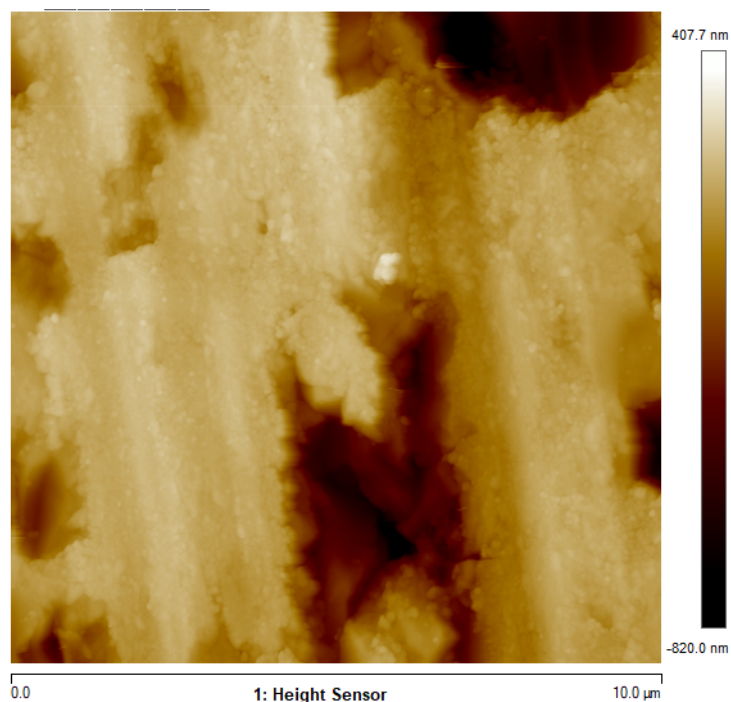


Figure 4.6 – Atomic Force Microscopy (AFM) image showing the poor surface quality of the samples. The linear pattern of irregular relief was visible at the naked eye.

Wet etching of the Au/Cr electrodes is quite straightforward and fortunately does not seem to etch or affect the ceramic. Also, a standard cleaning of 15 minutes at 70°C in EKC was done before any polishing. This step was routinely used at various points of the fabrication process. Again, the ceramic was seemingly unaffected by this strongly basic environment. Once both sides of the samples were free from metal, an effective polishing method was developed using the Logitech PM5 system at IEMN. The first step is to bond the sample to a 3 inch or 4 inch glass plate using a special paste and heat them in a dedicated Logitech machine during approximately one hour. Then, the glass plate is placed at the bottom of a cylindrical structure that can modulate the weight put on the sample. It is then put on a large rotating felt plate, with an additional sweeping achieved by a roller arm. In our case, the rotation speed is increased until the maximum value (70 rpm) for a total polishing time of 5 minutes. Throughout the process, small quantities of SF1 "slurry" are poured on the felt plate. Experiments with the Chemlox slurry were not conclusive, and the poor results obtained with water showed the important polishing role of the SF1 slurry. The results obtained after polishing are quite impressive, over a 10x10 μm window, a roughness of approximately 2 nm is ensured, with subnanometer roughness reached on smaller areas (see Fig. 4.8).

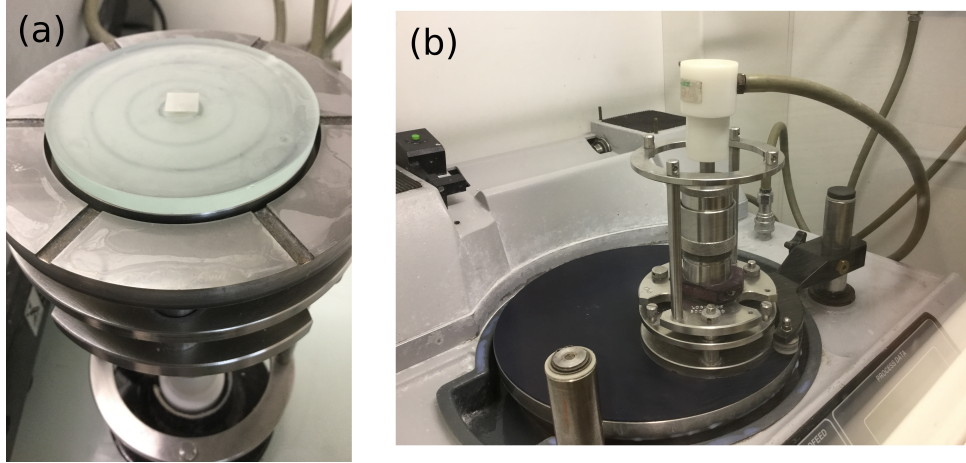


Figure 4.7 – Photographs of the equipment used to polish the PMN-PT substrates.

The second set of 10 substrates was obtained from another company called TRS Technologies, with 15x10x0.3 dimensions (mm). The slightly different color and transparency for the same thickness, as compared to CTG Materials samples hints at possible small differences in composition. These substrates are already polished by the manufacturer, and hence significantly more expensive. However, the surface quality was not as good as our home-polished samples to the point that we re-polished some of them.

With clean and polished substrates, new electrodes could be deposited on both sides of the samples. Because the goal is eventually to transmit the strain generated by the substrate to the magnetoelastic layer located above the electrode, it is important to have a thin electrode ( $\leq 100$  nm). Also, choosing stiff metals is important to ensure strong mechanical coupling (Young modulus between those of the ceramic and the multilayers), so we mainly considered Pt/Ti or Ru/Ti electrodes and avoided Au.

## 4.2.2 Lithography

The need to design magnetoelastic structures of variable size and geometry pointed at the use of lithography instead of focused ion-beam (FIB) techniques which are sometimes used to create nanostructure geometries. Another reason for not using FIB is that it is oftentimes difficult to control the depth of etching and the extent to which the integrity of local material is maintained. This is a problem since we deal with thin films and that electrode beneath the magnetoelastic material should not be damaged. The two alternatives were lift-off and dry-etching (or plasma etching), which were both explored. In any case it is necessary to use an electron-beam mask, given the lengthscales involved, as well as a

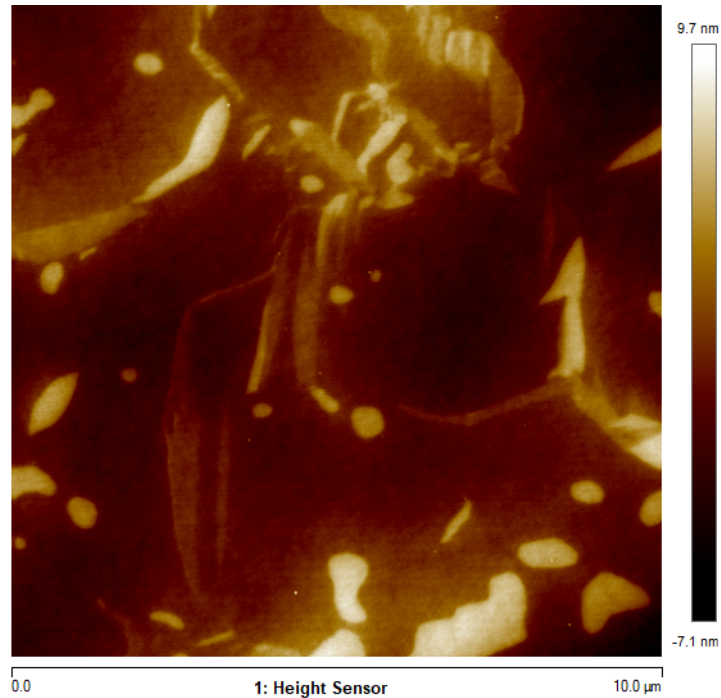


Figure 4.8 – AFM image of the polished surface. Attention should be brought to the range of the colorbar compared to Fig. 4.6.

positive resist. The lithography was initially tried on silicon wafers in order to find the appropriate parameters.

The LayoutEditor software was used to design electron beam mask files. Several versions were made and we will go on to briefly describe the shapes considered. First, ellipses were included, the goal being to look at the behavior of single-domain elements. Of course, the mask also contained elongated structures (rectangular or hourglass-shaped) corresponding to the geometries studied theoretically. Rings of constant and variable width (area between concentric or non-concentric circles), as well as long "pier"-like nanostripe and other shapes were drawn. Individual elements are placed sufficiently far from each other (several microns or tens of microns) to prevent magnetostatic interaction. The dimensions (length and width) of the nanostructures were variable, but in an effort to increase the likelihood of observing configuration with magnetic domains, all were significantly greater than what was simulated, from 200 nm to 2  $\mu\text{m}$  in width, and ten times these values in length.

By the end of the testing, the writing part of the fabrication was well mastered and yielded completely satisfying results. The different steps are listed below:

- Dehydration of the sample
- Spin-coating with closed lid (single layer) - Resist: PMMA 950K 4% and pre-bake
- Electron-beam lithography
- Post-exposure bake
- Development - Developer 1 MIBK and 2 ethanol

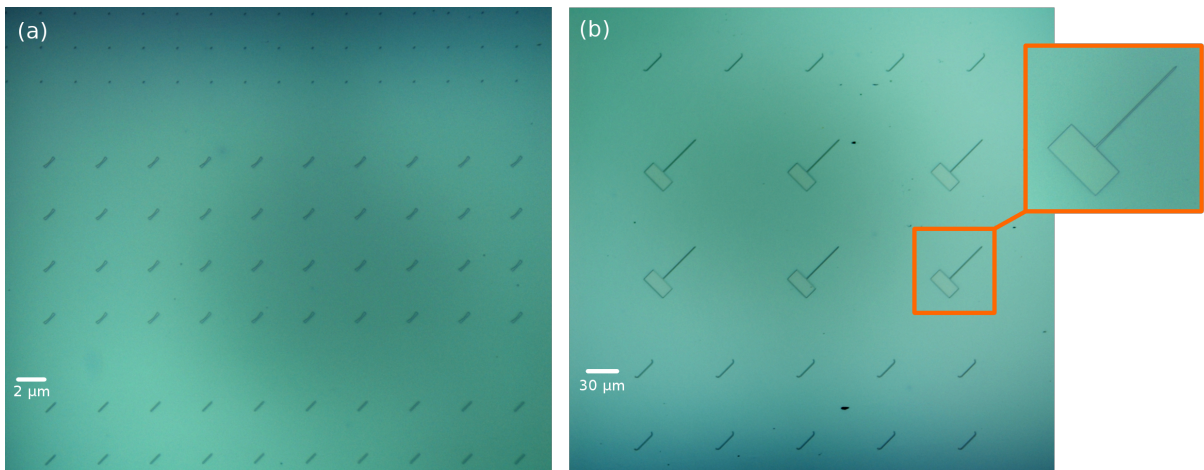


Figure 4.9 – Resist patterns observed at the optical microscope featuring (a) ellipses, hourglass-shaped and rectangular nanostructures, as well as (b) curves nanostructures and 'pier-like' structures (see inset).

Following these steps, the end result is of very high quality and reproduces accurately what is on the mask. Because of the obvious impact of electrons on the resist before development, we do not have SEM images showing the developed patterns. However, Fig. 4.9 shows screenshots taken from optical microscope observations.

### 4.2.3 Deposition of multilayers

The technique chosen to create multilayers of magnetoelastic materials is sputtering. It is widely used for the preparation of thin films as it provides nanometer precision on the obtained thickness. Sputtering refers to the process of ejection of atoms from a target using energetic gas ions (plasma), see Fig. 4.10. The plasma may or may not be chemically reactive. The plasma is created by applying a strong static or RF electric field that will ionize some of the gas particles. Using an oscillating field has the advantage of increasing the number of collisions between charged and neutral particles in the gas so that

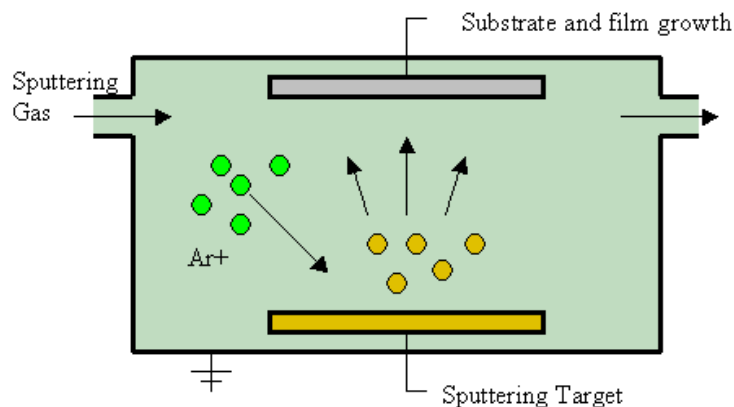


Figure 4.10 – Schematic view of sputter deposition. Public domain.

it increases the proportion of charged particles and therefore speeds up the deposition. Also, it reduces the accumulation of charges on the targets made of insulating materials. In the case of magnetron sputtering, magnetic fields are introduced to create helicoidal motion of charged particles around magnetic field lines at the Larmor frequency, thereby increasing the number of collisions. However, relying on magnetron sputtering may significantly decrease the lifespan of the target because of non-uniform wear on its surface due to the distribution of magnetic field lines.



Figure 4.11 – Photograph of the Leybold Z550.

At IEMN, different equipments exist for sputter deposition. The equipment used for the multilayers in our case is a Leybold Z550, with RF Argon plasma deposition (sputter

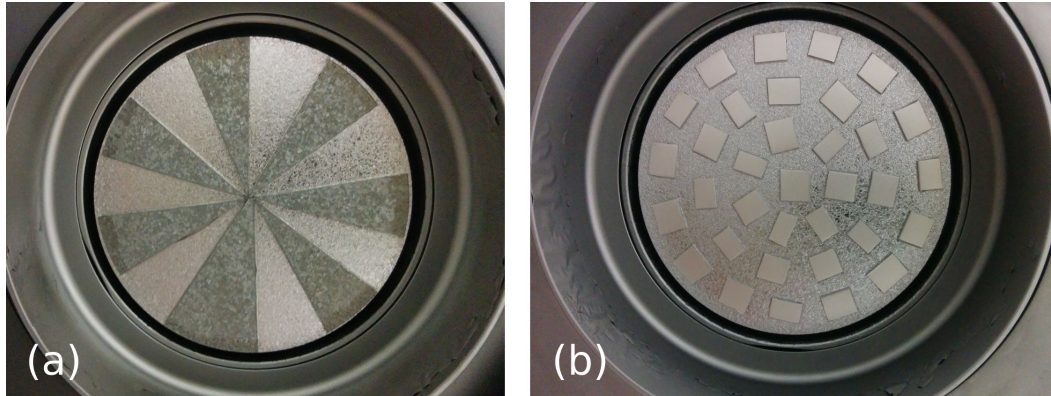


Figure 4.12 – 4 inch targets of (a) terbium and cobalt and (b) iron and cobalt used.

down) shown on Fig. 4.11. Several targets are included in the system, and each one that we used is composed of parts made of different metals (for instance pieces of Fe glued on a Co disk) in order to obtain the desired alloys (see Fig. 4.12). The compounds of different targets can be subsequently deposited on a substrate during a run, in a pattern of deposition programmed beforehand. The plasma is created near the targets which are fixed, whereas the plate on which the substrate is placed is mobile. 'Recipes' are prepared and consist of series of oscillations of the plate beneath the targets. Obviously, prior calibrations are required to know with satisfying precision how much is deposited in a given number of oscillations through the plasma.

For any deposition, fragments of silicon wafer are placed near the substrate for subsequent analyses (measurement of thickness actually deposited using a profilometer, characterization in Vibrating Sample Magnetometer and measurements of magnetostriction). These are visible in Fig. 4.13. During deposition, the establishment of an easy-axis is ensured by the presence of a static in-plane magnetic field created by macroscopic magnets placed around the substrate, also present on Fig. 4.13. The physical explanation of this phenomenon is still elusive to some extent. Due to the absence of airlock, a long period of time has to elapse before sufficient vacuum is achieved in the chamber. In order to improve the secondary vacuum, titanium is sputtered and liquid nitrogen is used in a cryogenic trap, as they respectively help reduce the amount of oxygen and water in the chamber. Also, an idle run on terbium-containing targets is necessary to remove the superficial oxidized material, as terbium is very much prone to oxidation.

During the PhD, we worked with 20 to 26 nm-thick multilayers of  $\text{TbCo}_2/\text{FeCo}$ . The layer put on top is always FeCo to limit oxidation, so that the structures were always

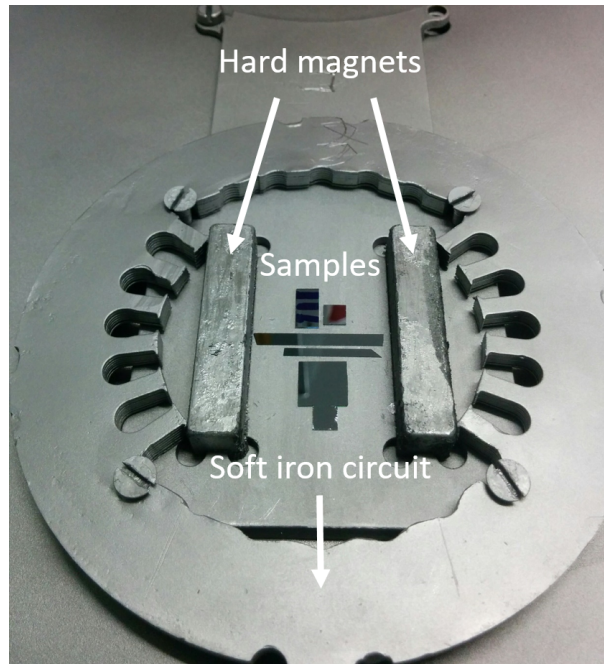


Figure 4.13 – Sample put in the chamber of the Leybold Z550 for sputter deposition.

constituted of 3 layers of  $\text{TbCo}_2$  and 4 layers of  $\text{FeCo}$ . The deposition process itself takes approximately ten to fifteen minutes overall.

#### 4.2.4 Lift-off and dry-etching methods

Having independently developed successful lithography and sputter deposition, it is worth pausing to reflect on the most convenient and efficient way to get the magnetoelastic patterns on the PMN-PT substrate. The two alternatives mentioned in 4.2.2 are lift-off and dry-etching. In the former case, the lithography is performed first on the substrate and the magnetoelastic alloy is sputtered on the resist. The lift-off consists in removing the resist and the multilayers on its surface so that only areas open during development remain covered with magnetoelastic material. In the latter case, the magnetoelastic material is sputtered directly on the substrate. Then, the lithography is performed on the multilayer and is followed by the deposition of a solid mask (usually metallic). This mask is removed by lift-off and the sample is subjected to dry-etching of the magnetoelastic material. The mask is subsequently removed and the expected patterns are apparent. Fig. 4.14 illustrates these two approaches step by step.

Since the lift-off solution is more straightforward and required less testing, it was tried first. The procedure described in the previous subsections was followed, although

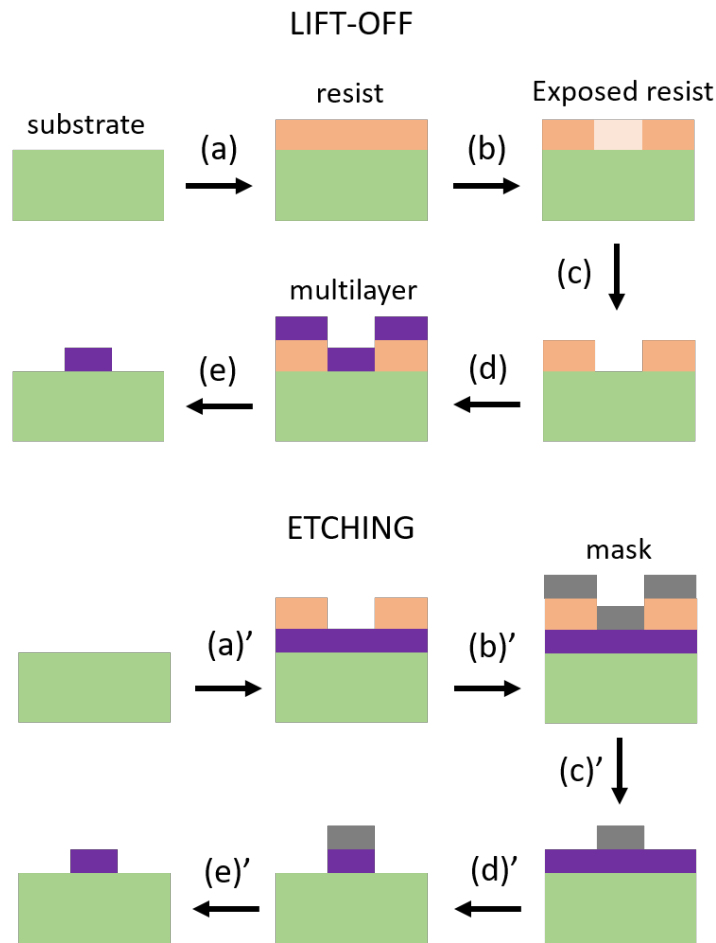


Figure 4.14 – Steps corresponding to the methods of lift-off and plasma etching. Step (a) is spin-coating, (b) is electron-beam exposure, (c) is development, (d) is sputter deposition and (e) is the lift-off of the multilayers *per se*. For etching, note that step (b)' corresponds to steps (a), (b) and (c) combined.

initially the spin-coating speed was lower, resulting in a 150 nm-thick coating. Lift-off was performed by placing the sample in SVC-14 solvent at 70°C for several hours. Smooth ultrasound treatment was also helpful, while stronger excitations proved harmful to the magnetoelastic structures (smaller elements are destroyed). A SEM image of a rectangular magnetoelastic element is shown on Fig. 4.15. While the shape is recognizable, the contour is far from smooth. In fact, the lighter contour hints at strong 'wall-like' bumps on the edges of every magnetoelastic element. The likely explanation for these irregularities is quite straightforward. Contrary to evaporation, the motion of the incoming particles in sputtering is isotropic: the direction of motion of ejected material is not directed at the substrate. Besides, the deposited thickness of resist is 150 nm, while only 20 nm

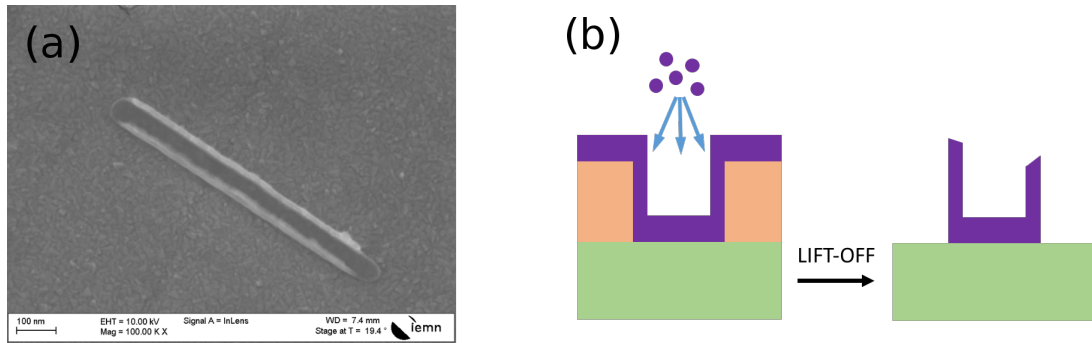


Figure 4.15 – (a) SEM image of a magnetoelastic element obtained by lift-off. (b) Interpretation of the presence of strong irregularities on the edges.

of magnetoelastic material is deposited. As a result, there is significant deposition of material on the vertical side of the resist, and these irregularities remain once the resist is removed (see Fig. 4.15).

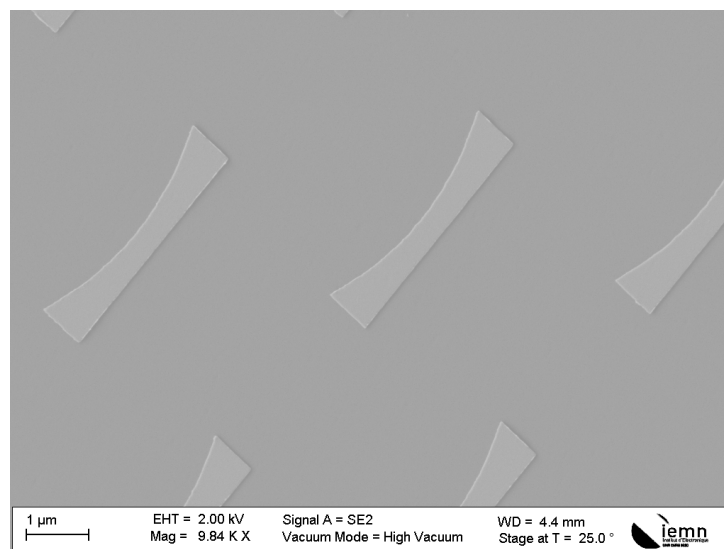


Figure 4.16 – SEM image of the magnetoelastic structures obtained by lift-off with updated parameters.

Several solutions to this problem may be put forward, the most obvious of which is to spin a thinner resist. This can be achieved by setting a higher rotation velocity. Reducing the thickness from 150 to 50 nm as well as other minor fine-tuning of the lift-off process helped significantly improve the results, as Fig. 4.16 shows. This was repeated several times, so that there is some confidence that the process developed is appropriate.

However, results proved less satisfying on PMN-PT, probably because of the sample size compared to larger fragments of wafers.

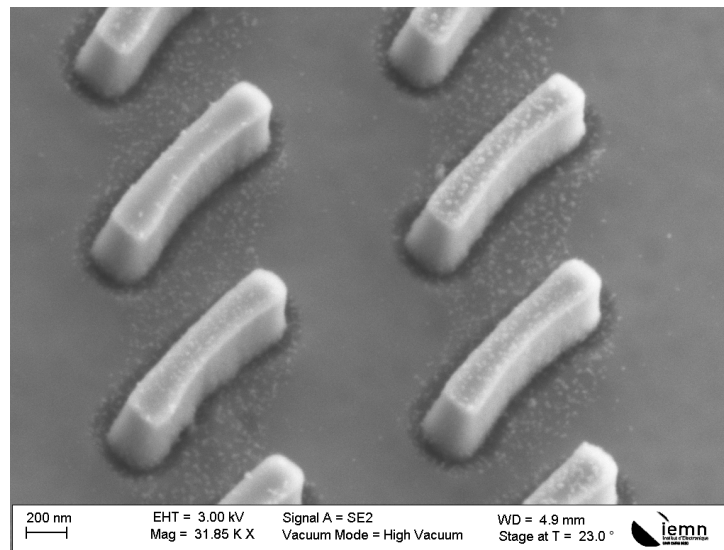


Figure 4.17 – SEM image showing the result of etching using  $\text{Cl}_2/\text{Ar}$ .

In parallel, we attempted to achieve the formation of magnetoelastic structures using dry-etching. Admittedly, these efforts did not yield similar success. The dry-etching was performed in a ICP-RIE (Inductively Coupled Plasma - Reactive-Ion Etching) Sentech system. Samples with full-surface deposition of 120 nm-thick multilayers were prepared to test plasma etching. Two different gases were considered:  $\text{CHF}_3$  and  $\text{Cl}_2/\text{Ar}$ . Surprisingly, the former seemingly failed to etch anything, as no effect was noticed after 10 minutes of etching. With  $\text{Cl}_2/\text{Ar}$ , which has a reactive component due to the presence of chlorine, the multilayer was successfully etched. Besides, the optical signal used for end point detection exhibited oscillation attributable to the successive etching of individual layers, which is very interesting in itself and for precise control over the etching process. A test was then carried out to etch the multilayer deposited under a pattern metallic mask. Nickel is most often used for the protective mask in dry-etching. However in our case this was not an option as the metallic multilayers are also etched by the nitric acid-based wet-etching solution used to remove nickel. The same goes for chrome. As a result, aluminum was chosen instead. After etching and lift-off, we obtained mixed results. First, the etching seemed to have adversely affected the multilayers and the mask in the sense that it was impossible to remove both by wet-etching. This may be due to impurities from reactive etching of the mask and the multilayer. Also, these impurities were scattered on the

surrounding surface and did not disappear after standard cleaning. As rather satisfying results were obtained by lift-off, there was no incentive to spend much more time trying to figure out why this happened and how to prevent it.

## 4.3 Characterization

This section covers the various measurements carried out on the materials. The piezoelectric substrate response to an electric field was obtained using strain-gauge measurements, and compared to data available in the literature. As for the magnetoelastic layers, their magnetic properties are extracted from experiments in a Vibrating Sample Magnetometer. Detailed information about the topography and local magnetism are obtained by Atomic and Magnetic Force Microscopy, respectively. Kerr microscopy was used to gain direct insight on the behavior of the magnetoelastic material subjected to magnetic field and mechanical stress.

### 4.3.1 Strain gauge measurements

The piezoelectric characterization of our PMN-PT substrate was performed using strain gauges. Basically, a strain gauge consists in a long and thin metallic stripe which resistance changes with its elongation in a linear fashion through the gauge factor  $k$ :  $\frac{\Delta l}{l}k = \frac{\Delta R}{R}$ . Therefore, the change in resistance provides precise information on the actual strain that causes the elongation of the metallic wire. A Wheatstone bridge is often used to allow the detection of minute variations of resistance and turns them into voltage signals.

The strain gauges used were bought from HBM and can measure the strain in two perpendicular directions simultaneously (XY setup). Each direction is characterized by a given gauge factor. We used cyanoacrylate to attach the strain gauges to PMN-PT substrates on which full-surface electrodes were deposited on both sides (see Fig. 4.18a). To facilitate the establishment of contact points on the surface as well as the connection with the strain gauge electrical output, a mount was specially fabricated to fix the substrate as part of an internship. It is shown on Fig. 4.18b.

The experiment set up first involves the calibration of the Wheatstone bridge and all the required electrical apparatus, in order to know how to quantitatively translate variations of voltage into variations of resistance. In principle, the strain is then easily calculated using the gauge factors that were approximately equal to 1.7. Here however, we only know the value of the strain within an additive constant. Indeed, when the strain gauge is attached to the substrate the actual strain at that moment (corresponding to

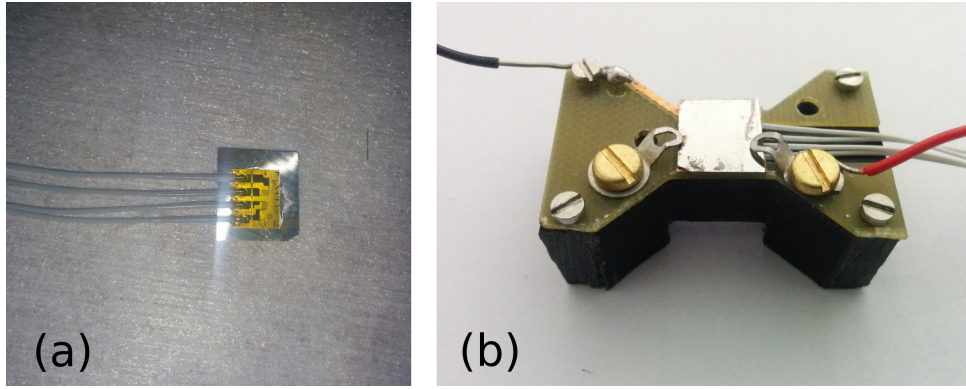


Figure 4.18 – (a) Photograph of a strain gauge attached to a sample. (b) Sample with strain gauge attached placed on the mount enabling easy fixing and convenient contact points.

zero elongation of the gauge) is unknown. In any case, since the magnetoelastic layer is also deposited on a pre-strained substrate, it is the variation measured that matters. During preliminary tests it was noticed that at some points that appeared like sharp transitions, a dynamical behavior of the system could be observed and it took time for the measured values to settle to an equilibrium. The general protocol for the experiment was that for each measurement, we waited for an equilibrium to be reached. In this sense, the approach chosen could be considered quasi-static. The applied voltage went from  $-200$  V to  $+200$  V, and then came back to  $-200$  V (since the substrate are  $300$  nm-thick, the corresponding range for the electric field is  $\pm 0.67$  MV/m). Depending on the local steepness of the curve, points were taken every  $10$  V or  $5$  V.

Samples from both vendors were characterized. The actual relationship between estimated strain (within an additive constant) and electric field is shown in Fig. 4.19. The obtained response is quite complex and requires some description. While linear portions do exist, the overall behavior is highly nonlinear. From one poled state and decreasing the amplitude of the applied electric, a linear region is described. It is worth mentioning that in accordance with prior discussion the variation of the strain is of opposite signs for the orthogonal directions X and Y (the piezoelectric coefficients are indeed of opposite signs locally). Going to negative (resp. positive) electric field on an initially positively (resp. negatively) poled substrate, there is a first critical field where the  $y$  strain varies abruptly to reach an extremum. In the context of a rhombohedral phase as shown in Fig. 4.2, this can be interpreted as the field at which the polarization switches from directions with a positive or negative  $z$  component (red resp. violet dot-dashed arrows),

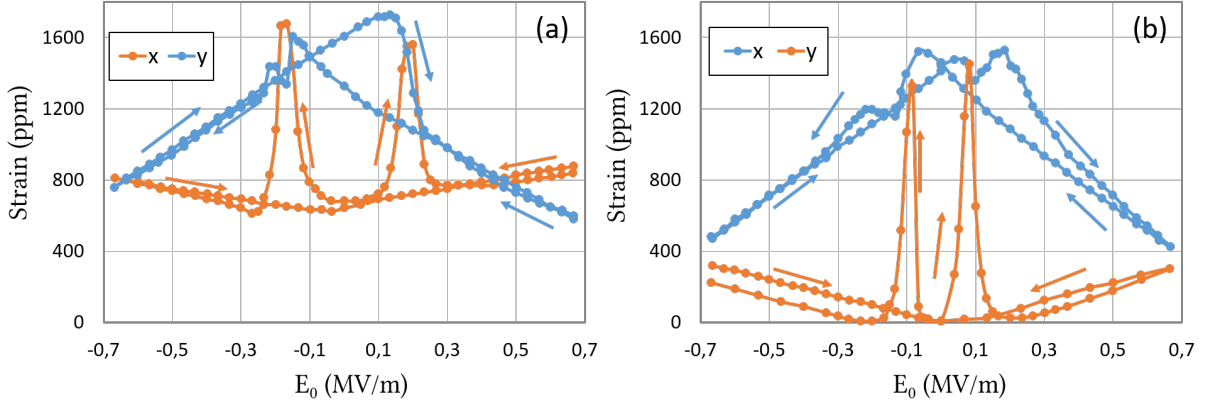


Figure 4.19 – Relationship between applied electric field and measured strain in both directions for samples from (a) CTG Advanced Materials and (b) TRS Technologies. The fact that the loop does not close in (b) may be attributable to history-dependent behavior or changes in experimental conditions over the course of the experiment.

to polarization directions in the  $xy$ -plane (blue dot-dashed arrows). When the amplitude of the field is further increased, the  $y$  strain suddenly jumps back to values similar to a normal poled response. This new transition constitutes the poling of the substrate in the other direction (polarization direction along the violet resp. red dot-dashed arrows). Another linear region is then described. The  $x$  strain also shows unusual but more complex behavior around these critical fields. It should be noted that within these transitions, the dynamics of the measured strains are such that several minutes are at times necessary for the system to reach equilibrium.

Admittedly, the modeling presented in previous chapters, in which a linear behavior was assumed, is insufficient to really describe the behavior of PMN-PT substrate. The piezoelectric coefficients used in the simulations correspond to the response at high frequencies [278], and do not correspond to what is measured in the linear regions at low frequencies [284]. In any case, this aspect only affects technological matters and from the physical point of view, the more interesting content is the behavior of the magnetic system considering a given strain or stress.

Similar measurements are reported in the literature. In Ref. [284], the authors applied an electric field with triangular waveform at a frequency of 0.01 Hz and the data was collected by a digital acquisition system. This point makes their approach slightly different from ours, where each measurement was made after the system reached equilibrium. It is difficult to comment beyond mere speculation on the impact of such a difference. In any

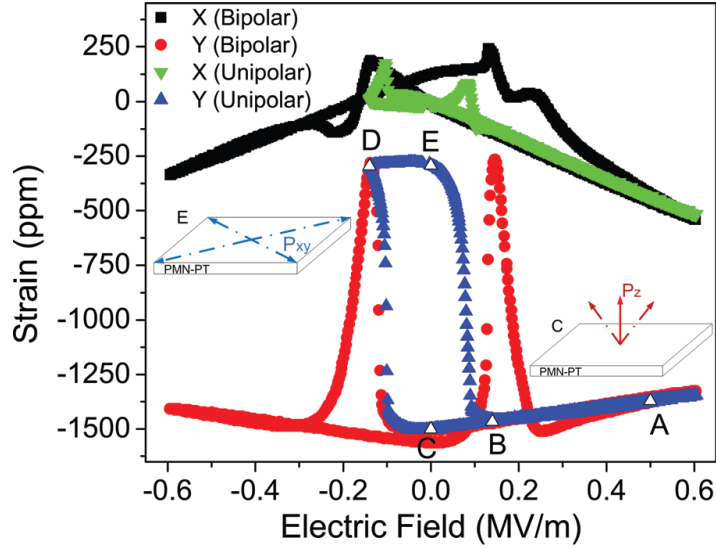


Figure 4.20 – Electric field-strain relationship reported in the literature. Black and red curves correspond to a measurement loop similar to what we did. Green and blue curves correspond to unipolar measurements. Figure from [284].

case, the results (black and red curves included in Fig. 4.20) are nonetheless qualitatively as well as—to some extent—quantitatively similar and confirm the strongly nonlinear behavior of (011)-cut PMN-PT. The differences with our measurements may be attributable to the protocol followed and normal variations between samples. Their investigations also included cycles with electric fields in a certain range so that the substrate is never fully poled in the opposite direction. In this way, they showed that it is possible to switch between two states of the substrate that are associated with very different strain values, as illustrated by the green and blue curves on Fig. 4.20. Besides, additional analyses in this paper suggest that the substrates do not seem prone to fatigue and that the permanent strains states are very stable in time. All these properties are interesting in the prospect of memory applications, for instance.

### 4.3.2 Magnetic characterization of sputtered layers

The layers deposited with the recipe described above can be characterized magnetically using the Vibrating Sample Magnetometer (VSM) set up at IEMN (EV9 model from ADE shown on Fig. 4.21). In a VSM, the sample is attached to an oscillating rod in the air gap of a magnetic circuit. The response of the sample to a magnetic field generated is then detected by additional coils using synchronous detection, given the small amount of magnetic material involved. In this manner, the different components of the magnetic



Figure 4.21 – Photograph of the Vibrating Sample Magnetometer.

moment can be estimated. In our case, a hysteresis loop between 2 T and -2 T is performed on the square silicon sample on which the deposition was made (see Fig. 4.13). The frequency of the vertical oscillations to which the sample is subjected is 75 Hz. The amplitude of magnetization is inferred by estimating the volume of material from the known surface of the square and the thickness deposited.

Fig. 4.22 shows an example of the hysteresis loops along the easy and hard axis for the typical multilayers deposited. From the data at high fields in these plots, one can deduce that the magnetization is about  $930 \times 10^3$  A/m. These two graphs clearly show the presence of a clear-cut uniaxial anisotropy through typical easy and hard axis curves. The points at which the magnetization reaches the magnetization at saturation on both plots defines the anisotropy field, which happens to be between  $40$  and  $50 \times 10^3$  A/m.

We can also use deflectometry tools available at IEMN to measure magnetostriction in these samples [283, 297]. During sputter deposition, a long and narrow fragment (beam) of silicon wafer is put in the chamber for that purpose (see Fig. 4.13). To measure magnetostriction, the beam is fixed at one of its extremities in a dedicated setup enabling the application of magnetic fields in order to measure the corresponding displacement using a deflected laser beam. For that purpose, the shape of the beam subjected to the strain induced by the magnetoelastic material is supposed to be parabolic. Knowing the amount of magnetic material as well as the dimensions and elastic parameters of the silicon substrate, it is possible to estimate the magnetostriction coefficient  $b$  (in MPa) and thus

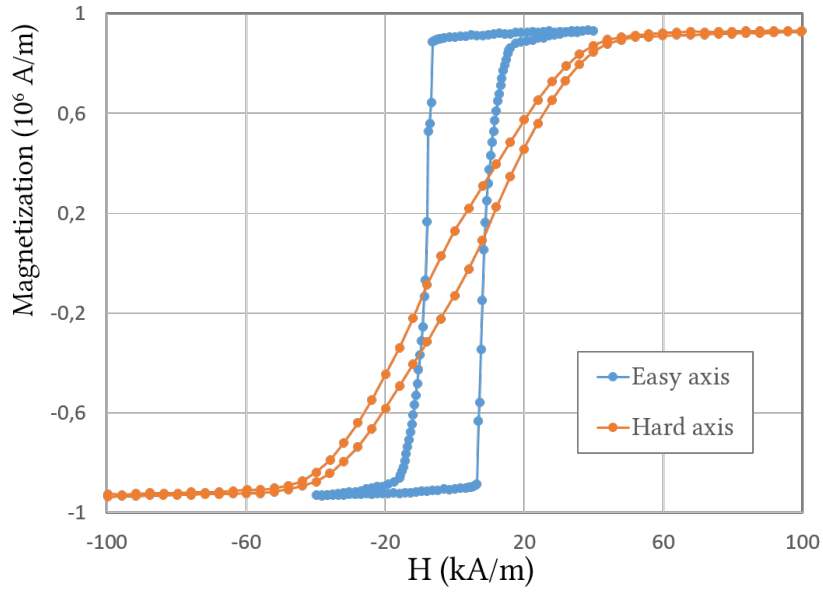


Figure 4.22 – VSM hysteresis loops performed on the test sample containing a thin film of the magnetoelastic multilayers deposited.

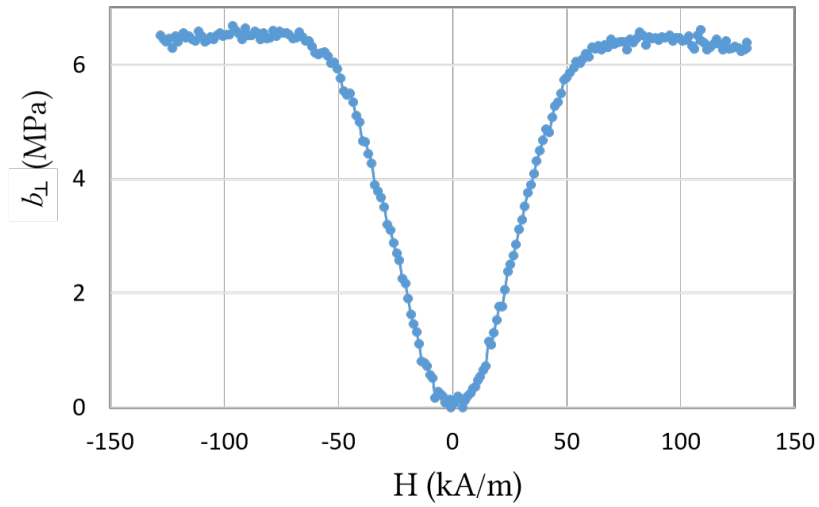


Figure 4.23 – Hard axis magnetostriction data for the test sample containing a thin film of the magnetoelastic multilayers deposited.

$b^{\gamma,2} = b_{\parallel}^{sat} - b_{\perp}^{sat}$ . Given the amorphous structure of the material, this physical quantity can be related to the maximum relative displacement  $\lambda_s$  in a simple way, involving elastic parameters of the thin film [2]:  $\lambda_s = -\frac{2(1+\nu)b^{\gamma,2}}{3E}$ . The values assumed are respectively

$E = 80$  GPa and  $\nu = 0.25$  of the Young's modulus and Poisson's ratio.

Despite the weakness of the signal associated with such thin multilayers, it was possible to perform a precise measurement of magnetostriction. The result of a field scan along the hard axis is shown on Fig. 4.23. In these multilayers, the larger proportion of FeCo reduces magnetostriction, with  $b^{\gamma,2} \approx 6.6$  MPa ( $\lambda_s \approx 0.7 \times 10^{-4}$ ). Typically, measurements on multilayers with layers of FeCo and TbCo<sub>2</sub> of equal thickness yield a magnetostriction coefficient  $\lambda_s \approx 1 \times 10^{-4}$ , *i.e.* around 100 ppm).

### 4.3.3 Atomic and Magnetic Force Microscopy

The technique referred to as Magnetic Force Microscopy (MFM) is a variant of Atomic Force Microscopy (AFM), which has to be succinctly described before introducing MFM. An atomic force microscope is essentially a type of scanning probe, in which a piezoelectric element is used to control the position or actuate the motion of a cantilever placed near the surface of the sample. The proximity between the tip of the cantilever (probe) and the sample induces a deflection of the cantilever due to interaction forces, in which various phenomena are involved (electrostatic force, van der Waals force...). This deflection can be measured with a detector using a reflected laser beam (see Fig. 4.24) or through the feedback signal of the piezoelectric element. There are three main modes of imaging, with the tip either in constant contact with the surface, in intermittent contact (tapping mode) or without any contact. The first of these three modes is now rarely used because of the superior performances of the other two. In these cases, the cantilever is made to oscillate around its resonance frequency.

With MFM, the tip used has a magnetic coating (oftentimes made of cobalt), and is hence subject to magnetic interactions that can be detected and yield information about the local state of magnetization. Let us consider a uniform magnetization of the tip and the corresponding magnetic moment noted  $\vec{m}$ . Under some assumptions (relatively hard materials, uniformity of magnetization and of magnetic field across the magnetic tip), the force exerted on the tip is the following:

$$F_i = \mu_0 m_j \frac{\partial H_j}{\partial x_i}. \quad (4.1)$$

In most cases, as in ours, the tip is initially magnetized along  $z$  ( $m = m_z$ ), that is perpendicularly to the surface of the sample. The expression above can simply be written

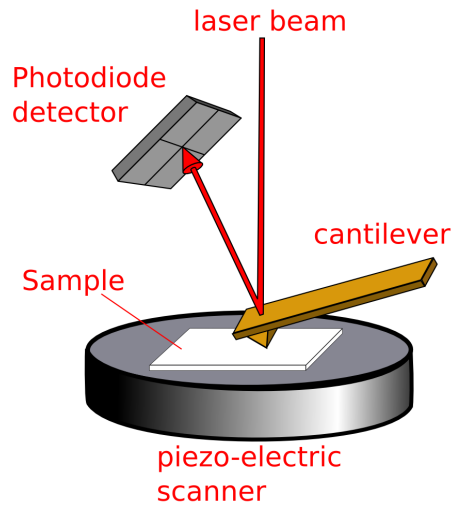


Figure 4.24 – Working principle of AFM. A cantilever interacts with the sample surface with the tip. The position of the cantilever is measured using a reflected laser beam. Figure from freesbi.ch.

as:

$$\vec{F} = F_z \vec{z} = \mu_0 m \frac{\partial H_z}{\partial z} \vec{z}. \quad (4.2)$$

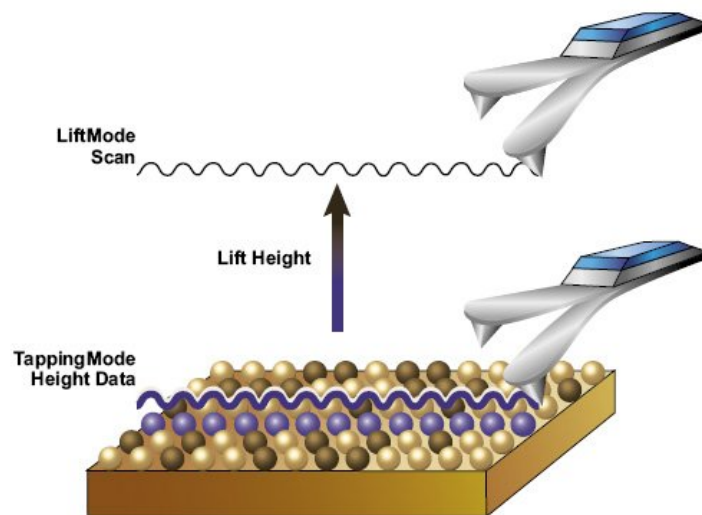


Figure 4.25 – Illustration of the Lift Mode. The second pass traces the topography, adding an offset height. Figure from Bruker.

The force is proportional to the vertical field gradient. What we are looking at is

therefore related to the out-of-plane components of the stray field, and simple domain configurations can readily be inferred from this information. It is worth noting that it is the phase data that contains magnetic information. In the case where MFM images is ambiguous or can be tied to several different solutions of micromagnetic equations, refined techniques that have been described to help reconstruct magnetic distributions from MFM data [298]. More details about MFM and its applications in general can be found in dedicated book chapters [299,300].

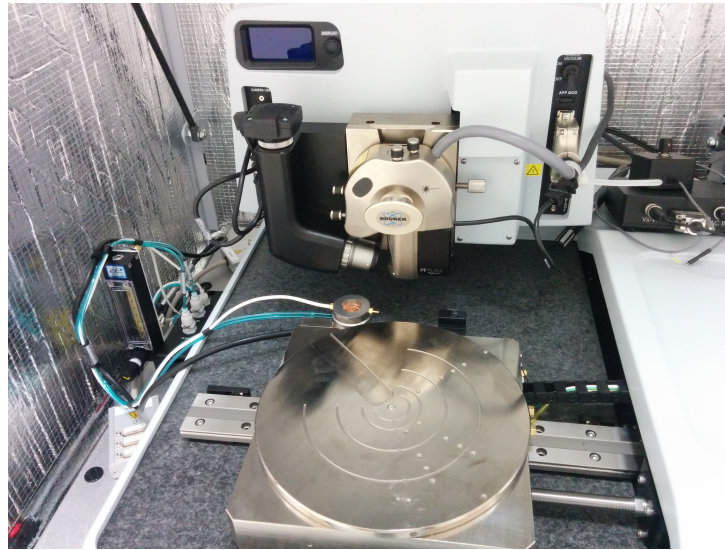


Figure 4.26 – Photograph of the AFM used.

During any operation, the image is formed by scanning the sample. In the case of MFM, there are two passes for each line (that is, two *traces* and two *retraces*). The first pass extracts topographic information in tapping mode. In the second pass the tip is raised to a given height and is maintained to a predetermined distance from the surface. This is called the *Lift Mode* and ensures that there is only a minimal influence of topography on magnetic imaging (see Fig. 4.25). In the case of the Linear Mode, the probe is kept at a constant altitude. One of its advantage is its relative insensitivity to artefacts related to strongly uneven surfaces, which will matter to our situation as explained later.

The AFM we used at IEMN is a Dimension Icon made by Bruker. It is shown on Fig. 4.26. The first AFM tests yielded information about the local topography on the multilayers patterns. In particular, much of the discussion of subsection 4.2.4 revolved around the profiles on the edges of the magnetoelastic structures obtained after lift-off. AFM data was collected on the samples obtained after lithography of different resist

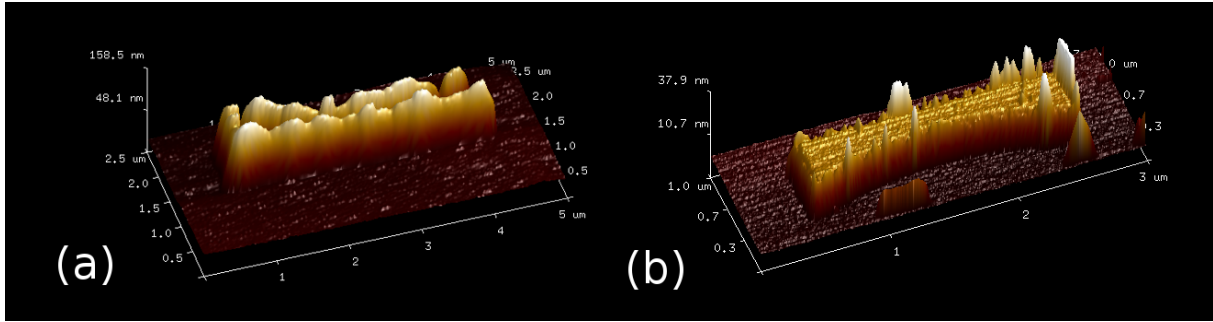


Figure 4.27 – 3D images allowing the comparison of the lift-off obtained before and after updating the parameters to spin a thinner resist layer. The profile is dramatically improved.

thicknesses in order to test the explanation for the presence of these wall-like bumps. Fig. 4.27 contains 3D images that turn out to be typical of the two samples. It is quite obvious that decreasing the thickness of the resist had a dramatic effect on the profile. This supports the interpretation developed in subsection 4.2.4.

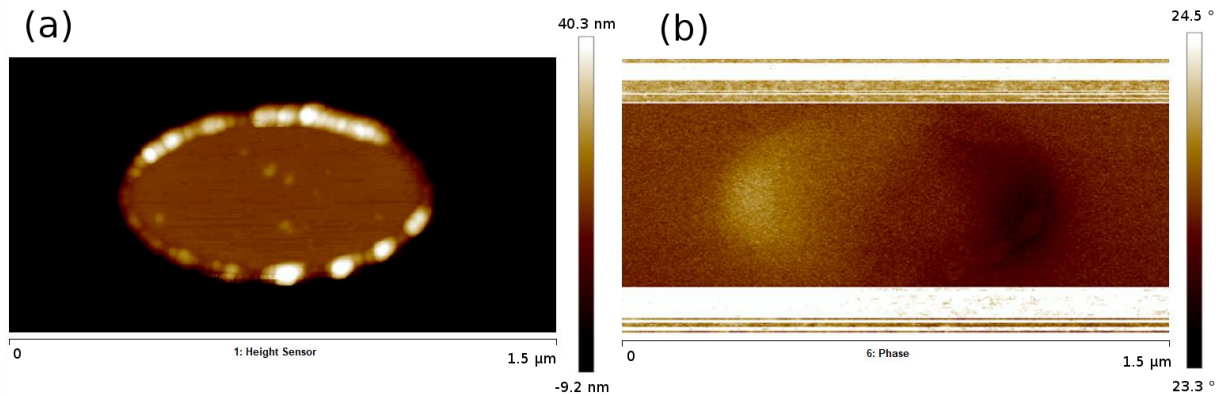


Figure 4.28 – (a) Topographical and (b) MFM data over an elliptical magnetoelastic element. The well-defined dipole configuration is synonymous with a monodomain distribution. Note that the contrast obtained correspond to about  $1^\circ$  in phase shift.

For magnetic imaging, several tips with different magnetization and coercivity are available. We used the MESP-V2 that has medium coercivity and magnetic moment, with which very clear magnetic signals are easily detected (for instance on the test magnetic tape provided by Bruker). Before any AFM measurement, the samples are saturated roughly along the hard axis  $90^\circ$  in the VSM in the hope of inducing non-uniform magnetization distributions and hence domain walls in the nanostructures. Looking at the

elliptical structures, good magnetic signal is obtained. Fig. 4.28 shows MFM data for a typical element. It seems clear that the magnetization is uniform, with two clear and distinct magnetic poles. It is interesting to note that the ellipses that we looked at all had the same left-right pattern of light and dark patches, suggesting parallel magnetization among them.

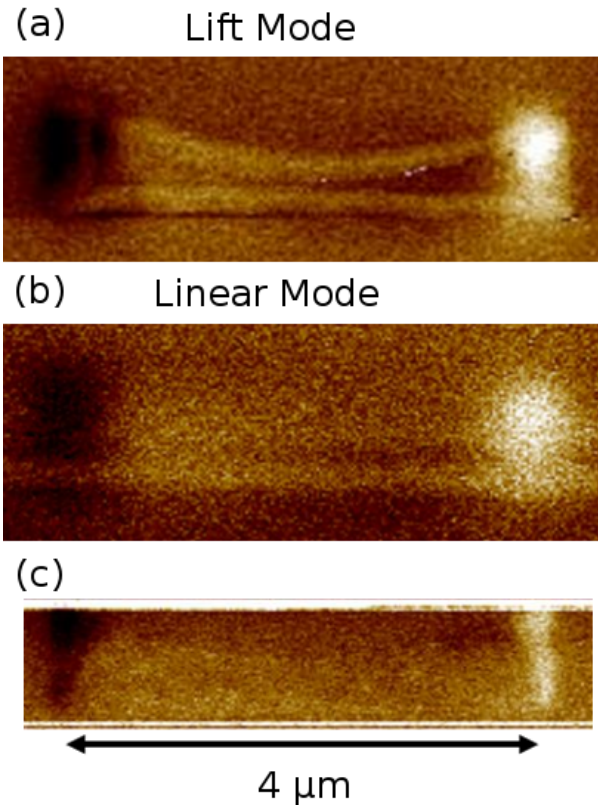


Figure 4.29 – MFM data of hourglass-shaped magnetoelastic nanostructures in (a) Lift Mode in which strong topography-related artefacts are observed and (b) and (c) Linear Mode, which prevents such artefacts. In (c), the contrast is concentrated on the extremities. Colorbar legends have been removed for clarity on this qualitative discussion.

MFM observations of the multilayers of elongated shape (hourglass and constant section nanostripes) lead to more complex results. First, it was found that the topography had tremendous effects on the phase signal observed as visible in Fig. 4.29a, despite the use of Lift Mode. This turned out to be an artefact linked to the topography: while the tip always stays at the same distance from the point of the surface located directly beneath it, it may get closer or farther from other nearby points of the surface. Problems of this kind are to be expected especially when the relief is steep, which is clearly the case

in our first samples (see subsection 4.2.4). It appeared that switching to Linear Mode significantly reduced these unwanted effects (see Fig. 4.29b). Another striking feature of preliminary measurements was the presence of four clearly defined high and low patches in signal contrast, visible on the first two scans of Fig. 4.29. This was initially considered evidence of a two-domain magnetic configuration. However, upon reflection the observed patterns was not compatible with this hypothesis, and the resulting skepticism motivated further scrutiny. Additional measurements showed instances where the contrast in the middle of the magnetoelastic element was strongly diminished (see Fig. 4.29c), so that these phenomena are now suspected of also being artefacts of built-in filters and averaging. In the end, the most probable hypothesis is that magnetization in the nanostructures is in fact uniform like in the ellipses, or that at least there are no domain walls.

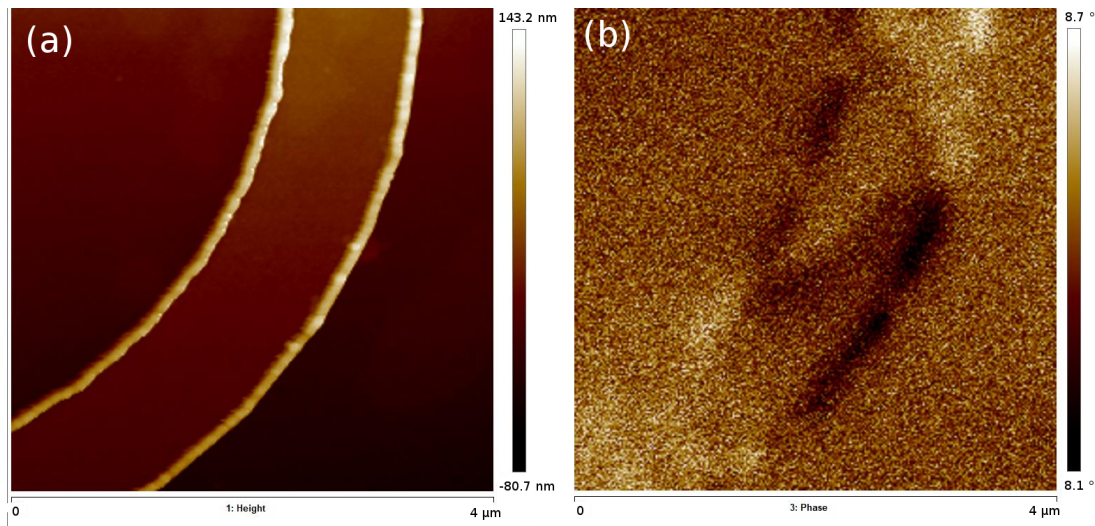


Figure 4.30 – (a) Topographical and (b) MFM data in a portion of a  $1\ \mu\text{m}$ -wide ring. The patterns observed may be due to the presence of a domain wall.

The only instance where we really think that MFM data hinted at the possible presence of a domain wall was in a ring of  $1\ \mu\text{m}$  width. Fig. 4.30 shows the topographical and phase data. In this particular instance, the profile on the edges was quite poor. However, the pattern within the surface of the magnetic material is reminiscent of what can be observed in the vicinity of domain walls in similar structures [17].

We did not have the opportunity to look at the samples while a magnetic field and a mechanical stress are applied. Possible options for improvement on this aspect are addressed in subsection 4.4.2. However, further measurements were carried out using Kerr microscope, as explained in the following subsection.

### 4.3.4 Magneto-optic Kerr microscopy

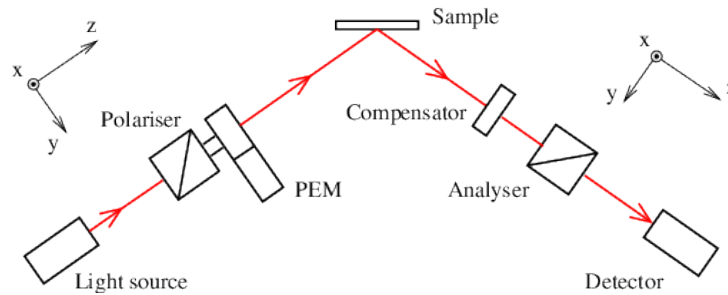


Figure 4.31 – Schematic of the setup needed to observe a magneto-optic Kerr effect. Note that the presence of a photoelastic modulator (PEM) and compensator is optional. Figure from [301]

Information about local magnetism can also be obtained using magneto-optical techniques, including the magneto-optic Kerr effect (MOKE). When light is reflected on a magnetized surface, it undergoes some change in intensity and polarization due to interaction with local magnetization. This change depends on the orientation of the magnetization, so that in the presence of multiple magnetic domains or inhomogeneous magnetization distributions, there is a contrast in the reflected signal. This allows for the direct observation of the magnetization distribution of samples. The general setup required for a Kerr microscope is shown on Fig. 4.31. The light is polarized (usually linearly, which is equivalent to the sum of two circularly polarized signals) before getting to the magnetic surface. In the general case, the reflection will rotate the axis of polarization (due to different phase velocities) and induce a small ellipticity (due to a difference of absorption). The variation of the polarization of the reflected light is then measured using an analyzer placed before the detector. For maximum sensitivity, the analyzer direction should be roughly orthogonal to that of the polarizer, which necessarily implies low-intensity signals. Depending on the relative orientation of the incident light with respect to local magnetization, one deals with polar (out-of-plane magnetization), longitudinal (magnetization along the incidence direction) or transverse (magnetization orthogonal to the incidence direction) MOKE. Of course, the strength of the magneto-optical response depends on the materials.

A Kerr microscope was set up at IEMN over the course of the PhD. It uses a M455L3 Thorlabs mounted LED of short wavelength (455 nm), which is interesting from the resolution point of view. However, it appears that green happens to be the best when it comes to strength of magneto-optical response for Fe and Co (which constitutes the uppermost

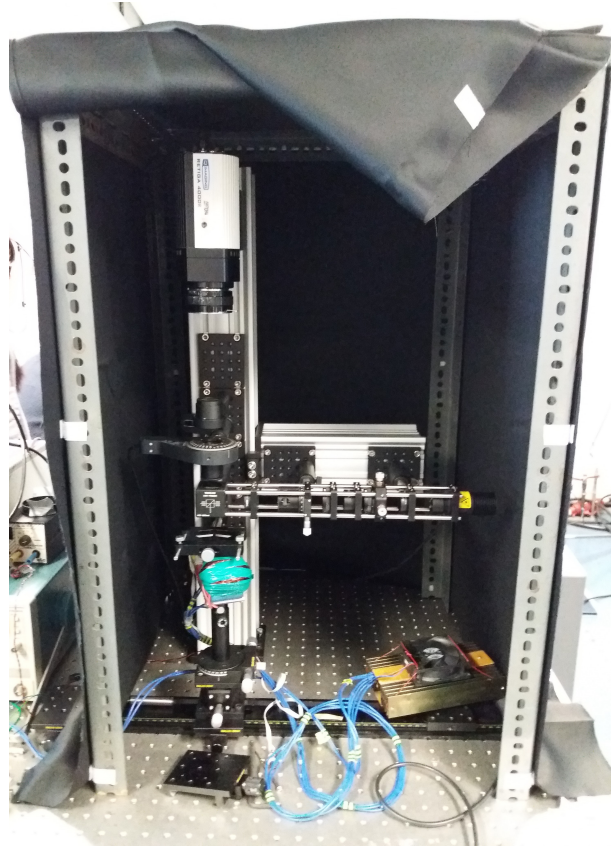


Figure 4.32 – Photograph of the Kerr microscope set up at IEMN.

layer in our samples) [302]. As for the detector, a ORCA-Flash4.0 V3 Hamamatsu camera was used. As Kerr imaging involves light of low intensity, the properties relevant for Kerr imaging include low-noise operation, high sensitivity and large dynamic range. The performance of the software associated with the camera is also crucial as it is often necessary to perform significant image processing in order to get clear results.

It appeared that some contrast linked to magnetization could be achieved using materials similar to the multilayers we used, although it was difficult to stabilize an image with a non-uniform magnetization distribution using an applied magnetic field. Besides, mechanical vibrations from the table added significant noise to the images, although there were successful efforts to reduce it. Since these materials did exhibit a magneto-optical response, we tried to look at our samples with this new microscope, using the mount shown in Fig. 4.18.

Because it is essentially an optical microscope, only elements that were microns across length and width put on the mask were visible. While small nanostructures were recogni-

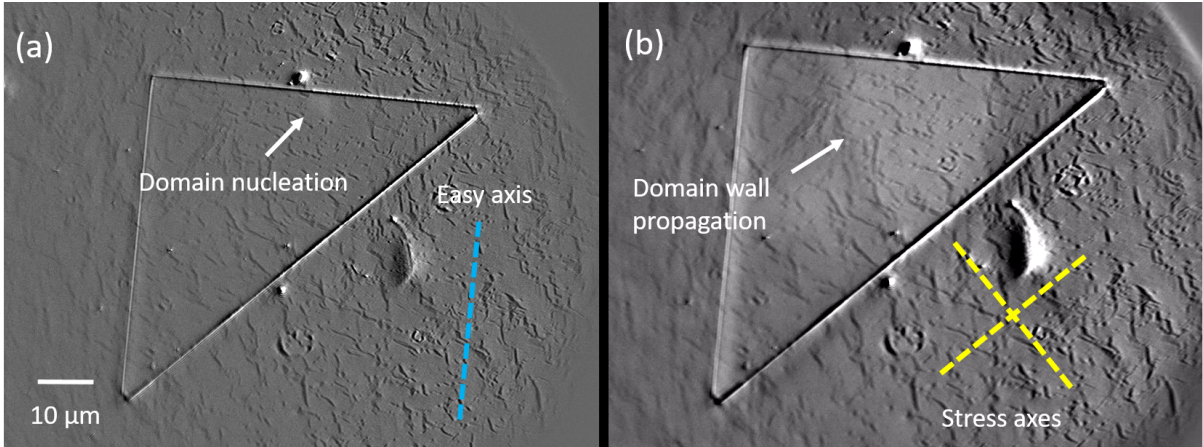


Figure 4.33 – Kerr images of a multilayer subjected to a magnetic field and mechanical stress induced by the piezoelectric substrate. The different magnetic domains are clearly visible.

zable, their size was too small for the microscope to give valuable insight on their internal magnetic structure, especially considering the noise induced by vibrations on the setup. However, large marks of isosceles triangles shape (hypotenuse:  $80 \mu\text{m}$  and therefore altitude of  $40 \mu\text{m}$ ) were large enough to look at their magnetic domain configuration. Even then, during cycles of applied magnetic field between saturating values, they were most of the time monodomain, although the magnetization switching was clearly achieved by domain wall propagation. The procedure followed was the following. First, a saturating (for instance negative) magnetic field is applied along the easy axis, so that the magnetization of the triangle is uniform. The amplitude of this magnetic field is then reduced until it reached a positive value close to the coercivity. In this region, the magnetic field is increased very slowly until nucleation of a small domain. At this point the magnetic field is kept at its value, and an electric field is applied on the PMN-PT substrate to generate stress components. We showed that it resulted in domain wall propagation because of the observable increase in area of the domain, with pinned domain walls. While this experiment does not involve the same geometry and magnetic domain structure as what was intended, it does show a magnetoelectric effect inducing domain wall propagation through a modification of anisotropy induced by mechanical stress.

## 4.4 Prospects

This section contains a discussion dealing with the ways in which the experimental state of affairs can be improved. Various considerations on how to find the optimal parameters pertaining to the quality of the lithography, lift-off and etching are put forward. Some thoughts on the failure to precisely manipulate domain walls in the proposed configuration follow. Finally, parallel work that we have been involved in on PMN-PT etching in the prospect of integration and efficient operation is presented.

### 4.4.1 Optimization of fabrication process

Although significant progress has been made on the lift-off process since the first tests, the profiles obtained still exhibit steep relief on the edges of the magnetoelastic structures. The approach chosen here was to reduce the thickness of the resist. This turned out to work quite well, although results were less satisfying on PMN-PT than on silicon wafers, probably due to the size of the substrate. Only limited progress is to be expected in this direction, since the spin-coating rotation speed is already close to the maximum available. Moreover, the thinner the layer of resist, the more difficult the liftoff will be. Using another resist is an option, although the lithography process would have to be overhauled. In this context, many would also consider usual bilayer e-beam structures (for instance spinning PMMA on top of copolymer), with significant undercut [303]. An even simpler idea is to deposit thicker multilayers in order to reduce the gap between the thickness of the multilayer and that of the resist. For wide nanostripes, this would probably not be a problem from the magnetic point of view. Other, more complicated options include the use of smooth anisotropic etching with a tilted angle to break the bumps and spikes on the edges after lift-off, for instance using Reactive Ion Beam Etching (RIBE).

Another problem was the damage caused by the necessary ultrasonic cleaning used during lift-off. Even at minimum power, there are significant risks that smaller elements get detached while long nanowires tend to break. It is possible that fine-tuning the cleaning parameters (mode of operation, power, time, temperature) may yield better results. Also, the choice of another metal for the electrode on which the multilayers are deposited may help increase their adherence.

Let us not forget that these issues disappear if we consider etching instead of lift-off (see Fig. 4.14). However, other problems need to be solved to obtain smooth profiles as well as clean samples. Here again a lot of parameters come into play (gas, flow rate, power, metal used for mask and so on). Also, the RIBE tool at IEMN is specially suited

for etching very thin films. This solution was tried once, with mixed results so that more time would be necessary to optimize the process. However, it remains an interesting option as this tool is able to remove in real-time the impurities generated by etching.

Finally, the combination of materials chosen in this thesis (TbCo<sub>2</sub>/FeCo sputtered multilayers on (011) PMN-PT bulk substrate) should not be seen as the only pair worth considering to achieve stress-induced domain wall motion as presented here. First, using PMN-PT thin films could be an opportunity with regard to integration and scaling, under the assumption that appropriate crystalline phase and orientation as well as good surface quality can be obtained on silicon wafers. Besides, other materials may exhibit superior intrinsic properties, better coupling, or allow more convenient processing or operation. We should also bear in mind that the research is not done in the vacuum but within a regulatory and social framework that tend to reflect economic, strategic and ecological concerns. Public health risks associated with the use of lead in commercial products resulted in a stringent worldwide regulation of lead-based products. As a result, there is a strong incentive for researchers to find lead-free alternatives, especially in the industry [304, 305]. Unfortunately, a lead-free candidate with competitive properties has yet to be found. We can make a similar point on the use of a rare-earth based material for the magnetoelastic phase. It remains to be seen how more abundant magnetostrictive elements—such as nickel—could replace them. The key issue here lies with the possibility to efficiently tailor the magnetic anisotropy as it is currently done in nanostructured terbium-based multilayers sputtered in the presence of a magnetic field.

#### 4.4.2 Control of domain walls in nanostructures

The failure to obtain an experimental validation of the phenomenon studied numerically should not shed doubt on the possibility of successfully observing domain wall motion induced by the combination of a uniform stress and a bias magnetic field. The basic physical mechanism involved—stress-triggered variation of effective anisotropy generating a Zeeman energy gap between adjacent domains—is quite simple and completely consistent with existing knowledge. Combining this strong *a priori* plausibility with the numerical evidence presented in this thesis, it would be surprising that such a phenomenon could not be observed experimentally.

It is possible that the phenomenon would not be easily observed because of the relative weakness of the energy gap that could fail to overcome domain wall pinning strength at room temperature, but this seems rather unlikely. First, with modern techniques and

know-how, it is possible to achieve very limited roughness in nanostructures. Second, the energy gap depends heavily on the strength of the magnetic field, which can be increased as high as the effective anisotropy along  $\vec{x}$  (uniaxial anisotropy + shape anisotropy) to force the depinning of the domain wall.

One important issue we faced relates to the creation of domain walls, which is a matter seldom covered in papers dealing with domain wall motion. First, it is probable that the patterns chosen for the nanostructures do not lend themselves to domain wall generation in such materials. Second, the process by which we thought domain walls could appear (saturation with orthogonal magnetic field and relaxation) may not be suited to such configurations, and in any case was implemented with poor precision over the saturation angle. Realizing this, we fabricated an electromagnet fixed on a Thorlabs mount that can rotate with a precision of less than  $1^\circ$ . However, to be of any use, such a device would have to be set up in the MFM so that after each saturation it would be possible to check for the presence of a domain wall in the examined nanostripe. Unfortunately this could not be achieved, and there were doubts that the field generated by the magnetic circuit would be strong enough to overcome the effective anisotropy of individual elements. Besides, the consequences of the proximity of the magnetic tip and variable magnetic field in the  $xy$ -plane remains an unsettled matter. Magnetic fields up to 3 T can be applied in ultra-high vacuum equipments at IEMN, but only perpendicularly to the sample and for the time being, there are no adequate magnetic tips available.

### 4.4.3 PMN-PT studs

In parallel with the work on magnetoelastic structures, there were efforts directed at more application-oriented matters. More precisely, investigations have looked at the conditions in which the control of individual magnetoelastic structures could be implemented in an array of such elements from an integration perspective. As discussed in subsection 4.1.3, the risk of inhibiting piezoelectrically-induced displacement as well as locally damaging the substrate suggests that some processing of the PMN-PT substrate may be useful. This is the reasoning behind the proposed patterning shown in Fig. 4.4, in which a stud of substrate is created. We should also note that this solution dramatically reduces the dissipated energy as the volume of dielectric involved is reduced. In any case, the development of an etching process of PMN-PT is necessary. In practice, given the small size of the stud (only microns across), it is necessary to arrange a "bridge" to ensure electrical contact of the surface of the stud. Prior multiphysics studies using the COMSOL<sup>®</sup> software showed that an aspect ratio of 1 (width to thickness) was a good compromise to

allow the piezoelectric material to effectively deform itself on its upper part. Therefore, quite deep etching is necessary.

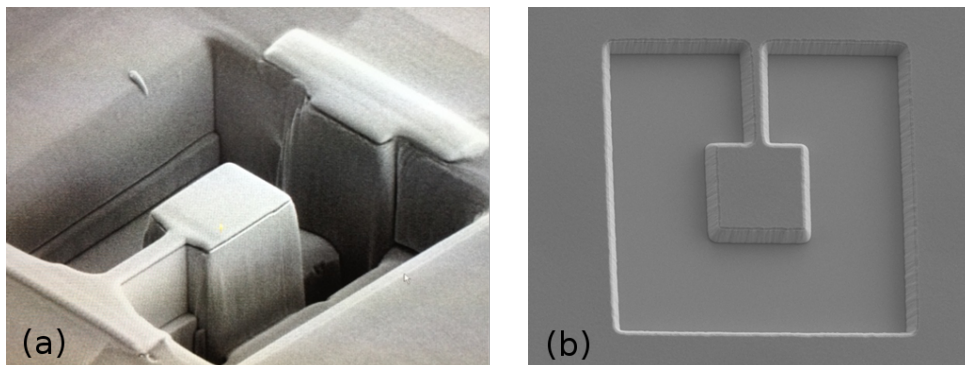


Figure 4.34 – (a) FIB an (b) plasma etching of the PMN-PT substrates to create  $5 \times 5 \mu\text{m}$  studs.

A first step consisted in depositing appropriate electrodes on a PMN-PT substrate. Then, preliminary tests involved Focused Ion Beam (FIB) to etch the substrate (see Fig. 4.34a). However, since etching in this fashion can only be done one site at a time, it is not suited to the eventual purpose of having arrays of studs. Plasma etching appears like a better option, and proved possible although the etching profile on PMN-PT substrates turned out to be much less straight than on silicon wafers. Crystalline orientations may be to blame on this issue. An example of a  $1 \mu\text{m}$  deep etching is shown on Fig. 4.34b, made possible by a nickel mask. Significant wear of the bridge was observed, and concern over its eventual disappearance because of the longer periods of etching necessary eventually led to a modification of the design. A simple parallelepipedic 'pier-like' structure of constant width is now considered. Given the depth of etching sought (several microns), a thick nickel protective mask is required. The most convenient technique to use in such cases is electrolysis.

Various scenarii have been put forward for the whole process, and one currently remains under consideration. They are summed up in 4.35. Other candidates were eliminated because they proved too complicated from an experimental point of view or that they yielded poor results. In the agreed-upon view, electrodes would have to be deposited first, before the lift-off of magnetoelastic elements is done. For the electrolysis, it is necessary to have a full-surface deposition of metal (so that the sample surface is conducting and acts as the cathode). Since it will be on top of the multilayers, gold was chosen as it can be wet-etched without damage to the multilayers. A negative resist is then spun to cover

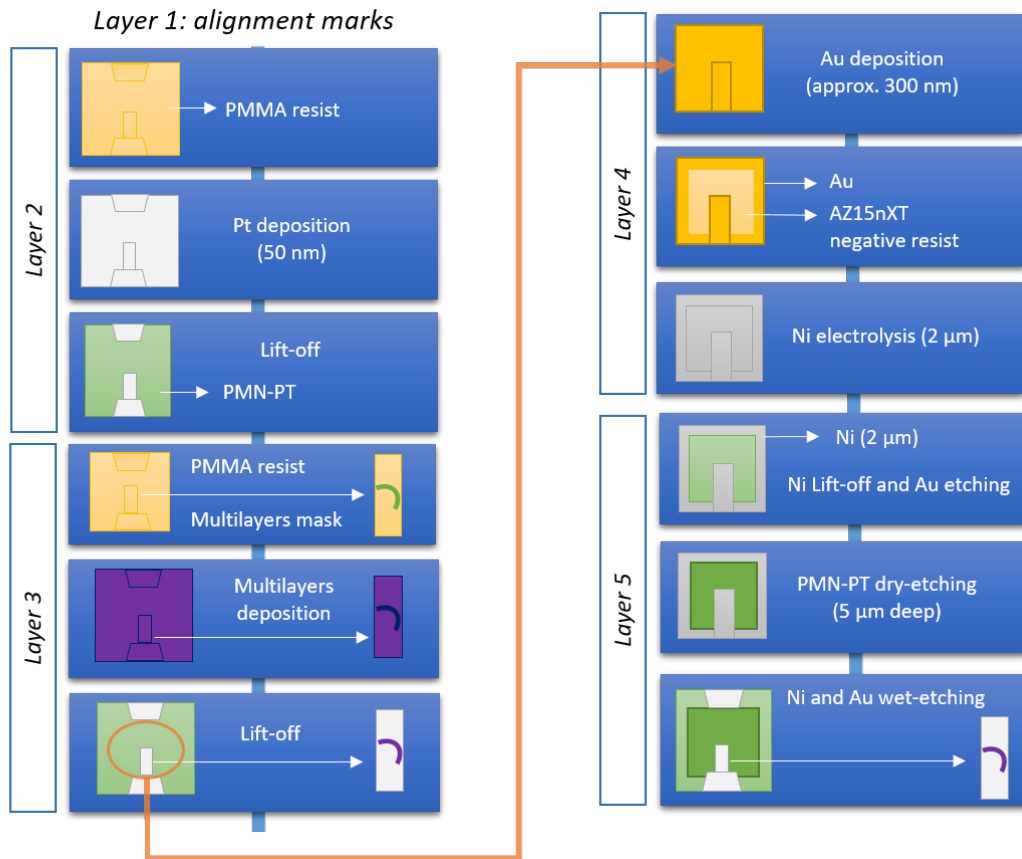


Figure 4.35 – Entire process broken down into simple steps, from bare substrate to etched surface with electrodes and magnetoelastic structures on studs.

the areas where the substrate is supposed to be etched. 2  $\mu\text{m}$  of nickel are deposited during the electrolysis. After lift-off, areas of the substrate to be dry-etched are open. Finally, after the deep etching of PMN-PT, the nickel and gold can be wet-etched one after the other.

## 4.5 Conclusion

In this chapter, we presented the various investigations pertaining to the attempt to experimentally observe the phenomenon studied numerically in previous chapters. The materials chosen for the implementation of the magnetoelectric coupling are (011)-cut PMN-PT for its particular piezoelectric properties, and rare-earth-based magnetoelastic multilayers routinely used at IEMN. On the fabrication process, few obstacles have been encountered, and at this point, a satisfying process has been developed. The successful

polishing of PMN-PT substrates allowed great surface quality on which lithography could be performed easily. TbCo<sub>2</sub>/FeCo multilayers were deposited by sputtering. The choice of lift-off of the multilayers yielded high-quality patterns with only limited abnormalities.

To begin on the characterization front, the piezoelectric properties of PMN-PT substrates were measured. The successful measurements hinted at a complex, nonlinear behavior that turned out to be consistent with data reported in the literature. The characterization of the multilayers deposited was done in the VSM, and confirmed the presence of a clearly defined uniaxial anisotropy. As for the magnetoelastic structures, AFM and MFM observations were carried out and we concluded that for the most part magnetoelastic elements had uniform magnetization. The use of a newly assembled Kerr microscope provided information about the magnetization distribution of larger elements. It was possible to observe a magnetoelectric effect on a sample subjected to a magnetic field and an electric field. Finally, several ideas on the possible opportunities for improvement on all these matters are discussed. The path toward integration, including work on deep-etching of PMN-PT substrates was also addressed.

# Conclusion

In this thesis we have proposed and studied in detail an innovative technique to induce the motion of transverse domain walls in nanostripes of constant and variable width.

As shown in chapter 1, this endeavor fits very well into current research trends in magnetism pertaining to the manipulation of magnetization and domain walls at the nanoscale. Magnetic fields and electric currents are routinely used to induce domain wall motion experimentally, and the study of the dynamics unveiled the complex behavior of magnetic domain walls, including the well-known Walker breakdown. The need to reduce energy consumption associated with device operation has led to efforts to find low-energy alternatives. Magnetoelectric materials are a promising example, since the use of an electric field offers advantages over electric currents. In particular, the mechanical coupling of a piezoelectric substrate and a magnetoelastic layer provides an interesting implementation of the magnetoelectric effect. Generally speaking, the application of a stress on a magnetic system is tantamount to the creation of an additional anisotropy. Among other works, previous investigations at IEMN showed the possibility to reversibly switch the magnetization of a magnetoelastic element with uniaxial anisotropy using a uniform stress and a static bias magnetic field arranged so that it breaks the quadratic symmetry. More precisely, if the easy axis is along  $\vec{x}$ , the magnetic field is generated along  $\vec{y}$  while the directions of uniaxial in-plane stress are given by the angle bisector. Several features conferred to this system relevant properties in the context of memory applications. The concept presented in this work capitalized on this previous experience to describe how the same combination of stress and magnetic field can give rise to controlled transverse domain wall motion in two-domain nanostructures. Further, another key idea in this work is the engineering of the potential landscape through a variable width.

While standard micromagnetic simulations were carried out and supported the proposition made, a simpler, *ad hoc* 1D model able to determine the magnetization distribution of minimal energy was developed and presented in chapter 2. This choice was motivated by two concerns: reducing the computational load involved, and providing to the user

full control on the parameters and algorithms used. As a first step, we gave a reminder of the classical micromagnetism equation governing the behavior of magnetization in the general case derived from variational methods. Then, the same approach was followed with more specific terms reflecting the geometry and configuration considered. The obtained equation was introduced into a relaxation procedure including a bisection-based solver, allowing both fast convergence and high accuracy as confirmed by the comparison against known analytical solutions. With an input geometry with a constant width, the numerical procedure described indefinite domain wall motion, leaving only one domain of lower energy. However, it was shown that if we consider a variable width (for instance hourglass-shaped), the domain wall can reach an equilibrium position, and returns to its original position at rest when the stress disappears. From this reversible behavior, a relationship between domain wall position and stress was established. Overall, energetic analyses showed that the phenomenon is caused by the action of the static magnetic field on two domains under the influence of an effective anisotropy resulting from the interplay between magnetocrystalline anisotropy and the applied stress. As such, the motion can be characterized as stress-triggered but field-driven. Looking at a piezoelectric generation of stress, we showed that such a system dissipates very small amounts of energy, mainly from Joule heating dissipation due to the charge and discharge cycle of the piezoelectric substrate.

The determination of equilibrium magnetization distributions does not yield information about the path followed by the magnetic system. The dynamics were therefore explored in chapter 3 through a second *ad hoc* 1D code. The outcome of the variational procedure was combined with the Landau-Lifshitz-Gilbert equation to obtain the desired dynamical system of equations. An implicit Euler algorithm based on the Newton method was used to solve this system, and was validated by its successful predictions on field-driven motion. The dynamics are influenced by the values of the applied stress and bias magnetic field, and it was shown that in a nanostripe with constant width, a steady-state motion is reached. From the physical point of view, stress-triggered motion stands apart from classical domain wall motion in that the corresponding domain wall shape features notable out-of-plane excursions in the vicinity of the domain wall. These excursions wane as the domain reaches its equilibrium position in a hourglass-shaped nanostructure. The extent of the out-of-plane component depends on the relative strength of compressive and tensile stress components, since they are associated with planar and uniaxial anisotropy, respectively. This is the reason why with the piezoelectric parameters considered the application of a negative and positive electric field does not result in the same dynamics

and domain wall shape. In any case, the values of velocities measured (up to 800 m/s and beyond, depending on parameters) compare favorably to those of more standard domain wall motion techniques. The plausibility that the failure of the code at high fields hinted at the existence of a phenomenon akin to a Walker breakdown was discussed.

Given the strong theoretical and numerical evidence presented, it seems likely that the phenomenon described can be observed in a real system. Chapter 4 covered experimental work carried out during the PhD. The choice of materials reflects the requirements of an efficient magnetoelectric coupling mediated by mechanical stress. When subjected to a vertical electric field, (011)-cut  $[\text{Pb}(\text{Mg}_{\frac{1}{3}}\text{Nb}_{\frac{2}{3}})\text{O}_3]_{1-x}-[\text{PbTiO}_3]_x$  (PMN-PT) around the morphotropic phase boundary generates large in-plane stress components of opposite signs. We saw how using rare-earth-based alloys in sputtered multilayers enables an interesting compromise between magnetization at saturation, magnetostriction and anisotropy. The fabrication process of magnetoelastic nanostructures on PMN-PT began by polishing the substrates to obtain surfaces of good quality. Both dry-etching and lift-off were tested, although only the latter yielded satisfying results. For that, positive resist lithography was successfully developed on PMN-PT, so that magnetoelastic multilayers could be deposited by sputtering before the lift-off was performed. As for characterization, piezoelectric measurements unveiled the strongly nonlinear nature of (011)-cut PMN-PT, with its hysteretic behavior that may prove useful for some applications. The magnetic properties of multilayers were measured by a vibrating sample magnetometer. The topography obtained by lift-off was probed by atomic force microscopy, while magnetic force microscopy provided information about the local magnetization of individual elements which happened to be mostly monodomain. A newly set up Kerr microscope allowed the magneto-optical observation of the system under magnetic field and electrically-induced stress, and a magnetoelectric effect was noticed. The potential ways forward and more application-oriented matters were discussed, including efforts put into the etching of PMN-PT to produce studs facilitating the piezoelectric actuation of individual devices.

Building on this work, there are both room for improvement and new lines of research to explore. On the numerical front, efforts could be put into analyzing the failure of the dynamical code further in order to bring support or dismiss the idea that there is indeed a Walker-like breakdown in the system studied. Such a finding might be significant from the physical point of view. Refined analyses using standard micromagnetic simulations could also help on this matter. On the experimental front, a collaboration with teams possessing complementary know-how on domain wall manipulation could very well result in the proper experimental observation of the phenomenon predicted, with the conditions

and geometry considered. Maybe other materials may prove more suitable. If successfully implemented, stress-triggered field-driven motion may prove both competitive and convenient. Further, the concept proposed paves the way for interesting variants. In particular, piezoelectrically actuated multistable systems may be of interest for some applications. Besides, the influence of a variable width on domain wall motion in general is also an interesting lead that may bring new insight on both fundamental and applied matters.

# Appendix A

## Domain wall with exchange and anisotropy energy

We analyze a specific domain wall configuration, which is important from both the theoretical and numerical points of view. We consider the simple case of a ferromagnetic stripe with only exchange and anisotropy energy contributions. The calculation is first carried out in the general case of a bounded geometry, and then extended to an infinite domain wall. Accordingly, the total energy can be deduced from Eq. (2.29), eventually obtaining

$$U = h\ell \int_{-\frac{L}{2}}^{+\frac{L}{2}} \left[ -K_u \cos^2 \Phi + A \left( \frac{d\Phi}{dx} \right)^2 \right] dx. \quad (\text{A.1})$$

The Lagrangian function of the variational problem is therefore

$$\mathcal{L} = -K_u \cos^2 \Phi + A\Phi'^2, \quad (\text{A.2})$$

where  $\Phi' \equiv \frac{d\Phi}{dx}$ . The associated Hamiltonian function is

$$\mathcal{H} = \frac{\partial \mathcal{L}}{\partial \Phi'} \Phi' - \mathcal{L} = A\Phi'^2 + K_u \cos^2 \Phi. \quad (\text{A.3})$$

Since  $\frac{\partial \mathcal{L}}{\partial x} = 0$ , we have the conservation of  $\mathcal{H}$ , leading to the simplified differential equation

$$\Phi' = \sqrt{-\frac{K_u}{A} \cos^2 \Phi + C_1}, \quad (\text{A.4})$$

where  $C_1$  is an integration constant. The boundary conditions

$$\Phi\left(-\frac{L}{2}\right) = 0 \quad , \quad \Phi\left(+\frac{L}{2}\right) = \pi, \quad (\text{A.5})$$

adopted to analyze the problem, guarantee the existence of the ferromagnetic domain wall. Separating the variables in Eq. (A.4), we obtain

$$\int_0^{\Phi} \frac{d\Phi}{\sqrt{C_2 + \sin^2 \Phi}} = \left(x + \frac{L}{2}\right) \sqrt{\frac{K_u}{A}}, \quad (\text{A.6})$$

where we used the first boundary condition and we introduced  $C_2 = AC_1/K_u - 1$ . The coefficient  $C_2$  can be calculated by considering the second boundary condition. We get

$$\int_0^{\pi} \frac{d\Phi}{\sqrt{C_2 + \sin^2 \Phi}} = 2 \int_0^{\frac{\pi}{2}} \frac{d\Phi}{\sqrt{C_2 + \sin^2 \Phi}} = L \sqrt{\frac{K_u}{A}}. \quad (\text{A.7})$$

We now introduce the integral [306]

$$\int \frac{dx}{\sqrt{1 + p^2 \sin^2 x}} = \frac{1}{\sqrt{1 + p^2}} F\left(\alpha, \frac{p}{\sqrt{1 + p^2}}\right), \quad (\text{A.8})$$

where  $\alpha = \arcsin \frac{\sqrt{1+p^2} \sin x}{\sqrt{1+p^2 \sin^2 x}}$  and  $F(\nu, q)$  is the incomplete elliptic integral of the first kind, defined as [307, 308]

$$F(\nu, q) = \int_0^{\nu} \frac{du}{\sqrt{1 - q^2 \sin^2 u}} = \int_0^{\sin \nu} \frac{dx}{\sqrt{(1 - x^2)(1 - q^2 x^2)}}. \quad (\text{A.9})$$

We therefore obtain the equation for  $C_2$  in the form

$$\frac{1}{\sqrt{1 + C_2}} K\left(\frac{1}{\sqrt{1 + C_2}}\right) = \frac{L}{2} \sqrt{\frac{K_u}{A}}, \quad (\text{A.10})$$

where we also used the complete elliptic integral of the first kind  $K(q)$  [307, 308]

$$K(q) = F\left(\frac{\pi}{2}, q\right) = \int_0^{\frac{\pi}{2}} \frac{du}{\sqrt{1 - q^2 \sin^2 u}} \quad (\text{A.11})$$

Similarly, we can rewrite Eq. (A.6) in terms of elliptic integrals

$$\sqrt{\frac{K_u}{A}} \left(x + \frac{L}{2}\right) = \frac{1}{\sqrt{1 + C_2}} F\left(\alpha_{\Phi}, \frac{1}{\sqrt{1 + C_2}}\right) \quad (\text{A.12})$$

where

$$\alpha_{\Phi} = \arcsin \frac{\sqrt{1 + C_2} \sin \Phi}{\sqrt{C_2 + \sin^2 \Phi}}. \quad (\text{A.13})$$

Equations (A.10) and (A.12), although in implicit form, solve the problem of the finite-length stripe with exchange and anisotropy energies. We finally observe that by defining  $\xi = \sqrt{1 + C_2}$ , these equations can be further simplified as follows

$$\sqrt{\frac{K_u}{A}} \left( x + \frac{L}{2} \right) = \frac{1}{\xi} F \left( \arcsin \frac{\xi \sin \Phi}{\sqrt{\xi^2 - \cos^2 \Phi}}, \frac{1}{\xi} \right), \quad (\text{A.14})$$

$$\frac{1}{\xi} K \left( \frac{1}{\xi} \right) = \frac{L}{2} \sqrt{\frac{K_u}{A}}. \quad (\text{A.15})$$

It is interesting to prove that, for  $L \rightarrow \infty$ , we obtain the classical wall calculation as found in [20]. To begin, we note that  $\xi \rightarrow 1^+$  and therefore  $\eta \equiv 1/\xi \rightarrow 1^-$  when  $L \rightarrow \infty$ . Equation (A.14), in terms of  $\eta$ , becomes

$$\sqrt{\frac{K_u}{A}} x + \eta K(\eta) = \eta F \left( \arcsin \frac{\sin \Phi}{\sqrt{1 - \eta^2 \cos^2 \Phi}}, \eta \right). \quad (\text{A.16})$$

Hence, the limiting case for  $L \rightarrow \infty$  is not trivial since both arguments of the elliptic function  $F$  in Eq. (A.16) depends on  $\eta \rightarrow 1^-$ . To cope with with this problem, we use the following property of the function  $F$  [307, 308]

$$\begin{aligned} F(\varphi, \sin \alpha) + F(\psi, \sin \alpha) &= K(\sin \alpha) \\ \text{if } \cos \alpha \tan \varphi \tan \psi &= 1, \end{aligned} \quad (\text{A.17})$$

with  $\sin \alpha = \eta$  and  $\varphi = \arcsin \frac{\sin \Phi}{\sqrt{1 - \eta^2 \cos^2 \Phi}}$ . Then Eq. (A.16) can be eventually rewritten as

$$\sqrt{\frac{K_u}{A}} x + \eta F(\psi, \eta) = 0, \quad (\text{A.18})$$

where  $\psi$  can be found through the relation

$$\tan \psi = \frac{1}{\cos \alpha \tan \varphi} = \frac{\sqrt{1 - \eta^2 \cos^2 \Phi - \sin^2 \Phi}}{\sin \Phi \sqrt{1 - \eta^2}}, \quad (\text{A.19})$$

leading to  $\sin \psi = \cos \Phi$ .

Consequently, substituting the expression of  $\psi$  into Eq. (A.18), we have  $\sqrt{\frac{K_u}{A}} x + \eta F(\arcsin \cos \Phi, \eta) = 0$ . Therefore, for  $L \rightarrow \infty$  (i.e.  $\eta \rightarrow 1$ ), we have that  $\sqrt{\frac{K_u}{A}} x + \eta F(\arcsin \cos \Phi, 1) = 0$ . Now, we use the property [307, 308]

$$F(\psi, 1) = \ln(\sec \psi + \tan \psi), \quad (\text{A.20})$$

and we can easily obtain the result

$$\begin{aligned}\Phi(x) &= 2 \arctan \left( \exp \left( \sqrt{\frac{K_u}{A}} x \right) \right) \\ &= \pi - \arccos \left[ \tanh \left( \sqrt{\frac{K_u}{A}} x \right) \right],\end{aligned}\tag{A.21}$$

which is the well-known solution for the infinitely long stripe with exchange and anisotropy energies [20].

# Appendix B

## Variational procedure

The minimization of the functional  $U$  defined in Eq. (2.6) can be performed as follows

$$\min_{\vec{w}: \|\vec{w}\|=1} U \rightarrow \min_{\vec{w}} \left[ U + \int_V \lambda (\vec{w} \cdot \vec{w} - 1) d\vec{r} \right], \quad (\text{B.1})$$

where  $\lambda = \lambda(\vec{r})$  is a Lagrange multiplier introduced to fix the norm of the unit vector  $\vec{w}$ . Therefore, we have to minimize

$$U' = \int_V \left[ u_{an} + u_{ex} + u_{me} + \lambda (\vec{w} \cdot \vec{w} - 1) \underbrace{-\mu_0 M_s \vec{H}_L \cdot \vec{w}}_{u_{Ze}} \right] d\vec{r}, \quad (\text{B.2})$$

with  $\vec{H}_l$  fixed. This functional assumes its extremal value when

$$\left. \frac{d}{d\beta} U' [\vec{w}(\vec{r}) + \beta \vec{k}(\vec{r})] \right|_{\beta=0} = 0 \quad \forall \vec{k}(\vec{r}), \quad (\text{B.3})$$

where the left-hand side represents the Gâteaux derivative of the functional  $U'$  [277]. If we define the quantity  $U''(\vec{w}) = U'(\vec{w}) - \int_V u_{Ze} d\vec{r}$ , Eq. (B.3) can be rewritten as

$$\left. \frac{d}{d\beta} U'' [\vec{w} + \beta \vec{k}] \right|_{\beta=0} - \left. \frac{d}{d\beta} \int_V \mu_0 M_s \vec{H}_l \cdot (\vec{w} + \beta \vec{k}) d\vec{r} \right|_{\beta=0} = 0, \quad (\text{B.4})$$

or, equivalently, as

$$\left. \frac{d}{d\beta} U'' [\vec{w} + \beta \vec{k}] \right|_{\beta=0} - \int_V \mu_0 M_s \vec{H}_l \cdot \vec{k} d\vec{r} = 0. \quad (\text{B.5})$$

Although in implicit form, this is the equation giving  $\vec{w}(\vec{r})$  in  $V$ . At this point, we can combine it with  $\vec{H}_l = \vec{H}_0 + \vec{H}_d$ . It is important to note that this substitution cannot be

made in  $U$  or  $U'$ , before the minimization, since  $\vec{H}_d$  is a function of  $\vec{w}$ . In Then, Eq. (B.5) becomes

$$\begin{aligned} & \left. \frac{d}{d\beta} U'' [\vec{w} + \beta \vec{k}] \right|_{\beta=0} - \int_V \mu_0 M_s \vec{H}_0 \cdot \vec{k} \, d\vec{r} \\ & - \iint_{V^2} \mu_0 M_s^2 \vec{k}(\vec{r}) \cdot \overline{\vec{N}}(\vec{r}, \vec{r}_0) \vec{w}(\vec{r}_0) \, d\vec{r}_0 d\vec{r} = 0, \end{aligned} \quad (\text{B.6})$$

where we used Eq. (2.7) for the demagnetization field. Equivalently, we can also write

$$\begin{aligned} & \left. \frac{d}{d\beta} U'' [\vec{w} + \beta \vec{k}] \right|_{\beta=0} - \left. \frac{d}{d\beta} \left( \int_V \mu_0 M_s \vec{H}_0 \cdot (\vec{w} + \beta \vec{k}) \, d\vec{r} \right) \right|_{\beta=0} \\ & + \left. \iint_{V^2} \frac{1}{2} \mu_0 M_s^2 [\vec{w}(\vec{r}) + \beta \vec{k}(\vec{r})] \cdot \overline{\vec{N}}(\vec{r}, \vec{r}_0) [\vec{w}(\vec{r}_0) + \beta \vec{k}(\vec{r}_0)] \, d\vec{r}_0 d\vec{r} \right|_{\beta=0} \\ & = 0. \end{aligned} \quad (\text{B.7})$$

where we used the symmetries described in Eqs.(2.9a) and (2.9b). We can then define an auxiliary function  $\tilde{U}'$

$$\tilde{U}' = U''(\vec{w}) - \int_V \mu_0 M_s \vec{H}_0 \cdot \vec{w} \, d\vec{r} - \iint_{V^2} \frac{1}{2} \mu_0 M_s^2 \vec{w}(\vec{r}) \cdot \overline{\vec{N}}(\vec{r}, \vec{r}_0) \vec{w}(\vec{r}_0) \, d\vec{r}_0 d\vec{r}, \quad (\text{B.8})$$

which can be minimized with  $\vec{H}_0$  fixed. We have therefore proved this series of equivalences

$$\min_{\vec{w}: \|\vec{w}\|=1} U \Big|_{\vec{H}_L \text{ fixed}} \Leftrightarrow \min_{\vec{w}} U' \Big|_{\vec{H}_L \text{ fixed}} \Leftrightarrow \min_{\vec{w}} \tilde{U}' \Big|_{\vec{H}_0 \text{ fixed}} \Leftrightarrow \min_{\vec{w}: \|\vec{w}\|=1} \tilde{U} \Big|_{\vec{H}_0 \text{ fixed}}, \quad (\text{B.9})$$

where  $\tilde{U}$  is defined in Eq. (2.11). Finally, the minimization of  $\tilde{U}$  with respect to the direction  $\vec{w}$ , with  $\overline{\vec{T}}$  and  $\vec{H}_0$  imposed, leads to the actual magnetization of the ferromagnetic body. We can therefore apply the methods of the calculus of variations to obtain the equation for  $\vec{w}$ . As before, we work with the Gâteaux derivative

$$\left. \frac{d}{d\beta} \tilde{U}' (\vec{w} + \beta \vec{k}) \right|_{\beta=0} = 0, \quad (\text{B.10})$$

where

$$\tilde{U}'(\vec{w}) = \tilde{U} + \int_V \lambda(\vec{r})(\vec{w} \cdot \vec{w} - 1) \, d\vec{r}. \quad (\text{B.11})$$

We obtain

$$\int_V \left[ \frac{\partial f_{an}}{\partial \vec{w}} \cdot \vec{k} - \frac{1}{2} \beta_{ij} \left( \frac{\partial k_l}{\partial x_i} \frac{\partial w_l}{\partial x_j} + \frac{\partial w_l}{\partial x_i} \frac{\partial k_l}{\partial x_j} \right) + 2\lambda k_l w_l - \mu_0 M_s H_{0i} k_i \right. \\ \left. - a_{iklm} T_{ik} (k_l w_m + w_l k_m) - \mu_0 M_s^2 \int_V N_{ij}(\vec{r}, \vec{r}_0) k_i(\vec{r}) w_j(\vec{r}_0) d\vec{r}_0 \right] d\vec{r} = 0, \quad (\text{B.12})$$

where we used again both symmetries of tensor  $\overline{\overline{N}}$ . To proceed from here, we use the divergence theorem in the form

$$\int_V \frac{\partial h}{\partial x_i} d\vec{r} = \int_{\partial V} h n_i dS. \quad (\text{B.13})$$

Now, if  $h = fg$ , we have

$$\int_V f \frac{\partial g}{\partial x_i} d\vec{r} = \int_{\partial V} fg n_i dS - \int_V g \frac{\partial f}{\partial x_i} d\vec{r}. \quad (\text{B.14})$$

This property can be used on the exchange terms to further elaborate Eq. (B.12), as follows

$$\int_V \left[ \frac{\partial f_{an}}{\partial \vec{w}} \cdot \vec{k} - \beta_{ij} k_l \frac{\partial^2 w_l}{\partial x_i \partial x_j} + 2\lambda k_l w_l - \mu_0 M_s H_{0l} k_l - 2a_{iklm} T_{ik} k_l w_m \right. \\ \left. - \mu_0 M_s^2 \int_V N_{ij}(\vec{r}, \vec{r}_0) k_i(\vec{r}) w_j(\vec{r}_0) d\vec{r}_0 \right] d\vec{r} + \int_{\partial V} \beta_{ij} k_l \frac{\partial w_l}{\partial x_j} n_i dS = 0, \quad (\text{B.15})$$

where we exploited the symmetry of tensor  $\beta_{ij}$ . The first integral of Eq. (B.15) being true for any smooth function  $k \in \mathbb{R}^3$ , we can write

$$\frac{\partial f_{an}}{\partial \vec{w}} - \beta_{ij} \frac{\partial^2 \vec{w}}{\partial x_i \partial x_j} - \mu_0 M_s \vec{H}_0 + 2\lambda \vec{w} - \mu_0 M_s \vec{H}_d - 2\overline{\overline{a}} : \overline{\overline{T}} \vec{w} = 0, \quad (\text{B.16})$$

where  $\left( \overline{\overline{a}} : \overline{\overline{T}} \vec{w} \right)_l = a_{iklm} T_{ik} w_m$ . The Lagrange multiplier  $\lambda$  can be finally eliminated by applying a cross-product with  $\vec{w}$ , which yields Eqs. (2.12) and (2.13).

From Eq. (B.15), we can also deduce the boundary conditions which can be applied to minimize the energy functional:  $\beta_{ij} k_l \frac{\partial w_l}{\partial x_j} n_i = 0$  on  $\partial V$ , where the perturbation vector  $\vec{k}$  is not free since it must verify the condition  $\left( \vec{w} + \beta \vec{k} \right) \cdot \left( \vec{w} + \beta \vec{k} \right) = 1$  when  $\vec{w} \cdot \vec{w} = \|\vec{w}\|^2 = 1$ . To the first order in  $\beta$  this translates to  $\vec{w} \cdot \vec{k} = 0$  and, therefore, we can say

that  $\vec{k} = \vec{w} \times \vec{w}$  for an arbitrary vector  $\vec{w}$ . Then,  $\vec{k}$  is not arbitrary but  $\vec{w}$  is completely free. By considering  $k_l = \epsilon_{lst} w_s w_t$ , we have  $\beta_{ij} \epsilon_{lst} w_s w_t \frac{\partial w_l}{\partial x_j} n_i = 0 \forall w_s$ , or  $\beta_{ij} \epsilon_{lst} w_t \frac{\partial w_l}{\partial x_j} n_i = 0 \forall s$  on  $\partial V$  ( $\epsilon_{lst}$  being the Levi-Civita permutation symbol). This condition can be strongly simplified when  $\beta_{ij} \propto \delta_{ij}$  (isotropic exchange). In this case we have  $\epsilon_{lst} w_t \frac{\partial w_l}{\partial x_i} n_i = 0 \forall s$ , where  $\frac{\partial w_l}{\partial x_i} n_i$  is the directional derivative of  $w_l$  along  $\vec{n}$ . So, it corresponds to  $\vec{w} \times \frac{\partial \vec{w}}{\partial \vec{n}} = 0$ . We also observe that  $\vec{w}$  is always perpendicular to  $\frac{\partial \vec{w}}{\partial \vec{n}}$  since  $\|\vec{w}\| = 1$ . Therefore, in order to impose  $\vec{w} \times \frac{\partial \vec{w}}{\partial \vec{n}} = 0$ , it is sufficient to have  $\frac{\partial \vec{w}}{\partial \vec{n}} = 0$  on  $\partial V$ .

# Appendix C

## Calculation of the demagnetization field

We provide here a technique to numerically evaluate the demagnetization field in our system. A similar approach can be found in the literature [309]. To begin, we consider Eq. (2.7) giving the demagnetization field for an arbitrary region  $V$ . In analogy with the theory of the electric dipole [269], we may introduce a magnetic scalar potential  $\phi$  such that

$$\vec{H}_d(\vec{r}) = -\vec{\nabla}\phi, \quad (\text{C.1})$$

where

$$\phi(\vec{r}) = \int_V \frac{1}{4\pi} \frac{\vec{M}(\vec{r}_0) \cdot (\vec{r} - \vec{r}_0)}{\|\vec{r} - \vec{r}_0\|^3} d\vec{r}_0. \quad (\text{C.2})$$

A useful development can be performed when the magnetization  $\vec{M}$  is uniform in a given region. In this case we can apply the divergence theorem

$$\int_V \text{div } \vec{w} d\vec{r} = \int_{\partial V} \vec{w} \cdot \vec{n} dS, \quad (\text{C.3})$$

where we consider  $\vec{w} = \frac{\vec{M}}{\|\vec{r} - \vec{r}_0\|}$ , with a constant field  $\vec{M}$ . Indeed, we obtain

$$\text{div } \vec{w} = \vec{M} \cdot \vec{\nabla} \frac{1}{\|\vec{r} - \vec{r}_0\|} = \vec{M} \cdot \frac{\vec{r} - \vec{r}_0}{\|\vec{r} - \vec{r}_0\|^3}, \quad (\text{C.4})$$

and therefore Eq. (C.3) reads

$$\int_V \vec{M} \cdot \frac{\vec{r} - \vec{r}_0}{\|\vec{r} - \vec{r}_0\|^3} d\vec{r} = \int_{\partial V} \frac{\vec{M} \cdot \vec{n}}{\|\vec{r} - \vec{r}_0\|} dS. \quad (\text{C.5})$$

As a conclusion, for a uniform magnetization  $\vec{M}$ , the scalar potential is given by

$$\phi(\vec{r}) = \frac{1}{4\pi} \vec{M} \cdot \int_{\partial V} \frac{\vec{n} dS}{\|\vec{r} - \vec{r}_0\|}, \quad (\text{C.6})$$

where  $\vec{n}$  is the unit vector normal to the external surface  $\partial V$  with area element  $dS$ . To calculate the total demagnetization field in a given point, we can partition the whole region in a given number of parallelepipedal layers. As discussed below, the parallelepipedal geometry allows for quick and simple computation of the demagnetization field through the scalar potential  $\phi$ . Then, we can add all the contributions to obtain the final result. Hence, we suppose  $\vec{M}$  uniform within the arbitrary parallelepiped  $[x_1, x_2] \times [y_1, y_2] \times [z_1, z_2]$ , and we calculate  $\phi$  through Eq. (C.6). We define the integral  $\vec{I} = \int_{\partial V} \frac{\vec{n} dS}{\|\vec{r} - \vec{r}_0\|}$  and we write the  $x$  component as

$$I_x = \int_{z_1}^{z_2} \int_{y_1}^{y_2} \frac{dy_0 dz_0}{\sqrt{(x - x_2)^2 + (y - y_0)^2 + (z - z_0)^2}} - \int_{z_1}^{z_2} \int_{y_1}^{y_2} \frac{dy_0 dz_0}{\sqrt{(x - x_1)^2 + (y - y_0)^2 + (z - z_0)^2}}. \quad (\text{C.7})$$

A change of variables leads to

$$I_x = \int_{z-z_1}^{z-z_2} \int_{y-y_1}^{y-y_2} \left( \frac{1}{\sqrt{(x-x_2)^2 + \xi^2 + \eta^2}} - \frac{1}{\sqrt{(x-x_1)^2 + \xi^2 + \eta^2}} \right) d\xi d\eta. \quad (\text{C.8})$$

Now, let us define the function  $\mathcal{F}(A, B, C, D, E, F)$  as

$$\mathcal{F} = \int_A^B \int_C^D \left[ \frac{1}{\sqrt{E^2 + \xi^2 + \eta^2}} - \frac{1}{\sqrt{F^2 + \xi^2 + \eta^2}} \right] d\xi d\eta, \quad (\text{C.9})$$

and we obtain the demagnetization potential in the form

$$\phi(\vec{r}) = \frac{1}{4\pi} [M_x I_x + M_y I_y + M_z I_z], \quad (\text{C.10})$$

where

$$I_x = \mathcal{F}(z - z_1, z - z_2, y - y_1, y - y_2, x - x_1, x - x_2), \quad (\text{C.11})$$

$$I_y = \mathcal{F}(x - x_1, x - x_2, z - z_1, z - z_2, y - y_1, y - y_2), \quad (\text{C.12})$$

$$I_z = \mathcal{F}(y - y_1, y - y_2, x - x_1, x - x_2, z - z_1, z - z_2). \quad (\text{C.13})$$

To lighten the notation, we chose to write it in more concise form

$$\phi(\vec{r}) = \frac{1}{4\pi} \left[ M_x \mathcal{F} \Big|_{321} + M_y \mathcal{F} \Big|_{132} + M_z \mathcal{F} \Big|_{213} \right]. \quad (\text{C.14})$$

where the symbol  $\mathcal{F} \Big|_{ijk}$  means that the function  $\mathcal{F}$  is calculated with variables specified in Eqs. (C.11), (C.12) and (C.13). Finally, the components of the demagnetization field can be derived as

$$\begin{aligned}
H_{dx} = -\frac{\partial\phi}{\partial x} = & -\frac{1}{4\pi} \left[ M_x \left( \frac{\partial\mathcal{F}}{\partial E} \Big|_{321} + \frac{\partial\mathcal{F}}{\partial F} \Big|_{321} \right) \right. \\
& + M_y \left( \frac{\partial\mathcal{F}}{\partial A} \Big|_{132} + \frac{\partial\mathcal{F}}{\partial B} \Big|_{132} \right) \\
& \left. + M_z \left( \frac{\partial\mathcal{F}}{\partial C} \Big|_{213} + \frac{\partial\mathcal{F}}{\partial D} \Big|_{213} \right) \right], \tag{C.15}
\end{aligned}$$

$$\begin{aligned}
H_{dy} = -\frac{\partial\phi}{\partial y} = & -\frac{1}{4\pi} \left[ M_x \left( \frac{\partial\mathcal{F}}{\partial C} \Big|_{321} + \frac{\partial\mathcal{F}}{\partial D} \Big|_{321} \right) \right. \\
& + M_y \left( \frac{\partial\mathcal{F}}{\partial E} \Big|_{132} + \frac{\partial\mathcal{F}}{\partial F} \Big|_{132} \right) \\
& \left. + M_z \left( \frac{\partial\mathcal{F}}{\partial A} \Big|_{213} + \frac{\partial\mathcal{F}}{\partial B} \Big|_{213} \right) \right], \tag{C.16}
\end{aligned}$$

$$\begin{aligned}
H_{dz} = -\frac{\partial\phi}{\partial z} = & -\frac{1}{4\pi} \left[ M_x \left( \frac{\partial\mathcal{F}}{\partial A} \Big|_{321} + \frac{\partial\mathcal{F}}{\partial B} \Big|_{321} \right) \right. \\
& + M_y \left( \frac{\partial\mathcal{F}}{\partial C} \Big|_{132} + \frac{\partial\mathcal{F}}{\partial D} \Big|_{132} \right) \\
& \left. + M_z \left( \frac{\partial\mathcal{F}}{\partial E} \Big|_{213} + \frac{\partial\mathcal{F}}{\partial F} \Big|_{213} \right) \right]. \tag{C.17}
\end{aligned}$$

In Eq. (2.40), we are working with a two-dimensional problem where  $M_z = 0$  and, therefore, the number of necessary components to compute  $\vec{H}_d$  is reduced. Moreover, the symmetry in Eq. (2.9a) allows us to prove that the operator relating  $\vec{H}_d$  and  $\vec{M}$  is always symmetric. As a result, we have

$$\frac{\partial\mathcal{F}}{\partial A} \Big|_{132} + \frac{\partial\mathcal{F}}{\partial B} \Big|_{132} = \frac{\partial\mathcal{F}}{\partial C} \Big|_{321} + \frac{\partial\mathcal{F}}{\partial D} \Big|_{321}, \tag{C.18}$$

a property which further reduces the complexity of Eqs.(C.15) and (C.16)

$$\begin{aligned}
H_{dx} = & -\frac{1}{4\pi} \left[ M_x \left( \frac{\partial\mathcal{F}}{\partial E} \Big|_{321} + \frac{\partial\mathcal{F}}{\partial F} \Big|_{321} \right) \right. \\
& \left. + M_y \left( \frac{\partial\mathcal{F}}{\partial A} \Big|_{132} + \frac{\partial\mathcal{F}}{\partial B} \Big|_{132} \right) \right], \tag{C.19}
\end{aligned}$$

$$\begin{aligned}
H_{dy} = & -\frac{1}{4\pi} \left[ M_x \left( \left. \frac{\partial \mathcal{F}}{\partial A} \right|_{132} + \left. \frac{\partial \mathcal{F}}{\partial B} \right|_{132} \right) \right. \\
& \left. + M_y \left( \left. \frac{\partial \mathcal{F}}{\partial E} \right|_{132} + \left. \frac{\partial \mathcal{F}}{\partial F} \right|_{132} \right) \right]. \tag{C.20}
\end{aligned}$$

To complete this discussion, one can observe that the integral in Eq. (C.9) can be calculated in closed form. This is very useful for the numerical implementation of the proposed procedure

$$\begin{aligned}
\mathcal{F} = & A \ln \frac{\sqrt{E^2 + A^2 + D^2} + D \sqrt{F^2 + A^2 + C^2} + C}{\sqrt{F^2 + A^2 + D^2} + D \sqrt{E^2 + A^2 + C^2} + C} \\
& + B \ln \frac{\sqrt{E^2 + B^2 + C^2} + C \sqrt{F^2 + B^2 + D^2} + D}{\sqrt{F^2 + B^2 + C^2} + C \sqrt{E^2 + B^2 + D^2} + D} \\
& + C \ln \frac{\sqrt{E^2 + A^2 + C^2} - A \sqrt{F^2 + B^2 + C^2} - B}{\sqrt{F^2 + A^2 + C^2} - A \sqrt{E^2 + B^2 + C^2} - B} \\
& + D \ln \frac{\sqrt{E^2 + B^2 + D^2} - B \sqrt{F^2 + A^2 + D^2} - A}{\sqrt{F^2 + B^2 + D^2} - B \sqrt{E^2 + A^2 + D^2} - A} \\
& + E \arctan \left( \frac{E^2 + A^2 - A \sqrt{E^2 + A^2 + D^2}}{D E} \right) \\
& - E \arctan \left( \frac{E^2 + A^2 - A \sqrt{E^2 + A^2 + C^2}}{C E} \right) \\
& - E \arctan \left( \frac{E^2 + B^2 - B \sqrt{E^2 + B^2 + D^2}}{D E} \right) \\
& + E \arctan \left( \frac{E^2 + B^2 - B \sqrt{E^2 + B^2 + C^2}}{C E} \right) \\
& - F \arctan \left( \frac{F^2 + A^2 - A \sqrt{F^2 + A^2 + D^2}}{D F} \right) \\
& + F \arctan \left( \frac{F^2 + A^2 - A \sqrt{F^2 + A^2 + C^2}}{C F} \right) \\
& + F \arctan \left( \frac{F^2 + B^2 - B \sqrt{F^2 + B^2 + D^2}}{D F} \right) \\
& - F \arctan \left( \frac{F^2 + B^2 - B \sqrt{F^2 + B^2 + C^2}}{C F} \right). \tag{C.21}
\end{aligned}$$

Moreover, all its derivatives can be computed in order to implement Eqs.(C.15), (C.16) and (C.17). This can be easily done in a symbolic environment.

# Appendix D

## Analytical treatment of domain wall motion

This appendix contains a short derivation of the classical Walker solution for the motion of a  $180^\circ$  domain wall in a slightly adapted version. Indeed, since in this thesis we work with head-to-head domain walls in thin films, this is the configuration chosen here instead of the original domain wall studied by Schryer and Walker, in which the easy axis is perpendicular to the direction of motion [75]. In order to guarantee simplicity in the derivation, we adopt the convention of spherical coordinates used by Schryer and Walker for the angles describing the direction of magnetization. Therefore, there will be some key differences between the convention used here (angles noted  $\phi$  and  $\theta$ ) - which mirrors that of Schryer and Walker - and what is used in chapters 2 and 3 (angles noted  $\Phi$  and  $\Theta$ ). The direction of motion is along  $\vec{z}$  so that the magnetization  $\vec{w}$  can be written  $(\cos \phi \cos \theta, \cos \phi \sin \theta, \cos \theta)$ .

We consider a ferromagnetic material with uniaxial anisotropy along the  $z$ -axis (constant  $K_u$ ), forming two domains with antiparallel magnetization along the direction of motion. A uniform magnetic field  $\vec{H}_1 = H_1 \vec{z}$  is applied. The exchange interaction is also taken into account. As for the demagnetization, a simplified form is introduced, corresponding to the demagnetization of a uniformly magnetized ellipsoid. At any point, its direction is opposed to local magnetization so that  $\vec{H}_d = -M_s \overline{\overline{N}} \vec{w}$ , with  $\overline{\overline{N}}$  a diagonal tensor with unit trace.

By analogy with Eq. (3.9), we can easily write the corresponding effective field:

$$\vec{H}_{\text{eff}} = \vec{H}_1 - M_s \overline{\overline{N}} \vec{w} + \frac{2}{\mu_0 M_s} \left( -K_u w_z \vec{z} + A \frac{\partial \vec{w}}{\partial z} \right). \quad (\text{D.1})$$

Following the same path as in subsection 3.1.4, we obtain the dynamical equations:

$$\begin{cases} \dot{\phi} &= -\frac{1}{\sin\theta} \frac{\gamma_0}{1+\alpha^2} (-s_w + \alpha r_w), \\ \dot{\theta} &= -\frac{\gamma_0}{1+\alpha^2} (r_w + \alpha s_w), \end{cases} \quad (\text{D.2})$$

The quantities  $r_w$  and  $s_w$  are as follows:

$$r_w = \frac{2A}{\mu_0 M_s} (\sin\theta\phi'' + 2\cos\theta\phi'\theta') + M_s \cos\phi \sin\phi \sin\theta (N_x - N_y), \quad (\text{D.3})$$

$$\begin{aligned} s_w &= -\sin\theta H_1 + \frac{2}{\mu_0 M_s} (-K_u \sin\theta \cos\theta + A(\theta'' - \sin\theta \cos\theta\phi'^2)) \\ &\quad + M_s \sin\theta \cos\theta (N_z - \cos^2\phi N_x - \sin^2\phi N_y). \end{aligned} \quad (\text{D.4})$$

In the case of an infinite ellipsoid along the  $z$ -axis, the element  $N_z$  of tensor  $\overline{\overline{N}}$  is zero.

Now, two assumptions will be made on the shape of the domain wall, which allow us to find a solution of the dynamical system above. The first assumption is that  $\phi = \phi_0$  is constant and uniform, this brings some simplification to the equation, since as a result  $\phi'$ ,  $\phi''$  and  $\dot{\phi}$  are all equal to 0. The second assumption is that  $\theta$  assumes the classical domain wall shape derived in appendix A and travels at a constant velocity  $v$ :

$$\theta(x, t) = \theta^\infty(\xi(x - vt)) = 2 \arctan(\exp \xi), \quad (\text{D.5})$$

where we introduced  $\tilde{K}_u = K_u + \frac{\mu_0 M_s^2}{2} (\cos\phi_0 N_x + \sin^2\phi_0 N_y)$  and  $\xi = \sqrt{\frac{\tilde{K}_u}{A}}(x - vt)$ . These assumptions lead to significant simplifications of the dynamical equations, due to the relationship between  $\theta$  and its derivatives:

$$\frac{d\theta^\infty}{d\xi} = \frac{2 \exp \xi}{1 + (\exp \xi)^2} = \sin \theta^\infty, \quad (\text{D.6})$$

since  $\exp \xi = \tan \frac{\theta^\infty}{2}$ . Therefore it follows that

$$\frac{\partial \theta}{\partial t} = \frac{\partial \xi}{\partial t} \frac{d\theta^\infty}{d\xi} = -\sqrt{\frac{\tilde{K}_u}{A}} v \sin \theta^\infty. \quad (\text{D.7})$$

Likewise,

$$\frac{\partial \theta}{\partial x} = \sqrt{\frac{\tilde{K}_u}{A}} \sin \theta^\infty, \quad (\text{D.8})$$

$$\text{and } \frac{\partial^2 \theta}{\partial x^2} = \frac{\tilde{K}_u}{A} \sin \theta^\infty \cos \theta^\infty. \quad (\text{D.9})$$

The first part of Eq. (D.2) reads

$$\alpha M_s \cos \phi_0 \sin \phi_0 \sin \theta^\infty (N_x - N_y) + \sin \theta^\infty H_1 - \frac{2}{\mu_0 M_s} \left( \tilde{K}_u \sin \theta^\infty \cos \theta^\infty - A \theta'' \right) = 0, \quad (\text{D.10})$$

and then using Eq. (D.9)

$$\alpha M_s \cos \phi_0 \sin \phi_0 \sin \theta^\infty (N_x - N_y) = -\sin \theta^\infty H_1. \quad (\text{D.11})$$

This equation yields the desired relationship giving the angle  $\phi_0$ :

$$\sin 2\phi_0 = \frac{2H_1}{\alpha M_s (N_y - N_x)} = \frac{H_1}{H_c}, \quad (\text{D.12})$$

where  $H_c = \frac{\alpha M_s (N_y - N_x)}{2}$  is the so-called Walker breakdown field. As the value of  $\sin 2\phi_0$  cannot exceed 1, there is a solution to this equation only when  $H_1 < H_c$ . As for the second part of Eq. (D.2),

$$\dot{\theta} = -\sqrt{\frac{\tilde{K}_u}{A}} v \sin \theta^\infty = -\frac{\gamma_0}{1 + \alpha^2} \left( \alpha (-\sin \theta^\infty) + M_s \cos \phi_0 \sin \phi_0 \sin \theta^\infty (N_x - N_y) \right). \quad (\text{D.13})$$

Using Eq. (D.12) ( $\sin \phi_0 \cos \phi_0 = \frac{1}{2} \sin 2\phi_0$ ) and dividing by  $-\sin \theta^\infty$ :

$$v = -\frac{\tilde{K}_u}{A} \frac{\gamma_0}{1 + \alpha^2} \left( \alpha H_1 + \frac{H_1}{\alpha} \right). \quad (\text{D.14})$$

In the end, the Walker solution is given by the following system:

$$v = -\frac{\gamma_0 H_1}{\alpha} \sqrt{\frac{A}{K_u + \mu_0 M_s^2 / 2 (\cos^2 \phi_0 N_x + \sin^2 \phi_0 N_y)}}, \quad (\text{D.15})$$

$$\sin 2\phi_0 = \frac{2H_1}{\alpha M_s (N_y - N_x)} = \frac{H_1}{H_c}. \quad (\text{D.16})$$

# Bibliography

- [1] William Fuller Brown. *Micromagnetics*. Number 18. Interscience Publishers, 1963.
- [2] Soshin Chikazumi and Chad D Graham. *Physics of Ferromagnetism 2e*, volume 94. Oxford University Press on Demand, 2009.
- [3] A. S. Arrott. Introduction to Micromagnetics. In Bretislav Heinrich and J. Anthony C. Bland, editors, *Ultrathin Magnetic Structures IV*, pages 101–148. Springer Berlin Heidelberg, 2005.
- [4] Yuri Mnyukh and Yuri Mnyukh. Paramagnetic State and Phase Transitions. *American Journal of Condensed Matter Physics*, 5(2):56–59, 2015.
- [5] SP Li, D Peyrade, M Natali, A Lebib, Y Chen, U Ebels, LD Buda, and K Ounadjela. Flux closure structures in cobalt rings. *Physical Review Letters*, 86(6):1102, 2001.
- [6] Etienne Lacheisserie and University Joseph Fourier. *Magnetism: Fundamentals, Materials and Applications*. Springer Science & Business Media, October 2002. Google-Books-ID: 2w840sO28pAC.
- [7] Charles Kittel. Physical Theory of Ferromagnetic Domains. *Reviews of Modern Physics*, 21(4):541–583, October 1949.
- [8] Alex Hubert and Rudolf Schäfer. *Magnetic domains: the analysis of magnetic microstructures*. Springer Science & Business Media, 2008.
- [9] IV Baryakhtar and BA Ivanov. Dynamic solitons in an uniaxial anti-ferromagnet. *Zhurnal Eksperimentalnoi i Teoreticheskoi Fiziki*, 85(1):328–340, 1983.
- [10] Se Kwon Kim, Yaroslav Tserkovnyak, and Oleg Tchernyshyov. Propulsion of a domain wall in an antiferromagnet by magnons. *Physical Review B*, 90(10):104406, 2014.

- [11] FDM Haldane. Nonlinear field theory of large-spin heisenberg antiferromagnets: semiclassically quantized solitons of the one-dimensional easy-axis Néel state. *Physical Review Letters*, 50(15):1153, 1983.
- [12] Albert Fert, Vincent Cros, and João Sampaio. Skyrmions on the track. *Nature Nanotechnology*, 8(3):152–156, March 2013.
- [13] V. D. Nguyen, O. Fruchart, S. Pizzini, J. Vogel, J.-C. Toussaint, and N. Rougemaille. Third type of domain wall in soft magnetic nanostrips. *Scientific Reports*, 5:12417, July 2015.
- [14] Yoshinobu Nakatani, André Thiaville, and Jacques Miltat. Head-to-head domain walls in soft nano-strips: a refined phase diagram. *Journal of Magnetism and Magnetic Materials*, 290-291, Part 1:750–753, April 2005.
- [15] R. D. McMichael and M. J. Donahue. Head to head domain wall structures in thin magnetic strips. *IEEE Transactions on Magnetics*, 33(5):4167–4169, September 1997.
- [16] M. T. Bryan, S. Bance, J. Dean, T. Schrefl, and D. A. Allwood. Transverse and vortex domain wall structure in magnetic nanowires with uniaxial in-plane anisotropy. *Journal of Physics: Condensed Matter*, 24(2):024205, 2012.
- [17] M. Kläui. Head-to-head domain walls in magnetic nanostructures. *Journal of Physics: Condensed Matter*, 20(31):313001, 2008.
- [18] Mai Lu and Paul J. Leonard. Micromagnetic simulation of thickness variation of Néel cap in hybrid Bloch–Néel domain wall. *Physica B: Condensed Matter*, 365(1–4):82–92, August 2005.
- [19] K. Ramstöck, W. Hartung, and A. Hubert. The phase diagram of domain walls in narrow magnetic strips. *Physica Status Solidi A*, 155(2):505–518, June 1996.
- [20] Landau and Lifshitz. On the theory of the dispersion of magnetic permeability in ferromagnetic bodies. *Phys. Z. Sowjetunion*, 1935.
- [21] D. B. Gopman, J. W. Lau, K. P. Mohanchandra, K. Wetzlar, and G. P. Carman. Determination of the exchange constant of Tb<sub>0.3</sub>/Dy<sub>0.7</sub>/Fe<sub>2</sub> by broadband ferromagnetic resonance spectroscopy. *Physical Review B*, 93(6):064425, February 2016.

- [22] G. Catalan, J. Seidel, R. Ramesh, and J. F. Scott. Domain wall nanoelectronics. *Reviews of Modern Physics*, 84(1):119–156, February 2012.
- [23] M. H. Kryder, E. C. Gage, T. W. McDaniel, W. A. Challener, R. E. Rottmayer, G. Ju, Y. T. Hsia, and M. F. Erden. Heat Assisted Magnetic Recording. *Proceedings of the IEEE*, 96(11):1810–1835, November 2008.
- [24] W. A. Challener, Chubing Peng, A. V. Itagi, D. Karns, Wei Peng, Yingguo Peng, XiaoMin Yang, Xiaobin Zhu, N. J. Gokemeijer, Y.-T. Hsia, G. Ju, Robert E. Rottmayer, Michael A. Seigler, and E. C. Gage. Heat-assisted magnetic recording by a near-field transducer with efficient optical energy transfer. *Nature Photonics*, 3(4):220–224, April 2009.
- [25] Robert L. Stamps, Stephan Breitzkreutz, Johan Akerman, Andrii V. Chumak, YoshiChika Otani, Gerrit E. W. Bauer, Jan-Ulrich Thiele, Martin Bowen, Sara A. Majetich, Mathias Kläui, Ioan Lucian Prejbeanu, Bernard Dieny, Nora M. Dempsey, and Burkard Hillebrands. The 2014 Magnetism Roadmap. *Journal of Physics D: Applied Physics*, 47(33):333001, 2014.
- [26] C. A. Ross. Patterned Magnetic Recording Media. *Annual Review of Materials Research*, 31(1):203–235, 2001.
- [27] C. H. Marrows and G. Meier. Domain wall dynamics in nanostructures. *Journal of Physics: Condensed Matter*, 24(2):020301, 2012.
- [28] R. Lavrijsen, M. A. Verheijen, B. Barcones, J. T. Kohlhepp, H. J. M. Swagten, and B. Koopmans. Enhanced field-driven domain-wall motion in Pt/Co<sub>68</sub>B<sub>32</sub>/Pt strips. *Applied Physics Letters*, 98(13):132502, March 2011.
- [29] Bernard Dieny and Ursula Ebels. Stockage de l’information: les acquis et les promesses du nanomagnétisme et de la spintronique. *Clefs CEA*, (56):62–66, 2007.
- [30] Supriyo Bandyopadhyay and Marc Cahay. Electron spin for classical information processing: a brief survey of spin-based logic devices, gates and circuits. *Nanotechnology*, 20(41):412001, October 2009.
- [31] C. Augustine, G. Panagopoulos, Behtash Behin-Aein, Srikant Srinivasan, Angik Sarkar, and K. Roy. Low-power functionality enhanced computation architecture using spin-based devices. In *2011 IEEE/ACM International Symposium on Nanoscale Architectures (NANOARCH)*, pages 129–136, June 2011.

- [32] Stuart S. P. Parkin, Masamitsu Hayashi, and Luc Thomas. Magnetic Domain-Wall Racetrack Memory. *Science*, 320(5873):190–194, April 2008.
- [33] Stuart Parkin and See-Hun Yang. Memory on the Racetrack. *Nature Nanotechnology*, 10(3):195–198, March 2015.
- [34] J. H. Franken, H. J. M. Swagten, and B. Koopmans. Shift registers based on magnetic domain wall ratchets with perpendicular anisotropy. *Nature Nanotechnology*, 7(8):499–503, August 2012.
- [35] Yurii P. Ivanov, Andrey Chuvilin, Sergei Lopatin, and Jurgen Kosel. Modulated Magnetic Nanowires for Controlling Domain Wall Motion: Toward 3D Magnetic Memories. *ACS Nano*, 10(5):5326–5332, May 2016.
- [36] D. A. Allwood, G. Xiong, C. C. Faulkner, D. Atkinson, D. Petit, and R. P. Cowburn. Magnetic Domain-Wall Logic. *Science*, 309(5741):1688–1692, September 2005.
- [37] Behtash Behin-Aein, Deepanjan Datta, Sayeef Salahuddin, and Supriyo Datta. Proposal for an all-spin logic device with built-in memory. *Nature Nanotechnology*, 5(4):266–270, April 2010.
- [38] Behtash Behin-Aein, Angik Sarkar, Srikant Srinivasan, and Supriyo Datta. Switching energy-delay of all spin logic devices. *Applied Physics Letters*, 98(12):123510, March 2011.
- [39] David B. Carlton, Nathan C. Emley, Eduard Tuchfeld, and Jeffrey Bokor. Simulation Studies of Nanomagnet-Based Logic Architecture. *Nano Letters*, 8(12):4173–4178, December 2008.
- [40] Peng Xu, Ke Xia, Changzhi Gu, Ling Tang, Haifang Yang, and Junjie Li. An all-metallic logic gate based on current-driven domain wall motion. *Nature Nanotechnology*, 3(2):97–100, February 2008.
- [41] D.E. Nikonov, G.I. Bourianoff, and T. Ghani. Proposal of a Spin Torque Majority Gate Logic. *IEEE Electron Device Letters*, 32(8):1128–1130, August 2011.
- [42] Gyorgy Csaba, A. Imre, G.H. Bernstein, W. Porod, and Vitali Metlushko. Nanocomputing by field-coupled nanomagnets. *IEEE Transactions on Nanotechnology*, 1(4):209–213, December 2002.

- [43] M. Sharad, C. Augustine, G. Panagopoulos, and K. Roy. Spin-Based Neuron Model With Domain-Wall Magnets as Synapse. *IEEE Transactions on Nanotechnology*, 11(4):843–853, July 2012.
- [44] Steven Lequeux, Joao Sampaio, Vincent Cros, Kay Yakushiji, Akio Fukushima, Rie Matsumoto, Hitoshi Kubota, Shinji Yuasa, and Julie Grollier. A magnetic synapse: multilevel spin-torque memristor with perpendicular anisotropy. *Scientific Reports*, 6:31510, August 2016.
- [45] A. Chanthbouala, R. Matsumoto, J. Grollier, V. Cros, A. Anane, A. Fert, A. V. Khvalkovskiy, K. A. Zvezdin, K. Nishimura, Y. Nagamine, H. Maehara, K. Tsunekawa, A. Fukushima, and S. Yuasa. Vertical-current-induced domain-wall motion in MgO-based magnetic tunnel junctions with low current densities. *Nature Physics*, 7(8):626–630, August 2011.
- [46] Joao Sampaio, Steven Lequeux, Peter J. Metaxas, Andre Chanthbouala, Rie Matsumoto, Kay Yakushiji, Hitoshi Kubota, Akio Fukushima, Shinji Yuasa, Kazumasa Nishimura, Yoshinori Nagamine, Hiroki Maehara, Koji Tsunekawa, Vincent Cros, and Julie Grollier. Time-resolved observation of fast domain-walls driven by vertical spin currents in short tracks. *Applied Physics Letters*, 103(24):242415, December 2013.
- [47] Claude Chappert, Albert Fert, and Frédéric Nguyen Van Dau. The emergence of spin electronics in data storage. *Nature Materials*, 6(11):813–823, November 2007.
- [48] N. Locatelli, V. Cros, and J. Grollier. Spin-torque building blocks. *Nature Materials*, 13(1):11–20, January 2014.
- [49] Marco Donolato, Paolo Vavassori, Marco Gobbi, Maria Deryabina, Mikkel F. Hansen, Vitali Metlushko, Bojan Ilic, Matteo Cantoni, Daniela Petti, Stefano Brivio, and Riccardo Bertacco. On-Chip Manipulation of Protein-Coated Magnetic Beads via Domain-Wall Conduits. *Advanced Materials*, 22(24):2706–2710, June 2010.
- [50] Gang Ruan, Greg Vieira, Thomas Henighan, Aaron Chen, Dhananjay Thakur, R. Sooryakumar, and Jessica O. Winter. Simultaneous Magnetic Manipulation and Fluorescent Tracking of Multiple Individual Hybrid Nanostructures. *Nano Letters*, 10(6):2220–2224, June 2010.

- [51] Elizabeth Rapoport and Geoffrey SD Beach. Dynamics of superparamagnetic microbead transport along magnetic nanotracks by magnetic domain walls. *Applied Physics Letters*, 100(8):082401, February 2012.
- [52] A Torti, V Mondiali, A Cattoni, M Donolato, E Albisetti, AM Haghiri-Gosnet, Paolo Vavassori, and R Bertacco. Single particle demultiplexer based on domain wall conduits. *Applied Physics Letters*, 101(14):142405, October 2012.
- [53] Hyunmin Sohn, Mark E. Nowakowski, Cheng-yen Liang, Joshua L. Hockel, Kyle Wetzlar, Scott Keller, Brenda M. McLellan, Matthew A. Marcus, Andrew Doran, Anthony Young, Mathias Kläui, Gregory P. Carman, Jeffrey Bokor, and Robert N. Candler. Electrically Driven Magnetic Domain Wall Rotation in Multiferroic Heterostructures to Manipulate Suspended On-Chip Magnetic Particles. *ACS Nano*, 9(5):4814–4826, May 2015.
- [54] P Vavassori, V Metlushko, B Ilic, M Gobbi, M Donolato, M Cantoni, and R Bertacco. Domain wall displacement in Py square ring for single nanometric magnetic bead detection. *Applied Physics Letters*, 93(20):203502, November 2008.
- [55] TL Gilbert. A lagrangian formulation of the gyromagnetic equation of the magnetization field. *Phys. Rev.*, 100:1243, 1955.
- [56] TL Gilbert and JM Kelly. Anomalous rotational damping in ferromagnetic sheets. In *Conference on Magnetism and Magnetic Materials, Pittsburgh, PA*, pages 253–263, 1955.
- [57] T. L. Gilbert. A phenomenological theory of damping in ferromagnetic materials. *IEEE Transactions on Magnetics*, 40(6):3443–3449, November 2004.
- [58] VG Baryakhtar. Phenomenological description of relaxation processes in magnets. *Zhurnal Eksperimentalnoi i Teoreticheskoi Fiziki*, 87(4):1501–1508, 1984.
- [59] Weiwei Wang, Mykola Dvornik, Marc-Antonio Bisotti, Dmitri Chernyshenko, Marijan Beg, Maximilian Albert, Arne Vansteenkiste, Bartel V. Waeyenberge, Andriy N. Kuchko, Volodymyr V. Kruglyak, and Hans Fangohr. Phenomenological description of the nonlocal magnetization relaxation in magnonics, spintronics, and domain-wall dynamics. *Physical Review B*, 92(5):054430, August 2015.

- [60] P. Podio-Guidugli. On dissipation mechanisms in micromagnetics. *The European Physical Journal B - Condensed Matter and Complex Systems*, 19(3):417–424, February 2001.
- [61] P. Podio-Guidugli and G. Tomassetti. On the steady motions of a flat domain wall in a ferromagnet. *The European Physical Journal B - Condensed Matter and Complex Systems*, 26(2):191–198, March 2002.
- [62] Vasil Tiberkevich. Nonlinear phenomenological model of magnetic dissipation for large precession angles: Generalization of the Gilbert model. *Physical Review B*, 75(1), 2007.
- [63] M. Lakshmanan. The fascinating world of the Landau–Lifshitz–Gilbert equation: an overview. *Philosophical Transactions of the Royal Society of London A: Mathematical, Physical and Engineering Sciences*, 369(1939):1280–1300, March 2011.
- [64] G. Bertotti, I. D. Mayergoyz, and C. Serpico. Identification of the damping coefficient in Landau–Lifshitz equation. *Physica B: Condensed Matter*, 306(1–4):102–105, December 2001.
- [65] Giorgio Bertotti, Isaak D. Mayergoyz, and Claudio Serpico. Chapter 2 - Basic Equations for Magnetization Dynamics. In *Nonlinear Magnetization Dynamics in Nanosystems*, Elsevier Series in Electromagnetism, pages 21–34. Elsevier, Oxford, 2009.
- [66] Herbert B. Callen. A ferromagnetic dynamical equation. *Journal of Physics and Chemistry of Solids*, 4(4):256–270, January 1958.
- [67] M. Lakshmanan and K. Nakamura. Landau-Lifshitz Equation of Ferromagnetism: Exact Treatment of the Gilbert Damping. *Physical Review Letters*, 53(26):2497–2499, December 1984.
- [68] J. Mallinson. On damped gyromagnetic precession. *IEEE Transactions on Magnetics*, 23(4):2003–2004, July 1987.
- [69] D. R. Fredkin and A. Ron. Microscopic derivation of the Landau-Lifshitz equation for ferromagnetic relaxation. *Physical Review B*, 61(13):8654–8655, April 2000.
- [70] M. D. Stiles. Adiabatic domain wall motion and Landau-Lifshitz damping. *Physical Review B*, 75(21), 2007.

- [71] WM Saslow. Landau–Lifshitz or Gilbert damping? That is the question. *Journal of Applied Physics*, 105(7):07D315, April 2009.
- [72] Ernst Schlömann. Structure of Moving Domain Walls in Magnetic Materials. *Applied Physics Letters*, 19(8):274–276, October 1971.
- [73] E. Schlömann, C. D. Graham, and J. J. Rhyne. Structure and energy of moving domain walls. *AIP Conference Proceedings*, 5(1):160–164, March 1972.
- [74] E. Feldtkeller. Magnetic Domain Wall Dynamics. *Physica Status Solidi B: Basic Solid State Physics*, 27(1):161–170, January 1968.
- [75] N. L. Schryer and L. R. Walker. The motion of 180° domain walls in uniform DC magnetic fields. *Journal of Applied Physics*, 45(12):5406–5421, December 1974.
- [76] J. C. Slonczewski. Dynamics of Magnetic Domain Walls. In *AIP Conference Proceedings*, volume 5, pages 170–174. AIP Publishing, March 1972.
- [77] H. Bourne and D. Bartran. A transient solution for domain wall motion. *IEEE Transactions on Magnetics*, 8(4):741–743, December 1972.
- [78] A. A. Thiele. Steady-State Motion of Magnetic Domains. *Physical Review Letters*, 30(6):230–233, February 1973.
- [79] O. A. Tretiakov, D. Clarke, Gia-Wei Chern, Ya. B. Bazaliy, and O. Tchernyshyov. Dynamics of Domain Walls in Magnetic Nanostrips. *Physical Review Letters*, 100(12):127204, March 2008.
- [80] D. J. Clarke, O. A. Tretiakov, G.-W. Chern, Ya. B. Bazaliy, and O. Tchernyshyov. Dynamics of a vortex domain wall in a magnetic nanostrip: Application of the collective-coordinate approach. *Physical Review B*, 78(13):134412, October 2008.
- [81] Junya Shibata, Gen Tatara, and Hiroshi Kohno. A brief review of field- and current-driven domain-wall motion. *Journal of Physics D: Applied Physics*, 44(38):384004, 2011.
- [82] T. Ono, H. Miyajima, K. Shigeto, K. Mibu, N. Hosoi, and T. Shinjo. Propagation of a Magnetic Domain Wall in a Submicrometer Magnetic Wire. *Science*, 284(5413):468–470, April 1999.

- [83] A. Thiaville, J. M. García, and J. Miltat. Domain wall dynamics in nanowires. *Journal of Magnetism and Magnetic Materials*, 242–245, Part 2:1061–1063, April 2002.
- [84] B. Hu and X. R. Wang. Instability of Walker Propagating Domain Wall in Magnetic Nanowires. *Physical Review Letters*, 111(2):027205, July 2013.
- [85] M. C. Depassier. Speed of field-driven domain walls in nanowires with large transverse magnetic anisotropy. *EPL (Europhysics Letters)*, 111(2):27005, 2015.
- [86] R. D. Benguria and M. C. Depassier. Reaction diffusion dynamics and the Schryer-Walker solution for domain walls of the Landau-Lifshitz-Gilbert equation. *Physical Review B*, 93(14):144416, April 2016.
- [87] Geoffrey S. D. Beach, Corneliu Nistor, Carl Knutson, Maxim Tsoi, and James L. Erskine. Dynamics of field-driven domain-wall propagation in ferromagnetic nanowires. *Nature Materials*, 4(10):741–744, October 2005.
- [88] Jusang Yang, Corneliu Nistor, G. S. D. Beach, and J. L. Erskine. Magnetic domain-wall velocity oscillations in permalloy nanowires. *Physical Review B*, 77(1):014413, January 2008.
- [89] Xin Jiang, Luc Thomas, Rai Moriya, Masamitsu Hayashi, Bastiaan Bergman, Charles Rettner, and Stuart S. P. Parkin. Enhanced stochasticity of domain wall motion in magnetic racetracks due to dynamic pinning. *Nature Communications*, 1:25, June 2010.
- [90] D. G. Porter and M. J. Donahue. Velocity of transverse domain wall motion along thin, narrow strips. *Journal of Applied Physics*, 95(11):6729–6731, June 2004.
- [91] Masamitsu Hayashi, Luc Thomas, Charles Rettner, Rai Moriya, and Stuart S. P. Parkin. Direct observation of the coherent precession of magnetic domain walls propagating along permalloy nanowires. *Nature Physics*, 3(1):21–25, January 2007.
- [92] André Bisig, Martin Stärk, Mohamad-Assaad Mawass, Christoforos Moutafis, Jan Rhensius, Jakoba Heidler, Felix Büttner, Matthias Noske, Markus Weigand, Stefan Eisebitt, Tolek Tyliczszak, Bartel Van Waeyenberge, Hermann Stoll, Gisela Schütz, and Mathias Kläui. Correlation between spin structure oscillations and domain wall velocities. *Nature Communications*, 4:2328, August 2013.

- [93] X. S. Wang, P. Yan, Y. H. Shen, G. E. W. Bauer, and X. R. Wang. Domain Wall Propagation through Spin Wave Emission. *Physical Review Letters*, 109(16):167209, October 2012.
- [94] S. Lemerle, J. Ferré, C. Chappert, V. Mathet, T. Giamarchi, and P. Le Doussal. Domain Wall Creep in an Ising Ultrathin Magnetic Film. *Physical Review Letters*, 80(4):849–852, January 1998.
- [95] F. Cayssol, D. Ravelosona, C. Chappert, J. Ferré, and J. P. Jamet. Domain Wall Creep in Magnetic Wires. *Physical Review Letters*, 92(10):107202, March 2004.
- [96] J. Kim, K. J. Kim, and S. B. Choe. Temperature Dependence of Domain-Wall Creep in Pt/CoFe/Pt Films. *IEEE Transactions on Magnetics*, 45(10):3909–3911, October 2009.
- [97] Pascal Chauve, Thierry Giamarchi, and Pierre Le Doussal. Creep and depinning in disordered media. *Physical Review B*, 62(10):6241–6267, September 2000.
- [98] Maximilian Albert, Matteo Franchin, Thomas Fischbacher, Guido Meier, and Hans Fangohr. Domain wall motion in perpendicular anisotropy nanowires with edge roughness. *Journal of Physics: Condensed Matter*, 24(2):024219, 2012.
- [99] P. J. Metaxas, J. P. Jamet, A. Mougin, M. Cormier, J. Ferré, V. Baltz, B. Rodmacq, B. Dieny, and R. L. Stamps. Creep and Flow Regimes of Magnetic Domain-Wall Motion in Ultrathin Pt/Co/Pt Films with Perpendicular Anisotropy. *Physical Review Letters*, 99(21):217208, November 2007.
- [100] Jonathan Leliaert, Ben Van de Wiele, Arne Vansteenkiste, Lasse Laurson, Gianfranco Durin, Luc Dupré, and Bartel Van Waeyenberge. Creep turns linear in narrow ferromagnetic nanostrips. *Scientific Reports*, 6:20472, February 2016.
- [101] Y Yokoyama, Y Suzuki, S Yuasa, K Ando, K Shigeto, T Shinjo, P Gogol, J Miltat, A Thiaville, T Ono, et al. Kerr microscopy observations of magnetization process in microfabricated ferromagnetic wires. *Journal of Applied Physics*, 87(9):5618–5620, April 2000.
- [102] A Himeno, T Ono, S Nasu, K Shigeto, K Mibu, and T Shinjo. Dynamics of a magnetic domain wall in magnetic wires with an artificial neck. *Journal of Applied Physics*, 93(10):8430–8432, May 2003.

- [103] M. Kläui, C. A. F. Vaz, J. Rothman, J. A. C. Bland, W. Wernsdorfer, G. Faini, and E. Cambril. Domain Wall Pinning in Narrow Ferromagnetic Ring Structures Probed by Magnetoresistance Measurements. *Physical Review Letters*, 90(9):097202, March 2003.
- [104] Colm C Faulkner, Michael D Cooke, Dan A Allwood, Dorothée Petit, Del Atkinson, and Russell P Cowburn. Artificial domain wall nanotraps in Ni<sub>81</sub>Fe<sub>19</sub> wires. *Journal of Applied Physics*, 95(11):6717–6719, May 2004.
- [105] Mathias Kläui, Henri Ehrke, Ulrich Rüdiger, Takeshi Kasama, Rafal E Dunin-Borkowski, Dirk Backes, Laura J Heyderman, Carlos AF Vaz, J Anthony C Bland, Giancarlo Faini, et al. Direct observation of domain-wall pinning at nanoscale constrictions. *Applied Physics Letters*, 87(10):102509, September 2005.
- [106] Dorothée Petit, Ana-Vanessa Jausovec, Dan Read, and Russell P Cowburn. Domain wall pinning and potential landscapes created by constrictions and protrusions in ferromagnetic nanowires. *Journal of Applied Physics*, 103(11):114307, June 2008.
- [107] LK Bogart, DS Eastwood, and D Atkinson. The effect of geometrical confinement and chirality on domain wall pinning behavior in planar nanowires. *Journal of Applied Physics*, 104(3):033904, August 2008.
- [108] Su Jung Noh, Yasuyoshi Miyamoto, Mitsunobu Okuda, Naoto Hayashi, and Young Keun Kim. Effects of notch shape on the magnetic domain wall motion in nanowires with in-plane or perpendicular magnetic anisotropy. *Journal of Applied Physics*, 111(7):07D123, March 2012.
- [109] D. Lacour, J. A. Katine, L. Folks, T. Block, J. R. Childress, M. J. Carey, and B. A. Gurney. Experimental evidence of multiple stable locations for a domain wall trapped by a submicron notch. *Applied Physics Letters*, 84(11):1910–1912, March 2004.
- [110] Jizhai Cui, Scott M. Keller, Cheng-Yen Liang, Gregory P. Carman, and Christopher S. Lynch. Nanoscale magnetic ratchets based on shape anisotropy. *Nanotechnology*, 28(8):08LT01, 2017.
- [111] D. Atkinson, D. A. Allwood, C. C. Faulkner, Gang Xiong, M. D. Cooke, and R. P. Cowburn. Magnetic domain wall dynamics in a permalloy nanowire. *IEEE Transactions on Magnetics*, 39(5):2663–2665, September 2003.

- [112] J. Gorchon, S. Bustingorry, J. Ferré, V. Jeudy, A.B. Kolton, and T. Giamarchi. Pinning-Dependent Field-Driven Domain Wall Dynamics and Thermal Scaling in an Ultrathin Pt/Co/Pt Magnetic Film. *Physical Review Letters*, 113(2):027205, July 2014.
- [113] Yoshinobu Nakatani, André Thiaville, and Jacques Miltat. Faster magnetic walls in rough wires. *Nature Materials*, 2(8):521–523, August 2003.
- [114] David M. Burn and Del Atkinson. Suppression of Walker breakdown in magnetic domain wall propagation through structural control of spin wave emission. *Applied Physics Letters*, 102(24):242414, June 2013.
- [115] V. L. Sobolev, H. L. Huang, and S. C. Chen. Domain wall dynamics in the presence of an external magnetic field normal to the anisotropy axis. *Journal of Magnetism and Magnetic Materials*, 147(3):284–298, June 1995.
- [116] S Glathe, I Berkov, T Mikolajick, and R Mattheis. Experimental study of domain wall motion in long nanostrips under the influence of a transverse field. *Applied Physics Letters*, 93(16):162505, October 2008.
- [117] Yoko Yoshimura, Kab-Jin Kim, Takuya Taniguchi, Takayuki Tono, Kohei Ueda, Ryo Hiramatsu, Takahiro Moriyama, Keisuke Yamada, Yoshinobu Nakatani, and Teruo Ono. Soliton-like magnetic domain wall motion induced by the interfacial Dzyaloshinskii-Moriya interaction. *Nature Physics*, 12(2):157–161, February 2016.
- [118] M. N. Baibich, J. M. Broto, A. Fert, F. Nguyen Van Dau, F. Petroff, P. Etienne, G. Creuzet, A. Friederich, and J. Chazelas. Giant Magnetoresistance of (001)Fe/(001)Cr Magnetic Superlattices. *Physical Review Letters*, 61(21):2472–2475, November 1988.
- [119] L. Berger. Low-field magnetoresistance and domain drag in ferromagnets. *Journal of Applied Physics*, 49(3):2156–2161, March 1978.
- [120] O. Boulle, G. Malinowski, and M. Kläui. Current-induced domain wall motion in nanoscale ferromagnetic elements. *Materials Science and Engineering: R: Reports*, 72(9):159–187, September 2011.
- [121] Gen Tatara, Hiroshi Kohno, and Junya Shibata. Microscopic approach to current-driven domain wall dynamics. *Physics Reports*, 468(6):213–301, November 2008.

- [122] A. Thiaville, Y. Nakatani, J. Miltat, and N. Vernier. Domain wall motion by spin-polarized current: a micromagnetic study. *Journal of Applied Physics*, 95(11):7049–7051, May 2004.
- [123] A. Thiaville, Y. Nakatani, J. Miltat, and Y. Suzuki. Micromagnetic understanding of current-driven domain wall motion in patterned nanowires. *Europhysics Letters (EPL)*, 69(6):990–996, March 2005.
- [124] Z. Li. Domain-wall dynamics driven by adiabatic spin-transfer torques. *Physical Review B*, 70(2), 2004.
- [125] Gen Tatara. Theory of Current-Driven Domain Wall Motion: Spin Transfer versus Momentum Transfer. *Physical Review Letters*, 92(8), 2004.
- [126] S. E. Barnes. Current-Spin Coupling for Ferromagnetic Domain Walls in Fine Wires. *Physical Review Letters*, 95(10), 2005.
- [127] M. Kläui, P.-O. Jubert, R. Allenspach, A. Bischof, J. A. C. Bland, G. Faini, U. Rüdiger, C. A. F. Vaz, L. Vila, and C. Vouille. Direct Observation of Domain-Wall Configurations Transformed by Spin Currents. *Physical Review Letters*, 95(2):026601, July 2005.
- [128] Peter J. Metaxas, Joao Sampaio, André Chanthbouala, Rie Matsumoto, Abdelmadjid Anane, Albert Fert, Konstantin A. Zvezdin, Kay Yakushiji, Hitoshi Kubota, Akio Fukushima, Shinji Yuasa, Kazumasa Nishimura, Yoshinori Nagamine, Hiroki Maehara, Koji Tsunekawa, Vincent Cros, and Julie Grollier. High domain wall velocities via spin transfer torque using vertical current injection. *Scientific Reports*, 3:1829, May 2013.
- [129] See-Hun Yang, Kwang-Su Ryu, and Stuart Parkin. Domain-wall velocities of up to  $750 \text{ ms}^{-1}$  driven by exchange-coupling torque in synthetic antiferromagnets. *Nature Nanotechnology*, 10(3):221–226, March 2015.
- [130] Kwang-Su Ryu, Luc Thomas, See-Hun Yang, and Stuart Parkin. Chiral spin torque at magnetic domain walls. *Nature Nanotechnology*, 8(7):527–533, July 2013.
- [131] A. V. Khvalkovskiy, V. Cros, D. Apalkov, V. Nikitin, M. Krounbi, K. A. Zvezdin, A. Anane, J. Grollier, and A. Fert. Matching domain-wall configuration and spin-orbit torques for efficient domain-wall motion. *Physical Review B*, 87(2):020402, January 2013.

- [132] Petr N Skirdkov, Konstantin A Zvezdin, Anatoly D Belanovsky, Julie Grollier, Vincent Cros, Caroline A Ross, and Anatoly K Zvezdin. Domain wall displacement by remote spin-current injection. *Applied Physics Letters*, 104(24):242401, June 2014.
- [133] R Tolley, T Liu, Y Xu, S Le Gall, M Gottwald, T Hauet, M Hehn, F Montaigne, EE Fullerton, and S Mangin. Generation and manipulation of domain walls using a thermal gradient in a ferrimagnetic TbCo wire. *Applied Physics Letters*, 106(24):242403, June 2015.
- [134] A. Mougin, M. Cormier, J. P. Adam, P. J. Metaxas, and J. Ferré. Domain wall mobility, stability and Walker breakdown in magnetic nanowires. *EPL (Europhysics Letters)*, 78(5):57007, 2007.
- [135] J. A. Otálora, J. A. López-López, A. S. Núñez, and P. Landeros. Domain wall manipulation in magnetic nanotubes induced by electric current pulses. *Journal of Physics: Condensed Matter*, 24(43):436007, 2012.
- [136] Zai-Dong Li, Qiu-Yan Li, X. R. Wang, W. M. Liu, J. Q. Liang, and Guangsheng Fu. Screw-pitch effect and velocity oscillation of a domain wall in a ferromagnetic nanowire driven by spin-polarized current. *Journal of Physics: Condensed Matter*, 22(21):216001, 2010.
- [137] Ravelosona. Threshold currents to move domain walls in films with perpendicular anisotropy. *Applied Physics Letters*, 90(7):072508, February 2007.
- [138] C. Burrowes, A. P. Mihai, D. Ravelosona, J.-V. Kim, C. Chappert, L. Vila, A. Marty, Y. Samson, F. Garcia-Sanchez, L. D. Buda-Prejbeanu, I. Tudosa, E. E. Fullerton, and J.-P. Attané. Non-adiabatic spin-torques in narrow magnetic domain walls. *Nature Physics*, 6(1):17–21, January 2010.
- [139] M. Yamanouchi, J. Ieda, F. Matsukura, S. E. Barnes, S. Maekawa, and H. Ohno. Universality Classes for Domain Wall Motion in the Ferromagnetic Semiconductor (Ga,Mn)As. *Science*, 317(5845):1726–1729, September 2007.
- [140] S. DuttaGupta, S. Fukami, C. Zhang, H. Sato, M. Yamanouchi, F. Matsukura, and H. Ohno. Adiabatic spin-transfer-torque-induced domain wall creep in a magnetic metal. *Nature Physics*, 12(4):333–336, December 2015.

- [141] Kyoung-Woong Moon, Duck-Ho Kim, Sang-Cheol Yoo, Cheong-Gu Cho, Sungmin Hwang, Byungnam Kahng, Byoung-Chul Min, Kyung-Ho Shin, and Sug-Bong Choe. Distinct Universality Classes of Domain Wall Roughness in Two-Dimensional Pt/Co/Pt Films. *Physical Review Letters*, 110(10):107203, March 2013.
- [142] Jae-Chul Lee, Kab-Jin Kim, Jisu Ryu, Kyoung-Woong Moon, Sang-Jun Yun, Gi-Hong Gim, Kang-Soo Lee, Kyung-Ho Shin, Hyun-Woo Lee, and Sug-Bong Choe. Universality Classes of Magnetic Domain Wall Motion. *Physical Review Letters*, 107(6):067201, August 2011.
- [143] V. Jeudy. Universal Pinning Energy Barrier for Driven Domain Walls in Thin Ferromagnetic Films. *Physical Review Letters*, 117(5), 2016.
- [144] Pierre Curie. Sur la symétrie dans les phénomènes physiques, symétrie d'un champ électrique et d'un champ magnétique. *Ann Fond Louis Broglie*, 19:137, 1994.
- [145] DN Astrov. The magnetoelectric effect in antiferromagnetics. *Sov. Phys. JETP*, 11(3):708–709, 1960.
- [146] DN Astrov. Magnetoelectric effect in chromium oxide. *Sov. Phys. JETP*, 13(4):729–733, 1961.
- [147] Lev Davidovich Landau, JS Bell, MJ Kearsley, LP Pitaevskii, EM Lifshitz, and JB Sykes. *Electrodynamics of continuous media*, volume 8. Elsevier, 2013.
- [148] IE Dzyaloshinskii. On the magneto-electrical effect in antiferromagnets. *Soviet Physics JETP-Ussr*, 10(3):628–629, 1960.
- [149] W. Eerenstein, N. D. Mathur, and J. F. Scott. Multiferroic and magnetoelectric materials. *Nature*, 442(7104):759–765, August 2006.
- [150] W. F. Brown, R. M. Hornreich, and S. Shtrikman. Upper Bound on the Magnetoelectric Susceptibility. *Physical Review*, 168(2):574–577, April 1968.
- [151] Claude Ederer and Nicola A. Spaldin. Weak ferromagnetism and magnetoelectric coupling in bismuth ferrite. *Physical Review B*, 71(6):060401, February 2005.
- [152] Simon Foner and Mitsugu Hanabusa. Magnetoelectric Effects in  $\text{Cr}_2\text{O}_3$  and  $(\text{Cr}_2\text{O}_3)_{0.8}\text{-(Al}_2\text{O}_3)_{0.2}$ . *Journal of Applied Physics*, 34(4):1246–1247, April 1963.

- [153] Shashank Priya, Rashed Islam, Shuxiang Dong, and D. Viehland. Recent advancements in magnetoelectric particulate and laminate composites. *Journal of Electroceramics*, 19(1):149–166, September 2007.
- [154] Thomas Lottermoser, Thomas Lonkai, Uwe Amann, Dietmar Hohlwein, Jörg Ihringer, and Manfred Fiebig. Magnetic phase control by an electric field. *Nature*, 430(6999):541–544, July 2004.
- [155] Byung-Kweon Jang, Jin Hong Lee, Kanghyun Chu, Pankaj Sharma, Gi-Yeop Kim, Kyung-Tae Ko, Kwang-Eun Kim, Yong-Jin Kim, Kyungrok Kang, Han-Byul Jang, Hoyoung Jang, Min Hwa Jung, Kyung Song, Tae Yeong Koo, Si-Young Choi, Jan Seidel, Yoon Hee Jeong, Hendrik Ohldag, Jun-Sik Lee, and Chan-Ho Yang. Electric-field-induced spin disorder-to-order transition near a multiferroic triple phase point. *Nature Physics*, 13(2):189–196, February 2017.
- [156] T. Niazi, M. Cormier, D. Lucot, L. Largeau, V. Jeudy, J. Cibert, and A. Lemaître. Electric-field control of the magnetic anisotropy in an ultrathin (Ga,Mn)As/(Ga,Mn)(As,P) bilayer. *Applied Physics Letters*, 102(12):122403, March 2013.
- [157] H. Ohno, D. Chiba, F. Matsukura, T. Omiya, E. Abe, T. Dietl, Y. Ohno, and K. Ohtani. Electric-field control of ferromagnetism. *Nature*, 408(6815):944–946, December 2000.
- [158] M Endo, S Kanai, S Ikeda, F Matsukura, and H Ohno. Electric-field effects on thickness dependent magnetic anisotropy of sputtered MgO/Co<sub>40</sub>Fe<sub>40</sub>B<sub>20</sub>/Ta structures. *Applied Physics Letters*, 96(21):212503, May 2010.
- [159] Martin Weisheit, Sebastian Fähler, Alain Marty, Yves Souche, Christiane Poinsignon, and Dominique Givord. Electric Field-Induced Modification of Magnetism in Thin-Film Ferromagnets. *Science*, 315(5810):349–351, January 2007.
- [160] S. J. Gamble. Electric Field Induced Magnetic Anisotropy in a Ferromagnet. *Physical Review Letters*, 102(21), 2009.
- [161] Mikhail Zhernenkov. Electric-field modification of magnetism in a thin CoPd film. *Physical Review B*, 82(2), 2010.

- [162] Uwe Bauer, Satoru Emori, and Geoffrey SD Beach. Electric field control of domain wall propagation in Pt/Co/GdOx films. *Applied Physics Letters*, 100(19):192408, May 2012.
- [163] L. Herrera Diez, A. Bernand-Mantel, O. Michele, L. Vila, P. Warin, A. Marty, L. Ranno, and D. Givord. Electric-field effect on coercivity distributions in FePt magneto-electric devices. *Applied Physics Letters*, 102(1):012409, January 2013.
- [164] Z. Huang, I. Stolichnov, A. Bernand-Mantel, J. Borrel, S. Auffret, G. Gaudin, O. Boule, S. Pizzini, L. Ranno, L. Herrera Diez, and N. Setter. Ferroelectric control of magnetic domains in ultra-thin cobalt layers. *Applied Physics Letters*, 103(22):222902, November 2013.
- [165] Fumihiko Matsukura, Yoshinori Tokura, and Hideo Ohno. Control of magnetism by electric fields. *Nature Nanotechnology*, 10(3):209–220, March 2015.
- [166] Uwe Bauer, Satoru Emori, and Geoffrey S. D. Beach. Voltage-controlled domain wall traps in ferromagnetic nanowires. *Nature Nanotechnology*, 8(6):411–416, June 2013.
- [167] Anne Bernand-Mantel, Liza Herrera-Diez, Laurent Ranno, Stefania Pizzini, Jan Vogel, Dominique Givord, Stéphane Auffret, Olivier Boule, Ioan Mihai Miron, and Gilles Gaudin. Electric-field control of domain wall nucleation and pinning in a metallic ferromagnet. *Applied Physics Letters*, 102(12):122406, March 2013.
- [168] Uwe Bauer, Satoru Emori, and Geoffrey SD Beach. Voltage-gated modulation of domain wall creep dynamics in an ultrathin metallic ferromagnet. *Applied Physics Letters*, 101(17):172403, October 2012.
- [169] Hong-Bo Chen, Ye-Hua Liu, and You-Quan Li. Electric field control of multiferroic domain wall motion. *Journal of Applied Physics*, 115(13):133913, April 2014.
- [170] Weiwei Lin, Nicolas Vernier, Guillaume Agnus, Karin Garcia, Berthold Ocker, Weisheng Zhao, Eric E. Fullerton, and Dafiné Ravelosona. Universal domain wall dynamics under electric field in Ta/CoFeB/MgO devices with perpendicular anisotropy. *Nature Communications*, 7:13532, November 2016.
- [171] Martin Gajek, Manuel Bibes, Stéphane Fusil, Karim Bouzehouane, Josep Fontcuberta, Agnès Barthélémy, and Albert Fert. Tunnel junctions with multiferroic barriers. *Nature Materials*, 6(4):296–302, April 2007.

- [172] E. Y. Tsymbal, A. Gruverman, V. Garcia, M. Bibes, and A. Barthélémy. Ferroelectric and multiferroic tunnel junctions. *MRS Bulletin*, 37(2):138–143, February 2012.
- [173] Yue-Wei Yin, Muralikrishna Raju, Wei-Jin Hu, Xiao-Jun Weng, Ke Zou, Jun Zhu, Xiao-Guang Li, Zhi-Dong Zhang, and Qi Li. Multiferroic tunnel junctions. *Frontiers of Physics*, 7(4):380–385, August 2012.
- [174] K. D. Belashchenko, O. Tchernyshyov, Alexey A. Kovalev, and O. A. Tretiakov. Magnetoelectric domain wall dynamics and its implications for magnetoelectric memory. *Applied Physics Letters*, 108(13):132403, March 2016.
- [175] R. Ramesh and Nicola A. Spaldin. Multiferroics: progress and prospects in thin films. *Nature Materials*, 6(1):21–29, January 2007.
- [176] Manfred Fiebig. Revival of the magnetoelectric effect. *Journal of Physics D: Applied Physics*, 38(8):R123, 2005.
- [177] J.P. Joule. On the effects of magnetism upon the dimensions of iron and steel bars. *Philosophical Magazine Series 3*, 30(199):76–87, February 1847.
- [178] N. C. Koon, C. M. Williams, and B. N. Das. Giant magnetostriction materials. *Journal of Magnetism and Magnetic Materials*, 100(1):173–185, November 1991.
- [179] G. Engdahl and I. D. Mayergoyz. Handbook of Giant Magnetostrictive Materials - 1st Edition.
- [180] R. Coehoorn. Electronic Structure Calculations for Rare Earth-Transition Metal Compounds. In Gary J. Long and Fernande Grandjean, editors, *Supermagnets, Hard Magnetic Materials*, number 331 in NATO ASI Series, pages 133–170. Springer Netherlands, 1991.
- [181] Sōshin Chikazumi. *Physics of magnetism*. Wiley, 1964.
- [182] William Fuller Brown. *Magnetoelastic interactions*, volume 9. Springer, 1966.
- [183] Louis Néel. Anisotropie magnétique superficielle et surstructures d’orientation. *Journal de Physique et le Radium*, 15(4):225–239, April 1954.
- [184] Etienne du Trémolet de Lacheisserie, Damien Gignoux, and Michel Schlenker. *Magnetism: II-Materials and Applications*. Springer Science & Business Media, December 2012.

- [185] I Dzyaloshinskii. The problem of piezomagnetism. *Sov. Phys. JETP*, 6:621, 1958.
- [186] W.-N. Zou, C.-X. Tang, and E. Pan. Symmetry types of the piezoelectric tensor and their identification. *Proc. R. Soc. A*, 469(2155):20120755, July 2013.
- [187] C.-W. Nan, L. Liu, N. Cai, J. Zhai, Y. Ye, Y. H. Lin, L. J. Dong, and C. X. Xiong. A three-phase magnetoelectric composite of piezoelectric ceramics, rare-earth iron alloys, and polymer. *Applied Physics Letters*, 81(20):3831–3833, November 2002.
- [188] Ce-Wen Nan, M. I. Bichurin, Shuxiang Dong, D. Viehland, and G. Srinivasan. Multiferroic magnetoelectric composites: Historical perspective, status, and future directions. *Journal of Applied Physics*, 103(3):031101, February 2008.
- [189] Jing Ma, Jiamian Hu, Zheng Li, and Ce-Wen Nan. Recent Progress in Multiferroic Magnetoelectric Composites: from Bulk to Thin Films. *Advanced Materials*, 23(9):1062–1087, March 2011.
- [190] S. Giordano, M. Goueygou, N. Tiercelin, A. Talbi, P. Pernod, and V. Preobrazhensky. Magneto-electro-elastic effective properties of multilayered artificial multiferroics with arbitrary lamination direction. *International Journal of Engineering Science*, 78:134–153, May 2014.
- [191] S.-T. Gu and Q.-C. He. Compact closed-form micromechanical expressions for the effective uncoupled and coupled linear properties of layered composites. *Philosophical Magazine*, 95(25):2793–2816, September 2015.
- [192] Stefano Giordano. Explicit nonlinear homogenization for magneto-electro-elastic laminated materials. *Mechanics Research Communications*, 55:18–29, January 2014.
- [193] S. Fusil, V. Garcia, A. Barthélemy, and M. Bibes. Magnetoelectric Devices for Spintronics. *Annual Review of Materials Research*, 44(1):91–116, 2014.
- [194] J Van Suchtelen. Product properties: a new application of composite materials. *Philips Res. Rep*, 27(1):28–37, 1972.
- [195] A. M. J. G. Van Run, D. R. Terrell, and J. H. Scholing. An in situ grown eutectic magnetoelectric composite material. *Journal of Materials Science*, 9(10):1710–1714, October 1974.

- [196] J. van den Boomgaard and R. a. J. Born. A sintered magnetoelectric composite material  $\text{BaTiO}_3\text{-Ni}(\text{Co},\text{Mn})\text{Fe}_2\text{O}_4$ . *Journal of Materials Science*, 13(7):1538–1548, July 1978.
- [197] Haribabu Palneedi, Venkateswarlu Annapureddy, Shashank Priya, and Jungho Ryu. Status and Perspectives of Multiferroic Magnetoelectric Composite Materials and Applications. *Actuators*, 5(1):9, March 2016.
- [198] Jungho Ryu, Alfredo Vázquez Carazo, Kenji Uchino, and Hyoun-Ee Kim. Magnetoelectric Properties in Piezoelectric and Magnetostrictive Laminate Composites. *Japanese Journal of Applied Physics*, 40(8R):4948, August 2001.
- [199] G. Srinivasan. Magnetoelectric bilayer and multilayer structures of magnetostrictive and piezoelectric oxides. *Physical Review B*, 64(21), 2001.
- [200] Mukesh Kumari, Chandra Prakash, and Ratnamala Chatterjee. Room temperature large self-biased magnetoelectric effect in non-lead based piezoelectric and magnetostrictive (0-3) particulate composite system. *Journal of Magnetism and Magnetic Materials*, 429:60–64, May 2017.
- [201] P. M. Shepley, A. W. Rushforth, M. Wang, G. Burnell, and T. A. Moore. Modification of perpendicular magnetic anisotropy and domain wall velocity in Pt/Co/Pt by voltage-induced strain. *Scientific Reports*, 5:7921, January 2015.
- [202] A. W. Rushforth. Voltage control of magnetocrystalline anisotropy in ferromagnetic-semiconductor-piezoelectric hybrid structures. *Physical Review B*, 78(8), 2008.
- [203] M. Weiler, A. Brandlmaier, S. Geprägs, M. Althammer, M. Opel, C. Bihler, H. Huebl, M. S. Brandt, R. Gross, and S. T. B. Goennenwein. Voltage controlled inversion of magnetic anisotropy in a ferromagnetic thin film at room temperature. *New Journal of Physics*, 11(1):013021, 2009.
- [204] Tien-Kan Chung, Gregory P. Carman, and Kotekar P. Mohanchandra. Reversible magnetic domain-wall motion under an electric field in a magnetoelectric thin film. *Applied Physics Letters*, 92(11):112509, March 2008.
- [205] Y.-H. Chu, M. P. Cruz, C.-H. Yang, L. W. Martin, P.-L. Yang, J.-X. Zhang, K. Lee, P. Yu, L.-Q. Chen, and R. Ramesh. Domain Control in Multiferroic  $\text{BiFeO}_3$  through Substrate Vicinality. *Advanced Materials*, 19(18):2662–2666, September 2007.

- [206] Ying-Hao Chu, Lane W. Martin, Mikel B. Holcomb, Martin Gajek, Shu-Jen Han, Qing He, Nina Balke, Chan-Ho Yang, Donkoun Lee, Wei Hu, Qian Zhan, Pei-Ling Yang, Arantxa Fraile-Rodríguez, Andreas Scholl, Shan X. Wang, and R. Ramesh. Electric-field control of local ferromagnetism using a magnetoelectric multiferroic. *Nature Materials*, 7(6):478–482, June 2008.
- [207] JJ Yang, YG Zhao, HF Tian, LB Luo, HY Zhang, YJ He, and HS Luo. Electric field manipulation of magnetization at room temperature in multiferroic  $\text{CoFe}_2\text{O}_4/\text{Pb}(\text{Mg}_{1/3}\text{Nb}_{2/3})_{0.7}\text{Ti}_{0.3}\text{O}_3$  heterostructures. *Applied Physics Letters*, 94(21):212504, May 2009.
- [208] Todd Brintlinger, Sung-Hwan Lim, Kamal H. Baloch, Paris Alexander, Yi Qi, John Barry, John Melngailis, Lourdes Salamanca-Riba, I. Takeuchi, and John Cumings. In Situ Observation of Reversible Nanomagnetic Switching Induced by Electric Fields. *Nano Letters*, 10(4):1219–1223, April 2010.
- [209] Kuntal Roy, Supriyo Bandyopadhyay, and Jayasimha Atulasimha. Switching dynamics of a magnetostrictive single-domain nanomagnet subjected to stress. *Physical Review B*, 83(22):224412, June 2011.
- [210] Tao Wu, Alexandre Bur, Kin Wong, Ping Zhao, Christopher S. Lynch, Pedram Khalili Amiri, Kang L. Wang, and Gregory P. Carman. Electrical control of reversible and permanent magnetization reorientation for magnetoelectric memory devices. *Applied Physics Letters*, 98(26):262504, June 2011.
- [211] DE Parkes, SA Cavill, AT Hindmarch, P Wadley, F McGee, CR Staddon, KW Edmonds, RP Champion, BL Gallagher, and AW Rushforth. Non-volatile voltage control of magnetization and magnetic domain walls in magnetostrictive epitaxial thin films. *Applied Physics Letters*, 101(7):072402, August 2012.
- [212] Xuemeng Han, Li Xi, Yue Li, Xiaobin Guo, Dong Li, Zhen Wang, Yalu Zuo, and Desheng Xue. Demonstration of magnetoelectric memory cell in (110)  $[\text{Pb}(\text{Mg}_{1/2}\text{Nb}_{2/3})\text{O}_3]_{0.68}\text{-}[\text{PbTiO}_3]_{0.32}/\text{Ru}/\text{FeCo}$  heterostructures. *Applied Physics Letters*, 105(12):122402, September 2014.
- [213] Yasuhiro Shirahata, Ryota Shiina, Diego López González, Kévin J. A. Franke, Eiji Wada, Mitsuru Itoh, Nikolay A. Pertsev, Sebastiaan van Dijken, and Tomoyasu Taniyama. Electric-field switching of perpendicularly magnetized multilayers. *NPG Asia Materials*, 7(7):e198, July 2015.

- [214] Hasnain Ahmad, Jayasimha Atulasimha, and Supriyo Bandyopadhyay. Reversible strain-induced magnetization switching in FeGa nanomagnets: Pathway to a rewritable, non-volatile, non-toggle, extremely low energy straintronic memory. *Scientific Reports*, 5, December 2015.
- [215] E. De Ranieri, P. E. Roy, D. Fang, E. K. Vehstedt, A. C. Irvine, D. Heiss, A. Casiraghi, R. P. Campion, B. L. Gallagher, T. Jungwirth, and J. Wunderlich. Piezoelectric control of the mobility of a domain wall driven by adiabatic and non-adiabatic torques. *Nature Materials*, 12(9):808–814, September 2013.
- [216] V. Zhukova, J. M. Blanco, M. Ipatov, and A. Zhukov. Magnetoelastic Contribution in Domain-Wall Dynamics of Magnetically Bistable Microwires. *IEEE Transactions on Magnetics*, 47(10):3783–3786, October 2011.
- [217] V. Zhukova, J. M. Blanco, M. Ipatov, and A. Zhukov. Magnetoelastic contribution in domain wall dynamics of amorphous microwires. *Physica B: Condensed Matter*, 407(9):1450–1454, May 2012.
- [218] Arcady Zhukov, Juan Blanco, Mihail Ipatov, Alexander Chizhik, and Valentina Zhukova. Manipulation of domain wall dynamics in amorphous microwires through the magnetoelastic anisotropy. *Nanoscale Research Letters*, 7(1):223, 2012.
- [219] Michael Foerster, Ferran Macià, Nahuel Statuto, Simone Finizio, Alberto Hernández-Mínguez, Sergi Lendínez, Paulo V. Santos, Josep Fontcuberta, Joan Manel Hernández, Mathias Kläui, and Lucia Aballe. Direct imaging of delayed magneto-dynamic modes induced by surface acoustic waves. *Nature Communications*, 8(1):407, September 2017.
- [220] N. A. Pertsev. Giant magnetoelectric effect via strain-induced spin reorientation transitions in ferromagnetic films. *Physical Review B*, 78(21), 2008.
- [221] NA Pertsev. Strain-mediated electric-field control of multiferroic domain structures in ferromagnetic films. *Applied Physics Letters*, 102(11):112407, March 2013.
- [222] A. Herklotz. Reversible strain effect on the magnetization of LaCoO<sub>3</sub> films. *Physical Review B*, 79(9), 2009.
- [223] Kuntal Roy, Supriyo Bandyopadhyay, and Jayasimha Atulasimha. Hybrid spintronics and straintronics: A magnetic technology for ultra low energy computing and signal processing. *Applied Physics Letters*, 99(6):063108, August 2011.

- [224] V. Novosad, Y. Otani, A. Ohsawa, S. G. Kim, K. Fukamichi, J. Koike, K. Maruyama, O. Kitakami, and Y. Shimada. Novel magnetostrictive memory device. *Journal of Applied Physics*, 87(9):6400–6402, May 2000.
- [225] Manuel Bibes and Agnès Barthélémy. Multiferroics: Towards a magnetoelectric memory. *Nature Materials*, 7(6):425–426, June 2008.
- [226] Nicolas Tiercelin, Yannick Dusch, Vladimir Preobrazhensky, and Philippe Pernod. Magnetoelectric memory using orthogonal magnetization states and magnetoelastic switching. *Journal of Applied Physics*, 109(7):07D726, April 2011.
- [227] A. K. Biswas, S. Bandyopadhyay, and J. Atulasimha. Energy-efficient magnetoelastic non-volatile memory. *Applied Physics Letters*, 104(23):232403, June 2014.
- [228] A. I. Morosov and A. S. Sigov. "Long leg" magnetoelectric memory. *Journal of Applied Physics*, 115(22):223909, June 2014.
- [229] Mohammad Salehi Fashami, Kuntal Roy, Jayasimha Atulasimha, and Supriyo Bandyopadhyay. Magnetization dynamics, Bennett clocking and associated energy dissipation in multiferroic logic. *Nanotechnology*, 22(15):155201, April 2011.
- [230] Noel D'Souza, Jayasimha Atulasimha, and Supriyo Bandyopadhyay. Four-state nanomagnetic logic using multiferroics. *Journal of Physics D: Applied Physics*, 44(26):265001, July 2011.
- [231] N. D'Souza, J. Atulasimha, and Supriyo Bandyopadhyay. Energy-Efficient Bennett Clocking Scheme for Four-State Multiferroic Logic. *IEEE Transactions on Nanotechnology*, 11(2):418–425, March 2012.
- [232] Noel D'Souza, Mohammad Salehi Fashami, Supriyo Bandyopadhyay, and Jayasimha Atulasimha. Experimental Clocking of Nanomagnets with Strain for Ultralow Power Boolean Logic. *Nano Letters*, 16(2):1069–1075, February 2016.
- [233] S. Srinivasan, A. Sarkar, B. Behin-Aein, and S. Datta. All-Spin Logic Device With Inbuilt Nonreciprocity. *IEEE Transactions on Magnetics*, 47(10):4026–4032, October 2011.
- [234] N. DrSouza, Jayasimha Atulasimha, and Supriyo Bandyopadhyay. An Ultrafast Image Recovery and Recognition System Implemented With Nanomagnets Possessing Biaxial Magnetocrystalline Anisotropy. *IEEE Transactions on Nanotechnology*, 11(5):896–901, September 2012.

- [235] F. Zavaliche, T. Zhao, H. Zheng, F. Straub, M. P. Cruz, P.-L. Yang, D. Hao, and R. Ramesh. Electrically Assisted Magnetic Recording in Multiferroic Nanostructures. *Nano Letters*, 7(6):1586–1590, June 2007.
- [236] Tuomas H. E. Lahtinen, Kévin J. A. Franke, and Sebastiaan van Dijken. Electric-field control of magnetic domain wall motion and local magnetization reversal. *Scientific Reports*, 2:258, February 2012.
- [237] Na Lei, Thibaut Devolder, Guillaume Agnus, Pascal Aubert, Laurent Daniel, Joo-Von Kim, Weisheng Zhao, Theodossis Trypiniotis, Russell P. Cowburn, Claude Chappert, Dafiné Ravelosona, and Philippe Lecoeur. Strain-controlled magnetic domain wall propagation in hybrid piezoelectric/ferromagnetic structures. *Nature Communications*, 4:1378, January 2013.
- [238] Giancarlo Consolo and Giovanna Valenti. Analytical solution of the strain-controlled magnetic domain wall motion in bilayer piezoelectric/magnetostrictive nanostructures. *Journal of Applied Physics*, 121(4):043903, January 2017.
- [239] Se Kwon Kim, Daniel Hill, and Yaroslav Tserkovnyak. Mechanical Actuation of Magnetic Domain-Wall Motion. *Physical Review Letters*, 117(23):237201, November 2016.
- [240] J. Dean, M. T. Bryan, T. Schrefl, and D. A. Allwood. Stress-based control of magnetic nanowire domain walls in artificial multiferroic systems. *Journal of Applied Physics*, 109(2):023915, January 2011.
- [241] M. T. Bryan, J. Dean, and D. A. Allwood. Dynamics of stress-induced domain wall motion. *Physical Review B*, 85(14):144411, April 2012.
- [242] Jia-Mian Hu, Tiannan Yang, Kasra Momeni, Xiaoxing Cheng, Lei Chen, Shiming Lei, Shujun Zhang, Susan Trolier-McKinstry, Venkatraman Gopalan, Gregory P. Carman, Ce-Wen Nan, and Long-Qing Chen. Fast Magnetic Domain-Wall Motion in a Ring-Shaped Nanowire Driven by a Voltage. *Nano Letters*, 16(4):2341–2348, April 2016.
- [243] Tuomas H. E. Lahtinen, Jussi O. Tuomi, and Sebastiaan van Dijken. Pattern Transfer and Electric-Field-Induced Magnetic Domain Formation in Multiferroic Heterostructures. *Advanced Materials*, 23(28):3187–3191, July 2011.

- [244] Kévin J. A. Franke, Ben Van de Wiele, Yasuhiro Shirahata, Sampo J. Hämäläinen, Tomoyasu Taniyama, and Sebastiaan van Dijken. Reversible Electric-Field-Driven Magnetic Domain-Wall Motion. *Physical Review X*, 5(1):011010, February 2015.
- [245] Ben Van de Wiele, Lasse Laurson, Kévin J. A. Franke, and Sebastiaan van Dijken. Electric field driven magnetic domain wall motion in ferromagnetic-ferroelectric heterostructures. *Applied Physics Letters*, 104(1):012401, January 2014.
- [246] Ben Van de Wiele, Jonathan Leliaert, Kévin J. A. Franke, and Sebastiaan van Dijken. Electric-field-driven dynamics of magnetic domain walls in magnetic nanowires patterned on ferroelectric domains. *New Journal of Physics*, 18(3):033027, 2016.
- [247] Jia-Mian Hu, Tiannan Yang, Jianjun Wang, Houbing Huang, Jinxing Zhang, Long-Qing Chen, and Ce-Wen Nan. Purely Electric-Field-Driven Perpendicular Magnetization Reversal. *Nano Letters*, 15(1):616–622, January 2015.
- [248] J. Stöhr, H. C. Siegmann, A. Kashuba, and S. J. Gamble. Magnetization switching without charge or spin currents. *Applied Physics Letters*, 94(7):072504, February 2009.
- [249] Ayan Kumar Biswas, Hasnain Ahmad, Jayasimha Atulasimha, and Supriyo Bandyopadhyay. Experimental Demonstration of Complete 180° Reversal of Magnetization in Isolated Co Nanomagnets on a PMN–PT Substrate with Voltage Generated Strain. *Nano Letters*, May 2017.
- [250] Nicolas Tiercelin, Yannick Dusch, Philippe Jacques Pernod, and Vladimir Preobrazhensky. Magnetoelectric memory, December 9 2014. US Patent 8,908,422.
- [251] Yannick Dusch. *Nano-Système Magnéto-Électro-Mécanique (NMEMS) ultra-basse consommation pour le traitement et le stockage de l'information*. PhD thesis, November 2011.
- [252] N. Tiercelin, Y. Dusch, S. Giordano, A. Klimov, V. Preobrazhensky, and P. Pernod. Strain Mediated Magnetoelectric Memory. In Jayasimha Atulasimha and Supriyo Bandyopadhyay, editors, *Nanomagnetic and Spintronic Devices for Energy-Efficient Memory and Computing*, pages 221–257. John Wiley & Sons, Ltd, 2016.
- [253] Nicolas Tiercelin, Yannick Dusch, Alexey Klimov, Stefano Giordano, Vladimir Preobrazhensky, and Philippe Pernod. Room temperature magnetoelectric memory

- cell using stress-mediated magnetoelastic switching in nanostructured multilayers. *Applied Physics Letters*, 99(19):192507, November 2011.
- [254] Yannick Dusch, Nicolas Tiercelin, Alexey Klimov, Stefano Giordano, Vladimir Preobrazhensky, and Philippe Pernod. Stress-mediated magnetoelectric memory effect with uni-axial TbCo<sub>2</sub>/FeCo multilayer on 011-cut PMN-PT ferroelectric relaxor. *Journal of Applied Physics*, 113(17):17C719, May 2013.
- [255] Stefano Giordano, Yannick Dusch, Nicolas Tiercelin, Philippe Pernod, and Vladimir Preobrazhensky. Combined nanomechanical and nanomagnetic analysis of magnetoelectric memories. *Physical Review B*, 85(15):155321, April 2012.
- [256] Stefano Giordano, Yannick Dusch, Nicolas Tiercelin, Philippe Pernod, and Vladimir Preobrazhensky. Stochastic magnetization dynamics in single domain particles. *The European Physical Journal B*, 86(6), June 2013.
- [257] S. Giordano, Y. Dusch, N. Tiercelin, P. Pernod, and V. Preobrazhensky. Thermal effects in magnetoelectric memories with stress-mediated switching. *Journal of Physics D: Applied Physics*, 46(32):325002, August 2013.
- [258] Yannick Dusch, Vasyl Rudenko, Nicolas Tiercelin, Stefano Giordano, Vladimir Preobrazhensky, and Philippe Pernod. Hysteretic magnetoresistance in stress controlled magnetic memory device. *Nanomatériaux et nanostructures*, 2:44–50, 2012.
- [259] Alexey Klimov, Nicolas Tiercelin, Yannick Dusch, Stefano Giordano, Théo Mathurin, Philippe Pernod, Vladimir Preobrazhensky, Anton Churbanov, and Sergei Nikitov. Magnetoelectric write and read operations in a stress-mediated multiferroic memory cell. *Applied Physics Letters*, 110(22):222401, May 2017.
- [260] M. H. Kryder and C. S. Kim. After Hard Drives – What Comes Next? *IEEE Transactions on Magnetics*, 45(10):3406–3413, October 2009.
- [261] Yannick Dusch, Nicolas Tiercelin, Alexey Klimov, Vasyl Rudenko, Yury Ignatov, Sami Hage-Ali, Philippe Pernod, and Vladimir Preobrazhensky. Patterned L10-FePt for polarization of magnetic films. *Journal of Applied Physics*, 109(7):07A720, April 2011.
- [262] T. Fischbacher, M. Franchin, G. Bordignon, and H. Fangohr. A Systematic Approach to Multiphysics Extensions of Finite-Element-Based Micromagnetic Simulations: Nmag. *IEEE Transactions on Magnetics*, 43(6):2896–2898, June 2007.

- [263] Christophe Geuzaine and Jean-François Remacle. Gmsh: A 3-D finite element mesh generator with built-in pre- and post-processing facilities. *International Journal for Numerical Methods in Engineering*, 79(11):1309–1331, September 2009.
- [264] Alexey Klimov, Nicolas Tiercelin, Vladimir Preobrazhensky, and Philippe Pernod. Inhomogeneous spin reorientation transition (srt) in giant magnetostrictive TbCo<sub>2</sub>/FeCo multilayers. *IEEE transactions on magnetics*, 42(10):3090–3092, 2006.
- [265] Martin Kružík and Andreas Prohl. Recent Developments in the Modeling, Analysis, and Numerics of Ferromagnetism. *SIAM Review*, 48(3):439–483, 2006.
- [266] Théo Mathurin, Stefano Giordano, Yannick Dusch, Nicolas Tiercelin, Philippe Pernod, and Vladimir Preobrazhensky. Stress-mediated magnetoelectric control of ferromagnetic domain wall position in multiferroic heterostructures. *Applied Physics Letters*, 108(8):082401, February 2016.
- [267] Théo Mathurin, Stefano Giordano, Yannick Dusch, Nicolas Tiercelin, Philippe Pernod, and Vladimir Preobrazhensky. Mechanically driven domain wall movement in magnetoelastic nanomagnets. *The European Physical Journal B*, 89(7):169, July 2016.
- [268] Izrail Moiseevitch Gelfand, Richard A Silverman, et al. *Calculus of variations*. Courier Corporation, 2000.
- [269] Julius Adams Stratton. *Electromagnetic theory. International series in pure and applied physics*. McGraw-Hill, New York, 1941.
- [270] Christian Miehe and Gautam Ethiraj. A geometrically consistent incremental variational formulation for phase field models in micromagnetics. *Computer Methods in Applied Mechanics and Engineering*, 245–246:331–347, October 2012.
- [271] Isaak D Mayergoyz, Giorgio Bertotti, and Claudio Serpico. *Nonlinear magnetization dynamics in nanosystems*. Elsevier, 2009.
- [272] Herbert B Keller. *Numerical solution of two point boundary value problems*, volume 24. SIaM, 1976.
- [273] Alfio Quarteroni, Riccardo Sacco, and Fausto Saleri. *Numerical mathematics*, volume 37. Springer Science & Business Media, 2010.

- [274] Marco Beleggia, Shakul Tandon, Yimei Zhu, and Marc De Graef. On the computation of the demagnetization tensor for particles of arbitrary shape. *Journal of Magnetism and Magnetic Materials*, 272-276, Supplement:E1197–E1199, May 2004.
- [275] M. Beleggia, S. Tandon, Y. Zhu, and M. De Graef. On the magnetostatic interactions between nanoparticles of arbitrary shape. *Journal of Magnetism and Magnetic Materials*, 278(1-2):270–284, July 2004.
- [276] Yongxin Y. Huang and Yongmei M. Jin. Phase field modeling of magnetization processes in growth twinned Terfenol-D crystals. *Applied Physics Letters*, 93(14):142504, October 2008.
- [277] A Kolmogorov and S Fomin. *Elements of the Theory of Functions and Functional Analysis, Moscow, 1974*. Dover, New York, 1999.
- [278] Feifei Wang, Laihui Luo, Dan Zhou, Xiangyong Zhao, and Haosu Luo. Complete set of elastic, dielectric, and piezoelectric constants of orthorhombic  $0.71\text{Pb}(\text{Mg}_{1/3}\text{Nb}_{2/3})\text{O}_3$ - $0.29\text{PbTiO}_3$  single crystal. *Applied Physics Letters*, 90(21):212903, May 2007.
- [279] Théo Mathurin, Stefano Giordano, Yannick Dusch, Nicolas Tiercelin, Philippe Pernod, and Vladimir Preobrazhensky. Domain-wall dynamics in magnetoelastic nanostripes. *Physical Review B*, 95(14):140405, April 2017.
- [280] Yaroslav Tserkovnyak, Arne Brataas, and Gerrit E. W. Bauer. Enhanced Gilbert Damping in Thin Ferromagnetic Films. *Physical Review Letters*, 88(11):117601, February 2002.
- [281] A. Clark, R. Abbundi, and W. Gillmor. Magnetization and magnetic anisotropy of  $\text{TbFe}_2$ ,  $\text{DyFe}_2$ ,  $\text{Tb}_{0.27}\text{Dy}_{0.73}\text{Fe}_2$  and  $\text{TmFe}_2$ . *IEEE Transactions on Magnetics*, 14(5):542–544, September 1978.
- [282] Eric E Fullerton, J. S Jiang, and S. D Bader. Hard/soft magnetic heterostructures: model exchange-spring magnets. *Journal of Magnetism and Magnetic Materials*, 200(1-3):392–404, October 1999.
- [283] Nicolas Tiercelin. *Phénomènes dynamiques non linéaires dans les films minces magnétostrictifs au voisinage de la transition de réorientation de Spin : Application aux micro systèmes*. PhD thesis, January 2000.

- [284] Tao Wu, Ping Zhao, Mingqiang Bao, Alexandre Bur, Joshua L. Hockel, Kin Wong, Kotekar P. Mohanchandra, Christopher S. Lynch, and Gregory P. Carman. Domain engineered switchable strain states in ferroelectric (011)  $[\text{Pb}(\text{Mg}_{1/3}\text{Nb}_{2/3})\text{O}_3]_{(1-x)}\text{PbTiO}_3$  (PMN-PT,  $x \approx 0.32$ ) single crystals. *Journal of Applied Physics*, 109(12):124101, June 2011.
- [285] S. W. Choi, R T. R. ShROUT, S. J. Jang, and A. S. Bhalla. Dielectric and pyroelectric properties in the  $\text{Pb}(\text{Mg}_{1/3}\text{Nb}_{2/3})\text{O}_3\text{-PbTiO}_3$  system. *Ferroelectrics*, 100(1):29–38, December 1989.
- [286] Michael T. Lanagan, Ning Yang, Dinesh C. Dube, and Sei-Joo Jang. Dielectric Behavior of the Relaxor  $\text{Pb}(\text{Mg}_{1/3}\text{Nb}_{2/3})\text{O}_3\text{-PbTiO}_3$  Solid-Solution System in the Microwave Region. *Journal of the American Ceramic Society*, 72(3):481–483, March 1989.
- [287] Xiangyong Zhao, Bijun Fang, Hu Cao, Yiping Guo, and Haosu Luo. Dielectric and piezoelectric performance of PMN-PT single crystals with compositions around the MPB: influence of composition, poling field and crystal orientation. *Materials Science and Engineering: B*, 96(3):254–262, December 2002.
- [288] Yiping Guo, Haosu Luo, Tianhou He, Haiqing Xu, and Zhiwen Yin. Domain configuration and ferroelectric related properties of the (110) cub cuts of relaxor-based  $\text{Pb}(\text{Mg}_{1/3}\text{Nb}_{2/3})\text{O}_3\text{-PbTiO}_3$  single crystals. *Japanese journal of applied physics*, 41(3R):1451, 2002.
- [289] K. K. Rajan, M. Shanthi, W. S. Chang, J. Jin, and L. C. Lim. Dielectric and piezoelectric properties of [001] and [011]-poled relaxor ferroelectric PZN-PT and PMN-PT single crystals. *Sensors and Actuators A: Physical*, 133(1):110–116, January 2007.
- [290] Rui Zhang, Bei Jiang, and Wenwu Cao. Single-domain properties of  $0.67\text{Pb}(\text{Mg}_{1/3}\text{Nb}_{2/3})\text{O}_3\text{-}0.33\text{PbTiO}_3$  single crystals under electric field bias. *Applied Physics Letters*, 82(5):787–789, February 2003.
- [291] Rui Zhang, Bei Jiang, and Wenwu Cao. Elastic, piezoelectric, and dielectric properties of multidomain  $0.67\text{Pb}(\text{Mg}_{1/3}\text{Nb}_{2/3})\text{O}_3\text{-}0.33\text{PbTiO}_3$  single crystals. *Journal of Applied Physics*, 90(7):3471–3475, October 2001.

- [292] Muhtar Ahart, Maddury Somayazulu, R. E. Cohen, P. Ganesh, Przemyslaw Dera, Ho-kwang Mao, Russell J. Hemley, Yang Ren, Peter Liermann, and Zhigang Wu. Origin of morphotropic phase boundaries in ferroelectrics. *Nature*, 451(7178):545–548, January 2008.
- [293] C. Tantigate, J. Lee, and A. Safari. Processing and properties of  $\text{Pb}(\text{Mg}_{1/3}\text{Nb}_{2/3})\text{O}_3$ - $\text{PbTiO}_3$  thin films by pulsed laser deposition. *Applied Physics Letters*, 66(13):1611–1613, March 1995.
- [294] Romain Herdier, M. Detalle, David Jenkins, Caroline Soyer, and Denis Remiens. Piezoelectric thin films for MEMS applications - A comparative study of PZT, 0.7PMN-0.3PT and 0.9PMN-0.1PT thin films grown on Si by RF magnetron sputtering. *Sensors and Actuators A: Physical*, 148(1):122–128, November 2008.
- [295] K. A. Bui-Thi, P. Lecoœur, M. Pham-Thi, and G. Garry. Phase optimisation of PMN-PT thin films deposited by Pulsed Laser Deposition on MgO substrates and Pt-coated silicon. In *2010 IEEE International Symposium on the Applications of Ferroelectrics (ISAF)*, pages 1–4, August 2010.
- [296] Kim Anh Bui Meura. *Réalisation des couches minces PMN-PT dans la technologie MEMS pour les applications hyperfréquences*. PhD thesis, Université Paris Sud-Paris XI, 2012.
- [297] E du Trémolet de Lacheisserie. Definition and measurement of the surface magnetoelastic coupling coefficients in thin films and multilayers. *Physical review B*, 51(22):15925, 1995.
- [298] T. Zhao, H. Fujiwara, G. J. Mankey, C. Hou, and M. Sun. Reconstruction of in-plane magnetization distributions from magnetic force microscope images. *Journal of Applied Physics*, 89(11):7230–7232, June 2001.
- [299] A. Thiaville, J. Miltat, and J. M. García. Magnetic Force Microscopy: Images of Nanostructures and Contrast Modeling. In Professor Herbert Hopster and Professor Hans Peter Oepen, editors, *Magnetic Microscopy of Nanostructures*, NanoScience and Technology, pages 225–251. Springer Berlin Heidelberg, 2005.
- [300] L. Abelman, A. van den Bos, and C. Lodder. Magnetic Force Microscopy — Towards Higher Resolution. In Professor Herbert Hopster and Professor Hans Peter Oepen, editors, *Magnetic Microscopy of Nanostructures*, NanoScience and Technology, pages 253–283. Springer Berlin Heidelberg, 2005.

- [301] K. Postava, A. Maziewski, A. Stupakiewicz, A. Wawro, L. T. Baczewski, S. Visnovsky, and T. Yamaguchi. Transverse magneto-optical Kerr effect measured using phase modulation. *Journal of the European Optical Society - Rapid publications*, 1(0), October 2006.
- [302] Gor Lebedev. *Composites multiferroïques pour dispositifs magnéto-électriques intégrés*. PhD thesis, Université de Grenoble, 2012.
- [303] Mark A McCord and Michael J Rooks. Spie handbook of microlithography, micro-machining and microfabrication. In *SPIE, Bellingham*, 2000.
- [304] M. Demartin Maeder, D. Damjanovic, and N. Setter. Lead Free Piezoelectric Materials. *Journal of Electroceramics*, 13(1-3):385–392, July 2004.
- [305] Chang-Hyo Hong, Hwang-Pill Kim, Byung-Yul Choi, Hyoung-Su Han, Jae Sung Son, Chang Won Ahn, and Wook Jo. Lead-free piezoceramics - Where to move on? *Journal of Materiomics*, 2(1):1–24, March 2016.
- [306] Izrail Solomonovich Gradshteyn and Iosif Moiseevich Ryzhik. *Table of integrals, series, and products*. Academic press, 2014.
- [307] M Abramowitz and IA Stegun. *Handbook of Mathematical Functions*. Dover Publishers, New York, 1970.
- [308] Frank WJ Olver. *NIST Handbook of Mathematical Functions Hardback and CD-ROM*. Cambridge University Press, 2010.
- [309] Romain Ravaud and Guy Lemarquand. Magnetic Field Produced by a Parallelepipedic Magnet of Various and Uniform Polarization. *Progress In Electromagnetics Research*, 98:207–219, 2009.

## **Magnetoelectric manipulation of transverse domain walls in magnetoelastic nanostructures**

The manipulation of magnetic domain walls—that separate regions of uniform magnetization—is associated with both fundamental and technological research interests. A large part of the literature on domain wall motion deals with the use of magnetic fields and electric currents. However, several concerns—most notably energy dissipation—motivates the search for alternatives. Among potential candidates, the mechanical stress-mediated magnetoelectric coupling in magnetoelastic/piezoelectric heterostructures seems promising. In this thesis, it is shown that the combination of a bias magnetic field and uniform mechanical stress can induce unidirectional domain wall motion in nanostructures with uniaxial anisotropy. Static and dynamic aspects of this phenomenon are studied by means of ad hoc numerical procedures simulating the mechanical coupling of 011-cut PMN-PT generating the stress, and TbCo<sub>2</sub>/FeCo multilayers magnetoelastic nanostructures. The design of the cross section profile in nanostructures allows to tailor the response of the system, enabling for instance the control of domain wall position in confined geometries. The associated dynamics stands apart from known regimes because of the shape of the domain wall. The existence of steady-state regimes in nanostripes of constant width shows that velocities comparable to those of other techniques can be obtained, for a fraction of the energy required. Experimental investigations resulted in the development of a successful fabrication process on PMN-PT and the exploration of the magnetoelectric effect.

**Keywords** domain wall, magnetoelastic, magnetoelectric, mechanical stress, piezoelectric, spintronic, nanostructures, nanotechnology

## **Manipulation magnétoélectrique de parois de domaine transverses dans des nanostructures magnétoélastiques**

La manipulation de parois de domaine magnétique, qui séparent des régions d'aimantation uniforme dans les matériaux, est associée à des enjeux à la fois fondamentaux et technologiques. De nombreux travaux portent sur le déplacement de parois par champs magnétiques et courants électriques. Cependant certaines préoccupations, notamment la dissipation d'énergie, motivent la recherche d'alternatives. Parmi les solutions potentielles, le couplage magnétoélectrique par l'intermédiaire de contraintes mécaniques dans des hétérostructures magnétoélastique/piézoélectrique paraît prometteur. Dans cette thèse, il est montré que l'association d'un champ magnétique de biais et de contraintes mécaniques uniformes peut engendrer le déplacement unidirectionnel d'une paroi de domaine transverse dans des nanostructures à anisotropie uniaxiale. Les considérations statiques et dynamiques de ce phénomène sont étudiées par le biais de procédures numériques ad hoc simulant le couplage mécanique entre substrat de PMN-PT de coupe 011 générant des contraintes, et nanostructures multicouches magnétoélastiques TbCo<sub>2</sub>/FeCo. Le design du profil de section des nanostructures permet de moduler la réponse du système, par exemple pour contrôler la position de parois confinées. La dynamique du système se distingue des régimes habituels de par la forme de la paroi de domaine. L'atteinte de régimes permanents dans des nanorubans montre que des vitesses comparables aux autres techniques sont obtenues, pour une dissipation d'énergie beaucoup plus faible. Des travaux expérimentaux ont permis de mettre au point une procédure de fabrication sur PMN-PT et d'explorer l'effet magnétoélectrique.

**Mots-clés** paroi de domaine, magnétoélastique, magnétoélectrique, contrainte mécanique, piézoélectrique, spintronique, nanostructures, nanotechnologie